Potassium acetate treatment as a potential means for stabilising extra sensitive, halloysite-rich soils in the Bay of Plenty, New Zealand — A novel approach to an old issue.

A thesis

submitted in fulfilment

of the requirements for the degree

of

Doctor of Philosophy in Science

at

The University of Waikato

by

Thomas Paul Robertson

THE UNIVERSITY OF
WAIKATO
Te Whare Wānanga o Waikato

2025

Abstract

Landslides are a rapid, destructive natural hazard that pose a significant risk to human life and infrastructure. Globally and in New Zealand, landslides are among the most significant hazards. Within New Zealand, it is estimated that the annual costs associated with landslides are between NZ$250–300 million, with over 600 fatalities recorded. While the types of landslides in New Zealand vary due to changeable geology and triggering conditions, one area that is particularly heavily affected is the Western Bay of Plenty region, specifically the Ōmokoroa peninsula, where numerous landslides have occurred. A key contributor to this instability is the presence of a series of weathered primary and reworked rhyolitic tephra deposits dominated by halloysite, known as the Pahoia Tephra, that exhibit a sensitive response. Based on successful tests undertaken in the Northern Hemisphere using potassium chloride salt wells, as well as a pilot study conducted on the same halloysitic materials, the research reported here aimed to treat a halloysite-rich sensitive soil with potassium acetate to determine if the soil could be regarded as strengthened.

Atterberg limit testing of the soil showed the untreated Pahoia Tephra to have a liquid limit higher than the natural moisture content (61%), meeting the requirements for an extra-sensitive soil, as was determined by field shear vane tests. Treatment with the potassium acetate increased the liquid limit (58%–65%) and reduced the liquidity index to below 1 (2.1 untreated, 0.57 treated). Treatment of the soil did produce a drastic increase in shear strength within the soil, with effective cohesion increasing from 4.2 kPa to 40.9 kPa following 12 months of treatment, while effective friction angle was slightly reduced from 29.8^{o} to 25.3^{o}. Stress paths of the soil show a large shift in behaviour, with samples no longer dilating during the pre-failure stage.

To explain these changes, various mineralogical and chemical analyses were undertaken. X-ray diffraction analysis showed no expansion of the clay and lack of intercalation (all halloysite showing 10.1 Å). The Fourier transform infrared testing yielded a similar result, with no notable shifts observed in the 3600 cm^{-1} wavenumber peaks. With this said, new peaks corresponding to an interaction between potassium acetate and the silica sheet present within halloysite were noted. Scanning electron microscope analyses showed, following 12 months of treatment of the soil, a shrinking of the clay spheroids over the duration of treatment.

From these findings, it was theorised that, while the potassium acetate did not intercalate into the halloysite spheroids themselves, the potassium acetate interacted with the external silica sheet so that it curled and rolled, resulting in a smaller spheroid, with acetate entering into the ditrigonal space within the silica sheet and displacing the H_2O ('water') present. This resulted in a twofold action, with the second action leading to the creation of stronger short-chain van der Waals forces between clay spheroids, thereby increasing cohesion within the soil.

While the initial aim of this research was achieved, a large number of avenues have been opened that certainly warrant further investigation.

Acknowledgements

I would like to thank a number of people who have been instrumental in helping me throughout the course of this thesis. Firstly, to Dr Danielle Bertram. While you haven't been here throughout the whole journey, your guidance, support and ability to put up with my incredibly poor grammar, aversion to consistent tenses, and lack of coherent writing at times over the past 4-5 years has been a saving grace. Your constant encouragement to get this PhD done, first as my colleague, then as supervisor, and finally as my chief supervisor has been invaluable to me and I cannot understate how fantastic you have been throughout. Though I'm sure you regret taking on the supervisorship as you correct yet another endash in my drafts.

Secondly to Dr Vicki Moon, my initial chief supervisor, who foolishly agreed to take me, a very average undergraduate student, on as a master's student back in 2016 and had to retire to finally get rid of me. I cannot express my thanks enough to you for taking a chance on me back then, and then continuing to stick with me until the end of my PhD.

To Professor David Lowe, your expertise and knowledge of all things soils has been an invaluable asset throughout this thesis, and your joie de vie for those soils certainly kindled a keen interest in my learning of the subject.

To my amazing partner Lauren, who for some reason stuck with and supported me throughout. You were my rock, the person who believed in me, even when I didn't. Thank you for being there for all the late night, long-winded ramblings of sensitive soil and basal spaces. Without you I do not think I could have achieved what I have. To my daughter Lily, you gave me the determination to finally get this PhD finished. To Moose, you gave me some well needed respite and quiet contemplation, even if it was chasing around after you slipped your harness. To my parents thank you for supporting me and believing in me, you laid a foundation for me to be able to grow and achieve this work.

To Jack, Sophia, and Cole, thank you for all the help you provided. From technical advice to Pokémon battles and yarns, you have been invaluable throughout this journey. Oh, and to Tess and Roj, yes you get a shout out too like I promised, even with all the grief and nuisance you caused me.

Table of Contents

List of Figures

List of Tables

Nomenclature

Ps	Particle Density
σ'	Effective Stress
Φ	Friction Angle
Φ’	Effective Friction Angle
µm	Micrometre
µs/cm	Micro Siemen per Centimetre
Å	Angstrom
AIPEA	Association Internationale Pour l’edute des Argiles
AL^{3+}	Aluminium Ion
ASTM	American Society for Testing and Materials
Ar	Adsorption Ratio
B	Saturation Ratio
BoP	Bay of Plenty
Ca^{2+}	Calcium Ion
cc	Cubic Centimetre
CD	Consolidated Drained
cm^{-1}	Centimetre (Spectroscopic)
Cs^{+}	Caesium Ion
CSL	Critical State Line
CU	Consolidated Undrained
C_u	Undisturbed Shear Strength
C_{ur}	Remoulded Shear Strength
D-Vol	Volume Change
e	Void Ratio
e_o	Initial Void Ratio
Δe	Change in Void Ratio
ESRI	Environmental Systems Research Institute
Fe^{3+}	Iron Ion
FTIR	Fourier Transform Infrared Spectroscopy
FVT	Field Vane Technique
g	Gram
H_2O	Water
H_3O^{+}	Hydronium Ion
ISO	International Standards Organisation
K^{+}	Potassium Ion
K_2CO_3	Potassium Carbonate
K-Acetate	Potassium Acetate
KCH_3COO	Potassium Acetate
KCl	Potassium Chloride
kgm^{-3}	Kilograms per Meter Cubed
kN	Kilonewton
kPa	Kilopascal
LI	Liquid Index
LL	Liquid Limit
LVDT	Linear Variable Displacement Transformer
m	Metre
m^2	Metres Squared
m^3	Metres Cubed
Ma	Million Years

Mc	Moisture Content
MCS	Mushroom Cap Shape
mg/L	Milligrams Per Litre
Mg^{2+}	Magnesium Ion
mm	Millimetre
MPa	Megapascal
mS	MilliSiemens
ms^{-1}	Metres Per Second
n	Porosity
Na^{+}	Sodium Ion
NH_4^{+}	Ammonium Ion
NMC	Natural Moisture Content
NZGS	New Zealand Geotechnical Society
NZS	New Zealand Standard
^{o}C	Degrees Centigrade
OH	Hydroxyl Group
PI	Plastic Index
PL	Plastic Limit
PSZ	Primary Shear Zone
Rb	Rubidium
S_r	Saturation Ratio
SSZ	Secondary Shear Zone
S_t	Sensitivity
S_u	Undrained Shear Strength
T_{100}	Time Taken for 100% Pore Pressure Dissipation
UCS	Unconfined Compressive Strength
UK	United Kingdom
V	Total voids
V_v	Volume of voids
WBoP	Western Bay of Plenty
XRD	X-Ray Diffraction

Chapter 1
Introduction

1.1 Background

Landslides are a rapid, destructive natural hazard that pose a significant risk to human life and infrastructure. Landslides are defined as a movement of slope-forming material, be it soil, rock or debris, that moves in a downward and outward direction along a slope due to failure of some kind (Varnes, 1958; Hungr et al., 2014). Movement may involve flowing, sliding, toppling, falling or spreading, with landslides often exhibiting a combination of these movements at the same time or during the lifetime of the failure.

On a global scale, landslides are among the most significant natural hazards, with studies undertaken in the 1970s showing that slope failures account for 14% of the total global casualties from natural hazards in any given year (Varnes, 1984). In contrast, the International Disaster Database (2015) suggested that landslides only accounted for 4.9% of all natural disaster events between 1990 and 2015, and only accounted for 1.3% of all fatalities. However, subsequent studies have determined this to be a significant underestimation (1400–2000% underestimation in fatal event counting and 331–430% underestimation in total fatalities) (Petley, 2012; Kirschbaum et al., 2015).While the risk to human life is a key factor tackling landslides, one aspect that should not be ignored is the impact from landslides to infrastructure and the environment. This impact though is frequently underestimated, often due to the co-occurrence of landslides with other natural hazard events (i.e. earthquakes, cyclones) resulting in the subsequent costs and damages being attributed to the overarching natural hazard event. Estimates in the early 2000s suggested that around US$20 billion is lost globally every year due to landslides, while in the US alone, between US$2–4 billion is lost annually (Crovelli, 2000; Sim et al., 2024).

Within New Zealand, it is estimated that the annual costs associated with landslides are between NZ$250–300 million, with over 600 fatalities recorded since 1843 (Rosser et al., 2017). However, these numbers are likely higher, as previously mentioned, fatalities and costs may be hidden due to landslides occurrence alongside other natural disasters (Rosser et al., 2017). Within New Zealand, landslide types vary due to the changeable geology across the country. Some recent examples of the impact of landslides in New Zealand include:

- The State Highway 3 (SH3) Manawatu Gorge landslide in 2017 (after multiple failures in the 1990s and 2010) resulted in the permanent closure of the gorge section of the road and, ultimately, re-alignment of SH3 (Stewart, 2021).
- The Cape Kidnappers debris avalanche in January 2018, during which two tourists walking beneath the eventual slip were caught and seriously injured. The slip, in which 25,500 m^3 of material was displaced, was determined to have no clear source and no apparent precursors, raising concerns about further failures within the area (Vilder et al., 2019).
- The pair of fatal landslides in the Auckland region in early 2023. The first followed the 27th of January, Auckland Anniversary Storm, when a fatal slip (just metres from a previous 1997 slip site) occurred in Parnell, Auckland. The second incident occurred during Cyclone Gabrielle in Muriwai, on the West Auckland coast, in February 2023. It is worth noting that the damage caused by all landslides during these events is estimated to have cost over US$8.6 billion (Brook & Nicoll, 2024).

One region in New Zealand that is heavily affected by landslides is the Bay of Plenty (BoP). In particular, the Western Bay of Plenty (WBoP) region, including Tauranga and the land to the north and west of the city, has experienced numerous large and small landslides. One key reason for this is the presence of sensitive volcanic-derived clay layers throughout the region (Moon et al., 2013). Globally, soils that elicit a sensitive response are a well-established contributor to slope instability, directly linked to large retrogressive landslides and flows that pose significant threats to infrastructure, local environments and human health (Quinn et al., 2011).

Sensitive soils are defined as soils where the ratio of undisturbed to remoulded shear strength at similar moisture contents is greater than 4 (Skempton & Northey, 1952). Within New Zealand, soils that exhibit a sensitive response are predominantly derived from weathered rhyolitic and andesitic tephra deposits. The sensitivity source varies: in some instances, sensitivity is derived from direct hydrothermal alteration of the soil following deposition; others have developed sensitivity following the weathering of tephra fall deposits derived from volcanic activity across the central North Island in the last two million years (Jacquet, 1990; Torrance, 1992; Lowe & Churchman, 2016).

Some of the most notable slips affected by these sensitive volcanic deposits in the WBoP region (including Tauranga City) include the Bramley Drive slip in Ōmokoroa in 1979

(along with numerous other slips occurring on the Ōmokoroa peninsula) (Gulliver & Houghton, 1980), the Ruahihi Dam canal failures in the 1980s (Burns & Cowbourne, 2003), the Ōtumoetai slips in 2005 (Hegan et al., 2005), the 2011 and 2012 slips in Ōmokoroa (Moon et al., 2013), the 2017 Cyclone Cook and Debbie failures across multiple areas within the region (Kluger et al., 2020) and, more recently, the 2023 Cyclone Gabrielle failures that impacted numerous areas within the region, including the near-fatal slips in Egret Drive on the Maungatapu Peninsula.

The continued recurrence of these failures across the WBoP region is a significant issue, as this impacts a wide range of facets for both local government and the people living there. Impacts from these failures include hazards posed to infrastructure, such as power lines, water pipes and mains systems (including sewerage), transport infrastructure, drainage and stormwater systems, as well as the overall safety of those living in affected areas. To date, several attempts have been made to understand and explain the methods of failure and the reasons that these failures occur within the soil with a reasonable degree of success (Gulliver & Houghton, 1980; Wyatt, 2009; Arthurs, 2010; Cunningham, 2012; Moon et al., 2013; Mills, 2016; Moon et al., 2017; Kluger et al., 2017, 2022). These studies have highlighted the Pahoia Tephra Sequence, a series of weathered primary and reworked rhyolitic tephra deposits containing halloysitic clay minerals, as a key contributor to the observed landslides.

Even with a reasonable understanding of why these failures occur, there has been limited consideration of a method to prevent further failures from occurring and mitigate future damage to property and infrastructure. Overseas, attempts to stabilise sensitive soil slides have shown success through the usage of potassium chloride (KCl) salt wells on sensitive soil deposits (illite clay) derived from a marine environment (Moum et al., 1968, 1971; Helle et al., 2015, 2017). Initial testing conducted in 2017 on halloysite-rich, sensitive soil deposits (Robertson, 2017) using potassium carbonate (K_2CO_3) based on testing undertaken in previous studies (Garrett & Walker, 1959; Wada, 1959a, 1959b, 1961; Carr et al., 1978) showed promise as a means of stabilising landslide-prone, sensitive clays. Further testing with alternative treatments was hampered due to Cyclones Cook and Debbie, which passed through the region in early 2017, causing widespread failures and posing a significant risk to researchers' attempts to sample fresh material.

1.2 Research Aim

The overarching research aim of this thesis is to determine whether a halloysite-rich, sensitive clay soil prone to large retrogressive landslides can be successfully treated with a potassium metal salt to reduce its sensitivity and increase the soil's strength, thereby reducing the likelihood of future failure within the soil.

To achieve this aim, several individual research objectives, as well as a subsequent research goal, have been developed. These questions investigate multiple aspects related to the geomechanics of the clay soil, the clay chemistry and its relation to the potassium metal salt used. These objectives are as follows:

1. Determine how potassium acetate can be introduced to samples of sensitive soil in the laboratory.
2. Quantify how geomechanical characteristics (including Atterberg limits, triaxial strength and failure characteristics) of the sensitive soil are influenced by the introduction of potassium acetate.
3. Determine the influence of potassium acetate on the clay on a chemical and physical scale.

These objectives lead to an overarching research goal of:

4. Synthesise objectives (2) and (3) by developing a working theory as to how potassium acetate influences the strength of the halloysite-rich sensitive soil (i.e. a mechanism), considering the chemical and physiological changes that produce the geomechanical changes observed in the clay.

Based on the expected behaviour of potassium acetate and sensitive clays, it is hypothesised that the treatment of a Bay of Plenty extra-sensitive, halloysite-rich clay soil will induce physical and chemical changes within the soil that allow for the 'stabilisation' of the soil in a geomechanical sense.

1.3 Thesis Outline

The thesis is structured as follows:

Chapter 1 briefly introduces the broad content of the issues faced within the Bay of Plenty with regards to sensitive soil landslides and their destructive nature, and presents the main research questions that this thesis will aim to address and answer.

Chapter 2 reviews published literature. This is split into three main sections. The first section covers sensitive soils and their slides; the second provides a closer, more detailed look at halloysite clays, while the third section reviews the literature on the halloysite-potassium acetate complex.

Chapter 3 provides an overview of the various potential sites identified within the Bay of Plenty, followed by the steps taken to filter out unsuitable sites and ultimately select an appropriate sampling site for this study. The selected site is also then characterised.

Following Chapter 3, the thesis is split into two parts. Each part includes chapters laid out as typically found within a thesis or scientific article (i.e., with an Introduction, Methods, Results, and Discussion/Conclusion). Part I (Chapters 4–8) covers geomechanical characterisation and triaxial strength testing. Part II (Chapters 9–13) encompasses clay chemistry and the testing used to determine clay chemistry characteristics and identify any changes following treatment with potassium acetate.

These parts are then followed by a subsequent discussion chapter (Chapter 14) that provides an explanation and theories of what has occurred. This will then be followed by a chapter concluding this research (Chapter 15), providing a summary of the findings and an indication of potential future work.

Chapter 2
Literature Review

2.1 Introduction

This chapter reviews existing literature to provide context for the research undertaken in this thesis. The review is presented in three sections. The first section examines sensitive material sourced from overseas and in New Zealand; the second section provides a detailed analysis of halloysite; and the third section explores halloysite–potassium acetate interactions and its subsequent complexes.

2.2 Sensitive Soil and Its Landslides

2.2.1 Sensitive Soils

Sensitive soils are a phenomenon found across the globe. Soils that exhibit sensitive tendencies have been found in several areas of both the Northern and Southern hemispheres, although the former is far more prevalent. Sensitive deposits can be found in Japan, Canada, Norway, Sweden and New Zealand (Thakur et al., 2017; Jacob et al., 2023). The source of this sensitivity is, in some cases, well-established (Scandinavia) and, in others, less clearly understood (New Zealand).

2.2.2 Definition of Sensitivity

Sensitivity in soil is defined as the ratio of a cohesive soil's undisturbed to remoulded strength at the same moisture content in undrained conditions (Eq. (2.1)).

$$S_T = \frac{C_u}{C_{ur}} \tag{2.1}$$

In this equation, undisturbed strength is denoted as C_u, remoulded strength as C_{ur}, and sensitivity as S_T (Terzaghi, 1944). The values derived from this equation vary depending on the soil tested and allow for the soil's level of sensitivity to be established. The mechanism used to establish this varies with Norway and Sweden generally using the drop cone method (Thakur et al., 2017), while New Zealand uses Field Vane Techniques (FVT) and Japan uses Unconfined Compression Strength testing (UCS) to establish sensitivity (Burns et al., 2005; Tanaka et al., 2012).

Early sensitivity classifications employed a six-stage classification system, with ranges from <1 to >16. Early findings indicated that these classifications were suitable for almost all clay soils, except for heavily over-consolidated clays and boulder clays (Skempton & Northey, 1952). Several of these classifications are shown in Table 2.1. While covering the bulk of soils, it became apparent that Skempton and Northey's (1952) range (Table 2.1a) was not sufficient to adequately describe the kinds of quick clays that were found in Norway; this limitation was addressed in 1953 with four new descriptors added to address the degree of 'quickness' (Rosenqvist, 1953) (Table 2.1b). New Zealand generally adheres to the classification system derived in the New Zealand Geotechnical Society (NZGS) (2005) "Field guide for soil and rock" (Table 2.1c), with values ranging from <2 to >16, essentially a simplified version of Skempton and Northeys original 1952 classification.

Table 2.1 (a) Ranges for sensitivity in clays from Skempton & Northey (1952), with no additional designation for soils with a sensitivity greater than 16 (other than quick). (b) Ranges of sensitivity in clays, as refined by Rosenqvist (1953), with considerations made for Scandinavian clays, of which often produced sensitivities in excess of 16. Rosenqvist (1953) further split these up to allow for a more specific description of how 'quick' quick clays would be (c) The ranges of sensitivity utilised within New Zealand as per the NZGS (2005) "Field guide for soil and rock", these values based on those determined by Skempton and Northey (1952).

(a)

S_t	Designation
0–1	Insensitive Clays
1–2	Clays of low sensitivity
2–4	Clays of medium sensitivity
4–8	Sensitive Clays
8–16	Extra-sensitive clays
16+	Quick clays

(b)

S_t	Designation
1	Insensitive Clays
1–2	Slightly Sensitive Clays
2–4	Medium sensitive clays
4–8	Very sensitive clays
8–16	Slightly quick clays
16–32	Medium quick clays
32–64	Very quick clays
64+	Extra quick clays

(c)

S_t	Designation
<2	Insensitive
2–4	Moderately Sensitive
4–8	Sensitive
8–16	Extra sensitive
16+	Quick

To date, there is no single global standard for quantifying soil sensitivity, with countries containing sensitive material often having their own classification systems, an issue highlighted by Holtz and Kovacs (1981) in their comparison of Swedish and USA classification systems (Table 2.2).

Table 2.2. Comparison of sensitivity classification systems within soil across differing countries, as highlighted by Holtz and Kovacs (1981). This ultimately highlights the potential issues with using differing descriptors across different countries, especially in literature. I.e., where in the US a soil may be designated as 'quick', under the Swedish classification that soil may be regarded as 'medium sensitivity'.

		S_t
Classification	**USA**	**Sweden**
Low Sensitivity	2 – 4	<10
Medium Sensitivity	4 – 8	10 – 30
High Sensitivity	8 – 16	30 – 50
Quick	> 16	50 – 100
Extra Quick		>100

Although the classification systems are part of identifying sensitive soils, if a soil sensitivity rating falls within the "quick" range, further criteria may be applied to qualify the soil as quick instead of being extra sensitive. Some researchers have suggested that a remoulded shear strength of no greater than 0.5 kPa should be achieved for clays within this range to be defined as quick (Torrance, 1992). Within Norway, in addition to the 0.5 kPa requirement for designating soil as quick, a remoulded shear strength of <2 kPa is additionally required for soil to be regarded as sensitive (NGI, 2011). Sweden, however, only requires a remoulded shear strength of 0.4 kPa to designate a soil as quick (Rankka et al., 2004). In contrast, Canadian standards do not apply any additional criteria; instead, they are based on the sensitivity measurement made in the field (CGSFC, 2013). Within New Zealand, the NZGS field handbook does not specify specific remoulded shear strength criteria for designating soil as quick. Still, it is suggested by various authors that a maximum remoulded shear strength of 0.5 kPa, as used in Norway be the benchmark for defining a clay as quick (Torrance, 1992).

2.2.3 Sources of Sensitivity in Soils

As stated, sensitive soils are a global phenomenon that occurs in various environments and originates from diverse sources and deposits. These include soils that are sourced from glacially derived, varved lacustrine, marine, volcanically derived, and fluvially

reworked deposits (Skempton & Northey, 1952; Torrance, 1983; Jacquet, 1990; Rankka et al., 2004; Joussein et al., 2005; Thakur et al., 2017). The various forms of sensitive soil sources will be further discussed below. Where exactly the sensitivity derives from varies. Some suggest sensitivity is related to the electrical potential of the diffuse double layers within deposits, where the larger the electrical potential, the higher the sensitivity (Appelo & Postma, 2005; Mitchell et al., 2005). The presence of non-expanding clays is almost universally noted, with expanding clay minerals, such as smectites, determined as a reducing factor in landslide-prone clays in Canada (Quigley, 1980; Torrance, 1983; Berry & Torrance, 1998). Similarly, a high porosity allowing the sensitive clay to have a natural water content in excess of the liquid limit is a frequent feature, especially in increasingly sensitive quick clays.

Glacially Derived Deposits

Across Scandinavia, eastern Canada, Russia, Alaska and parts of the UK, glacially derived sensitive soils significantly impact infrastructure and human life. These deposits are often equated with some of the more significant and damaging landslides, with both primary damage (direct impact from the soil movement) and secondary damage from events such as tsunamis and seiches observed (Tavenas et al., 1971; Locat et al., 2017; Liu et al., 2021). With these deposits more frequently being found on land either occupied by humans or being converted for occupation, they pose a real risk (Giles, 2020; Liu et al., 2021).

Glacially derived deposits are generally young, with, as suggested by their name, the deposits forming in the period following the last ice age. After the peak of the Northern Hemisphere's last glaciation, the large glacial sheets covering portions of Europe and Canada began to recede. This recession of the ice sheets led to the release of large volumes of ground rock material into the environment, both fresh and marine. This ground 'rock flour' formed during glaciation, with the advancing glaciers' bottom edge entraining and grinding the underlying crystalline metamorphic terrain into fine clay-like powder (Locat, 1995). Due to the type of rock ground, often 2:1 clays such as illite were formed, which, upon the retreat of the glaciers, were carried into marine environments with large volumes of glacial meltwater. In these marine environments, the illite clays sank to the sea floor, flocculating in the water column as a result of the charged nature of the clay surfaces, resulting in illite deposits on the sea floor with edge-to-edge 'house of cards' like structures with trapped salt-rich water within the pore spaces (Skempton & Northey, 1952; Torrance, 1983; Locat et al., 2017).

As a secondary result of the retreat of the glaciers, the tectonic plates of Northern Europe and Canada began to undergo isostatic rebound. As such, those illite deposits, formerly found within a marine lacustrine environment, were now exposed to sub-aerial environments, allowing for the exposure and infiltration into the soil of meteoric water (Brand & Brenner, 1981; Locat et al., 2011). This meteoric water subsequently began to dissolve and remove the salt component in the soil. This loss of a large volume of monovalent cations (in particular sodium) resulted in a collapse of the structure of the 'house of cards', producing a sensitive response to remoulding.

Varved and Lacustrine Deposits

Sensitivity in some clay soils can be attributed to deposition in lacustrine environments. These are found predominantly in the Northern Hemisphere in Canada, Russia, Japan and some parts of Scandinavia (Torrance, 1983). Generally, these formed in large, landlocked inland depressions following the end of the last ice age. These inland depressions were filled with fresh meltwaters from the receding ice sheets, resulting in seasonal variation in the sediment-water ratio entering into the lake and varying the layers of silt/sand to clay content. Varving of the deposit changes dependant on the summer and winter inflows into the lake, with summer flows generally having a silt/sand ratio higher the closer to the source and a tapering deposit of clay and winter deposits being more uniformly spread due to settling through the water column (Quigley, 1980)

The formation of sensitivity in these deposits is thought to originate from several possible sources. One theory is a loss of flocculated structure in the clay following compaction in the sediments. This flocculated structure forms in both summer and winter. The former (summer deposition) forms due to edge-to-edge bonding as the sediment flow passes through the bottom of the lake, and the latter (winter deposition) forms from an ordered structure due to slow deposition in the lake (Smith, 1978). The second possible source is the adsorption ratio of monovalent (sodium $(Na)^{+}$, potassium (K^{+})) to divalent cations (magnesium (Mg^{2+}), calcium (Ca^{2+})). Sensitivity is thought to source from the ratio of monovalent cations to mono and divalent cations (equation (2.2)). Sensitivity is expected to be present where the adsorption ratio (Ar) exceeds 75% (Penner, 1965; Söderblom, 1969; Moum et al., 1971; He et al., 2015).

$$Ar = \frac{Na^{+} + K^{+}}{Na^{+} + K^{+} + Mg^{2+} + Ca^{2+}} \tag{2.2}$$

Volcanically Derived Deposits

Sensitive material can also be found in volcanically derived deposits. The term 'volcanically derived deposit' encompasses material from a volcanic eruptive source, including pyroclastic materials, regardless of the environment of deposition. These deposits include tephra fall beds, ignimbrites and volcanic tuffs (Torrance, 1983). Unlike sensitive soils derived from glacial sources, volcanically derived sensitive soils are not restricted to the Northern Hemisphere. They are found across sites in New Zealand, Japan, Malaysia, Cameroon, several Central American countries, as well as various others (Aomine & Wada, 1962; Quantin et al., 1984; Bailey, 1990a; Adamo et al., 2001; Ndayiragije & Delvaux, 2004; Joussein et al., 2005; Y. Takahashi et al., 2018).

The development of sensitivity in these soils is not entirely clear. Differing deposits may have a variety of contributing factors. Torrance (1992) suggested that sensitivity in volcanic clays may be sourced from two main causes. The first is observed in distal tephra fall deposits. In these instances, the fallout tephras are deposited in an ordered, gentle fashion, allowing for the generation of a large void ratio. This allows for the development of a 'house of cards' style network in the subsequent clays. This is then followed by reworking of some fashion, resulting in a collapse of this network, similar to those observed in the glacial clays of the Northern Hemisphere (Jacquet, 1990; Torrance, 1992). As a result of this reworking, weak short-range bonds between clay particles result, allowing for easy reworking and the development of high sensitivities (Smalley et al., 1984; Moon, 2016; Kluger et al., 2017).

A second leading cause is thought to be the colloidal material found in these deposits. Where the sensitive clays of the Northern Hemisphere are generally dominated by 2:1 illite clay minerals, sensitive volcanic soils often are found to comprise Aluminium (Al)-rich allophane derived from the synthesis of dissolution products weathered from glass mainly in rhyolitic and andesitic tephras (e.g., Lowe and Percival, 1993; Lowe, 1995; McDaniel et al., 2012). It is thought that allophane, comprising tiny nanoscale spherules, acts as a dispersing agent and disrupts the surrounding clay structure, resulting in sensitive responses and generating behaviours of a high undisturbed shear strength but low remoulded shear strength (Jacquet, 1990; Torrance, 1992). In addition to this, the 1:1 clay mineral halloysite has been observed in both New Zealand and Japan as a newly recognised "culprit" in several large-scale retrogressive failures, including flow slides with long runouts (Smalley et al., 1984; G. J. Churchman et al., 2016; Moon, 2016; Kluger et al., 2017, 2022; Kameda et al., 2019; Kameda, 2022).

2.2.4 Sensitive Soils in New Zealand

Soils that exhibit a sensitive response, as identified per the NZGS 2005 handbook for soil and rock, are widespread throughout northern New Zealand. These soils usually exhibit a 'low' level of sensitive response. With this said, there are soils in New Zealand that exhibit a significant sensitive response and actively cause challenges in their environment (Knauf, 2022). These soils generally are from some form of volcanic (typically pyroclastic) deposit (i.e. non- or weakly-welded ignimbrites, tephra-fall deposits) that at some point may have been reworked to produce a sensitive response, and are predominantly found in the upper central North Island affecting areas such as the Bay of Plenty, Waikato and the Auckland region (Smalley et al., 1984; Jacquet, 1990; Arthurs, 2010; Cunningham, 2012; Churchman et al., 2016; Mills, 2016; Moon, 2016; Kitchen, 2021).

While these soils share some similarities (low remoulded shear strength, high void ratio and porosity, and natural water contents in excess of the liquid limit) with certain Northern Hemisphere counterparts (such as Sweden and Canada), a significant difference between the two is the variation in clay mineralogy. While 2:1 clays dominate most sensitive soil deposits in the Northern Hemisphere (Thakur et al., 2017b). Clays in New Zealand that exhibit sensitive responses are dominated by 1:1 clay minerals such as halloysite and Al-rich allophane, a nanocrystalline mineral (Jacquet, 1990; Lowe, 1995; Churchman & Lowe, 2012; Moon, 2016).

Halloysite can exhibit highly sensitive responses, with sensitivities in several cases falling within the extra sensitive to quick range, and numerous examples of typical large retrogressive sensitive soil failures observed within the Bay of Plenty region. Some of these failures include (as recorded, there are likely further failures unrecorded) the Bramley Drive Failure originally in 1979, along with further reactivations in 2011 and 2012, the Ruahihi Canal Failure in 1981, the Hamurana Drive failures around 1979, numerous failures in and around Ōtumoetai and Maungatapu in 2005, and the more recent widespread failures in Ōmokoroa (2017) and Maungatapu (2023) (Gulliver & Houghton, 1980; Smalley et al., 1984; Wyatt, 2009a; Arthurs, 2010; Cunningham, 2012; Moon et al., 2013; Lowe & Churchman, 2016; Mills, 2016; Moon, 2016; Kluger et al., 2017; Beetham, 2023). The common theme between almost all the landslide events mentioned above is the presence of halloysite. This coincidence will be explored in greater detail in the latter parts of this review.

2.2.5 Landslide Categorisation in Sensitive Soils

Landslides in sensitive clays are a contentious feature, with many attempts made to attribute a single form of failure to sensitive clays. Four main types of landslides have been observed within Canadian and Scandinavian sensitive clays. These are described as single rotational slides, multiple retrogressive slides (referred to as earth slides by some), spreads, and translational progressive landslides, with the last three described as rapid and covering areas exceeding 10,000 m² (Karlsrud et al., 1986; Tavenas, 1986). Locat *et al.* (2011) further refined these failures, relating them to progressive failures and separating them into three main types of failure. These are categorised as progressive flow slides, translational progressive slides and progressive spreads (Locat et al., 2011; Hungr et al., 2014).

Progressive Flow Slides

Progressive flow slides (referred to herein as flow slides) are attributed to the failure mechanism in sensitive slopes, resulting in sizable retrogressive scarp heads and relatively long runout deposits from the resultant landslides. The mechanism of failure within these flow slides is as follows.

The first slide is a smaller initial triggering near the slope base, in which the involved material completely remoulds (Figure 2.1a). This subsequently leads to an unstable scarp face where the internal driving and resisting moments are unbalanced. A second slide occurs (usually soon after the original failure), leading to the remoulding of that material and a new head scarp (Figure 2.1b). This mechanism continues until the resisting moment once again outweighs the driving moments, and a new primary head scarp forms (Figure 2.1c) (Locat et al., 2011)

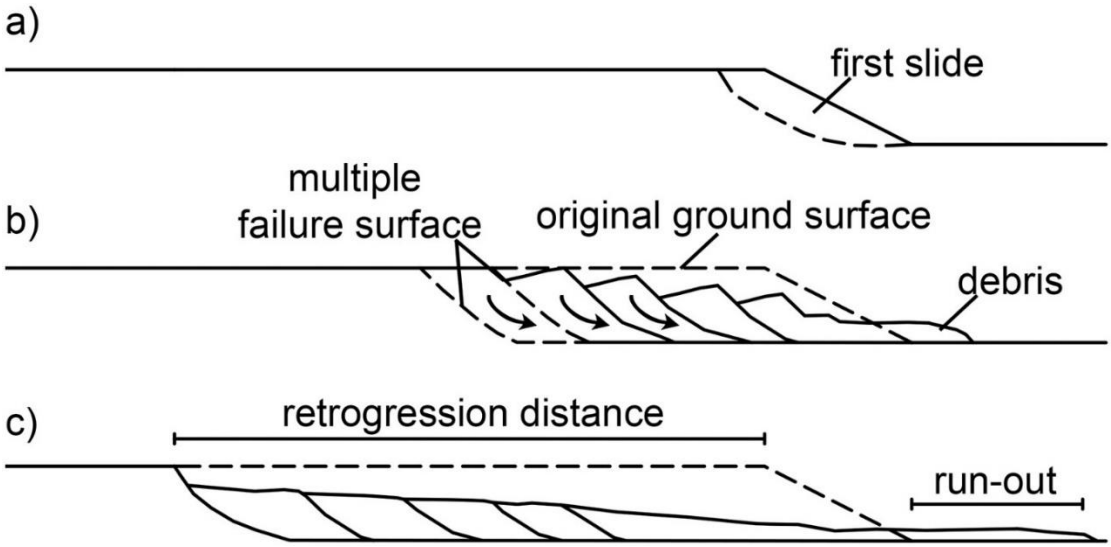

Figure 2.1. An example of how progressive landslides develop within sensitive soil deposits, where a sensitive soil may initially fail, and proceed to regress with multiple resultant failures as the slope attempts to reach a point of stability. From Troncone et al. (2023)

Flow slides usually lead to some of the largest, most visually destructive failures observed, with these being well described in the literature (Bjerrum, 1955; Tavenas, 1986). Examples of these failures include the Ullensaker landslide in Norway (Bjerrum, 1955) and Saint-Jean-Vianney in Quebec (Tavenas et al., 1971).

Translational Progressive Slides

The second form of landslides observed in sensitive clays is an event where a shear surface parallel to the ground forms, resulting in the displacement of a large block of soil downslope. These are characterised by Locat *et al.* (2011) as failures with a zone of subsidence at the head of the slope, accompanied by a compressive heave zone beyond the slope toe, typically located in a zone of flatter ground (Figure 2.2). An example is the Surte Landslide in Sweden in 1950.

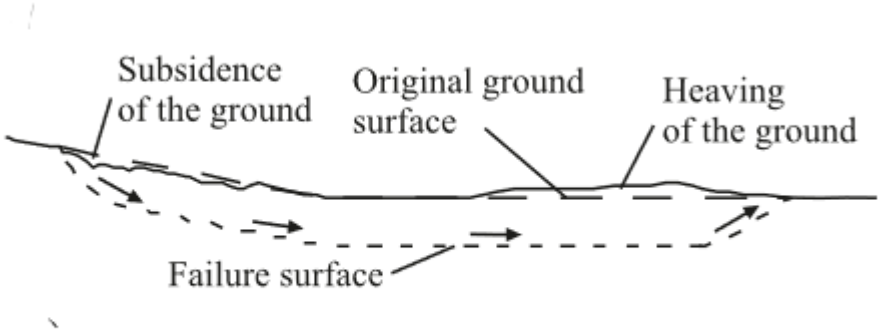

Figure 2.2. An example of translational progressive slides within sensitive soil, where the failure surface is parallel to the ground surface, resulting in a translational failure and heaving of the toe of the failure. From Bernander (2000)

Progressive Spread Slides

In spread slide failures, similarly to progressive flow slides, the first block at the head of the failing soil becomes unstable. Subsequently, the soil behind this block progressively fails and displaces. This secondary block results in a relatively intact block of clay. Failure continues backwards, with the next block failing and dropping, forming horst and graben-like structures (Figure 2.3). Horst blocks (upshifted blocks) are typically sharp wedges pointing upwards, while grabens are blocks that have flat to horizontal surfaces and are downshifted. These blocks generally fail above a specific sensitive clay surface that provides the shearing surface as the blocks 'ride' along the failed material (Locat et al., 2011).

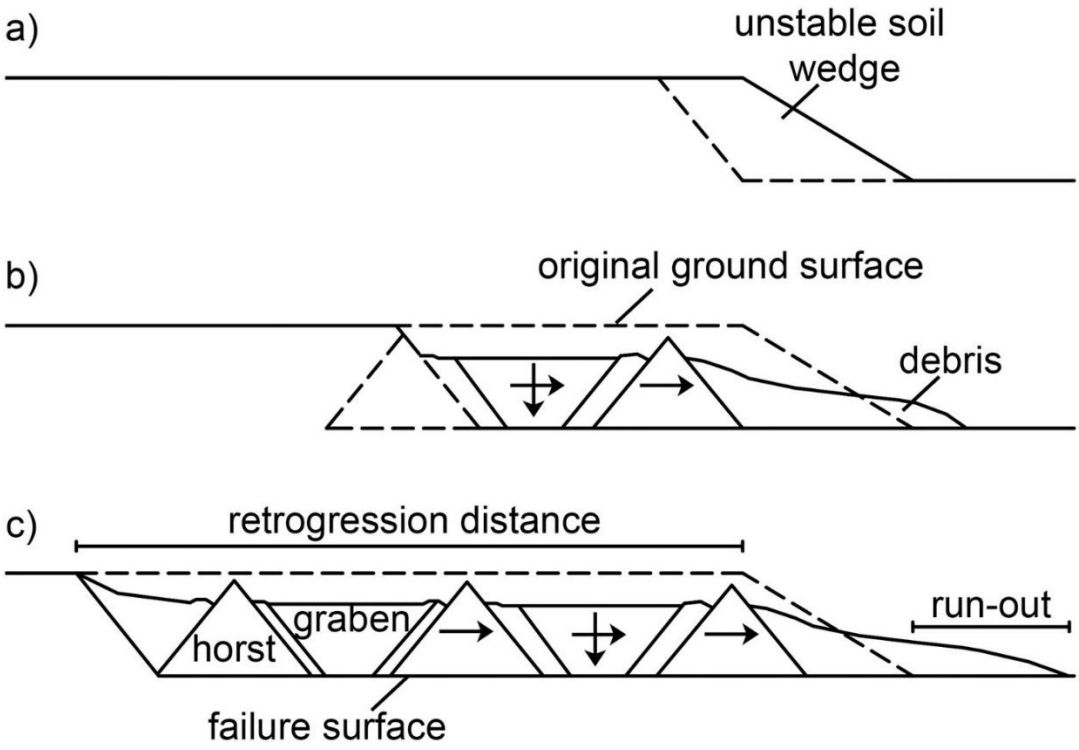

Figure 2.3 . An example of a progressive spread slide in sensitive soils, where an initial soil wedge in sensitive material fails, resulting in horst and graben-like failures in the material behind the original failure block. From Troncone et al. (2023)

It is noted that in many cases with progressive spread slides, they are constrained at the head scarp by a rotational failure surface that extends beneath the resultant horst and graben surface to the toe of the slope. These failures are observed frequently in both Canada and Scandinavia, with examples including the Sköttorp landslide in Sweden (Odenstad, 1952), the Saint-Ambroise-de-Kildare and Saint Liguori slides in Canada (Tavenas, 1986; Ouehb, 2007)

2.2.6 Mechanisms of Failure in New Zealand Sensitive Soils

Within New Zealand, failures in sensitive clays are usually smaller than those found in the Northern Hemisphere. Similarly, the mode of failure differs from those described by Locat et al. (2011). Most hypotheses regarding the mechanisms of failure for sensitive clays are derived from slides around the Western Bay of Plenty area, particularly within or near Tauranga. Since the 1980s, several mechanisms have been proposed detailing how failure may occur. While the slides are widespread across the city, several traits are consistently shared between sensitive clay slides. These traits include semi-circular head

scarps, typical of deep-seated rotational slips, and a constrained, upper, bowl-shaped scarp, usually located above the sensitive material surface. In addition to this, the upper bowl-shaped scarp is typically benched on the more intact underlying material, with the lower failed portion of the slope appearing more like a translational block failure. This mechanism was expanded in further detail by Gulliver and Houghton (1980) who, in their report on land instability in Ōmokoroa, proposed a model detailing the failure process in the soils within the peninsula (Figure 2.4). Gulliver and Houghton suggest that an upper soil wedge block of soil fails along the sensitive layer; this block subsequently causes the toe wedge to fail. This is followed by smaller failures in the upper scarp until a stable angle in the upper face is reached.

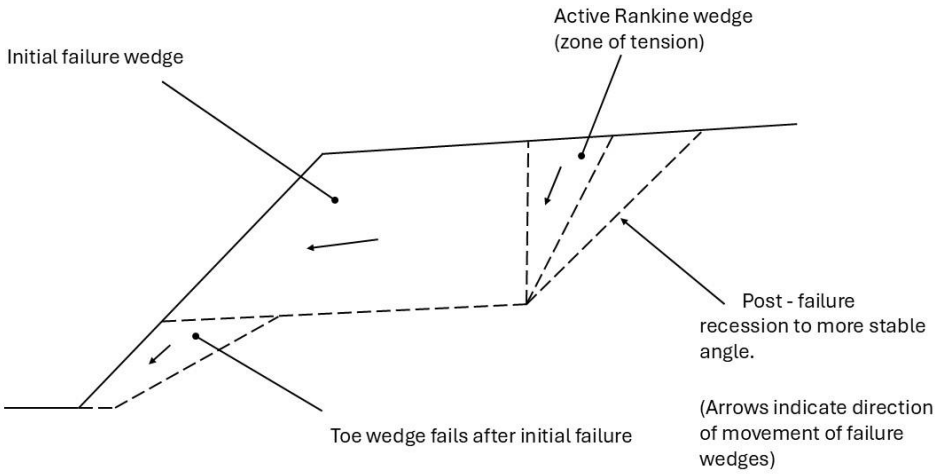

Figure 2.4 . A suggested failure mechanism for failure in a New Zealand sensitive soil, found in Ōmokoroa, New Zealand. In this mechanism, a large block of soil above the sensitive clay layer fails initially, subsequently causing the toe wedge below to fail. Following this large block failure, additional material fails in the active rankine wedge, as well as further material failure at the head of the failure, as the soil looks to achieve a stable angle in the headscarpFrom Gulliver and Houghton (1980).

A similar mechanism was observed elsewhere in Maungatapu and Ōtumoetai in subsequent failure events in later years (Bird, 1981; Bell et al., 2003). The propagation of failure was explored by Mills (2016), who found good agreement with several studies conducted in Scandinavian quick clays on the formation of localised shear bands within

the soil leading to the generation of a weak band of essentially remoulded soil while *in situ* (Thakur, 2007; Gylland et al., 2013; Gylland et al., 2014). As a result, it was proposed that through a cyclic loading system, strain localisation occurs within the sensitive material *in situ*, leading to the formation of a remoulded zone within the slope, which, when presented with the correct conditions, may lead to the large failures observed (Kluger, 2017; Moon et al., 2017). Furthermore, Kluger et al. (2017) proposed a new attraction-detachment mechanism within sensitive clay soils on the Ōmokoroa peninsula, particularly for the Bramley Drive landslide. Within the landslide, it was noted the dominance of a unique, mushroom cap shaped halloysite that was posited to be the source of sensitivity. This is discussed in more detail later in section 2.3.3 and 2.3.4.

Remediation of areas containing sensitive clay material is essential in reducing potential risks to infrastructure and human life. One key remedial method used in stabilising sensitive soil is the use of a chemical reagent. The addition of various chemicals may lead to an increase in strength. One such method is the use of lime. First used in the 1970s, lime piles are mixed *in situ* at depth, capitalising on the soil's pozzolanic reaction between calcium oxide and aluminium-bearing minerals (Broms & Boman, 1979). To date, the use of lime as a stabilisation method in clays is one of, if not the most used, techniques applied globally.

However, it should be noted that applying lime is not the only method used in the chemical amelioration of soils. In several instances, more discrete methods of strengthening are used. The term discrete here refers to methods that do not rely on destroying the natural clay and forming new cementitious bonds, as observed with lime. Alternative methods to strengthen soils were first applied in the early 1950s following a significant landslide in Norway (<100,000 m^3) which destroyed a highway at Bekkelaget and resulted in the loss of four lives (Eide & Bjerrum, 1955). Following the failure, sodium chloride (NaCl) was applied to the debris, strengthening and stabilising the material, and eventually allowing for the rebuilding of the destroyed highway (Torrance, 2014).

This method was further adapted in the late 1960s when, through testing with various metal salts, potassium chloride (KCl) proved to be the most effective in stabilising intact quick clay. Subsequent testing during the 1970s with additional (2629) salt wells over a large-scale quick clay landslide in Ulvensplitten, Norway, further reaffirmed the positive results observed in the lab (Moum et al., 1971). These tests have shown extended success in recent research (Helle et al., 2015, 2017), with treated quick clays strengthening to

provide a response that is neither quick nor sensitive. Although the KCl trials demonstrated success over a large area in Norway, their benefits to sensitive soil remediation outside of Norway have not been established, with only limited studies supporting the data collected in Norway (De Rosa et al., 2016).

Strengthening sensitive soils in New Zealand has, for the most part to date, been limited to lime and blending with less sensitive material (Knauf, 2022). Some research has been conducted on the usage of chemical amelioration through more discrete methods (Robertson, 2017), which showed potential promise and requires further research.

2.3 Halloysite

2.3.1 Halloysite — A Background

First described in the early 1800s, halloysite is a long-range 1:1 dioctahedral clay mineral of the kaolin subgroup (Berthier, 1826; Churchman and Carr, 1975; Churchman et al., 2016). Halloysite is a mineral that occurs widely in both soil and rock, forming through the alteration (by weathering and synthesis) of a wide variety of parent material, both igneous and non-igneous deposits, and occurring in Andisols, Ultisols, and other soils derived from volcanic and pyroclastic materials (Parfitt & Wilson, 1985; Churchman & Sumner, 2000; Churchman & Lowe, 2012; Hewitt et al., 2021).

Globally, halloysite is well-represented, with deposits found in both the Northern and Southern hemispheres, including the UK, China, Japan, Australia, and New Zealand, to name a few. Various forms of halloysite are found in nature, with ferro-halloysite (iron-rich), hydrated halloysite (previously referred to as meta-halloysite) (10 Å) and dehydrated halloysite (7 Å) described throughout the literature. The AIPEA (Association Internationale Pour l'etude des Argiles) nomenclature committee came to the agreement that in literature, halloysite should be referred to either as halloysite (10.1 Å) or halloysite (7 Å) to distinguish between its hydrated and dehydrated forms, respectively, with the term meta-halloysite excluded (Brindley, 1961; G. J. Churchman & Carr, 1975; Joussein et al., 2005).

As stated, the clay forms from the alteration of both unconsolidated and consolidated (rock) parent materials, most commonly rhyolitic and andesitic pyroclastic material, or reworked equivalent materials, with some rare variations in arid zone basalt weathering where ferro-halloysite is preferentially formed (see global review by Churchman and Lowe, 2012). In New Zealand, halloysite is commonly found in weathered, primarily

rhyolitic (silica-rich) tephra deposits across the central and northern North Island. These deposits have usually undergone rapid, low-temperature synthesis commonly in a moist environment (including in poorly drained situations) following the dissolution of silicic-rich volcanic glass, with relatively large amounts of silicon (Si) compared with aluminium (Al) being the key feature (Churchman & Sumner, 2000; Chadwick et al., 2003; Ndayiragije & Delvaux, 2004; Lowe & Churchman, 2016; Churchman et al., 2016a).

These parameters are collectively referred to as the silicon leaching model for the genesis of halloysite and allophane. Parfitt et al. (1983, 1984), Lowe (1986, 1995), and Singleton et al. (1989) have shown that the concentration of Si in soil solutions and the availability of Al largely determine the nature of the aluminosilicate secondary minerals formed from volcanic glass by weathering (mainly via hydrolysis) and synthesis. In particular, halloysite tends to result when Si is relatively high, whereas allophane is favoured by a lower Si. In the silicon-leaching model, if Si concentrations in the soil solution are <~10 gm^{-3} (ppm), allophane will form, but if concentrations are >~10 $gm^{-3,}$ then halloysite forms (Figure 2.5). Where the silicon concentration is close to 10 ppm, either or both minerals may form (Lowe, 2019; Hewitt et al., 2021).

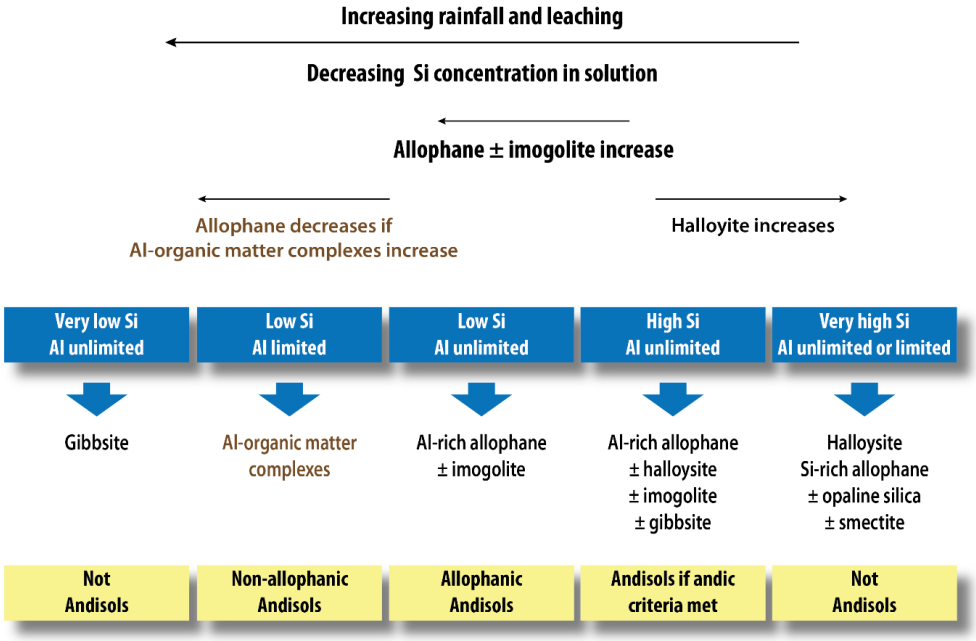

Figure 2.5 Relationship between environmental conditions and the formation of allophane, halloysite, and other minerals, as predicted by the silicon-leaching model and the availability of aluminium. From Hewitt et al. (2021).

2.3.2 The Structure of Halloysite

A polymorph of the kaolin subgroup of minerals, halloysite has a similar composition to kaolinite, distinguished by the interlayer H_2O ('water') between the individual clay sheets that is easily be driven off, giving hydrated and dehydrated end members (section 3.2.1) in a series of forms. This interlayer H_2O (or evidence of its removal) characterises halloysite relative to kaolinite (Churchman & Carr, 1975; Cunningham et al., 2016). Halloysite can adopt a continuous series of hydration states, from 2 to 0 molecules of H_2O per $Si_2Al_2O_5(OH)_4$ aluminosilicate layer (the fundamental clay unit cell), and these are interpreted as a type of interstratification of the two end-member types (Churchman et al., 1972, 2016; Churchman & Lowe, 2012; Cunningham et al., 2016).

When examining halloysite clay unit cells, the outer portion of the clay is typified by a basal oxygen plane, where three basal oxygens are bonded to a silicon ion. This silicon ion sits within the Si-plane and shares an O-OH bond with apical oxygen internally; this acts as a bridge between the silicon and aluminium ions, with an aluminium ion subsequently then connected to the surface -OH groups that usually make up the 'inner' surface of a halloysite colloid (Bailey, 1990; Singh, 1996; Joussein et al., 2005). Figure 2.6 shows a side profile schematic diagram of the halloysite/kaolinite unit cell.

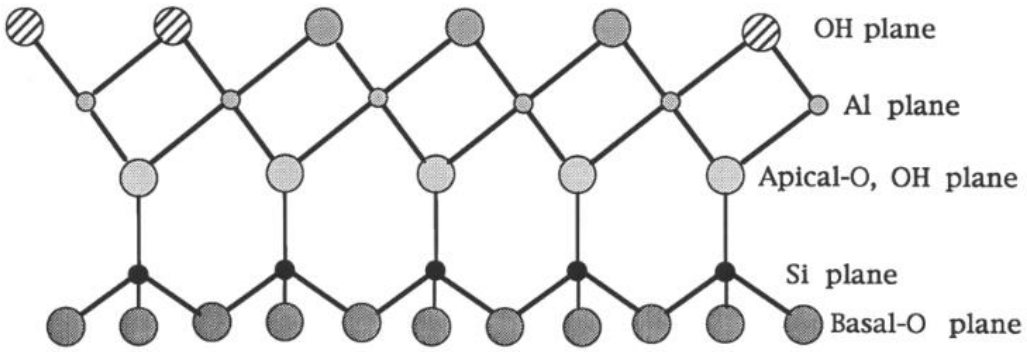

Figure 2.6 A cross-section of the kaolinite/halloysite unit cell. Note here the lack of interlayer waters to distinguish between halloysite and kaolinite. From Bailey (1990).

Two distinct shapes are observed when looking at the halloysite unit cell's 'top-down' profile. These are related to the 3D profile in the silica-oxygen bonds, and orientation of the alumina-hydroxyl bonds, with the former appearing as a tetrahedron and the latter as an octahedron. As such, this top-down view shows that the silica tetrahedron forms a ditrigonal shape (Figure 2.7a), while the alumina octahedron forms a hexagonal unit

(Figure 2.7b). This clay unit yields the typical 7 Å basal peak response observed in X-Ray Diffraction (XRD) testing (Singh, 1996).

(a) (b)

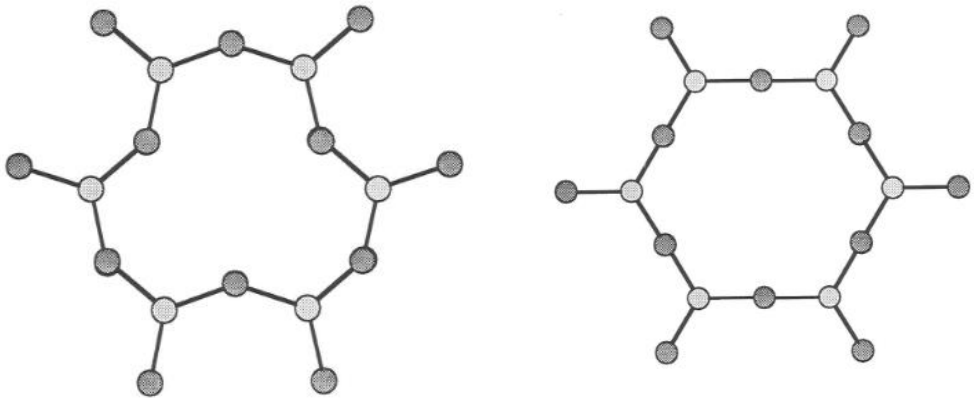

Figure 2.7. (a) A top-down view of the halloysite silica tetrahedron, with the silica sheet taking a ditrigonal shape. (b) A top-down view of the alumina octahedron reveals a hexagonal shape, allowing for the intrusion of water into the hexagonal recess. From Bailey (1990).

While sharing similar chemical make-up and basic sheet structure, one of the key differences between halloysite and kaolinite, as noted above, is the presence of interlayer H_2O within the halloysite unit cell. This water typically resides in the interlayer space between the outer octahedral sheet of the halloysite unit cell and the inner tetrahedral sheet, resulting in the expanded form. This is typically referred to as 10 Å halloysite.

The presence of interlayer water has a unique influence on the halloysite sheets. Hydration of the interlayer space causes deflections and bending of the tetrahedral and octahedral sheets, sometimes referred to as a scrolling mechanism. On the macro scale, the scrolling mechanism produces unique forms of circular nanotubes and spheroidal forms of halloysite. Stretching initiates in the tetrahedral sheet due to the size imbalance between the tetra and octahedral sheets (the former being larger).

This bending subsequently allows access to the inner hydroxyl of the clay. Furthermore, this realignment and increased disorder of the clay unit, resulting from stretching, increase the likelihood of isomorphous substitution of Al^{3+} into the silanol sheet (Mitchell et al., 2005; White, 2013). It is important to make clear here, though, that the amount of water present within the halloysite is not infinite; in fact, it is restricted to a maximum of 2 molecules of H_2O per unit cell; this results in a roughly 3 Å monolayer of water that exists

in the interlayer space between clay units resulting in a sheet-like morphology making up the clays internal structure (Churchman & Carr, 1975; Churchman et al., 2016).

Halloysite Sheet Charging

As stated, halloysite sheet structures are made of outer silanol and aluminium sheets. Figure 2.8 shows a typical arrangement of a halloysite nanotube. Within the clay sheets, it is important to note that, while ideally all charges are balanced, imbalances occur due to broken edge interactions and isomorphous substitution (the exchange of Al^{3+} and Fe^{3+}). This is often observed through the clay's Cation Exchange Capacity (CEC) or its ability to accept positive cations onto its surface (Matocha, 2005). While research on surface charge has not been extensive, Guimares *et al.* (2010) modelled and determined the surface charges present on halloysite through electrostatic field determination.

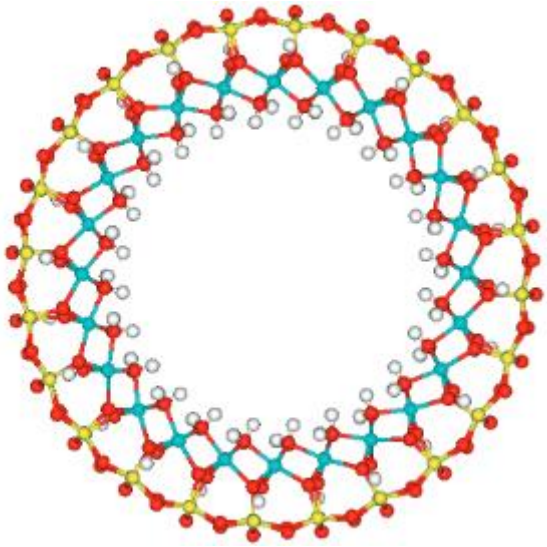

Figure 2.8 A side view of a full halloysite nanotube, showing the bonding between the silica sheet on the outer surface, to the inner water (white circles) and alumina sheet. Where the yellow atoms are silicon, blue are aluminium, red are oxygen and white is water. From Guimares et al. (2016)

In this research, Guimares et al. (2010) observed a charge imbalance with silanol sheets exhibiting negative to neutral charging, while aluminol sheets exhibited positive charging (Figure 2.8). The lower overall charging on the surface of the outer layer of the outer surface (when compared to the inner aluminium sheet) relates to the strong bonding between Si-O units. This lower external charge also accounts for the noticeably lower cation exchange capacities observed in some halloysites, especially those dominated by spheroids (Theng et al., 1984). Kluger et al. (2017) used differences in charge distribution

of Mushroom-Cap-Shaped (MCS) spheroidal halloysite (based on models developed by Guimares et al., 2010) to develop a new mechanism enabling failure of sensitive layers to generate flow sliding.

They suggested that short-range electrostatic and van der Waals interactions enabled the MCS spheroids to form interconnected aggregates by attraction between the edges of numerous paired silanol and aluminol sheets that are exposed in the openings and the convex silanol faces on the exterior surfaces of adjacent MCS spheroids (Figure 2.9). Slope failure is often a frequent feature in soils dominated by MCS spheroids. During failure, the weak attractions are overcome with multiple, weakly attracted MCS spheroids separated from one another resulting in repulsion between the exterior MCS surfaces. This subsequently leads to low remoulded shear strength, a high sensitivity, and a high propensity for flow sliding (Kluger et al., 2017).

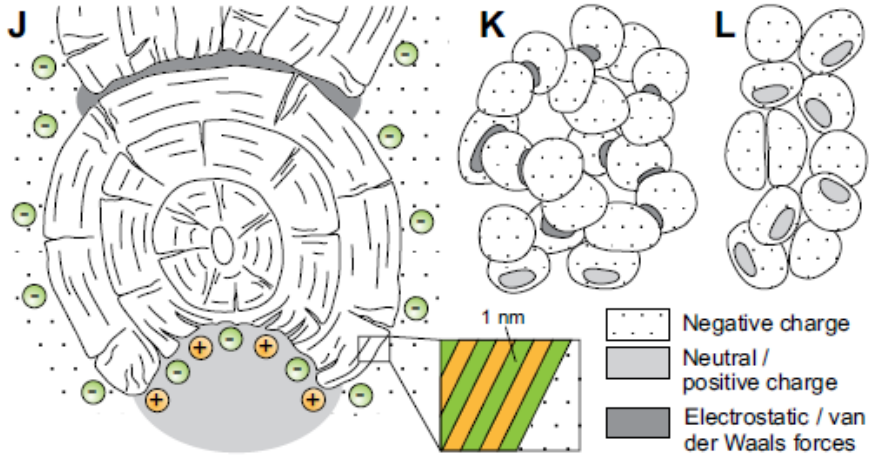

Figure 2.9. A theoretical view of a variety of features relating to the suspected behaviour and makeup of halloysite MCS spheroids. As denoted by J, a concept diagram of the external charge distribution on an MCS spheroid, as well as a cross sectional snapshot of the charge balance of the internal MCS spheroid sheets. Additionally as shown by K and L, the pre-disturbance (K) chain of MCS spheroid chain, and post disturbance (L) loosely organised MCS spheroids. Note the lack of clear open face to cap surface attraction in the post disturbance stage. . Image is sourced from Kluger et al. 2017.

2.3.3 Halloysite Morphologies

Morphology refers to the differing shapes and orientations a clay mineral may display while retaining the same fundamental chemical and overall physical structure. Morphologies can include textural to shape differences caused by variations in source material, weathering environment and more (Keller et al., 1986). Halloysite itself has four

distinct, unique morphologies, along with numerous sub-morphologies. These are detailed further in Table 2.3. The source of these differing morphologies remains a topic of ongoing research, with some authors suggesting that controls relate to key constituents within the soil, including iron, organic matter, and parent material (Cravero & Churchman, 2016; Lowe & Churchman, 2016; Churchman et al., 2016a).

Table 2.3 A summary of the various morphologies of halloysite found across the globe, with sub-morphologies and their occurrences included. Sourced from Jouessein et al. (2005), Cunningham et al. (2016), and Kluger et al. (2017).

Morphologies	Sub-morphologies	Occurrences
Tubular	Long and thin tubes, short and stubby tubes, fibre	Cryptokarstic sediment, volcanic glass and pumice, feldspar and mica alteration.
Platy	Platy and tabular, crumpled lamellar	Volcanic ash soils, weathered pyroclastics, lateritic profiles, fissures within granite, hydrothermal alteration, and tuff beds (e.g., Texas, Brazil, Guatemala)
Books	Book form	Weathered, old silicic volcanic ash (tephra) deposits in a moist regime, Tauranga region, northern New Zealand
Spheroidal	Pseudo-spherical, spheroidal, spherulitic, irregular lath with a rolling edge, mushroom-cap, glomerular, cylindrical	Weathered volcanic ash and pumices, volcanic glass in a marine environment, rhyolitic tephras, weathered granite/gabbros (e.g., Guatemalan soils, New Zealand, Scotland)
Prismatic	Prismatic, rolled, crinkly and walnut meat	Volcanic ash soils, weathered granite (Japan)

While the Bay of Plenty region is home to nearly all forms of halloysite, it has further been found to be home to novel sub-morphologies (Cunningham et al., 2016). One morphology in particular that has been linked as a potential culprit in creating sensitivity within the Bay of Plenty is the spheroidal morphology (Kluger et al., 2017).. Another is the first known occurrence of book forms, which may be more prevalent in North Island, having been possibly misidentified as kaolinite books (Cunningham et al., 2016).

Spheroidal Halloysite

Described by Bailey (1990) as a ball shape consisting of layers rolled up within the spheroid, similar to an onion, the term 'spheroidal' has been used as an encompassing term to cover various shapes. Joussein *et al*. (2005) used 'spheroidal' as the umbrella term for morphologies described as pseudo-spheroidal, cylindrical, disk, irregular lath with a rolling edge, glomerular, or onion-like, among others. Spheroidal halloysites are commonly found in Quaternary soils formed from volcanic ash, but have been observed in older sequences (Cretaceous, early Tertiary) (Cravero & Churchman, 2016). Deposits containing this morphology have been found worldwide, including in tropical climates (i.e., Guatemala) and temperate climates, including Japan and New Zealand. Spheroids generally range between 0.05 to 0.5 μm in diameter (Churchman & Theng, 1984; Joussein et al., 2005)

Controls on the formation of spheroidal halloysite are still not entirely clear, with a lack of consensus on what particular trigger is required for spheroidal halloysite to form preferentially over other morphologies (Cravero & Churchman, 2016). Suggestions on controls include the weathering of pumice and volcanic glass within marine environments (Joussein et al., 2005a), the amount of iron (Fe) present within the source material, and, as a result, bound to the octahedral sites within the halloysite (Theng et al., 1984; Adamo et al., 2001; Papoulis et al., 2004). The amount of organic matter and microbial activity may also influence the formation of spheroids (Tazaki, 2005).

Kirkman (1981) argued that only allophane develops into halloysites that can form these spheroids, though this mechanism has been discredited due to the opposite structural forms of allophane nanoballs and halloysite spheroids (Churchman and Lowe, 2012). Bailey (1990) noted that spheroidal halloysites were synthesised at low temperatures in supersaturated silicon solutions, forming from a dissolution precipitation mechanism. This potentially accounts for the prevalence of spheroidal halloysites in lower temperature climates with high rainfall, usually with source material of highly weathered volcanic glass able to supply the supersaturated solutions for the spheroid to form from. This mechanism, though, warrants further research.

At sites in Ōmokoroa, particularly those linked to landslides in extra-sensitive soils, a distinct sub-morphology has been noted within halloysite deposits of the culprit-sensitive clay layer. An incomplete spheroid dominates the morphology (Smalley et al., 1980, 1984;

Kluger, 2017) . Kluger *et al.* (2017) postulated that charge imbalances between the outer surface of one spheroid and lumen opening of another spheroid contributed to long continuous chains of agglomerated halloysite which upon remoulding break the weak bonds between the halloysites resulting in a weak remoulded strength observed.

2.3.4 Halloysite — Unique Features

Halloysite exhibits a number of unique features that impact how the clay acts when manipulated and subjected to differing environments and chemicals. These include three key factors that have the potential to significantly impact this research. These unique features include dehydration behaviour, pH-dependent edge surfaces, and potassium selectivity.

Dehydration Behaviour

As previously discussed in section 2.3.1, halloysite can be found in two formats. Its hydrated 10 Å form and its dehydrated 7 Å state. This dehydration action is of note due to its potential impacts on research undertaken in the lab following transport from *in situ* conditions. Under its 10 Å condition the halloysite has a monolayer of water existing in the interlayer space between halloysite unit cells. This water is not bound to the clay structure. It is readily lost even under 'normal' conditions (1 atmosphere, 20ºC, 50% humidity), causing the collapse to 7 Å and irreversible re-expansion by water (Giese, 1988; Joussein et al., 2005; Churchman et al., 2016).

It is worth noting here that in most instances, normal conditions will only partially dehydrate halloysites, with temperatures over 200º C and humidities near 0% required for complete dehydration due to weak hydrogen bonding that may exist between some aluminol sheets and water molecules, as well as water molecules that can be trapped within the clay sheet (Hughes, 1966). This is particularly noticeable in spheroidal halloysites, where pores form within the clays, which can trap water within the inner spheroidal layers, resulting in incomplete dehydration of the clay (Berthonneau et al., 2015).

The language used previously describing the collapse to 7 Å and the irreversible re-expansion by water was specific due to the fact that re-expansion of the clay sheet from 7 Å to around 10 Å can only be achieved in the lab through chemical treatment. As stated by Cunningham et al. (2016, p.351):

> "Under ambient environmental conditions, dehydration of halloysite is an irreversible process... However, the effective reversal of the basal spacing change associated with the dehydration of halloysite by the addition of formamide provides a common test for distinguishing halloysites from kaolinite (Churchman et al., 1984, 2016)".

Through the intercalation of particular chemicals such as formamide and certain potassium metal salts into the interlayer space of dehydrated halloysite, re-expansion of the interlayer space is achieved, though this is frequently lost upon rewashing (Churchman & Carr, 1973; Carr et al., 1978; Churchman et al., 1995; Frost et al., 2000; Joussein et al., 2006; Ferrante et al., 2017).

pH Dependent Edges

As discussed in section 2.3.2, each sheet has a positive or negative (or weakly positive to neutral) charge for clay minerals that indicates the availability of bonding sites on the clay mineral itself. This charge imbalance results from the number of hydrogen ions, or lack thereof, bonded to the clays. The excess or deficiency of hydrogen on the clay surface is a function of soil pH (Mitchell et al., 2005). Where pH is the logarithmic measurement of the volume of hydronium (H_3O^+) ions present in a given medium (Buck et al., 2002). With lower pHs, an excess of hydrogens is present, resulting in the formation of excess H_3O^+, while higher pH has a deficiency in hydrogens, forming OH^- ions. These ions desire to either donate (on the acidic side) positive ions (proton donor) or accept (on the alkaline side; proton acceptor) positive ions such that a neutral pH is reached, in this instance, to try and form stable, neutral H_2O.

Due to the natural imbalance in charge on the clay surface from broken edges and isomorphous substitution, clays can accept or donate the hydrogens that the hydronium or hydroxyl groups are searching for. Subsequently, clays have a pH at which all the charges on the clay surface are balanced, referred to as the Point of Zero Charge (PZC). At this point, the clay surface is regarded as stable and is the point at which clays will flocculate when in solution (Mitchell et al., 2005; Kollannur & Arnepalli, 2019). Figure 2.10 provides an example of how this PZC appears when looking at the charge balance on the aluminol sheet, where on the alkaline side the clay donates hydrogen ions, resulting in an excess negative charge on the sheet, and on the acid side it accepts hydrogen ions resulting in a net positive charge (Theng & Wells, 1995)

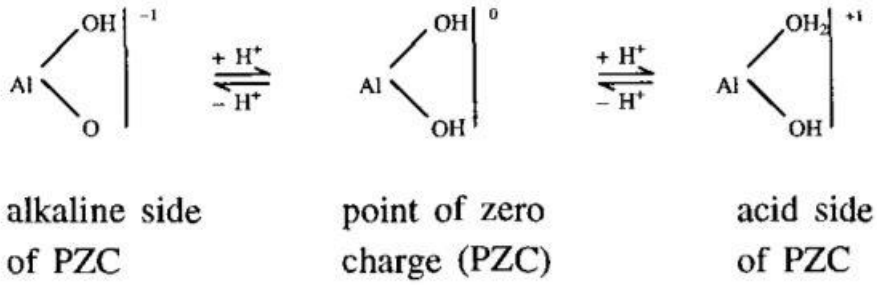

Figure 2.10. A summary diagram showing how the pH of the halloysite alumina sheet, and which side of the PZC that pH is, affects the charging of the sheet. Note when halloysite is on the alkaline side of the PZC, a net negative charge occurs on the clays surface, due to the loss of a surficial hydrogen. The inverse occurs when on the acid side of the PZC, where an excess hydrogen is donated to the alumina sheet causing a positive charge imbalance. From Theng and Wells (1995).

Halloysite, like all clays, has its own unique PZC. These vary from soil to soil as no universal constant PZC pH is known. With this said, the PZC values for most halloysites are regarded to be quite low (pH= 2.2–3.5) (Theng & Wells, 1995). More recent research has suggested a higher degree of complexity exists, though, with regards to the PZC, with the aluminol (pH = >7) and silanol (pH = 2.2–3.5) sheets having significantly differing PZC pHs. This complexity relates to the bond style, angle and strength, with the oxygens of the silanol sheet being much more accepting of hydrogens and the converse for aluminol sheets (Berthonneau et al., 2015; Ferrante et al., 2017)

Potassium Selectivity

A further unique feature exhibited by halloysite is its selectivity in cation uptake. Halloysite will preferentially take up and intercalate low-activity monovalent cations over divalent cations. Cations preferentially uptaken include potassium (K^+), caesium (Cs^+) and ammonium (NH_4^+) (Garrett & Walker, 1959). However, K^+ is the most preferentially selected cation. The cause of this preferential uptake remains a topic of debate among researchers. Some have suggested that the preference may be linked to zeolites or mica-rich layers found interstratified within the halloysite sheets (Boettinger et al., 1995; Chorover et al., 1999). Interstratification appears to occur in limited cases due to the sparing occasions where these minerals are found in addition to halloysite within soil columns (T. Takahashi et al., 2001; Joussein et al., 2006).

More recent studies have suggested that K^+ selectivity is controlled by various factors, with a combination of influences. One of these key controls is believed to be the presence of iron (Fe) oxides and hydroxides within the soil alongside the halloysite. The hypothesis suggested is that Fe (hydr)oxides have a high point of zero charges (pH ~8.8) and, as such, are positively charged until the halloysite environment becomes sufficiently alkaline. Due to the external (convex) surface of halloysite being negatively charged, Fe (hydr)oxides act as a buffer to any incoming cations (seeking to bond and donate their excess electrons) and subsequently prevent bonding. It is not until the pH is raised sufficiently that any surface-cation interactions can occur, and even then, only the lower valence, smaller-sized ions (such as K) can overcome the resultant buffer force enacted by the Fe (hydro)oxides (Takahashi et al., 2018).

2.4 Halloysite — Potassium Complex

As stated in section 2.3.4 halloysite is selective for potassium due to clay-cation interactions. While potassium may exist as its free form in nature on occasion (K^+), most studies have introduced potassium to halloysite as some form of metal salt. These salts are often alkaline and are accompanied by a negatively charged anionic species. The metal salts are often unique in appearance, nature and behaviour. The interaction of individual species with halloysite is a factor that has been explored extensively and has had a good description throughout the literature.

2.4.1 Halloysite — Potassium Salt Interactions

Focus on the interaction between potassium salt and halloysite was first established in 1959 following determinations of the reaction between halloysite and certain phosphates (in particular ammonium phosphate) in which an interlayer complex that oriented itself between clay unit layers was noted (Wada, 1959b). These results triggered an expanded study in which researchers looked to see if they could replicate and examine if the resultant complexes were stable (Wada, 1959a). Wada (1959a) observed the preference for monovalent cations, especially those of low activity (K^+, NH_4^+, Rb^+, Cs^+), with a specific preference for both potassium and ammonium ions, a trait observed by other researchers (Garrett & Walker, 1959).

This oriented penetration in between clay layers was a trait observed through the usage of XRD measurements, with oriented penetration of the clay at differing angles and measurement of incident X-rays allowing for an indication of the unit size of the clay, in

particular its *d* spacing, or distance between one siloxane sheet to the next (siloxane + aluminol + interlayer space usually occupied by H_2O). As previously noted, (10 Å) halloysite typically exhibits a *d* spacing of 10.1 Å. To determine whether any interaction between halloysite and metal salt occurs, researchers typically look for an expansion in basal spacing. Garrett and Walker (1959) undertook a series of analyses using various salts looking for this specific behaviour. They determined that the largest impacts on the halloysite *d* spacing were observed for potassium carbonate (13.6 Å) and potassium trimethylacetate (12.0 & 19.8 Å) (Table 2.4). Wada (1959a) observed similar increased basal spacing following the interaction between halloysite and potassium acetate (14.3Å)

Table 2.4. A table showing the various basal spacings corresponding to grinding with some potassium salts. Note these are rehydration basal spacings following dehydration of the initial halloysite soil. Recreated from Garett and Walker (1959).

Salt	Basal Spacing (Å)	Solubility (Molal) at 110°C
$KOOC.C(CH_3)_3$	12 and 19.8	Very Soluble (unmeasurable)
KNO_3	10.6	31
K_2CO_3	13.6	24
KBr	10.6	9.2
KCl	10.3	8
$KClO_3$	7.5	5.6
K_2SO_4	7.6	2.6
$KClO_4$	7.5	1.9

This intercalation complex can be a helpful tool for both distinguishing between halloysites and kaolinite, as well as providing an indication of the potential proportions of the 1:1 clay minerals within a certain sample (Churchman et al., 1984; Theng et al., 1984; Janik & Keeling, 1993). With intercalation occurring with organic and inorganic compounds, an exploration into the complexes formed has increased in recent years; researchers are exploring potential industrial and scientific applications with usage from catalysts to electromagnetic radiation protection (Adamczyk et al., 2020). Potassium acetate (KCH_3COO) is one such metal salt that has been extensively tested, and its complex with halloysite is extensively reported throughout the literature. Thus, it was selected for usage in this research.

2.4.2 Halloysite — Potassium Acetate Interactions

The interaction between halloysite and potassium acetate (hereafter referred to as K-acetate) is noteworthy. Upon interaction with hydrated halloysite, even in small amounts (2–10 mmol/g), potassium acetate displaces the interlayer water causing an expansion in

the *d*001 XRD reflection, expanding the clay from its natural 10.1 Å out to a value between 11.5 Å and 14 Å, depending on how hydrated said halloysite was (Wada, 1959a; Frost et al., 2000; Li et al., 2017; Adamczyk et al., 2020). Furthermore, this complex is resistant to the 7 Å collapse caused by dehydration, and has been observed to re-expand the 7 Å form of halloysite back to the 11–14 Å range (Frost et al., 2000a).

Within the clay, several interactions occur between the potassium ion, the acetate ion, and the silanol-aluminium sheets. These interactions are observed through Fourier Transform Infrared Spectroscopy (FTIR) and similar forms of infrared spectroscopy. Some key changes observed are downshifts in the 3620 cm^{-1} and 3695 cm^{-1} peaks, leading to the formation of a broad peak at 3600 cm^{-1} and at 3585 cm^{-1}, and the appearance of new peaks associated with the potassium acetate complex. In the 1250–1750 cm^{-1} range, doublet OH bands at 1593 and 1565 cm^{-1} may appear, typical of a hydrated ionic salt (K-acetate) present within the silicate layers in clay (Zich et al., 2013). This is typically also accompanied by changes to the acetate FTIR bands at 1420 and 1350 cm^{-1} with downshifting for the 1420 cm^{-1} peak and splitting of the 1350 cm^{-1} peaks (Frost, 1997; Frost et al., 2001; Cheng et al., 2010a, 2010b, 2011). It is worth noting here, however, that almost, if not all, research undertaken on the halloysite–potassium acetate intercalate complex has been conducted on the tubular form of halloysite. Limited information is available in the literature regarding spheroidal halloysite and its features, with Berthonneau et al.'s (2017) paper likely being the most informative guiding piece of literature.

2.5 Conclusion

This chapter has reviewed the literature surrounding the sensitive soils and their composition and behaviour. Found across the globe and within New Zealand, these soils may be sourced from a variety of parent material and formation conditions, but generally exhibit similar characteristics (high void ratio, high natural water content, low liquid limit, low remoulded strength). These soils are a key contributor to land instability causing spreads and landslides the world over. Within New Zealand, sensitive soils are usually dominated by the kaolin subgroup 1:1 clay mineral halloysite. Derived mainly from the synthesis of the dissolution products primarily of rhyolitic glass shards from pyroclastic (tephra) deposits in moist, silicon-rich environments, halloysite exhibits unique (hydration) behaviour, and it has a variety of natural morphologies that can play a role in causing sensitivity in the soils (e.g., Kluger et al., 2017).

In addition, halloysite also has a unique behaviour in its ability to interact with organic salts and form intercalate complexes. These complexes often cause changes in behaviour of the clay, such as re-expansion of the dehydrated form of halloysite as well as expansion of the clay's basal size in its hydrated form. While overseas research (using illite clays) has shown good success in strengthening quick clays, limited information is available on the effectiveness of applying similar techniques within New Zealand. Based on the information provided within this review, from metal salts available, to provide the best possible outcome for eliciting a strength response from a treatment, potassium acetate is the strongest candidate. Due to the potential expansion of the clay and, thus, the potential for increased colloid interaction, this option is expected to provide the optimum outcome.

Chapter 3
Site Selection and Characterisation

3.1 Introduction

This chapter presents information concerning the procedures employed to first select a field site that not only contains sensitive soil but also is safely accessible and which has shown instability in recent times. Second, that site is subsequently characterised so that the site geomorphology and stratigraphy, as well as strengths and sensitivity of the targeted soils, are accounted for. These two steps are undertaken such that, an appropriate, safe field site is selected

3.2 Procedure

As the primary purpose of this research is to attempt to strengthen sensitive pyroclastic soils through a treatment regime using the addition of potassium acetate, it was imperative that the site selected met five key criteria to ensure the greatest chance of success. These requirements were as follows:

1) The site contained soil that provided a sensitive response, which, at a minimum, recorded a field indication of 'extra sensitive' when tested by a calibrated shear vane (as per the standard testing methodology laid out by NZGS, 2005).
2) The sensitive soil layer was either exposed within the failure scarp or within 1 m of the soil surface. This criterion ensured that a representative field moisture content was achieved and New Zealand health and safety requirements around trenching were not exceeded.
3) The sensitive soil layer was thick enough to extract a homogenous, cohesive, undisturbed triaxial core of 150 mm in length.
4) The site was accessible by foot and safe enough to obtain samples without danger from slip reactivation or water-related hazards.
5) Compliance and approval for access to the site could be obtained from property owners, council, or other relevant stakeholders.

Once potential sites were identified, it was further required that access to these areas be permitted only if there was a minimum of one month of dry weather for health and safety reasons.

A two-stage approach was developed to identify sites that met these parameters. Firstly, an initial desktop study was undertaken, noting aspects such as historical failures, ease of access, and existing literature. Data such as council reports, geotechnical reports, bulletins, published works, aerial imagery, and drone imagery were utilised to narrow down and select a specific site. The second stage involved an in-person investigation of the site to establish aspects such as accessibility, geomorphology, and soil unit characterisation, which assisted in selecting an appropriate site.

3.3 Stage 1: Desktop Study

3.3.1 New Zealand

Sensitive soils, which are found worldwide, as mentioned previously in Chapter 2, are also present in New Zealand. These soils are predominantly found in the upper and central parts of the North Island. Specifically, the areas around South Auckland, the Bay of Plenty, Coromandel, Taranaki and the Upper and Middle Waikato Basin regions all have extensive deposits of sensitive material that are the source of several issues relating to landsliding. Found in deposits of weathered volcanic material such as primary or reworked ignimbrites and tuff deposits and altered tephra fall deposits, sensitive soils, while an issue throughout these areas, pose a significant hazard within the Bay of Plenty region..

3.3.2 Bay of Plenty

The Bay of Plenty, particularly the Western Bay of Plenty and Tauranga, is a region historically prone to sensitive soil landsliding, with large retrogressive landslides that have caused damage to infrastructure and the environment found throughout. On this basis, the Western Bay of Plenty (WBoP) was selected as an area of particular focus. Following this, the first of the two-stage process of selecting a site was employed. Within this first stage, several key steps were undertaken; these were:

- Establish the key source material for sensitive soils throughout the region from literature and technical reports.

- Identify areas prone to landsliding from historical reports, literature, technical reports and press releases.
- Refine sites such that they can be regarded as 'fresh' or historical/relic failures, the determination of which is made later.
- Undertake a series of specific site characterisations to determine optimal sites.

Bay of Plenty — Source Material

Most of the Bay of Plenty is underlain by pyroclastic and associated deposits of some form. These soils range from deposited *in situ* ignimbrites, tephra-fall deposits, and sedimentary deposits. Additionally, soils consisting of reworked pyroclastic materials, buried former soils (paleosols), and soils formed from colluvial and alluvial deposits (usually made up of former, now reworked, pyroclastics) also occur. The bulk of these deposits are encompassed within the Matua Subgroup (part of the Tauranga Group defined by Kear and Schofield, 1978), with soils within this group ranging from (hard) welded ignimbrites to weathered and, in some cases, reworked and primary tephra-fall deposits. Soils of the Matua sub-group include deposits that post-date the Waitеariki Ignimbrite (aged ~2.25 Ma) (Pittari et al., 2021; Prentice et al., 2022) through to the upper constraining bed of the sub-group, the c. 45,000-year-old Rotoiti Tephra Formation (which includes Rotoehu Ash) (Briggs et al., 1996; Briggs et al., 2005; Briggs et al., 2006; Hopkins et al., 2021). Rotoehu Ash is underlain by one or more members of the weathered Hamilton Ash Formation (Hamilton Ashes hereafter), dated between ~0.34 Ma (basal Rangitawa Tephra or H1 bed) and » 45,000 cal yr BP (Lowe, 2019), by one or more members of the strongly weathered Kauroa Ash Formation (Kauroa Ashes hereafter), dated between 2.3 Ma and > 0.78 Ma, and the Te Puna Ignimbrite, dated at ~1.1 Ma (likely to be a correlative of Kidnappers Ignimbrite on the basis of composition) (Prentice et al., 2022).

The Te Puna Ignimbrite and the Kauroa Ashes together are also sometimes known locally as the Pahoia Tephra sequence, and the Pahoia Tephras per se comprise thick layers of interbedded altered tephra-fall and ignimbrites (i.e., interbedded clays, silts, pumice sands and gravels) that are older than 0.34 Ma and younger than 1.1 Ma (Kluger et al., 2017). The Kauroa Ashes are distinguished from the (older) Pahoia Tephras in this study. The interlayered stratigraphy of the Pahoia Tephras has been split into two parts, referred to informally as the upper and lower Pahoia Tephras. The former is a more sandy/pumiceous unit, while the latter is a unit of interbedded altered tephras dominated by heavily dilatant silts and clays, including (at Bramley Drive) a 0.3 m-thick, white, highly sensitive clay-

rich layer that failed in 1979, generating a flow slide (Kluger et al., 2017). The Pahoia Tephra and its equivalent deposits can be found throughout the Bay of Plenty, stretching from Katikati to the lower-lying parts of the Bay of Plenty at Opotiki (e.g., see (Pullar et al., 1973; Manning, 1996; Briggs et al., 2006)).

Bay of Plenty — Areas Prone to Soil Failure and Mass Wasting

Landslides have previously occurred in several areas within the region, especially on the peninsulas within the Tauranga Harbour (Te Awanui). One heavily impacted peninsula is the Ōmokoroa Peninsula. Located 12 kilometres northwest of Tauranga City, it extends roughly five kilometres into the Tauranga Harbour, tending in a southwest-northeast orientation (Figure 3.1). Already established as an area of high susceptibility to landsliding, including in 2017 after multiple cyclonic events, Ōmokoroa suffered several significantly large-sized landslides (Kluger et al., 2020). These have resulted in extensive remedial work in several places throughout the peninsula, as well as the evacuation and permanent 'red zoning' (deemed unsafe for habitation) of several residences due to the hazard posed by the resultant failure scarps.

Other areas noted for large retrogressive landslides elsewhere in the region include the Maungatapu Peninsula, found southeast of Tauranga City, as well as in the suburbs of Ōtumoetai and Matua (Hegan et al., 2005; Mills, 2016), found northwest of the central city, and at Tauriko and Ruahihi (Burns & Cowbourne, 2003; Wyatt, 2009; Cunningham et al., 2016), both to the southwest (inland) of Tauranga. Additionally, the Maungatapu peninsula south of the city, which extends northeast into the Tauranga Harbour, is the site of several historically damaging landslides (Maungatapu Road, Te Hono Street), as well as a number of more recent highly damaging slips (Te Hono Street and Egret Drive) (Bird, 1981; Oliver, 1997). The Otumoetai and Matua peninsulas exhibit similar histories, with damaging landslides from sensitive sources found throughout the underlying sequences.

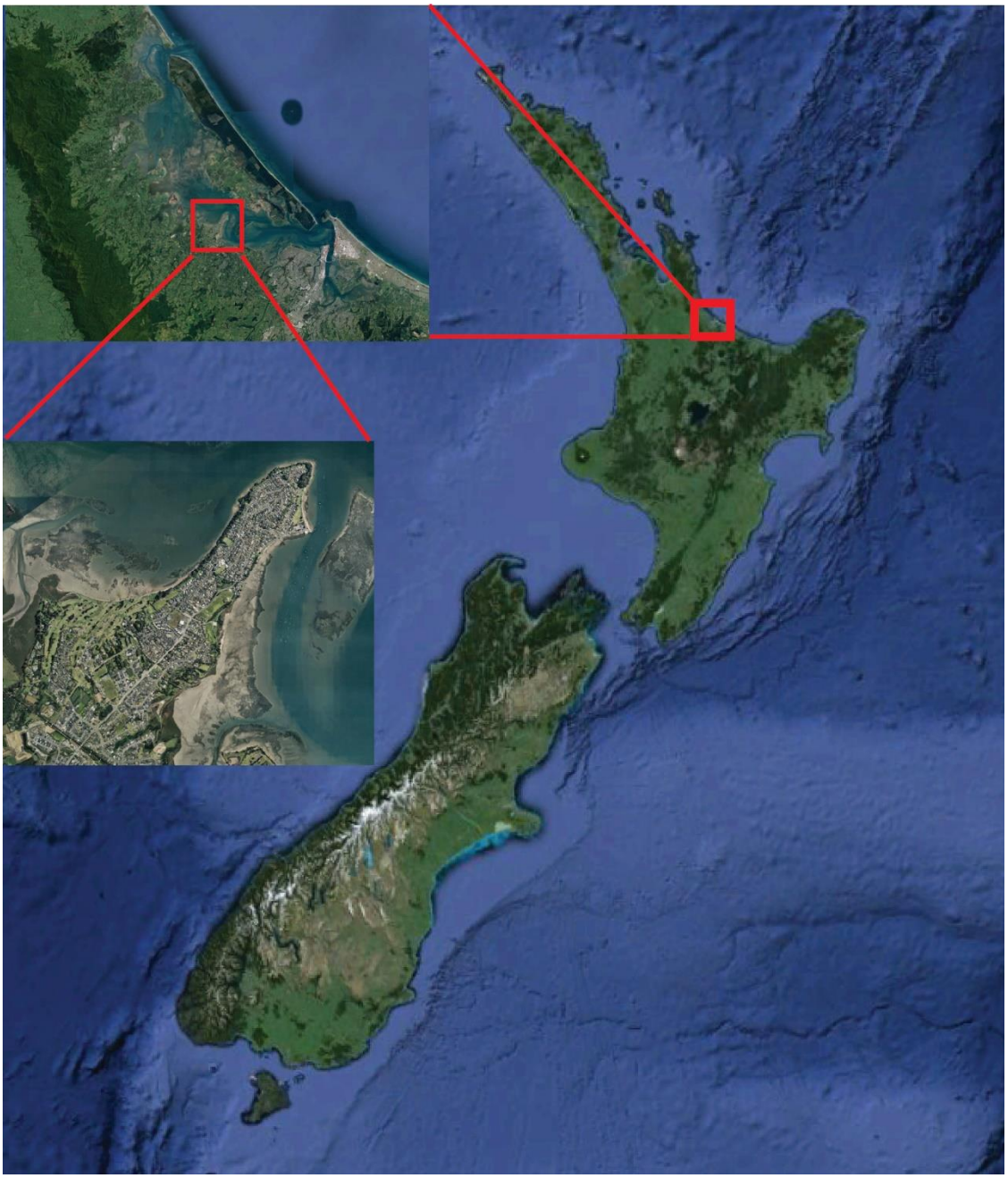

Figure 3.1. A scaled image of the Ōmokoroa Peninsula with zoomed-out images of the Western Bay of Plenty (top left) and New Zealand was provided to contextualise the peninsula's location. All images are oriented north-south.

Bay of Plenty— Site Selection Refinements

Although some locations containing sensitive material pre-exist within Tauranga and the Western Bay of Plenty, these are often relict sites, with failures occurring some time ago. As such *in situ,* sensitive material has been either overgrown by plant growth in the years following the failure (e.g., Te Hono Street, Maungatapu), remediated to make sites safe (e.g., Ruamoana Place, Ōmokoroa and Landscape Road, Ōtumoetai), or has been

extensively overtopped by colluvium from subsequent failures in the upper scarp since the last major reactivation (e.g., Bramley Drive, Ōmokoroa). Such features ultimately made the sensitive material inaccessible at these sites.

Consequently, relatively 'fresh' failure scarps were sought out as these sites provided the best chance of providing material that would be relatively undisturbed, easily able to be sampled and which had not undergone a high degree of overconsolidation. It should be noted that 'fresh' failure scarps were designated as failures that had occurred within the two years of the sampling. Two years was the arbitrary time applied in this instance due to the proximity of time between the failures throughout the Bay of Plenty and the physical testing of the sites. At the start of this PhD in 2018, Ōmokoroa contained several large landslides that met the 'fresh' criteria and thus were selected for further refinement.

Bay of Plenty— Site Specific Characterisations

A total of 26 individual landslides were identified following the Cyclones Debbie and Cook events in 2017 (Kluger et al., 2020). These are shown in Figure 3.2.

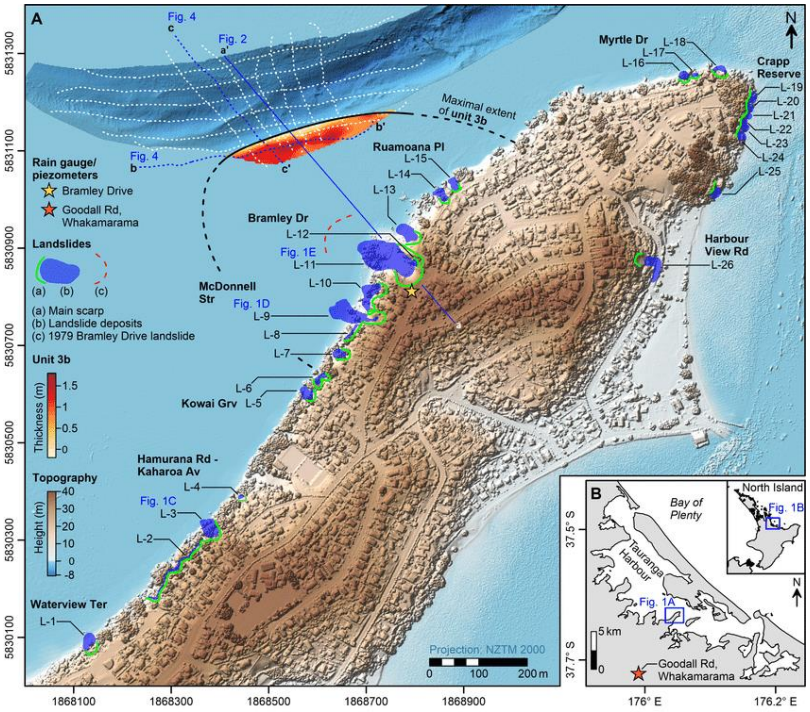

Figure 3.2. Distribution of landslides throughout the Ōmokoroa Peninsula following Cyclones Debbie and Cook in 2017. Image is sourced from Kluger et al. (2020). Note the significant increase in slips on the northwestern coast of the peninsula. These slips were not only larger in number, but also in size.

The bulk of these sites were located on the coastal cliffs of the northwestern side of the peninsula, with two sites, Beach Grove Road (Figure 3.3 a) and Harbour View Road (Figure 3.3 b), found inland, also considered.

(a) (b)

Figure 3.3 (a) The landslide scarp found on Beach Grove Road, Ōmokoroa, following the 2017 cyclone events. (b) The landslide scarp left following the clean-up of the landslide debris along Harbour View Road, Ōmokoroa, following the 2017 cyclone events. While both landslides had large amounts of water ejected following failure, note how Harbour View Road has a much higher volume of fines and clay material.

3.4 Stage 2: Site Investigation

Stage two utilised various tools to assist and ultimately identify the site of highest suitability. These tools include the use of aerial drone imagery to evaluate slips based on key physical characteristics, visual in-person inspection, geomorphic mapping, and physical testing of the soil. Through the deployment of these tools, the potential sampling locations were narrowed down from an initial 26 possible locations to one specific landslide.

3.4.1 Aerial Drone Imagery and Historical Records

Following the twin cyclone events in early 2017, the WBoP District Council engaged contractors to undertake aerial surveillance and inspection of landslide scarps throughout the Ōmokoroa peninsula. Using these images, three criteria that characterise failures in these sensitive soils were employed to eliminate landslides that were unlikely to contain sensitive material. These physical characteristics included:

- A large, bowl-shaped headscarp, potentially retrogressive in nature, with said headscarp being sharp and unstable.

- A long, fluidised landslide deposit runout. These contained large volumes of fine remoulded material, which created sediment plumes in the coastal waters.
- Appearance of '2 stage' failure scarp, an upper bowl-shaped failure scrap failing on top of a benched soil unit (often white in colour) with the lower portion (usually ignimbrite) presenting evidence of translational failure onto the shore platform.

These features were supplemented by a field inspection, undertaken soon after the main failure events, with follow-up inspections prior to sampling undertaken to reaffirm site suitability.

On this basis, five sites from the original 26 were identified from a combination of field and drone inspections following the 2017 failures. These five sites are named based on the closest major road. These were Ruamoana Place (Figure 3.4a and b), McDonnel Street (Figure 3.4c and d), Kowhai Grove (Figure 3.4e and f), Waterview Terrace (Figure 3.4g and h) and Harbour View Road (Figure 3.3 b).

Figure 3.4(a) An aerial image of the Ruamoana Place landslide following the 2017 cyclone events within Ōmokoroa (as supplied by the WBoP District Council). (b) The same Ruamoana Place landslide was taken from the ground near the landslide scarp a few weeks after the landslide event. (c) The McDonnel Street landslide, as seen from the beach below, which failed a few days after the primary cyclone event. (d) Aerial drone imagery of the McDonnell Street landslide taken within 24 hours of the mass wasting event. (e) The Kowhai Grove landslide, as seen from the beach below the landslide a few days after the event had occurred; note the semi-intact deck carried down by the landslide debris. (f) The Kowhai Grove landslide photo was taken from aerial drone imagery soon after the landslide. Note the large amount of visible water exuding from the landslide scarp (supplied by WBoP District Council). (g) The Waterview Terrace landslide as seen from the beach below the landslide scarp. (h) The same landslide scarp at the Waterview Terrace taken from above via drone imagery (supplied by the WBoP District Council).

Of the five locations, three were identified to have had large failures in the past, as noted in various articles. In Gulliver and Houghton's (1980) report, Ruamoana Place, Kowhai Grove and Harbour View Road were all areas that suffered large, retrogressive failures either in the 1979 rainfall event that triggered the Bramley Drive slip or that had occurred previously at some point in the 1960s. Kowhai Grove specifically was subject to multiple large rotational failures during the 1979 event. These were both at the current location of the 2017 slip, as well as further southwest along the coast at the modern-day Ōmokoroa bowling green. This evidence can still be seen at the Hamurana Reserve, where a large remnant scarp remains. While McDonnell Street is not directly referenced in the literature, aerial imagery on Google Earth shows previous failures at the site during the 2012 Cyclone Wilma event.

Two of the five identified sites (Ruamoana Place and Harbour View Road) were quickly ruled out due to extensive remedial work undertaken within a year of the failures. The former, Ruamoana Place, had several drains installed, as well as extensive earthworks and slope face remodelling. The latter, Harbour View Road, was similarly remediated, though on this site, the slope was cut back and covered with geotextile fabric, gravel, and boulders of varying sizes.

Of the remaining three sites, McDonnel Street, the largest of the 2017 failure events, was removed as an option due to a lack of accessibility and health and safety concerns about a shed overhanging the scarp face, as seen in Figure 3.4. (c) and (d)**.** The lack of accessibility, due to the ignimbrite face at the landslide base being over 2 m high, made access to the landslide scarp bowl nearly impossible. The shed of the former property remained overhanging the site until at least 2020–2021, when remedial works were undertaken on the site, and the shed and property were removed.

Waterview Terrace and Kowhai Grove were subsequently selected as the two sites of preference for sampling, and further field investigations were undertaken to determine site viability. Field investigations involved access into the landslide scarps, creation of geomorphological maps, soil stratigraphy mapping, and determination of field strength of soil within the scarps to identify the sensitive soil layers.

3.4.2 Site Geomorphology

Geomorphic maps were created based on field observations at the sites following the failures in May 2017. These were initially drawn in the field before being recreated in the ArcMap software suite using conventional ESRI geomorphological symbols.

Waterview Terrace

The slip at Waterview Terrace (Figure 3.5) was a relatively well-constrained complex failure, with elements of both a small rotational and translational slip seen within the failure scarp. The slip surface spanned 17 m in a southwest-northeast orientation following the natural coastline. Within the slip, extending to the upper face, two distinctive failures are observed, split and constrained on either side by a sharp ridgeline extending 6–8 m northwest. A convex slope break extended roughly 2.5 m northwest as the slip extended through the underlying ignimbrite before following a small valley towards the harbour.

On the right edge of the slide (northeastern up the coast), the slip tended translational, benching onto the underlying ignimbrite, with a sharp cliff forming due to the large blocks of ignimbrite that had sheared off. The talus extended 20–30 m out into the harbour, with the bulk of the material comprising soft remoulded silts and clayey silts intermixed with larger chunks of overlying Hamilton Ash clays and underlying ignimbrite blocks. Due to the complexity of failure and the intermingling of rotational and translational failures at Waterview Terrace, Kluger *et al.* (2020) determined the failure volume to be somewhere in the range of 2290 m^3. However, the volume of material displaced attributed to the rotational failure is likely to be lower than this.

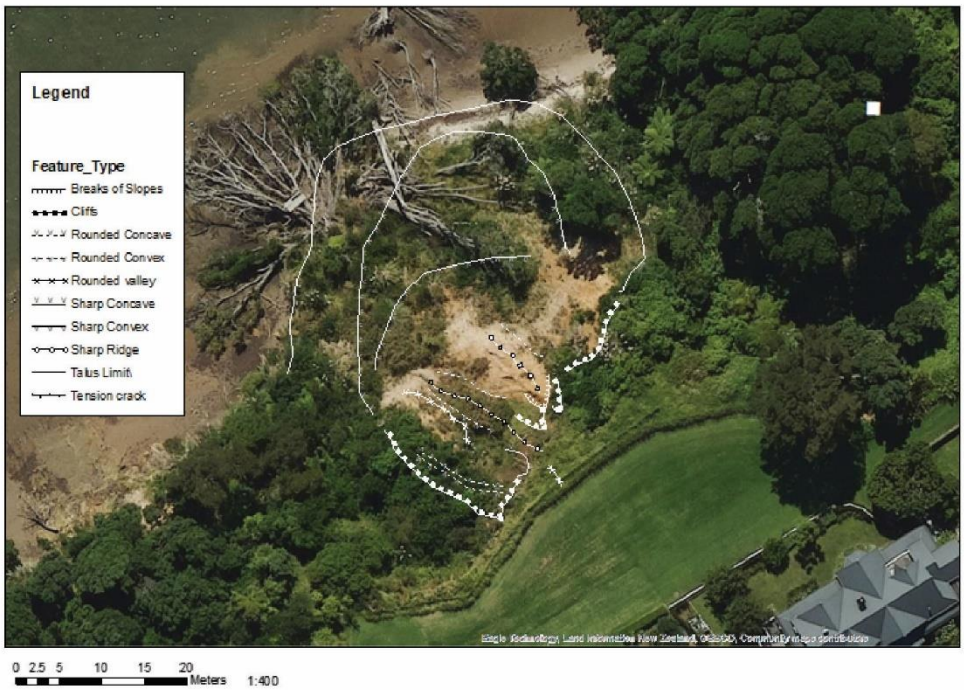

Figure 3.5. An annotated aerial photo provided the geomorphological characteristics of the Waterview Terrace landslide, which was identified following the landslide event in mid-2017. Geomorphological symbols are standard ESRI symbols and are shown in the legend.

Kowhai Grove

The slip at Kowhai Grove (Figure 3.6), while more constrained laterally, was a much larger, deeper-seated failure occurring in a portion of the coastline that was much steeper and further set back from the initial cliff face when compared to the Waterview Terrace slip. The slip was approximately 200 m northeast of the Hamurana Reserve along the coastline. Details around the slip evolution are unclear. Local reports suggested an initial failure occurred before midnight on the 5th of April, with the bulk of failure occurring at some point during the early morning of the 6th of April 2017. One confirmed aspect was a report of water 'gushing' out of the slope under high pressure, supported by drone imagery at the time. The slip itself, as seen in other previous failures around Ōmokoroa, was complex in nature.

The slide was comprised of a deeper-seated rotational failure benching onto the underlying ignimbrite, with a shallower translational failure occurring in said ignimbrite either before or preceding the deeper-seated rotational failure. The rotational failure slide surface was approximately 9 m below the former topsoil, a total of 20 m in height above the shore platform. The rotational slip was narrower than it was long, with the remnant bowl measuring approximately 24 m in length and 12 m in width. Once again, due to the

complex nature of the failure and approximations of slip surface locations, Kluger *et al.* (2020) estimated that around 4,500 m^3 of material had been displaced, though this may be an overestimate. The slip surface had a very narrow upper portion with a small valley formed in the remaining upper soil before descending to a sharply angled edge, cutting into the underlying ignimbrite. The slip is accompanied by two smaller translational slips immediately along the coastline.

Figure 3.6. An annotated aerial image of the 2017 Kowhai Grove landslide provides a geomorphological context to the landslide. Standard geomorphological ESRI symbols are used and are shown in the legend.

3.4.3 Site Stratigraphy and Soil Descriptions

To further establish the feasibility of each site for further investigation, a stratigraphic log of the exposed soil face within the scarps was created. Of the two sites, the resultant scarp face was much wider and longer at Kowhai Grove than at Waterview Terrace. For the sites to be defined as suitable for this study, they had to meet an extra requirement in that the soils must, at a minimum, meet the threshold of fitting the definition of 'extra sensitive' (S_t=8–16) as defined in the NZGS 2005 Field Description of Soil and Rock Guidelines (Burns et al., 2005).

Waterview Terrace

The stratigraphic log for the exposed soil face at the Waterview Terrace scarp is shown in Figure 3.7a. As found elsewhere on the peninsula, the site's upper soil layers are comprised of Younger Ashes and Rotoehu Ash. These are then separated from the underlying Hamilton Ashes (see Lowe et al., 2001; Lowe, 2019) by a distinctive dark-brown paleosol. The paleosol grades downwards into the upper Pahoia Tephra units. The thicknesses of units were difficult to discern due to colluvial deposits from failures of the Younger Ashes (i.e., tephra deposits post-dating Rotoehu Ash) and Rotoehu Ash onto the Hamilton Ashes. Upper portions of the Pahoia Tephra (sandy clays/silts) were present within the scarp bowl, though these were quite thin, with the Te Puna Ignimbrite evident within the scarp beneath the debris material. This distribution of soils is illustrated in the annotated image of the scarp face (Figure 3.7b).

(a)

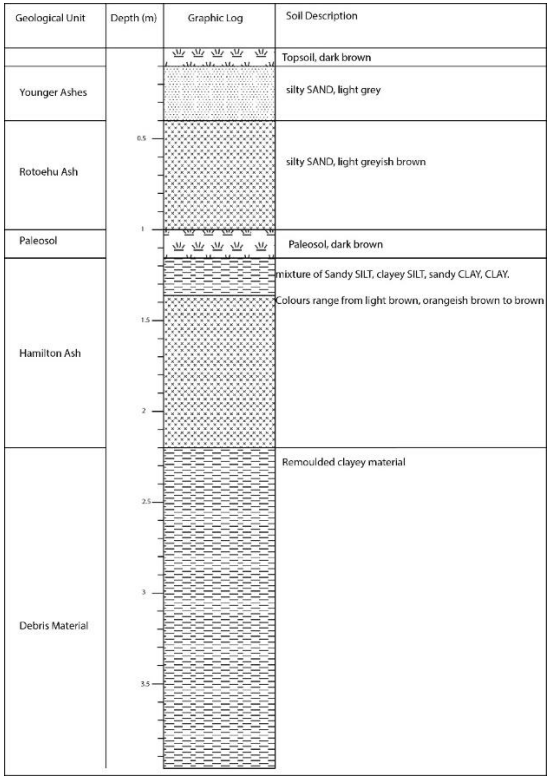

(b)

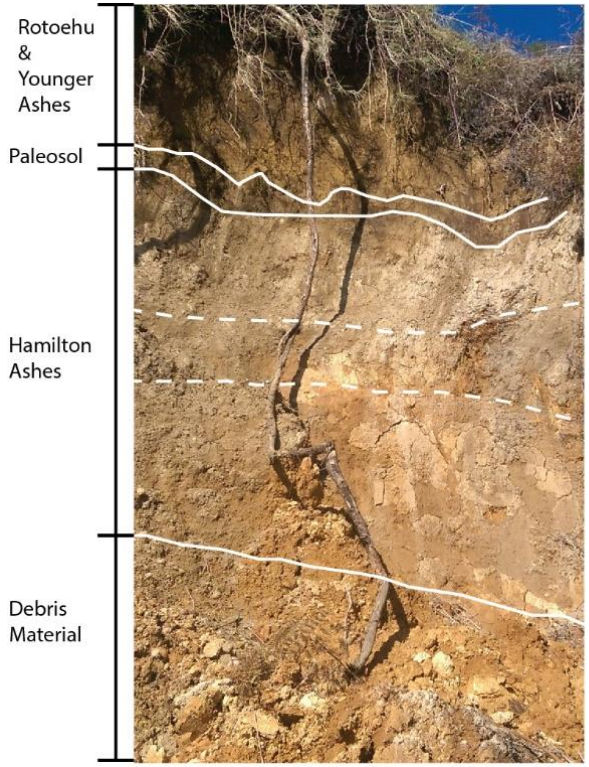

Figure 3.7. (a) A stratigraphic face log of the exposed soils observed within the Waterview Terrace landslide scarp. (b). An annotated photo of the differing soil layers within the Waterview Terrace landslide scarp. Solid lines denote a change in the unit, while dashed lines denote a change within the unit (i.e., specific horizons within the Hamilton Ashes).

Material within the scarp bowl was soft, with the soil having extensive manganese oxide concretions and/or nodules throughout (Figure 3.8). The soil appeared to be a clayey SILT, with some sands. Samples exhibited a dilatant response but retained some strength upon mechanical remoulding. Blocks of Te Puna Ignimbrite also appeared within the lower portion of the scarp (Figure 3.8). These blocks were almost entirely SILT with some sands to sandy SILT, with dilatant behaviour observed.

Figure 3.8. Samples of soils found within the Waterview Terrace landslide scarp. From left to right, the soil is representative of Pahoia Tephra, a slightly more weathered Pahoia Tephra, and Te Puna Ignimbrite

The Pahoia Tephra present within the scarp itself was inconsistent in thickness on either side of the bowl, with a slightly thicker lens of clayey SILT present on the left (southwest) face of the bowl, being much lighter in colour (brownish-grey) (see left soil sample in Figure 3.8) than the material present on the right face (northeast). This material was much darker (see centre soil sample in Figure 3.8), almost exhibiting an orange-brown complexion. Further, the Pahoia Tephra material in the right face was much stiffer and appeared to have a higher clay content, with the soil barely dilating. Additionally, material from the right edge appeared to have pumiceous inclusions within the chunk, accompanied by orange mottling (likely iron oxides).

Table 3.1 presents the shear vane strength readings from three locations within the scarp bowl. These were taken in what appeared to be three differing units present within the bowl on the scarp's left, right, and back faces. All readings were undertaken in accordance with NZGS 2001 Guideline for Hand Held Shear Vane Tests. Descriptors for sensitivity

were determined in accordance with the NZGS 2005 Field Description of Soil and Rock Guidelines. Soils from the back and right face exhibited stiff consistency with an undrained shear strength (S_u) between 50–100 kPa. In contrast, the left face was much weaker, with this falling in the firm range (25–50 kPa). Soil sensitivity ranged from 3.8 to 4.9, with soils falling within the upper "moderately sensitive" to lower "sensitive" range. Remoulded shear strength (S_{ur}) is also shown in the table.

Table 3.1. Shear vane readings of soils within the Waterview Terrace landslide scarp.

Soil	S_u (kPa)	S_{ur} (kPa)	S_t	Descriptor
Left Face	44	9	4.9	Sensitive
Right Face	75	20	3.8	Moderately Sensitive
Back Face	61	15	4.1	Sensitive

These findings indicated that Waterview Terrace, as a site, was not suitable for this study, as it contained a distinct lack of 'extra sensitive' clay material. Further, subsequent weathering and erosion of the clay scarp made access to the bowl increasingly challenging, specifically with the underlying Te Puna Ignimbrite actively eroding to leave steep faces.

Kowhai Grove

The stratigraphic log for the exposed face at Kowhai Grove and the annotated images for the layer locations on the scarp face can be seen in Figure 3.9. (a and b. The Kowhai Grove slip scarp was located further back from the coastline compared to the Waterview Terrace scarp, and was much larger overall. The Kowhai Grove scarp face was also 'cleaner' and discerning soil layers were much clearer than at the Waterview Terrace site.

The upper layers of the site are made up of Younger Ashes and Rotoehu Ash (roughly 1 m in thickness); these are underlain by a paleosol overlying the Hamilton Ashes, with around five of the eight Hamilton Ash layers identified (roughly 3.5 m thick) (see Lowe, 2019). The Hamilton beds are then distinguished from the Kauroa Ashes by a thick, distinctive dark brownish-black paleosol. The Kauroa Ashes are around 4.4 m thick and are in contact with the Pahoia Tephras. The bottom of the scarp bowl appears to have a thinning layer of lower Pahoia Tephras running from the base of the scarp face leading to the bowl edge, where the unit transitions to the underlying Te Puna Ignimbrite.

(a)

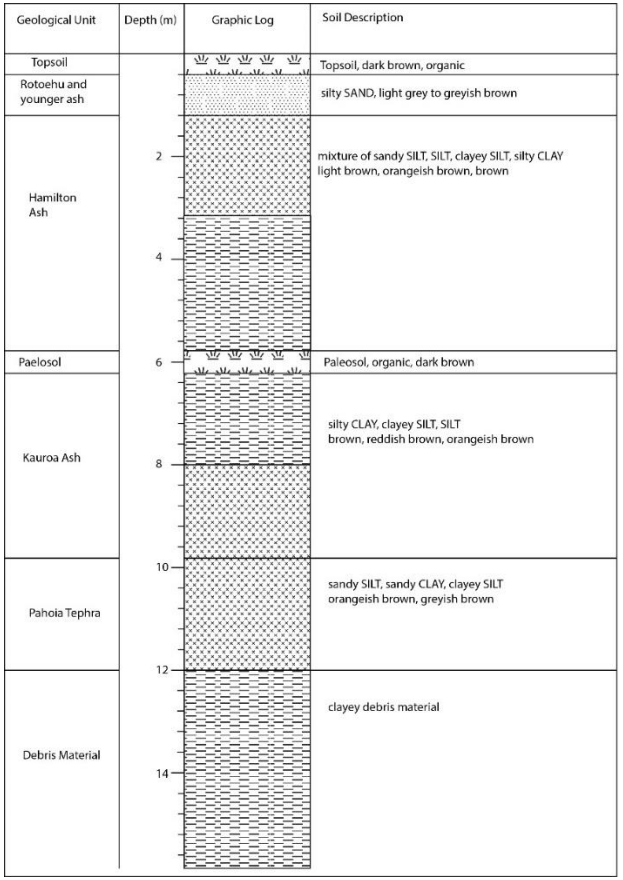

(b)

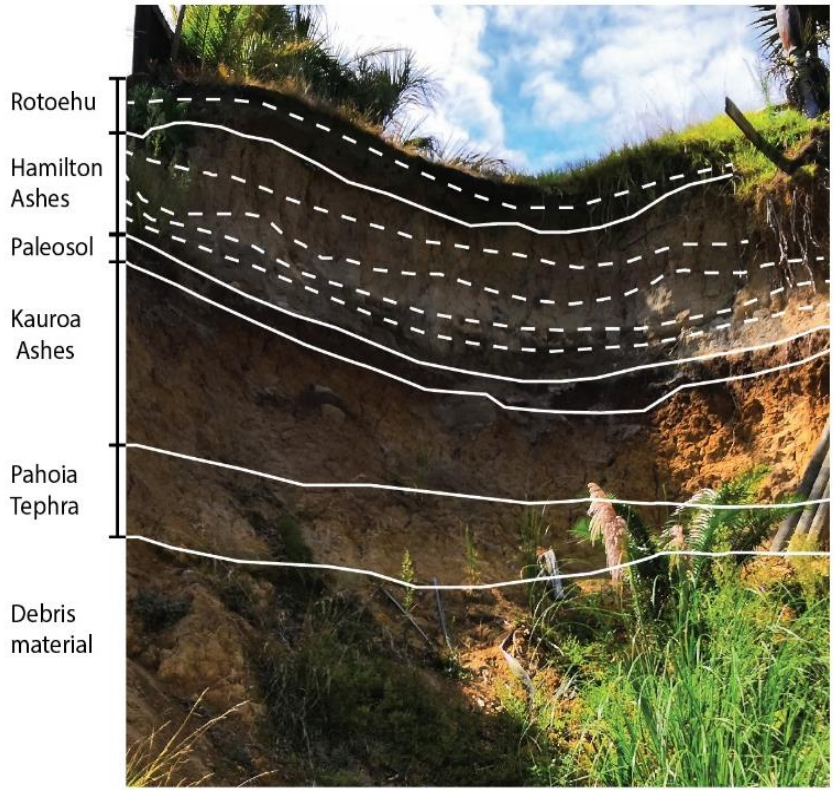

Figure 3.9. (a) A stratigraphic log of the soils found within the Kowhai Grove landslide. (b) An annotated image of the soils found within the Kowhai Grove landslide. Solid lines denote differing units, while dashed lines are horizons within a unit

The thickness and makeup of the lower Pahoia Tephra varied throughout the scarp bowl. The thickness of the layer increased with distance from the lower edge towards the scarp face. Auger profiles taken at 2 and 4 m from the lower edge of the scarp showed a 0.4 m thickness increase with every metre back from the lower bowl edge. Augers were terminated upon contact with the underlying Te Puna Ignimbrite. In deviation from the general 2001 NZGS guidelines, shear vane strength measurements were taken with soil makeup changes, as well as at every 300 mm interval.

Auger 1, taken 2 m from the lower edge of the bowl, showed three distinct soil layers, with around 90 mm of Pahoia Tephra present (420 mm total thickness). The layers were comprised of clayey SILT material, likely colluvium, pumiceous sandy CLAY with some silts and a pumiceous SAND with trace sands. The sandy CLAY did not present as 'extra sensitive' when tested with a shear vane (Table 3.2).

Table 3.2. The shear vane strengths are derived from soils within the Kowhai Grove landslide scarp. Values were measured using calibrated hand shear vane, though a slight variation in the typical NZGS (2001) methodology was applied, with shear vanes taken both at every 300 mm, and every determined change in soil layer.

Soil	S_u (kPa)	S_{ur} (kPa)	S_t	Descriptor
Auger 1				
Debris (300 mm)	18	13	1.4	Insensitive
Pumice Clay	65	22	3.0	Moderately Sensitive
Auger 2				
Debris (300 mm)	19	15	1.3	Insensitive
Clayey SILT (Dark Brown)	71	14	5.1	Sensitive
Mottled clayey SILT (600 mm)	82	17	4.8	Sensitive
clayey SILT	62	9	6.9	Sensitive
Sensitive Layer	**57**	**5**	**11.4**	**Extra Sensitive**
Pumiceous Layer (900 mm)	68	27	2.5	Moderately Sensitive

Auger 2, drilled 4 m from the lower edge, had an increasing number of layers (seven distinct layers), with an 'extra sensitive' layer identified approximately 0.8 m below the scarp surface. Similar to the first auger, a thick (400 mm) deposit of debris from the upper portion of the slope overlays the soil, comprising a mixture of clayey material from the upper parts of the Pahoia Tephra, chunks of Kauroa Ash, and Hamilton Ashes found within the debris deposit. This is followed by a layer of clayey SILT with some sands

(270 mm thick), which had large amounts of manganese mottles in the lower portion (200–270 mm). This is followed by a 60 mm-thick unit of clayey SILT and a 160 mm-thick ‘extra sensitive’ layer of clayey SILT. Distinguishing this sensitive layer from those around it was challenging. This is illustrated in Figure 3.10, showing the similarity in colour and overall look within a small test pit dug to the side of the auger hole. A distinction was made through physical interaction with the soil, with sensitive material having a much clearer loss of strength when being ‘remoulded’ upon extraction from the auger head.

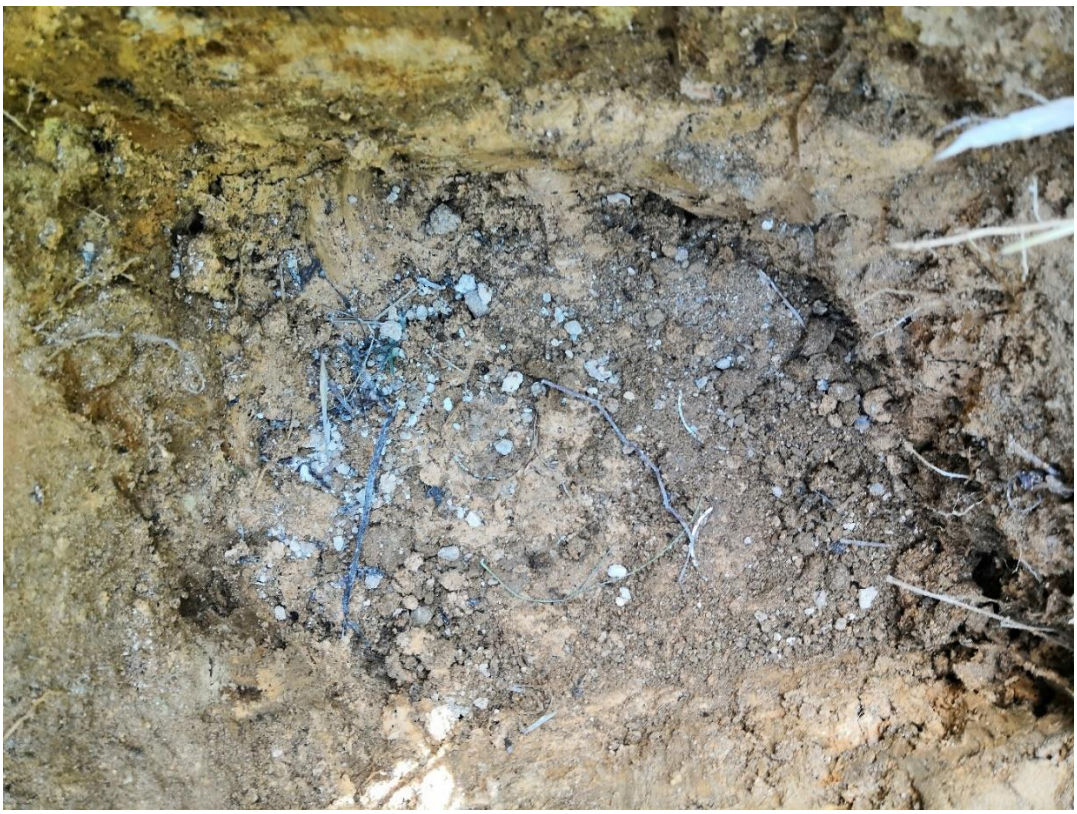

Figure 3.10. An image of a small test pit dug into the Kowhai Grove landslide scarp. Some features of note in this are stark colour change (top right of image) where the soil transitions from the dark brown clayey SILT to an underlying light greyish brown clayey SILT. Sensitive material is hard to distinguish within this image due to the uniformity in which the soil appears. The only visible evidence is the slight smearing of clays between the wall and the base of the test pit, as the pit begins to go into the sensitive layer. Some detritus has fallen into the pit from around the edges.

This sensitive material is subsequently underlain by a pumiceous sandy CLAY, similar to that found in Auger 1, becoming increasingly sandy upon contact with the underlying Ignimbrite.

Two further augers (Augers 3 and 4) were undertaken 1 m to the left and right of Auger 2 to examine the extent of the material. However, neither auger holes found the same soil, nor did they have soil that responded in an extra-sensitive fashion upon testing with a handheld shear vane. Further augers closer towards the scarp face were not undertaken due to concerns about the stability of the scarp face at the time.

Based on the data collected about the Kowhai Grove landslide site, it was the most appropriate location within Ōmokoroa to select as the field site. Especially as it met all five criteria established for selecting an appropriate site. This included a sensitive soil layer that not only recorded a response of 'extra sensitive' (criterion 1) but was found within 800mm of the soil surface (criterion 2) and was 160mm in length (criterion 3). In addition to this, the site was easily accessible by foot (criterion 4) and had approval from the WBoP District Council to access as the failure had occurred on what was regarded as council land (criterion 5).

3.5 Sampling Procedure and Laboratory Preparation

3.5.1 Field Sampling

Following identification of the sensitive layer at the Kowhai Grove landslide site, a narrow pit was excavated into the slope to allow access to the sensitive soil layer. Ideally, a block sample would be extracted and transported to the lab using a Sherbrooke sampler or similar alternative. Individual samples would then be trimmed using a soil lathe from the larger block, thus reducing the potential disturbance that may occur during transport and storage of the cores.

While this would have been the optimal sampling methodology, due to the large amount of material that would need to be extracted to ensure sufficient soil cores were created, it was decided that, given the potentially unstable nature of the landslide scarp, the least material removed and disturbed was regarded as the safest approach.

As such, samples were extracted using thin-walled stainless steel tubes (approximately 150 mm x 50 mm), with the tubes gently driven into the soil at a steady rate using primary body weight applied to a bespoke core driver. Due to the soft nature of the soil, and difficult access, mechanical application of force by either a piston or other method was unachievable. Care was taken to reduce any potential for disturbance. Following the driving in of cores, a narrow channel around the sampled soil was further excavated, with these channels extending approximately 50 mm beyond the end of the driven cores. The

soil was then cut underneath each core, and they were individually extracted. Cores were then sealed with multiple layers of Glad Wrap before being individually wrapped in bubble wrap.

Wrapped cores were then placed into a large hard-carry foam container lined with foam. This was filled with soaked paper towels, and water was sprayed into the air of the box before being sealed for transport. This was undertaken to ensure that samples were kept in a high-humidity environment, with the goal of preventing potential dehydration during transport. Multiple boxes were used to reduce the weight of the soil being transported from the landslide back to the transport site.

3.5.2 Laboratory Preparation

Research-grade 99% pure potassium acetate from Merck was used to undertake this research. The potassium acetate was stored in an airtight container within the laboratory's chemical storage, with care taken to ensure the humidity in the storage was as low as possible. This is due to the highly deliquescent nature of potassium acetate.

When preparing the 2 $molL^{-1}$ solution of potassium acetate for use in treating the soil cores, a single, large batch was made, with a mixture of the 99% potassium acetate and de-ionised water used to create the solution.

Four soil cores were then immersed in the 2 $molL^{-1}$ potassium acetate in ten-litre Klip-It containers, with the solute extending approximately seven centimetres above the cores. This was repeated until six containers were prepared. While only four containers were required (for 1, 3, 6, and 12 months), additional containers were prepared to account for the potential loss of cores during extraction and any further possible testing that may occur beyond the 12-month period.

3.5.3 Sample Disturbance

While multiple attempts were made to minimise disturbance to the soil as much as possible between sampling and testing within the triaxial apparatus, there was still a potential for disturbance to have occurred. As such, it is necessary to quantify this. The specifications set out in Lunne *et al.* (1997) have been used, where the comparison of Δe to e_o provides an indication of disturbance (i.e., $\Delta e/e_o$). In this instance, Δe refers to the change in void ratio when loading to the vertical stress expected *in situ*, and e_o refers to the initial void ratio. Table 3.3 shows the disturbance ratios of the soils from this research,

as well as the average disturbance. The disturbance ranges from 0.11 to 0.22, with averages ranging from 0.16 to 0.19.

Table 3.3. The sample disturbances for all soil cores tested at all time points and confining stresses, along with the average disturbances at each testing point, are also included. Disturbances range from 0.11 to 0.22, with averages ranging from 0.16 to 0.19.

Confining Stress (kPa)	Untreated	1 Month	3 Month	6 Month	12 Month
120	0.21	0.15	0.14	0.17	0.11
160	0.20	0.17	0.16	0.22	0.18
200	0.17	0.20	0.19	0.19	0.21
Average	0.19	0.17	0.16	0.19	0.16

To determine what level, or 'grading', of disturbance has occurred, it is necessary to determine the Over-Consolidation Ratio (OCR) of the soil. With the OCR determining the specific range applied to the soil. The OCR is determined by the maximum preconsolidation stress, or in this instance, the previous *in situ* stress experienced by the soil prior to failure (200 kPa) divided by the current overburden stress (12.6 kPa). This resulted in an OCR of 15.87.

While this is higher than the range of OCR suggested by Lunne *et al.* (1997), in this instance, the higher OCR parameters have been used (where < 0.03 = very good to excellent, 0.03–0.05 is good to fair, 0.05–0.1 is poor, and > 0.10 is very poor). As a result, the soil cores in this instance are universally classified as very poor, as all have a value higher than 0.10, indicating a reasonably high level of disturbance.

3.6 Conclusions

For the purposes of this study, identifying an appropriate field site to allow for the collection of extra-sensitive material within the Bay of Plenty was essential. To achieve this, the selected location needed to meet five criteria. An initial desktop study was conducted to identify the the most suitable location within New Zealand to sample. From this, the Bay of Plenty, particularly the Ōmokoroa Peninsula, was deemed the most suitable area for testing. To further refine site selection, a site investigation was undertaken using aerial drone imagery, historical records, site geomorphological maps and field investigations. From an initial 26 sites, five were selected based on aerial drone imagery, of which three were eliminated due to either remedial works or hazards present at the site. Subsequently, two sites, Waterview Terrace and Kowhai Grove, were geomorphologically mapped, as well as investigated to determine the soils present within

the landslide scarps. From the two, Waterview Terrace was deemed inappropriate due to the lack of extra-sensitive soil material, while Kowhai Grove met all five of the key criteria.

Part I

Triaxials and Geomechanics

Chapter 4

Part I — Introduction

This chapter will look to explore the various geomechanical parameters of the Pahoia Tephra. Parameters examined include wet and dry bulk densities, particle density, porosity, void ratio, saturation ratio and particle sizes. Atterberg limits for both untreated soil and treated soils are determined with values plotted on a Casagrande plasticity chart. Speed of travel through remoulded soil by K-acetate is also measured. In addition to this consolidated undrained tests on untreated and treated samples at three confining stresses are undertaken to observe changes in both the soils strength and behaviour under shear. Post failure cores are also examined for further validation of behavioural changes during shear. These values are subsequently discussed in detail with reference to relevant literature.

Chapter 5

Part I — Methods

Detailed in this chapter are the various methods employed to establish the geomechanical characteristics of the soils used during this research. As well as the methods utilised during triaxial testing. Methods used during geomechanical characterisation include bulk density tests, moisture content, particle density testing, and particle size testing. Atterberg limit testing was also undertaken to characterise the mechanics of the Pahoia tephra sampled for this research. For triaxial testing, consolidated undrained tests were selected as the primary method of strength testing

5.1 Moisture Content

The moisture content (Mc) of soil was determined in accordance with NZS 4402:1986 Test 2.1. Soil samples were dried at 110 ºC for 24 hours in a convection oven before being cooled in a silica bead desiccator for 24 hours and weighed. Where soils may have contained metal salts, corrections to the weights were made following the guidelines in ASTM D5550-14.

5.2 Bulk Density

Bulk densities (ρ) were calculated in accordance with ISO 17892-2 (2014) using the linear measurement method. For soils treated with Potassium Acetate (K-acetate), bulk densities were determined from the treated soil cores used for triaxial testing.

5.3 Particle Density

The particle density (ρ_s) was determined following ASTM D5550-14. Samples were tested using an Anton Paar Quantachrome Ultrapycnometer 1000. In deviance from the stated standard, lab-grade nitrogen gas was used instead of helium gas due to shortages in helium supplies. Calibration checks of the pycnometer were undertaken prior to usage of the equipment as per Anton Paar standard methodology. Temperature drift was monitored to ensure temperature did not drift outside the normal working range. Due to the presence of salt within treated samples, corrections were applied as per ASTM D5550-14 standard (5.1), where G_{sc2} is corrected particle density, M_{salt} is the mass of pycnometer specimen including salt, V_{ps} is the volume of pycnometer specimen, W_C is water content corrected for salinity (5.2), ρ_{salt} is the density of salt and ρ_w corresponds to the density of

water. For equation 5.2, Wc is water content corrected for salinity, Mw is the mass of water without salt, and Ms is the mass of the specimen, including salt.

$$G_{sc2} = \frac{M_{salt} - [\frac{W_c(\frac{S}{1000})M_s}{1 + w_c(\frac{S}{1000})}}{\{V_{ps}\left[\frac{W_c\left(\frac{S}{1000}\right)M_s}{\left(1 + W_c\left(\frac{S}{1000}\right)\right)\rho_{salt}}\right]\}\rho_w} \tag{5.1}$$

$$W_c = \frac{(1 + \frac{S}{1000 - S})M_w}{M_{salt} - [\left(\frac{S}{1000 - S}\right)M_w]} \tag{5.2}$$

5.4 Porosity, Void Ratio, and Saturation Ratio

Porosity (*n*) (derived from Carey *et al.* (1996)) and void ratio (*e*) (derived from Jamiolkowski *et al.* (1995)) were determined from Equations (5.3) and (5.4), respectively. While the saturation ratio (S_r) is shown in Equation (5.5).

$$n = (1 - \frac{\rho_d}{\rho_s}) \times 100 \tag{5.3}$$

$$e = \frac{V_v}{V_s} = \frac{n}{1 - n} \tag{5.4}$$

$$Sr = \frac{V_w}{V_V} \tag{5.5}$$

Where ρ_d, ρ_s, V_v, V_s, V_w, refer to the dry bulk density, particle density of the sample, volume of voids, volume of the solids and volume of water, respectively.

5.5 Particle Size

Particle sizes in the sub 2 μm–4 mm range were measured using a Malvern Mastersizer 3000 laser particle sizer, following the University of Waikato (UoW) Standard Operating Procedure (SOP). The Malvern Mastersizer 3000 was selected as the primary method of particle size analysis due to the expected large fraction of silt and clay particles, making sieve analysis unhelpful. Additionally, laser particle analysis was utilised in favour of the hydrometer analysis due to the rapid testing time, repeatability of results, and higher accuracy in measuring fine particles. Prior to testing, the samples were air-dried, the aggregates were broken up, and the material was passed through a 2 mm sieve. Following drying, samples were rehydrated in water, and a minimum of three random samples were drawn from the subsequent soil-water mixtures. Refractive Index (RI) and Absorption (A) parameters were set to 1.52 and 0.01, respectively, as per Cunningham (2012), with laser obscuration set to between 15–20 %. All samples were tested in a water suspension as opposed to other potential suspension media (i.e. acetone). Some concerns were raised surrounding the dissolution of salt material from the clay into the water suspension, thus affecting the rate of light diffraction (and subsequently affecting measurement by the laser particle sizer). Following discussions with UOW technical staff, it was determined that the effect would likely be negligible. Results are presented as percentages of the total volume within the clay (<2 μm), fines (<63 μm), and sand fractions (fine medium and coarse < 2000 μm).

5.6 Atterberg Limit

5.6.1 Liquid Limit

The Liquid Limit (LL) was determined via the fall cone method in accordance with BS EN ISO 17892-12:2018. In line with the standard, as no material larger than 0.4 mm was present within the soil (as determined by particle size analysis), the soil was mechanically remoulded by hand using metal spatulas on a glass plate. Due to the high natural water content of the soil, no water was added during the remoulding process. Instead, the soil was slowly air-dried over 8 hours, with mixing occurring every 15 minutes to achieve homogeneity during the drying process. A multi-point test was undertaken using an 80 g/30 ^{o} cone, and the liquid limit was derived from the equivalent 20 mm penetration from a plotted trendline.

Following the initial drying of the soil, standard protocol was followed, with 5-7 ml of liquid mixed thoroughly into the paste and left to rest in a sealed container for an hour before being tested. While this methodology was within the scope of the BS EN ISO 17892-12:2018 standard, a 'reverse' drop cone test was undertaken. During the drying process, a fall cone test was undertaken at hourly intervals to ensure no significant changes to the soil's characteristics occurred due to drying.

5.6.2 Plastic Limit

The Plastic Limit (PL) was determined following the BS EN ISO 17892-12:2018. Soil was rolled into 3 mm threads on a glass plate until samples began to shear and crack apart. This was repeated on a 20 g sub-sample, generating two tins of 10 g soil thread 'worms'. Plasticity is defined as per Sowers (1979), where PL soil descriptions are:

- 0 – Non Plastic
- <7 – Slightly Plastic
- 7-17 – Medium Plastic
- >17 – Highly Plastic

5.6.3 Plastic Index

The Plasticity Index (PI) was calculated per BS EN ISO 17892-12:2018. This value represents the numerical difference between liquid and plastic limits, as shown in Equation 5.6.

$$PI = LL - PL \tag{5.6}$$

5.6.4 Liquid Index

The Liquidity Index (LI) was computed according to BS EN ISO 17892-12:2018. This value compares the soil's field (natural) moisture content to the plasticity index. It indicates where the soil *in situ* sits compared to its plastic and liquid limits. It is calculated from Equation (5.7).

$$LI = \frac{Natural\ Moisture\ Content\ (NMC) - PL}{PI} \tag{5.7}$$

5.6.5 Activity

Activity measures the plasticity of the clay fraction (<2 μm) within the sample tested. This is calculated as shown in Equation (5.8).

$$Activity = \frac{PI}{\%\ clay\ content\ (< 2\mu m)} \tag{5.8}$$

5.7 Conductivity / Ion Diffusion

The rate of metal salt diffusion through the soil was undertaken based on the methodology developed by Helle et al. (2015). Remoulded soil was placed into a cling film-lined rectangular container (215 x 155 x 80 mm). A small channel (10 x 75 x 40 mm, approximately 30 ml of solution) was made at one end, with a minimum of 40 mm left between the channel and all surrounding edges. This was done to ensure that solute could not travel along the edges or sides of the container. This channel was filled with 2 $molL^{-1}$ K-acetate. Three conductivity sensors were placed into the soil at 30 mm, 90 mm, and 150 mm from the channel. Conductivity was logged every 6 hours until an equilibrium value (3.5 mS^{-1}= 2 $molL^{-1}$ K-Acetate value) was achieved. A diagram of the setup is shown in Figure 5.1 below.

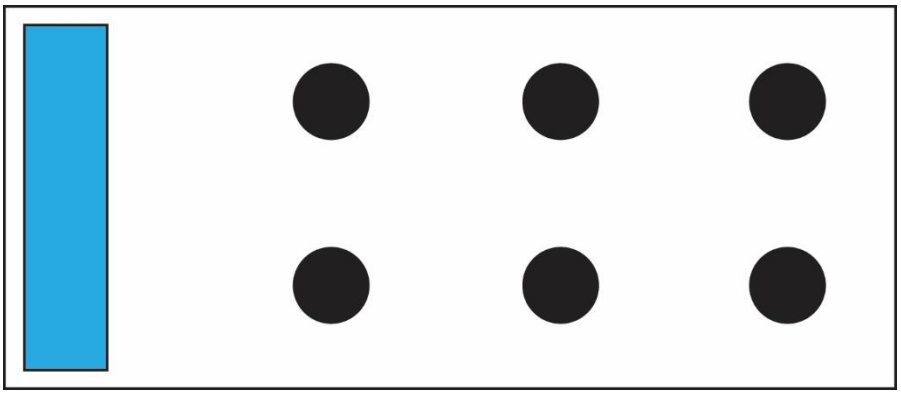

Figure 5.1. An outline diagram of the conductivity test undertaken. The blue square represents the salt well, with black circles (spaced every 300 mm) representing the conductivity probes.

5.8 Triaxial Testing and Apparatus

Effective and total strength parameters were derived from Triaxial testing. This was selected as opposed to other shear failure methods, such as direct shear box testing, due to the versatility of the triaxial test that allow for control of stresses along three principal axes under conditions of axial symmetry (Craig 1997). Further, triaxial testing allows for the exploration of various confining stresses for the soil, creating conditions closer to those experienced *in situ* during scenarios where failure may be induced. It also allows for comparison of some results to values derived in previous studies on soils sampled within the Tauranga basin area (Wyatt, 2009; Arthurs, 2010; Cunningham, 2012; Mills, 2016). All testing was undertaken following BS 1377-Part 9:1990, with any deviations outlined in the methods below.

5.8.1 Triaxial Apparatus

CU tests were run at a constant strain rate through an IMPACT 50kN load frame, with a base platen raised at a speed determined per BS1377-Part 9a. The cell and back pressure to the sample were controlled by GDS Instrument 3 MPa pressure rams that provided real-time data on the system's pressure (kPa) and volume displacement (mm^3). The system was fully electronic, with load (IMPACT 5kN load cell), strain (IMPACT 25mm LVDT), volume changes (GDS pressure rams), and pore pressure (GDS 2MPa pore pressure transducer) being monitored and recorded in real-time on an 8 Channel GDS Instruments control box with a 9,600 baud rate. All data and pressure rams were monitored, processed, and controlled within the GDS lab software. Figure 5.2 shows a simplified view of the triaxial setup

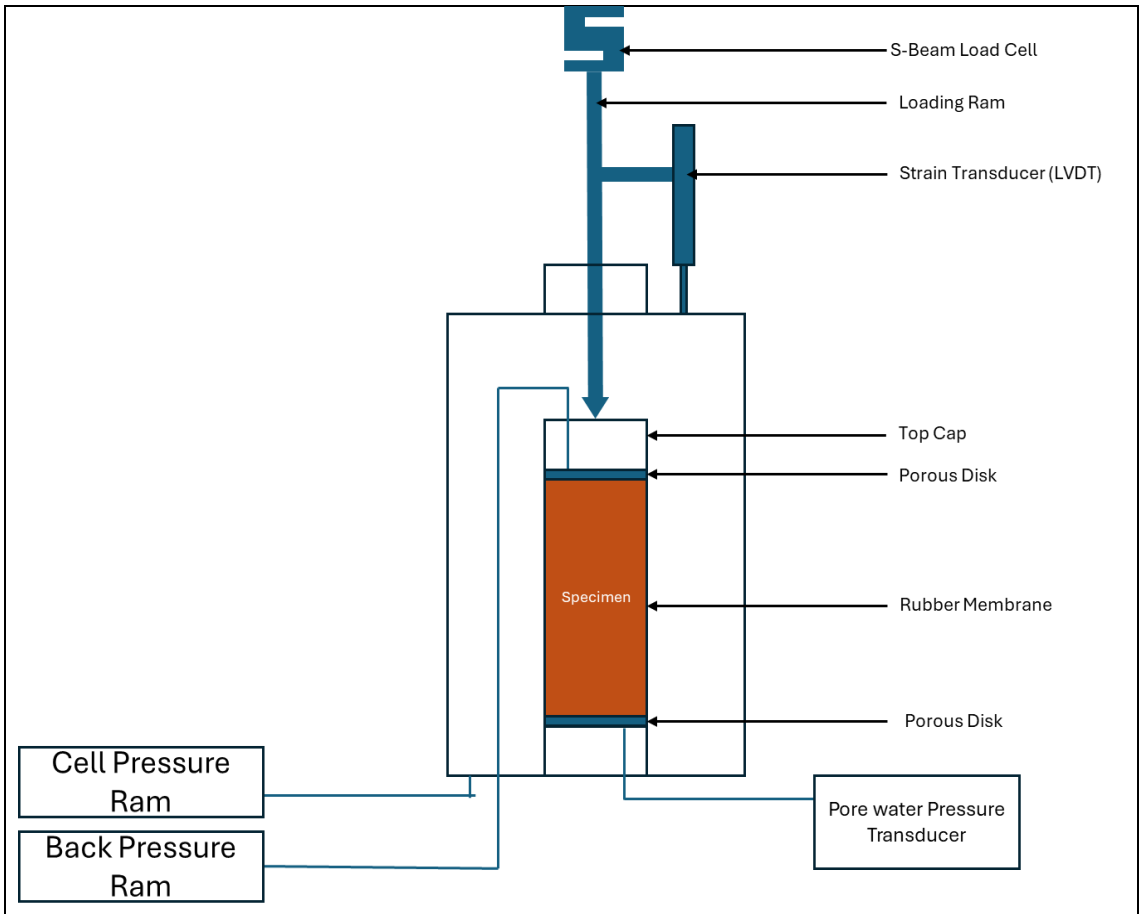

Figure 5.2. A simplified diagram of the triaxial apparatus used within this study. Not shown here is the de-aired water tank, of which supplied de-aired water to the cell and back pressure rams as well as the cell. The S-beam load cell was rated to 5 kN, with and LVDT travel of 25mm.

Pore pressure was monitored from the base of the cell, with back pressure monitored through the top cap. Several valves were present throughout the system to allow for the isolation of differing parts. Pressure rams were calibrated using a GDS Instruments field-cal kit on a 6-monthly calibration cycle. Pore pressure sensors were subsequently calibrated using pre-calibrated pressure rams on a similar calibration cycle. Load cells were calibrated annually by an external IANZ-accredited organisation. LVDTs were calibrated annually using a VJ Tech LVDT calibration tool.

De-aired water to the system was supplied by an IMPACT de-airing tank, and the water de-aired via vacuum with a rocker pump. Water was considered de-aired when no air bubbles were visible within the de-aired water tank. A Mettler Toledo oxygen meter was used to monitor the level of dissolved oxygen present within a sub sample of water from

the tank. An average value of 1.65 ± 0.22 mg/L was measured, this below the two mg/L recommended for de-aired water (Head 1998).

One aspect that deviated from the norm during testing was the presence of 2 IMPACT toxic interface chamber cells attached in-line for both the pore pressure and back pressure lines.

Toxic interface chambers consisted of two 60cc chambers, the upper made of clear polycarbonate and the lower stainless steel. Each chamber is separated by an inert Viton diaphragm, ensuring that any chemicals potentially present within the water are isolated to one side of the system. Due to the potentially corrosive nature of potassium acetate when interacting with certain metals, the toxic chamber was used to preserve equipment. Before each run, each side of the chamber was filled with fresh de-aired water and the system pressure was tested to ensure a 1:1 response on both sides of the chamber. This was achieved by applying a set pressure via the pressure ram to one side of the system and monitoring the pressure response in the other channel via the pore pressure sensor. Similarly, upon completion of testing, all parts of the triaxial system that had been in contact with corrosive chemicals were extensively flushed and cleaned with distilled water. The conductivity of the flushed water was then monitored until a value between 0.5 – 3 μs/cm was achieved

5.8.2 Consolidated Undrained Testing

Consolidated Undrained (CU) testing was selected as the preferred method for testing the soils in this study. Although a Consolidated Drained (CD) test could have been undertaken it was deemed unsuitable, due to sensitive soils' propensity to undergo rapid changes and generate of excess internal pore pressures during failure. Given the inherently slow drainage and pore pressure dissipation associated with CD testing, the method was considered inappropriate due for accurately capturing the soils behaviour under the conditions anticipated during mass wasting. Tests were undertaken on three trimmed specimens, extracted via 200 mm length, 50 mm diameter stainless steel cores that were subsequently trimmed to 100mm length, 50 mm diameter (2:1 height to diameter ratio) and tested at three differing confining pressures.

5.8.3 Confining Stress

In deviation from the conventional selection of confining stresses, where the three confining stresses consist of ‘below normal’, ‘normal’ and ‘above normal’ stress, stresses

for this study were either at or below normal. These limits were selected based on the work of Kluger et al. (2017). In this work, the authors suggest a 'threshold' effective confining stress below 'normal' would trigger failure in sensitive soil slopes within the Pahoia Tephra following heavy rainfall. This value was suggested to be around 36 %. As such, for this study, a reduction of 40 % and 20 % of the normal confining stresses were selected.

5.8.4 Testing Procedure

Testing took between 2–3 days to complete. The saturation stage took approximately 8 hours, consolidation around 12–16 hours, and compression around 14–24 hours. It should be noted that the length of testing was controlled by the testing Coefficient F as set out in BS 1377-1990. Coefficient F is based on the type and number of drains and the dissipation of 95 % of excess pore pressure induced by shear. Due to the faster nature of CU tests, Coefficient F is smaller than its CD counterpart (CU=0.53, CD=8.5). However, BS1377: 1990 states that the CU coefficient F=0.53 only applies in the case of non-sensitive soils, and as such, F=8.5 should be used instead.

5.8.5 Saturation and B-Check

Saturation of a sample is undertaken to ensure all voids are filled with water and that no air is present. This is achieved by slowly raising the pore pressure within the sample to a minimum value of 300 kPa, the pressure at which air dissolves into a solution. BS 1377:1990 states that the cell pressure and back pressure must be raised in increments such that the back pressure is no less than 10 kPa below cell pressure at any given time of saturation. The GDSLab software utilised a saturation ramp program where cell and back pressures are gradually and continuously ramped up to a pre-set value over time. Samples were generally saturated to a cell pressure maximum of 500 kPa, with a back pressure maximum of 490 kPa, over an 8-hour period, resulting in an increase of approximately 1.05 kPa per minute.

Following saturation, a B-Check is undertaken to determine the level of saturation within the voids of a specimen. A B-check monitors the pore pressure change following a 50 kPa increase in cell pressure with no change in back pressure, as shown in Equation (5.9).

$$B = \frac{\Delta u}{\Delta \sigma_3} = \frac{\Delta u}{50} \tag{5.9}$$

Where Δu refers to the change in pore water pressure

When B ≥ 0.95, the specimen is considered saturated, with less than 5 % of voids potentially unfilled with water. Upon B ≥ 0.95, consolidation is undertaken.

5.8.6 Consolidation

To ensure correct consolidation confining pressures are selected, it is important to determine the *in situ* stresses and conditions a sample will likely have experienced in what can be deemed its 'normal' state. To determine this, several factors must be considered, including sampling depth, bulk densities, thickness of the overlying strata, and the water table depth.

As sampling in this instance has been undertaken in a failure scarp, estimates were made on sample depth based on pre-existing LIDAR values of the hillslope prior to failure. Similarly, estimates were made regarding the overlying strata due to the lack of available borehole data and the hazards associated with accessing the site's slope face. Estimates were made based on a clinometer and known horizontal distances from the user and the slope face. Bulk densities were established from gamma density core logs of the nearby Bramley Drive landslide, with densities determined via averaging of values for soil between marker paleosols. Water tables were similarly estimated based on borehole logs of the nearby Bramley Drive landslide. Final calculations of effective confining pressures were determined using Equation (5.10):

$$\sigma_3' = \sigma - u = \rho g z - \gamma_w z_w \tag{5.10}$$

Where g, z, γ_w, and z_w refers to gravity ($9.81\ m/s^2$), soil depth, unit weight of water ($9.81\ kN/m^3$), and the depth of the water table, respectively.

This produced confining stresses of 120 kPa, 160 kPa, and 200 kPa. The 'normal' stress state, 200 kPa, was established on the basis of the sampled soil being around 13.15 m below the previous soil surface, with an overburden bulk unit weight of 1614 kg m^{-3} (as established from gamma density core logs) and a water table of approximately 8.15 m below the soil surface. Reduced confining stresses were determined in line with the proposed reduction in confining stress presented in Kluger *et al.* (2022). In that work, Kluger *et al.* (2022) suggested that a reduction of around 25 % would be sufficient to cause failure. To ensure a 'guaranteed' failure based on this value a reduction of 40 % in confining stress was selected as the lower end (120 kPa), while a 20 % reduction (160

kPa) was selected as an intermediate confining stress, as this allowed for both a clear 40 kPa step in confining stress and an examination of soil behaviour at a stress close to that suggested in literature.

Following the achievement of saturation within the sample, the GDS software automatically ramps cell pressure to achieve the desired confining stress, and the sample enters the consolidation stage. Samples are consolidated until 95 % of excess pore pressure has been dissipated. Time to consolidate varied between specimens, though samples generally required at least 8 hours to achieve full consolidation and, in some cases, more than 30 hours.

To determine an appropriate testing time, specimen volume change during consolidation is plotted against the square root time (T100) in accordance with BS1377:1990. Testing time is then determined by multiplying T100 by the coefficient F (8.5).

5.8.7 Compression

Compression was applied upon completion of consolidation, with compression occurring until 20 % axial strain was achieved regardless of whether a failure criterion specified in BS1377:1990 was achieved. This was to allow for the observation of any post-failure behaviour within the soils. Generally sensitive soils reach a peak deviator stress following loading (1–2 % axial strain) before entering a post-failure remoulding stage. Measurements were recorded within the GDSLab software every 2 seconds. One aspect of the test that deviated from those conducted on similar soils in the past is the lack of requirement in closing the back pressure valve. As such, during shear, an open back pressure line allowed for a measurement of pore pressure from both the top and bottom of the sample simultaneously. This subsequently allowed for monitoring of potential pressure gradients forming within samples during shear, a trait speculated to exist by Mills (2016). Corrections for membrane resistance were made automatically by the GDSLab software during recording.

Chapter 6

Part I — Results

6.1 Soil Characteristics

6.1.1 Moisture Content and Density

Moisture content, bulk density (wet and dry), particle densities, porosity, void ratio, and saturation ratio are presented in Table 6.1

Table 6.1: Moisture content, bulk densities (wet/dry), particle density, porosity, void ratio and saturation ratio for untreated and treated soils used within this study. Errors presented are standard deviations

Sample	Moisture content (%)	Wet bulk density (kgm^{-3})	Dry bulk density (kgm^{-3})	Particle density (kgm^{-3})	Porosity (%)	Void ratio	Saturation ratio (%)
Untreated	67±1.5	1,576±10	944±6.4	3282±0.04	71	2.48	89
1 month	57±1	1,628±34	1,036±14	2847±0.02	63	1.75	93
3 months	60±2.5	1,627±27	1,026±27	2894±0.02	65	1.82	93
6 months	60±1	1,599±19	996±10	2914±0.03	66	1.96	91
12 months	63±1.7	1,632±12	1,017±40	2870±0.02	65	1.83	95
Average Treated	60±2	1622±15	1019±17	2881±290	65±1	1.84±0.1	93±2

Moisture contents for untreated samples were high at around 67 %. Treatment of soil cores resulted in a drop in moisture contents to values ranging between 56 and 63 %, with an average drop of 7 % moisture content following treatment.

Wet bulk densities were, on average, 1576 kgm^{-3} for the untreated samples. Upon treatment the wet bulk density increased to an average of 1622 kgm^{-3}. Dry bulk density of untreated samples was low (944 kgm^{-3}) and increased to an average of 101kg m^{-3}.

Particle density for untreated soil was 3282 kg m^{-3} and showed a notable decrease for treated samples to an average of 2882 kg m^{-3}. For the untreated soil, when compared to values found for previous studies, particle density was quite similar to the soil from Robertson's 2017 study (3,182 kg m^{-3}) but was significantly higher than a number of other studies on soils from within the Ōmokoroa area (2200–2600 kg m^{-3}). Treated samples all exhibited a drop of approximately 300–400 kg m^{-3} in particle density, though no clear relation between length of treatment and particle density was evident (Figure 6.1).

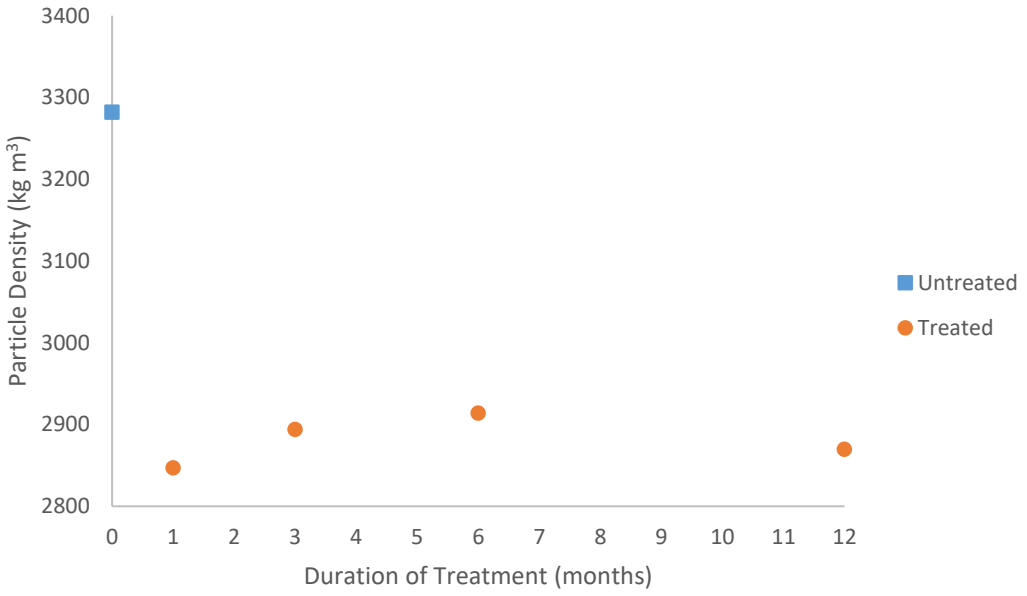

Figure 6.1. Particle density for untreated (blue square) and treated (orange dots) samples plotted against their respective soaking times in months. A large drop off exists between untreated and treated, while treated samples were within 100 kg m^{-3} of one another.

Porosity was reasonably high (71 %) for untreated soil, and showed a drop with treatment to 65 % on average. The void ratio showed a similar trend with a value of 2.48 in untreated soil, reducing to an average of 1.84 after treatment. Saturation ratios were between 89–95 %, indicating that most samples were close to full saturation, with a slight increase (89 % untreated, 93 % treated). While saturated soils are not uncommon in the Tauranga region, these soils were collected late in the summer after a notable dry period (~2 months).

6.1.2 Particle Size

Results of laser particle size measurements of treated and untreated soils are shown in Table 6.2. Note these are the averaged results. These are further visualised in Figure 6.2 below.

Table 6.2: Summary of particle sizes determined for untreated and treated soils. Values were determined as the average of 3 runs for each soil.

	Clay (<2µm)	**Silt (2-60 µm)**				**Sand (60-2000µm)**			
Sample	Total %	Fine %	Medium %	Coarse %	Total %	Fine %	Medium %	Coarse %	Total %
Untreated	25.4	39.19	17.27	13.67	70.13	4.33	0.14	0	4.47
1 Month	25.1	38.96	17.31	13.79	70.06	4.44	0.4	0	4.84
3 Month	25.3	39.22	17.25	13.74	70.21	4.12	0.37	0	4.49
6 Month	25.8	39.16	17.22	13.76	70.14	4.01	0.05	0	4.06
12 Month	25.2	39.21	17.34	13.56	70.11	4.38	0.31	0	4.69

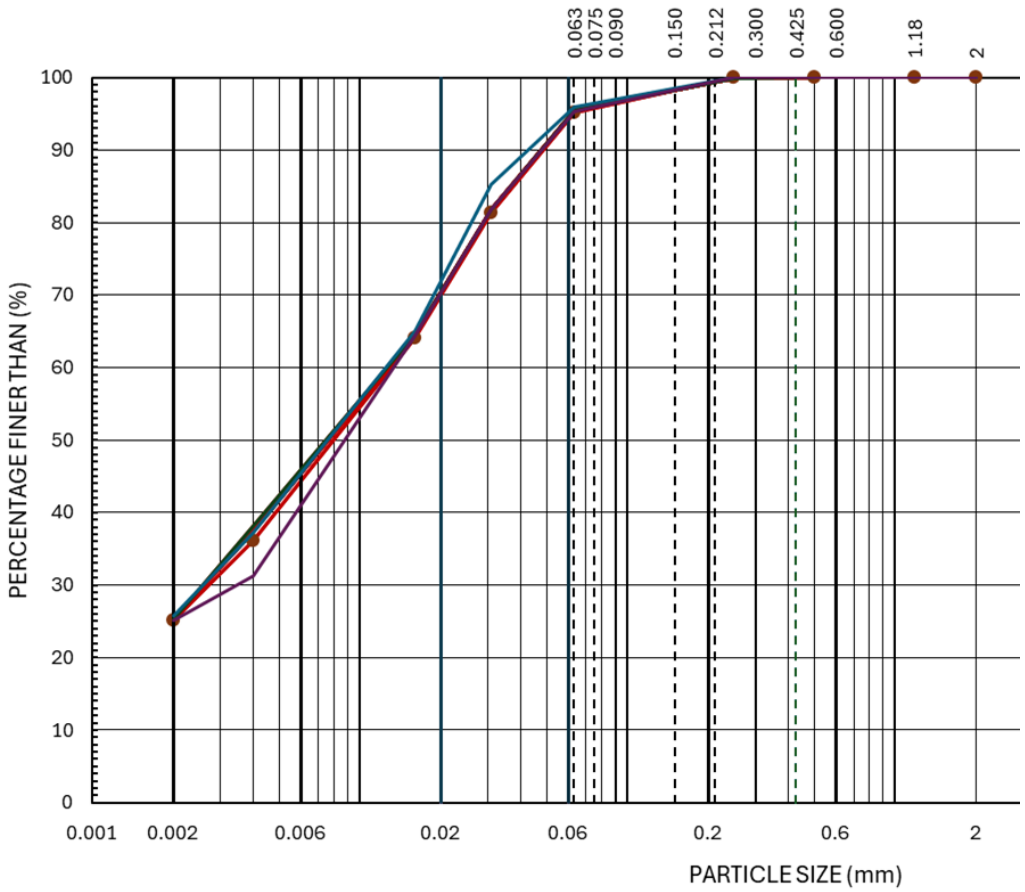

Figure 6.2.Particle size analysis chart showing the average particle sizes for each of the five sampling points used throughout this research. Not almost all samples fall relatively close together with some minor variations. Additionally the chart cuts off at just beyond 2 mm due to no particles present greater than 2 mm.

Variability was low (less than 0.05%), with good agreement regardless of whether soil had been treated or not. The soil was dominated by the silt fraction (approximately 39% on average), with a reasonable proportion of clay (25% on average) and a small sand fraction (4.5%), made up almost entirely of fine sands. Particle sizing indicated the soil was a clayey SILT with trace sands. This showed good agreement with field observations of the soil.

6.1.3 Atterberg Limits

Atterberg limits and the associated calculated parameters are presented Table 6.3. It is worth noting that Atterberg limits for soils mixed with K-acetate solute are compared to the sample mixed with distilled water (named distilled water).

Table 6.3 Summary of Atterberg limit test results for Pahoia tephra mixed with distilled water, K-acetate as well as dried from field moisture. Note some variance did exist between the distilled water and field moisture liquid limits , though these were offset by changes in the plastic limit (indicating a similar working range). Note Activity was determined using equation 5.8, with the clay percentages applied drawn from the results presented in table 6.2.

Treatment	Liquid Limit (%) & R^2	Plastic Limit (%)	Liquidity Index	Plastic Index (%)	Activity
Distilled Water	55 – 0.94	43±0.2	2.10	12	0.25
Field moisture (Dried)	59– 0.99	46 ±0.2	1.71	13	0.28
Potassium Acetate (4 mol/L)	62- 0.98	46±1	1.32	17	0.36
Potassium Acetate (2 mol/L)	65 – 0.97	46±1.8	1.13	19	0.41
Potassium Acetate (2 mol/L 18 Months soakage)	63 – 0.98	45±0.08	0.57	18	0.39

Samples tested with distilled water show a Plasticity Index indicative of a medium plastic soil (12%). The clays are of low activity, and upon distilled water addition the soil has a high liquidity index (2.10). Similar results are seen for samples dried from field moisture, though these are lowered (1.71), possibly a result of the drying of the soil.

Potassium Acetate (herein shortened to K-Acetate) treated samples all showed an increase in Liquid and Plastic limits, resulting in an increased plasticity index (boundary of medium/high plasticity). Activity also increased (average 0.39) though all soils remain low activity. One point to note is the liquidity index is notably reduced, for samples that had been soaked for 18 months.

When classified on the Casagrande classification chart (Figure 6.3), all soils plotted below the A-line (MH range), which is indicative of a soil exhibiting behaviour of a high compressibility silt. Soil behaviour, as classified by the Casagrande plasticity chart, aligns with the determination made of soil type through field and lab classification (silt-dominated soil with a high degree of plasticity).

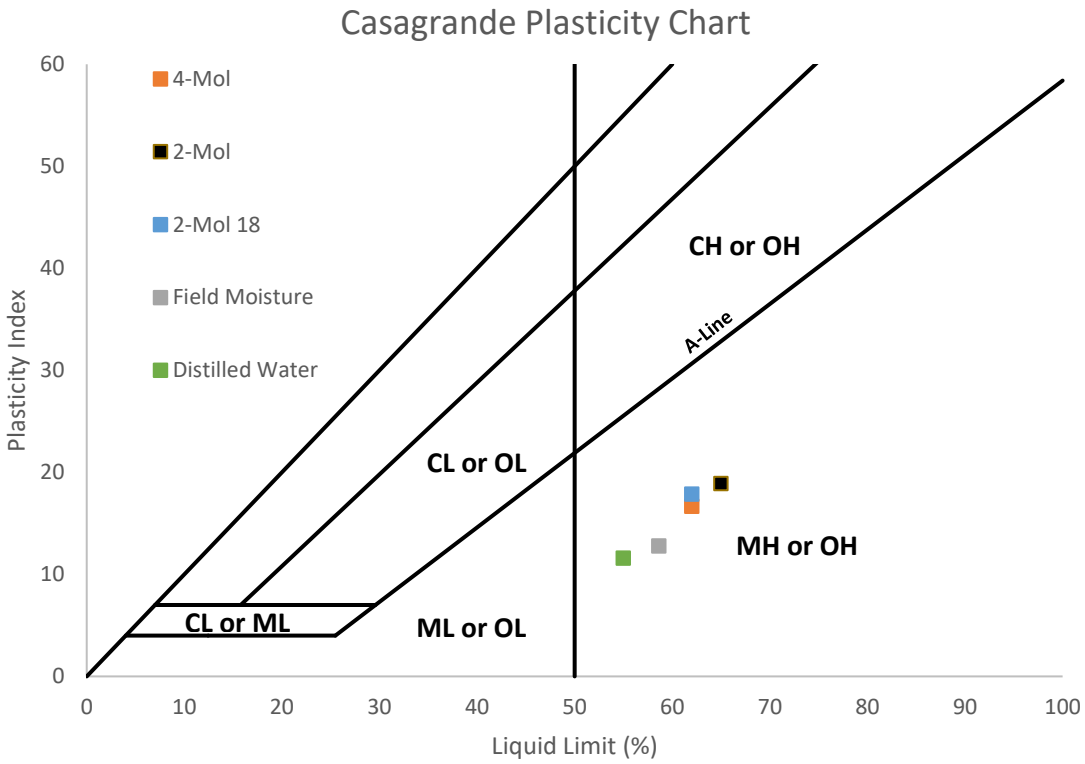

Figure 6.3. Samples tested using a fall cone plotted onto a Casagrande plasticity chart to determine soil characterisation. All samples are characterised as silts or organics with high plasticity regardless of treatment.

6.1.4 Conductivity

Conductivity within the soil paste showed a clear increase over time, with it taking approximately 240 hours (10 days) to achieve conductive equilibrium with the original solute (3.4 mS^{-1}) at the furthest monitored point (150 mm). Figure 6.4 shows the change in conductivity at the three monitored points within the soil paste. The ion plume of the solute showed relatively rapid movement within the soil, with a change in conductivity (0.05mS^{-1}) measured at the 30 mm point after the first 6 hours of monitoring, with solute conductive equilibrium at 30 mm achieved within 48 hours. The first changes were detected after 12 hours and 24 hours at 90 mm and 150 mm, respectively. A relatively rapid uptick in conductivity was observed at 90 mm, taking 144 hours to achieve equilibrium. 150mm showed a much slower increase by comparison, requiring another 100 hours (244 hours total) to reach equilibrium.

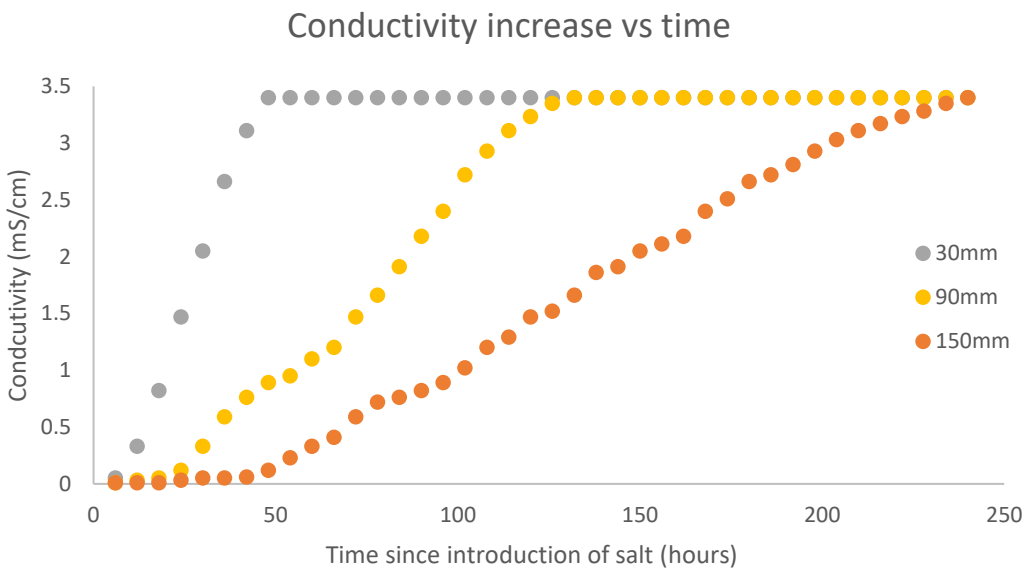

Figure 6.4 Conductivity measured at 30mm (grey points), 90mm (yellow points) and 150mm (orange points) from the salt well. Conductivity is measured in mS/cm. The ion plume was detected reasonably quickly at 30 mm (48 hours), while it took 240 hours for the full strength to be observed at 150mm.

6.2 Triaxial Testing

CU effective stress tests were performed on 150 mm long cores of sensitive material collected from the Kowai Grove landslide, Ōmokoroa. The results obtained from these tests include consolidation curves, shear behaviour, stress paths, and post-failure characterisations.

6.2.1 Consolidation Behaviour

Time to T_{100}

Upon completion of the saturation and B-check, samples were consolidated until pore pressure was at a minimum, 95% dissipated (T_{100}). Table 6.4 presents the time taken to achieve T_{100} for all samples tested. These are further presented in Figure 6.5**,** where T_{100} is plotted at each confining pressure against the time of immersion of soil cores.

Table 6.4. Time taken to achieve full dissipation of pore pressures (T_{100}) for untreated and treated soils following consolidation. There was little consistency within the data for confining pressure, though some loose correlations did exist across the length of treatment. Note untreated samples were tested at 150 kPa and 225 kPa as opposed to 160 and 200 kPa.

Pressure (kPa)	Untreated (min)	1 Month (min)	3 Month (min)	6 Month (min)	12 Month (min)	R^2 Value
120	144	72.25	121	110.5	36	0.53
160	132.25	90.25	81	64	49	0.75
200	110.25	169	144	100	72.25	0.57

The curves in Figure 6.5 show an overall trend of T_{100} decreasing with increasing length of treatment. At 120 and 200 kPa confining stresses a reasonable level of correlation was observed with R^2 values of 0.53 and 0.57 being produced respectively, while samples at 160 kPa showed much more consistency in their change with an R^2 of 0.75 produced

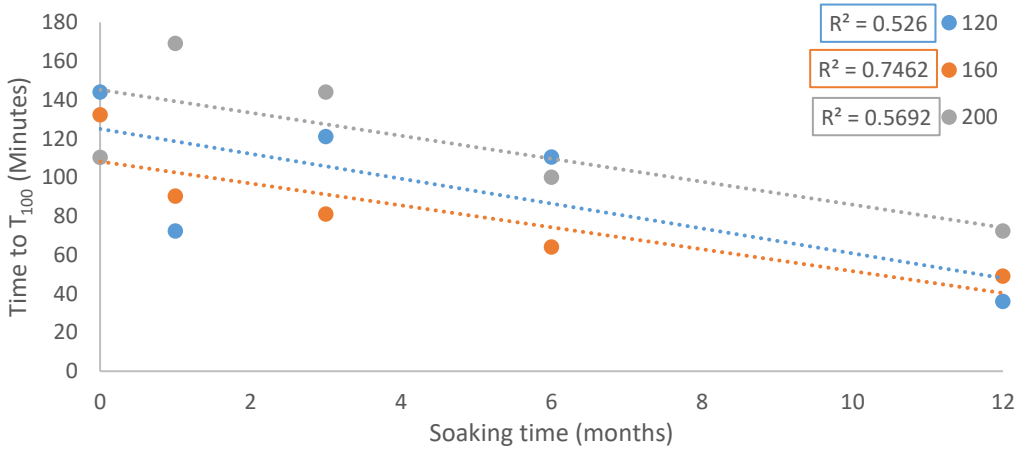

Figure 6.5 .A scatter plot of time taken to achieve full consolidation (T_{100}) in minutes against the soakage time of the soils. Samples are distinguished based on their confining stress. Loose correlations do exist for the 120 and 200 kPa samples, while the 160 kPa samples showed reasonably good correlation.

When plotting the T_{100} for immersed cores against the respective confining stress at each length of treatment (Figure 6.6) several trends emerge. The first of these is the lack of consistency in T_{100} for samples immersed for 3 and 6 months, with no correlation observed for these lengths of soaking (R_2= 0.13 and 0.05. respectively). All other samples (untreated, 1-month, 12-month) showed a strong correlation between T_{100} and the confining stress. One unexpected aspect was the shift in the overall trend, with T_{100} after

both 1 and 12 months of treatment showing an increase with increasing confining stress, while the untreated soil displayed the inverse.

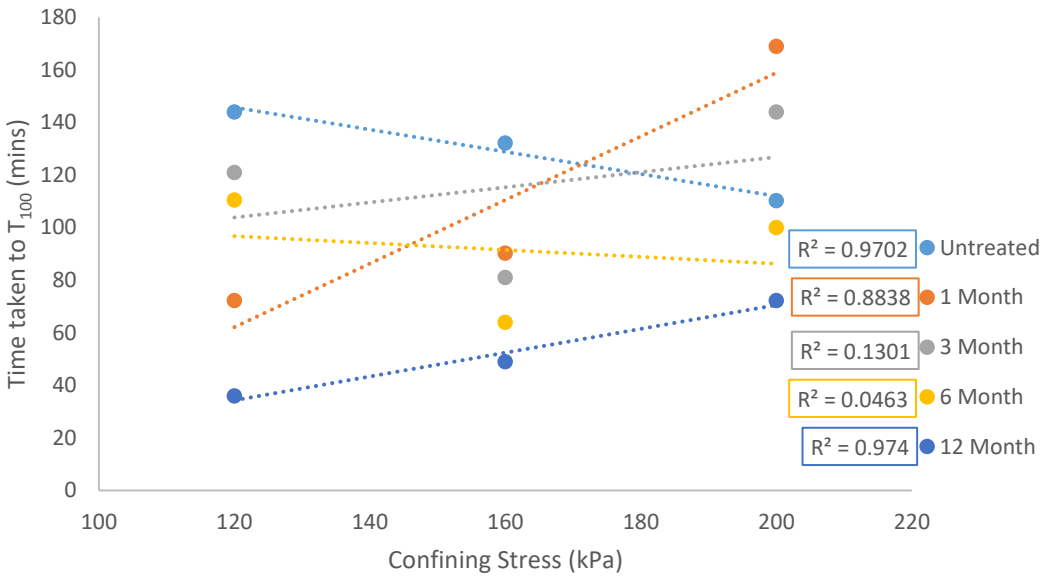

Figure 6.6. Time taken to reach T_{100} for samples at their respective soakage lengths. Some strong correlations do exist (untreated, 1 month, 12 months), though samples at the 3 and 6 months show no correlation at all.

Change in Void Ratio

While time to T_{100} showed a number of loose correlations, void ratio changes during consolidation showed some notable trends. These changes in void ratio have been calculated as the subtraction of the consolidated void ratio from the initial void ratio. These are presented in Table 6.5. Overall, the void ratio has decreased following consolidation.

Table 6.5. Change in void ratio following consolidation of treated and untreated samples at the respective confining stresses. Note untreated samples were tested at 150 kPa and 225 kPa as opposed to 160 and 200 kPa.

Confining Pressure (kPa)	Untreated	1 Month	3 Month	6 Month	12 Month
120	0.52	0.27	0.26	0.34	0.20
160	0.49	0.29	0.31	0.43	0.31
200	0.40	0.34	0.33	0.38	0.39

At respective confining stresses (Figure 6.7), there were weak to no correlations between length of treatment and confining stress. With this said, for the treated cores, with the exception of the 6-month cores ($R^2 = 0.17$), there was a strong correlation present between confining stress and void ratio change ($R^2 > 0.9$). Meanwhile, untreated soil cores showed a decrease in void ratio change with increasing confining stress. This behaviour was altered with treatment, with treated cores displaying an inverse relationship (increasing confining stress resulting in increasing void ratio change), with the steepest of these being for samples treated for 12 months.

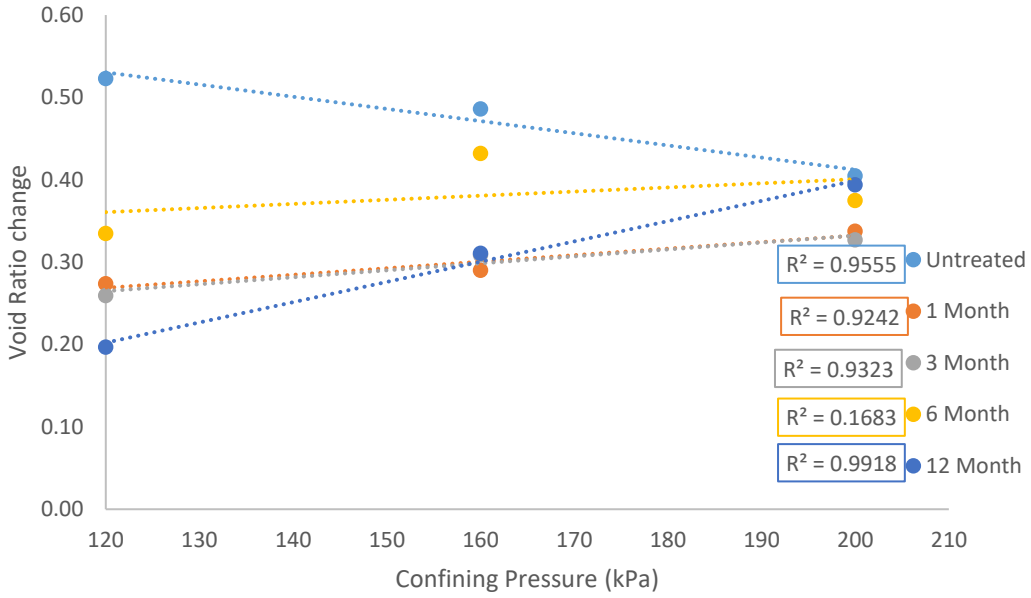

Figure 6.7 Void ratios change for treated and untreated samples plotted against confining pressure. Strong correlations were observed for nearly all samples, with the 6 months samples the only showing little to no correlation.

D-Vol and Permeability

While void ratio changes during consolidation, the source of this change (i.e the expelled liquid) was also monitored during testing. D-vol, or total volume expelled during the consolidation cycle, is plotted against soakage time in Figure 6.8. For samples consolidated at 200 kPa, there is a very strong correlation ($R^2 = 0.98$) between the volume expelled from the sample and the length of treatment, with an increased volume expelled with increased soaking time. A similar trend was displayed by the 160kPa stress, albeit far less clearly correlated ($R^2 = 0.6$), but at the lowest confining stress (120 kPa), there was no correlation between the immersion period and D-Vol ($R^2 = 0.08$). Another aspect

that was observed from the consolidation data and reflected in the D-vol was the reduction in the volume expelled from samples after six months of immersion.

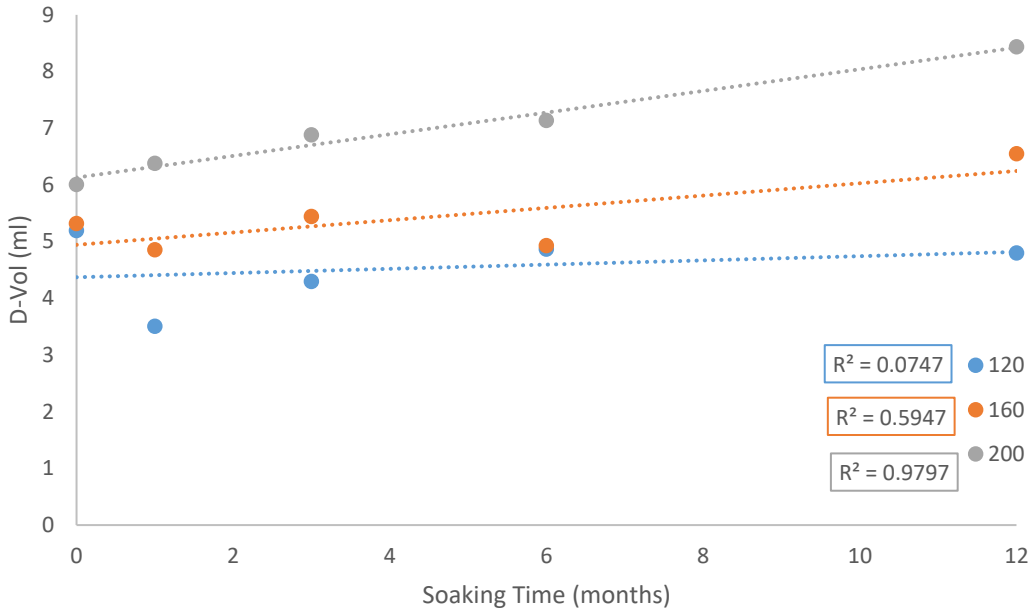

Figure 6.8 . A scatter plot showing the volume of liquid expelled during consolidation (D-Vol) plotted against soaking time. From the data no correlation appears to exist for samples at the lowest confining stress (120 kPa), while 160 kPa showed some correlation ($R^2 = 0.59$) and 200 kPa showed a strong relationship. Note untreated samples were tested at 150 kPa and 225 kPa as opposed to 160 and 200 kPa.

Permeability over the course of treatment (Figure 6.9) showed an increase as the length of treatment increased, with samples becoming more permeable over time regardless of the confining stress. Samples showed a strong correlation at the 160 and 200 kPa confining stresses ($R^2 = 0.98$ & $R^2 = 0.92$, respectively). The lowest confining stress showed a weaker correlation ($R^2 = 0.61$) but did show a marked increase in permeability at the longest (12 month) soaking time. Deviation in the trends did occur, with the samples soaked for six months (Figure 6.9), showing a drop in overall permeability across the board. While there is a clear increase in permeability over time, it is worth noting that the data does not show a linear increase over the 12 months from untreated. Instead, it shows that samples at the 200 kPa mark have a lower permeability at 1 and 3 months when compared to the natural permeability before increasing at the 6-month time point. Similarly, samples at the 120 kPa pressure point exhibited a small increase in permeability before dropping away quite significantly and having a reduced permeability after the 1-month time point, with the 12-month sample having a drastically higher permeability.

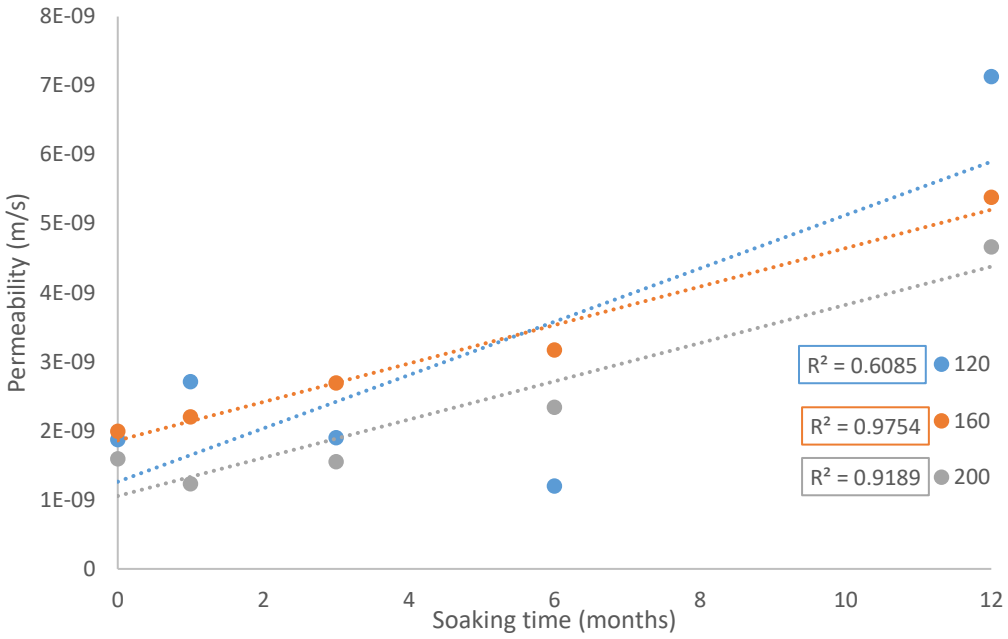

Figure 6.9. A scatter plot showing permeability for untreated and treated samples over the 12 months of treatment. All samples showed a correlation for increasing permeability with soaking time, with 160 and 200 kPa confining stresses both having R2 values in excess of 0.9, while 120 kPa was less strongly correlated (R 2=0.61). Note untreated samples were tested at 150 kPa and 225 kPa as opposed to 160 and 200 kPa.

6.2.2 Triaxial Shear Behaviour

Table 6.6 shows the key parameters derived from CU triaxial tests undertaken on the untreated and treated soils. Stress-strain curves, as well as pore water pressure curves, are shown at each respective confining stress (Figure 6.10a, b, and c). Across all confining pressures, there is a rapid increase in peak deviator stress, with a similar increase in pore pressure prior to peak deviator stress with increasing length of treatment. Both are accompanied by a distinct drop in following failure, though pore pressure typically increased prior to 20% axial strain. The strain at failure was relatively small, with failure occurring at points between 3.3 % and 6 %.

Table 6.6. A summary table of the various parameters measured during the consolidated undrained triaxial tests undertaken on untreated and treated sensitive Pahoia Tephra samples.

	Deviator Stress (kPa)	Rate of Change (kPa/month)	Strain at Failure (%)	PWP at Failure (kPa)	Force at failure (kN)	Strain Softening (%)
Untreated (120 kPa)	130.0		5.5	55.1	238.1	21.20
1 Month (120 kPa)	171.7	41.7	4.9	62.0	316.0	21.13
3 Month (120 kPa)	164.4	-3.6	5.7	60.1	301.4	16.50
6 Month (120 kPa)	183.0	6.2	5.2	59.9	343.7	21.55
12 Month (120 kPa)	215.1	6.4	4.8	62.1	398.2	16.26
Untreated (150)	149.0		4.6	87.7	287.2	31.55
1 Month (160 kPa)	201.9	52.8	3.3	86.8	352.4	31.50
3 Month (160 kPa)	203.7	0.9	3.8	93.7	366	31.07
6 Month (160 kPa)	208.9	1.7	4.6	89.3	379.9	28.16
12 Month (160 kPa)	212.5	0.6	3.4	99.4	373.7	27.25
Untreated (225 kPa)	185.0		3.5	130.3	336.6	36.92
1 month (200 kPa)	217.5	32.5	5.3	112.8	397.0	22.93
3 Month (200 kPa)	216.7	-0.4	6.0	115.6	392.8	23.65
6 Month (200 kPa)	212.9	2.4	5.9	114.7	414.9	20.16
12 Month (200 kPa)	242.5	3.1	4.2	124.0	434.6	13.79

(a)

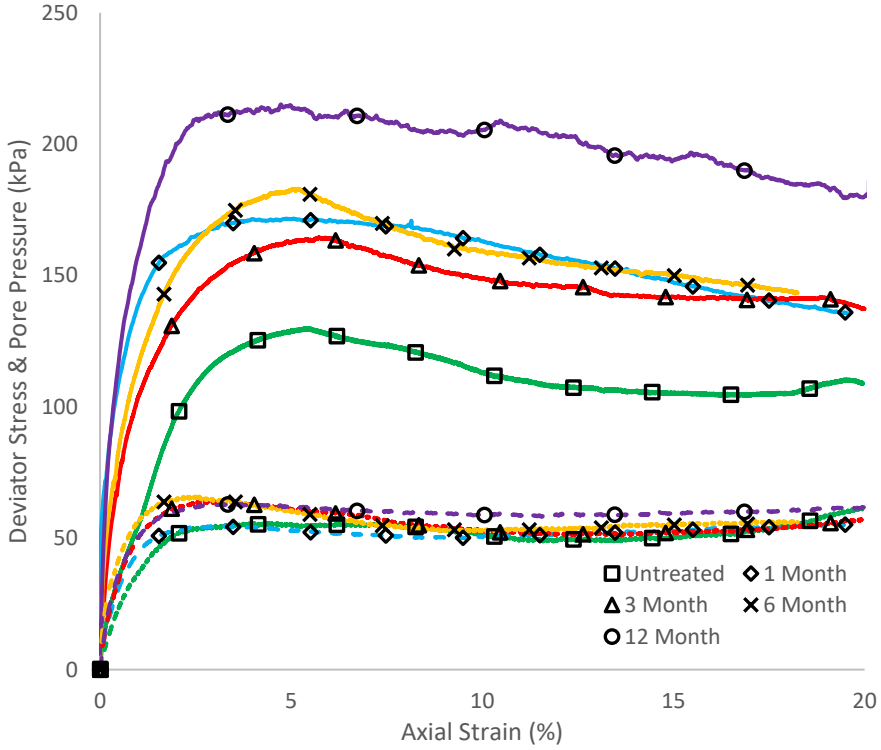
Deviator Stress & Pore Pressure (kPa)
250
200
150
100
50
0
0
5
10
15
20
Axial Strain (%)
Untreated
1 Month
3 Month
6 Month
12 Month

(b)

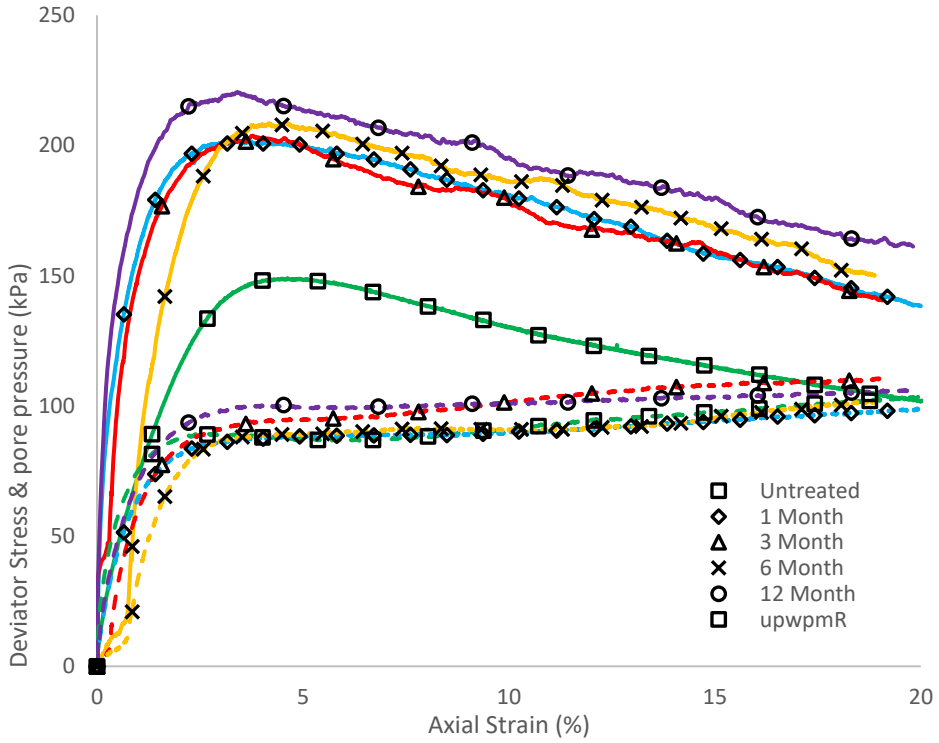
Deviator Stress & pore pressure (kPa)
250
200
150
100
50
0
0
5
10
15
20
Axial Strain (%)
Untreated
1 Month
3 Month
6 Month
12 Month
upwpmR

(c)

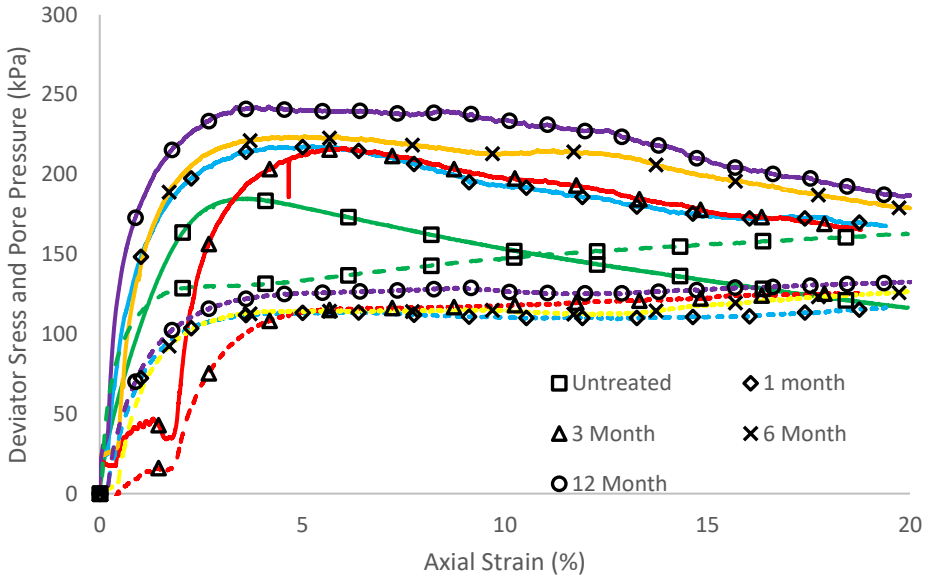

Figure 6.10.(a) Deviator stress (solid-coloured lines) and pore water pressure (dashed coloured lines) for samples tested at 120 kPa. (b) Deviator stress (solid-coloured lines) and pore water pressure (dashed coloured lines) for samples tested at 160 kPa (c) Deviator stress (solid coloured lines) and pore water pressure (dashed coloured lines) for samples tested at 200 kPa

Excess Pore Water Pressures

Excess pore pressures showed a similar trend to deviator stresses with a rapid rise in pressures, reaching an initial peak. Behaviour following this peak varied with confining stresses. Samples tested at 120 kPa showed an initial lowering in pore pressure following peak deviator stress, before rising once again between 10–15 % axial strain, and continuing to rise towards the end of the test at 20 % axial strain. In some instances (1 month 200 kPa, 6 Month 200 kPa), this rise resulted in final pore water pressures higher than the pore water pressure at failure. The higher confining pressures showed a slow increase following peak excess pore pressure. When observing the rate of change for deviator stress per month across the 12 months (Figure 6.11), it can be seen the bulk of the deviator stress increases occur within the first month of treatment (32–55 kPa increase) with the remaining changes in deviator stress being minor (<10 kPa) by comparison.

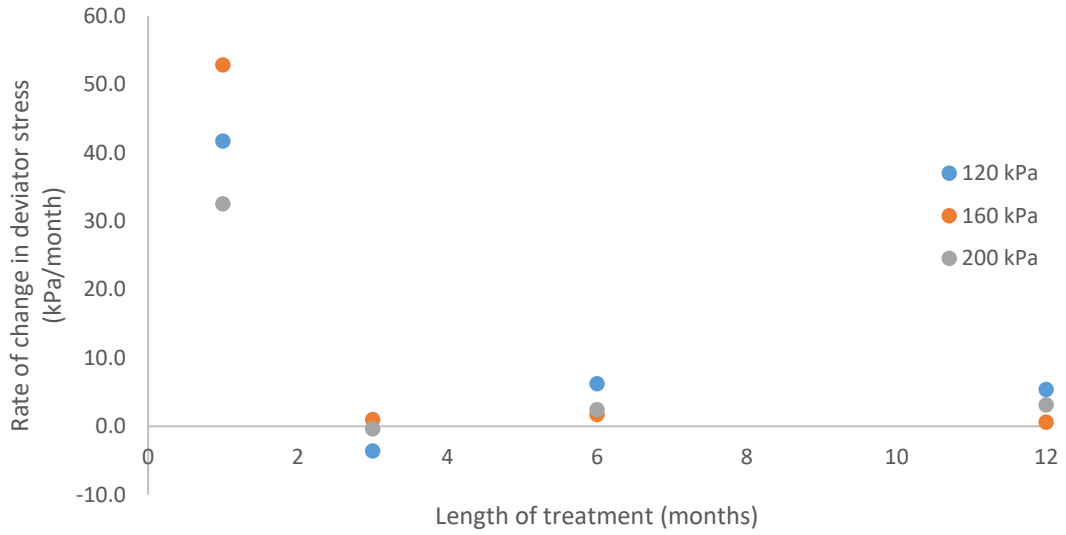

Figure 6.11 A scatter plot showing the rate of change (kPa/month) against the length of time the tested core had been soaked for. Samples are split into their respective confining pressures, where 120 kPa = light blue, 160 kPa = orange and 200 kPa = light grey.

6.2.3 Triaxial Pore Pressure Variations

When looking at pore pressure differences within the sample a number of differences emerge. Figure 6.12a, Figure 6.13a**,** Figure 6.14a, Figure 6.15a, and Figure 6.16a show the plotted pore pressure response at the base (solid lines) and top (dashed lines) of samples during shear. Within each figure, plotted data is divided into the three confining stresses (light blue = 120 kPa, grey = 160 kPa, dark blue = 200 kPa), with each individual figure representing the length of treatment (untreated, 1 month, 3 month, 6 months, 12

months respectively). Figure 6.12b, Figure 6.13b, Figure 6.14b, Figure 6.15b, and Figure 6.16b shown alongside these plots show the difference between excess pore pressure at the top and base of samples (plotted values = excess pore pressure top - excess pore pressure bottom) against axial strain. As axial strain differed between samples, the strain at failure for the three samples was averaged and is shown as a solid yellow vertical line.

Regardless of confining stress and duration of treatment, all samples showed deviation between the pore pressures measured at the top and bottom of the sample. The degree of deviance, and location, though was not consistent across all samples.

Untreated

Untreated samples (Figure 6.12a, and b) showed the generation of a difference between the top and bottom of samples tested at 120 kPa and 225 kPa (5–10 kPa and 20+ kPa), while samples at 150 kPa showed minimal difference (within 1–2 kPa). These all generally favoured the top of the sample.

(a) (b)

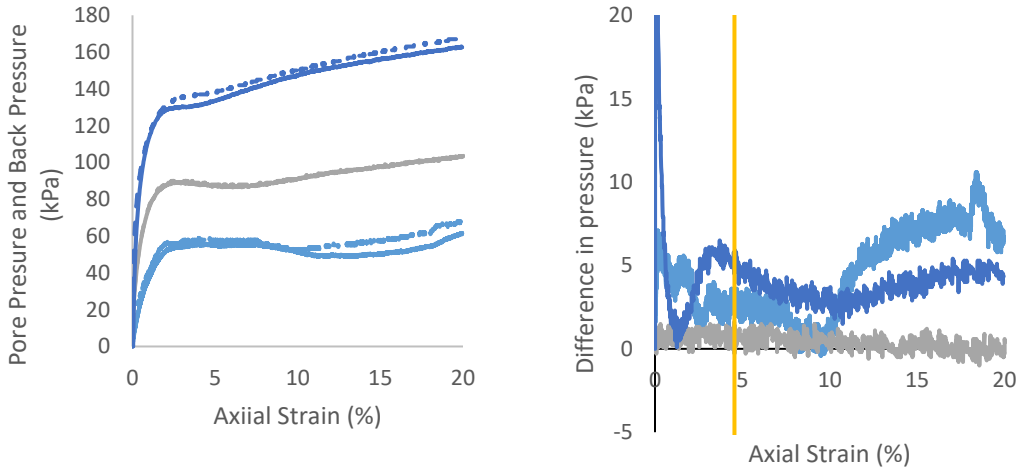

Figure 6.12. (a). pore pressure vs back pressure plotted against axial strain. Dashed lines are back pressure, while pore pressures are the solid line. (b). Difference in pressures between back and pore pressures plotted against axial strain where the vertical solid yellow line represents the averaged axial strain across all 3 confining stresses.

1 Month Soaked Cores

After 1 month of soaking, (Figure 6.13a and b) a consistent increase in deviance between top and bottom for excess pore pressures was evident for samples tested at 120 and 200 kPa, (15 kPa and ~ 8 kPa). The sample tested at 160 kPa, on the other hand, showed excess pore pressure at the top of the sample to be lower than the base (as shown as a negative difference) with variation initially of around -5 kPa measured, though this gradually reduced as the sample reached peak deviator stress (3.3 % axial strain). Following peak deviator stress, as the sample remoulded, the pore pressure imbalance began to shift and become positive (higher at the top of the sample).

(a) (b)

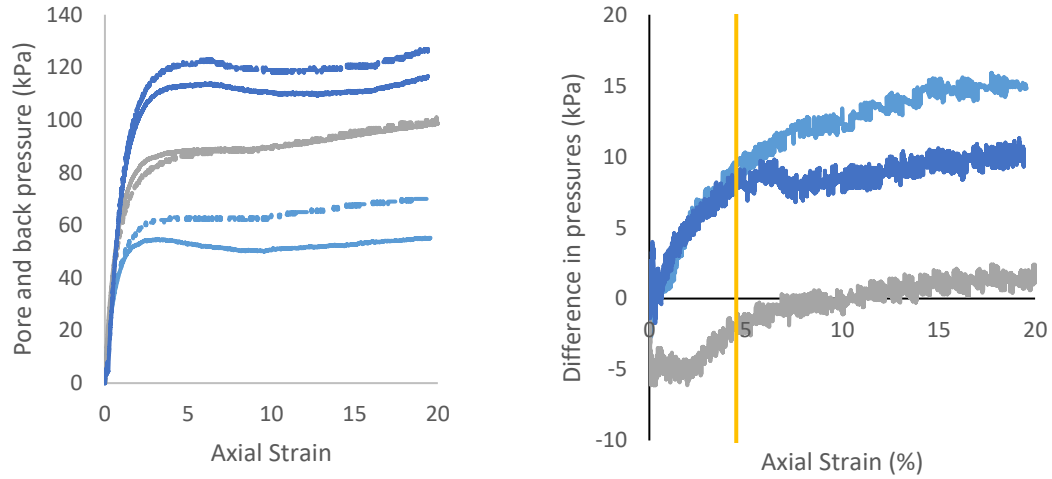

Figure 6.13. (a) pore pressure vs back pressure plotted against axial strain for samples treated for 1 month. Dashed lines are back pressure, while pore pressures are the solid line. (b). Difference in pressures between back and pore pressures plotted against axial strain where the vertical solid yellow line represents the averaged axial strain across all 3 confining stresses.

3 Month Soaked Cores

For samples soaked and tested after 3 months (Figure 6.14a, and b) all samples showed an imbalance of pressure in favour of the top of the sample following failure (approximately 4 kPa). For the lower 2 confining pressures (120, 160 kPa) up to around 2 % axial strain, pressures were favoured towards the base, though these were minor (2 – 4 kPa). Samples at 200 kPa showed similar behaviour, though only after an initial period of inconsistency, likely related to the load not being fully distributed as a result of loading ram seating issues. Overall differences were minimal.

(a) (b)

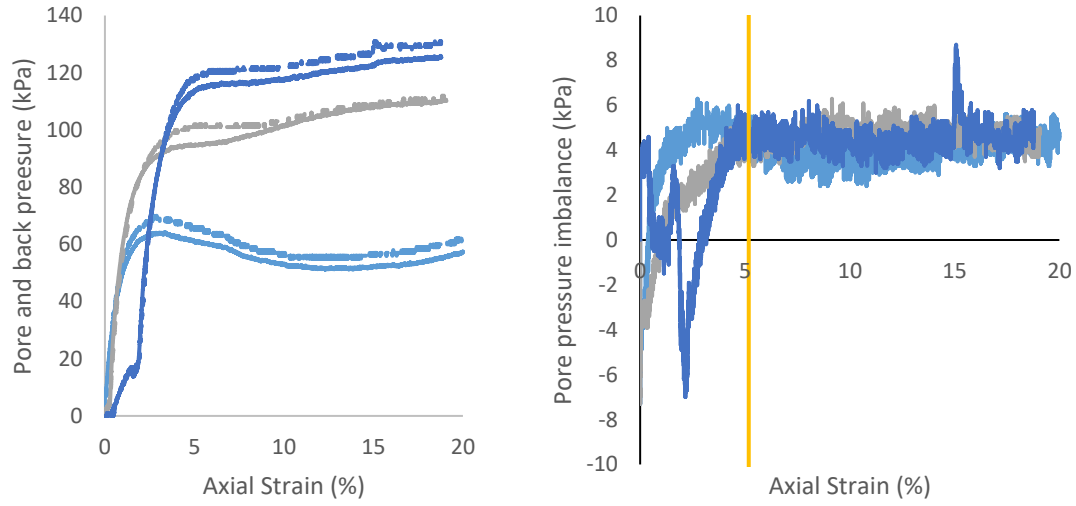

Figure 6.14. (a) pore pressure vs back pressure plotted against axial strain for samples treated for 3 months. Dashed lines are back pressure, while pore pressures are the solid line. (b). Difference in pressures between back and pore pressures plotted against axial strain where the vertical solid yellow line represents the averaged axial strain across all 3 confining stresses

6 Month Soaked Cores

For samples tested at the 6-month mark, all three confining pressures showed consistent behaviour in pressure imbalance (Figure 6.15a and b). Samples initially had a noticeable favouring of higher pressures in the base of the sample (-9, -15 and -13kPa, respectively) before balancing out and becoming very slightly positive (favouring the top of the sample) following failure

(a) (b)

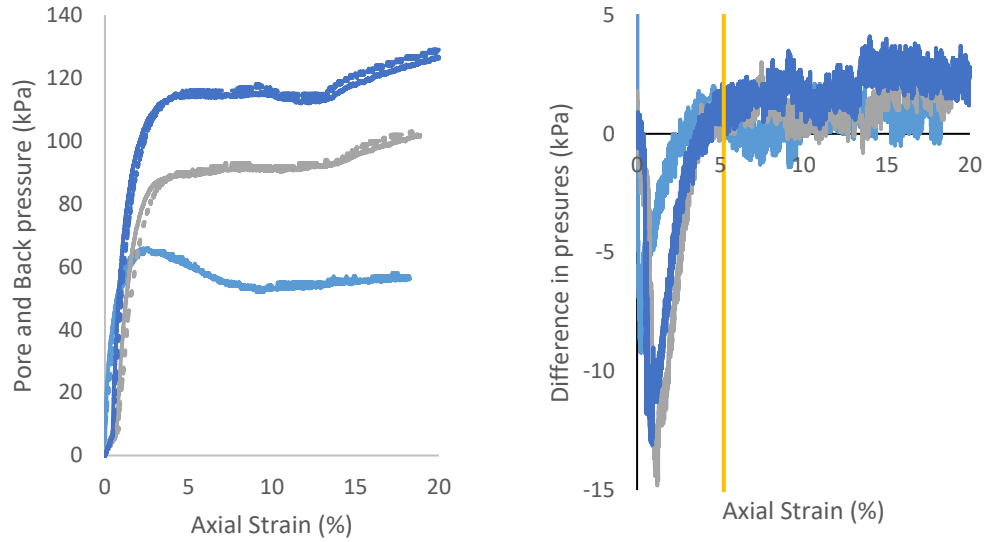

Figure 6.15. (a). pore pressure vs back pressure plotted against axial strain for samples treated for 6 months. Dashed lines are back pressure, while pore pressures are the solid line. (b). Difference in pressures between back and pore pressures plotted against axial strain where the vertical solid yellow line represents the averaged axial strain across all 3 confining stresses.

12 Month Soaked Cores

After 12 months soaking (Figure 6.16a and b), samples showed similar behaviour to the 6 month samples, with an initial favouring of the base of the sample for the 120 and 160 kPa samples (-8 kPa and -13 kPa, respectively) before gradually balancing out and becoming closer to 0 kPa following failure. The 200 kPa sample on the other hand did not show this, with an initial increasing bias to the top of the sample, before reverting to the base of the sample prior to failure. Parity was achieved early at 2 % axial strain before increasingly favouring the base. This was remedied with a return to parity by 20 % axial strain.

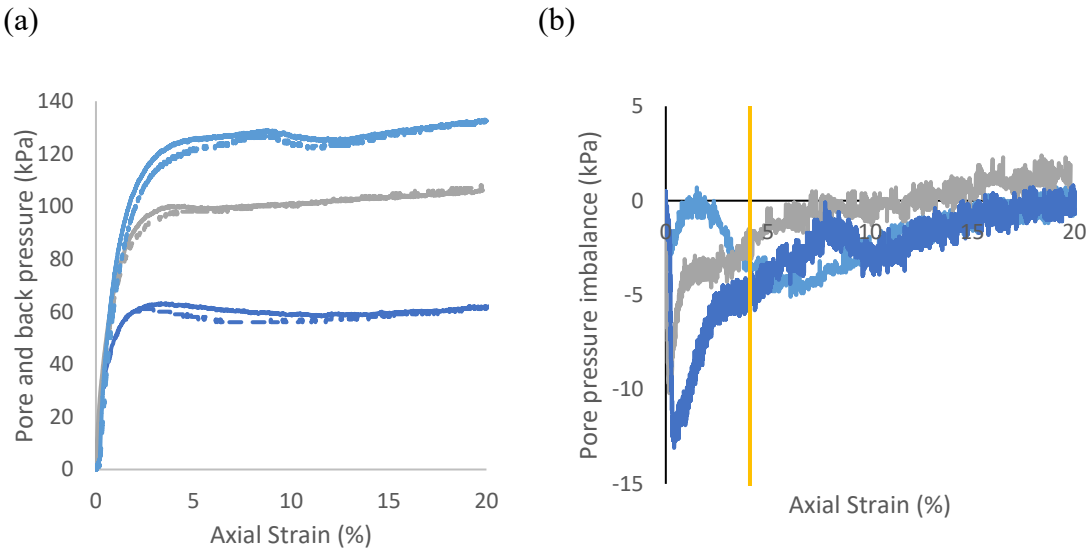

Figure 6.16. (a). pore pressure vs back pressure plotted against axial strain for sample soaked for 12 months. Dashed lines are back pressure, while pore pressures are the solid line. (b). Difference in pressures between back and pore pressures plotted against axial strain where the vertical solid yellow line represents the averaged axial strain across all 3 confining stresses.

6.2.4 Strain Softening and Confining Pressures

For untreated samples, strain softening increases with increasing confining stress, from an average of 19 ± 3 kPa at 120 kPa confining stress, to 30 ± 2 kPa at 160 kPa and 24 ± 9 kPa at 200 kPa confining stress. For treated samples however, there was little relation between strain softening and confining stress across individual treatments (Figure 6.17). The only sample that showed any degree of strong correlation was within the untreated samples, with a very clear, strong (R^2 = 0.97) correlation. All treated samples showed little to no correlation (R^2 = 0.03–0.24). One inconsistency noted was the strain softening for samples at 160 kPa confining pressure being consistently higher than its lower (120 kPa) and higher (200 kPa) confining pressure counterparts.

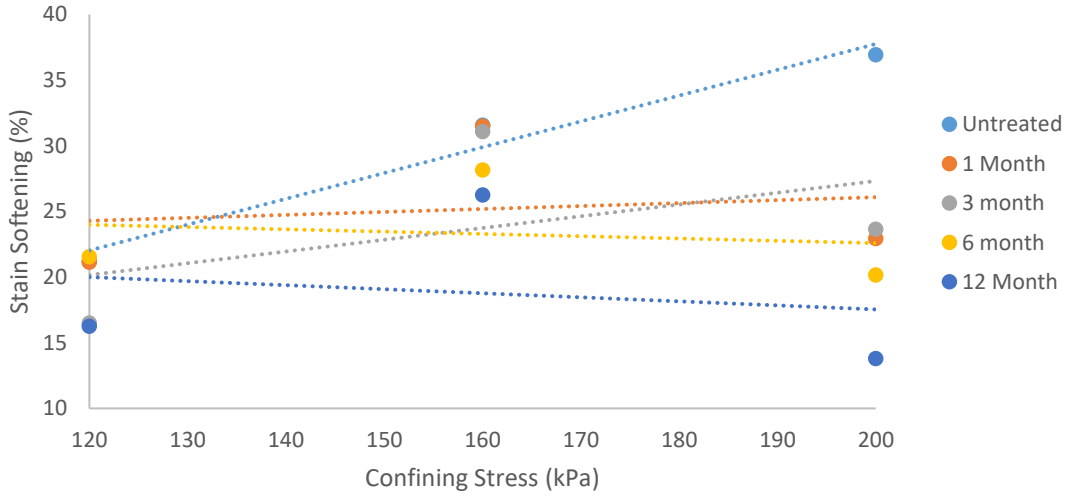

Figure 6.17. Strain softening plotted against confining stress for the samples at their 3 tested confining stresses. Linear trendlines are plotted, though R^2 values are not shown, as these are discussed in text prior.

When looking at strain softening at the specific confining stresses, strain softening shows a decrease over the time that the cores are treated (Figure 6.18). The degree of change varies with confining stress, with the largest change observed at 200 kPa confining stress (23 % reduction), while the lowest change was measured at 160 kPa confining stress (5.29 % reduction). Samples tested at 120 kPa confining stress did show a drop in strain softening over the 12 months, with the 3 and 12 months samples showing the lowest degree of strain softening (16.5 % and 16.26 %), it should be noted that after 6 months strain softening measured was higher (21.55 %) than the initial untreated sample (21.20 %). When looking at correlations, samples tested at 200 kPa showed a reasonable

correlation between the strain softening and soaking time (R^2=0.7), though this ismarked by a large initial drop, before slowly reducing over the remaining 11 month. Comparatively, samples tested at 160 kPa confining stress showed a clear correlation for strain softening over soaking time (R^2=0.95). Samples tested at the lowest confining pressure (120 kPa) were far less consistent (R^2=0.34) and showed little to no correlation .

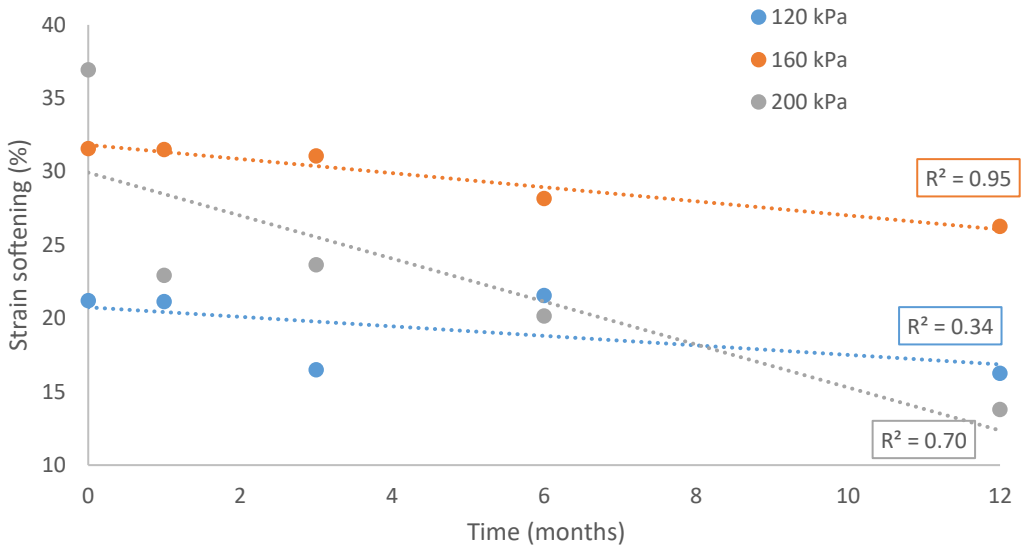

Figure 6.18. Strain softening plots for samples at their respective confining stresses across the 12 months of treatment for the soil. Linear trends are plotted with R^2 values included. 200 kPa samples show the largest reduction, with a reasonable correlation, while 160 kPa samples show a gradual, well related reduction over time. 120 kPa samples show little in the way of consistency with the length of treatment

6.2.5 Triaxial Stress Paths (PQ Plots)

Stress paths in two dimensions depict the evolution of P' and q' stresses within sheared samples. These values are defined by Equations (6.1) and (6.2) below.

$$p' = \frac{\sigma_1{}' + \sigma_3{}'}{2} \tag{6.1}$$

$$q' = \frac{\sigma_1' - \sigma_3{}'}{2} \tag{6.2}$$

Where σ'_1 and σ'_3 represent effective vertical and horizontal stresses within the triaxial test.

Graphs of stress paths at each confining stress are presented in Figures 6.18, 6.19 and 6.20.

120 kPa

At the lowest confining stress (120 kPa) (Figure 6.19) in the initial loading region, the untreated sample deviates left initially before moving right quite drastically prior to failure, indicating an initial contraction followed by dilation of the sample in the moments before failure. This is followed by a drop in q at failure and progressing back along the Critical State Line (CSL). Samples treated for 1 and 12 months display quite different behaviour initially, with both progressing sharply right in the strain hardening region prior to peak stress, with stress paths looping right and back onto themselves as the sample reaches peak deviator stress. Following this loop, samples proceed along the sample CSL.

For samples treated at 3 and 6 months, the initial stress path is relatively straight before shifting drastically to the right prior to failure, before dropping in q' and proceeding along the CSL. Indicative of sample dilation in the pre peak region, before contracting heavily following failure.

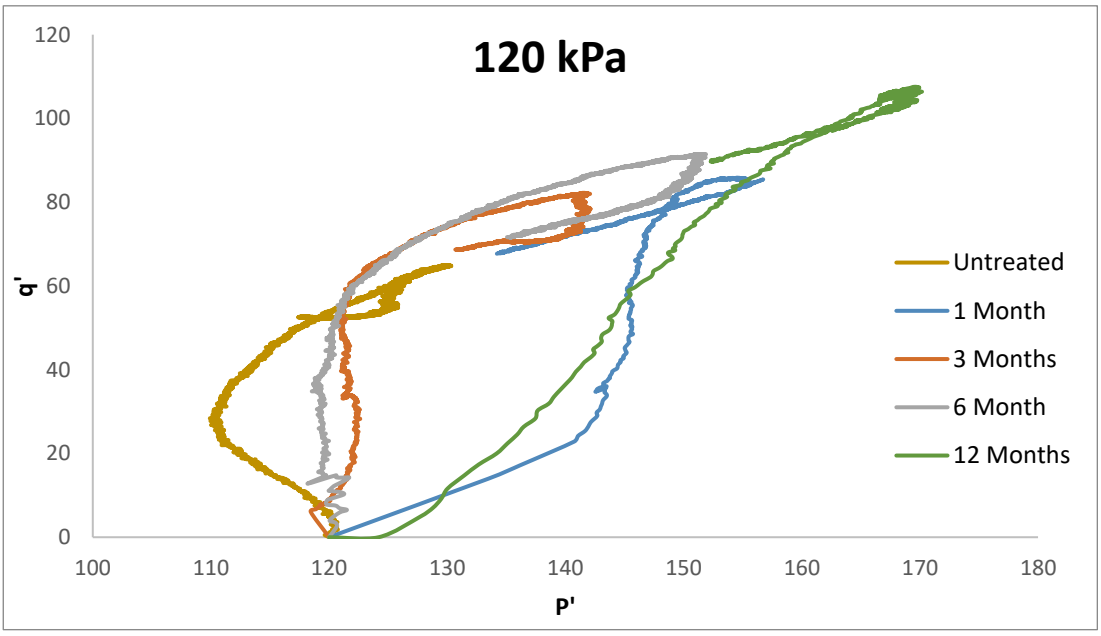

Figure 6.19. Stress paths for untreated and treated soils tested at 120 kPa confining stress. Note behaviour tending left towards 0 is indicative of contraction, while the opposite indicates dilation.

160 kPa

Stress paths for samples tested at 160 kPa (Figure 6.20) showed some similar behaviours to those tested at 120 kPa, though no samples looped back on themselves prior to peak deviator stress. Untreated samples acted in much the same fashion as at the 120 kPa confining stress with an initial shift left, before proceeding back right before peak stress and contracting. Treated samples showed deviance from the behaviour observed at 120 kPa (lack of looping prior to failure) but exhibited consistent behaviour across treatment times with stress paths proceeding right and dilating during initial loading, before proceeding left and contracting upon failure. Samples tested after 1, 3, and 6 months soaking all exhibited a failure point in roughly the same location on the p'q' plot before proceeding along a roughly similar CSL. The 12-month samples, on the other hand, achieved a larger q' than the samples prior to it.

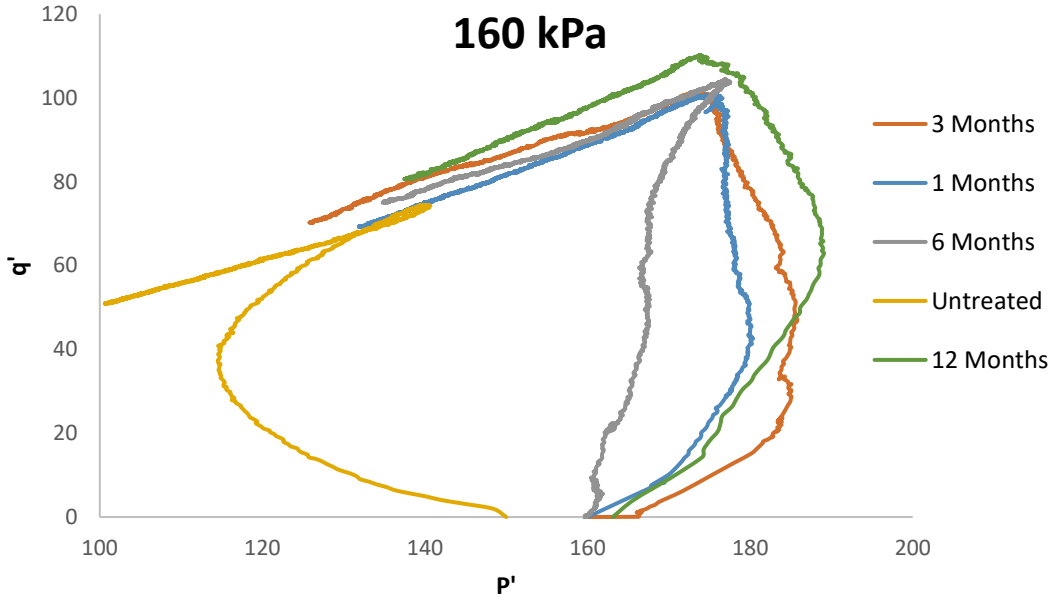

Figure 6.20. Stress paths for untreated and treated soil samples sheared at 160 kPa confining stress. The untreated (gold) sample showed a sharp deviation left (contraction) initially before reverting right (dilatant) prior to failure. Treated samples (1 month = blue, 3 months = orange, 6 months = green, 12 months = orange) showed either slightly (12 months) or reasonably (1, 3, 6 months) dilatant behaviour prior to failure.

200 kPa

Samples tested at 200 kPa confining stress (Figure 6.21) showed a similar variety of behaviour. The untreated sample, as with 120 and 160 kPa showed a stress path trending left initially before returning right prior to failure. This was followed by a movement left along the CSL following failure. Similarly to 160 kPa, samples at 1, 3, and 6 months showed a slight deviation to the right initially before a slight move left prior to failure, before all proceeding along the CSL in roughly the same place. The 12-months soaked sample on the other hand, as prior, proceeded much further right (dilating), before returning left before failure. All samples exhibited significant contraction following failure.

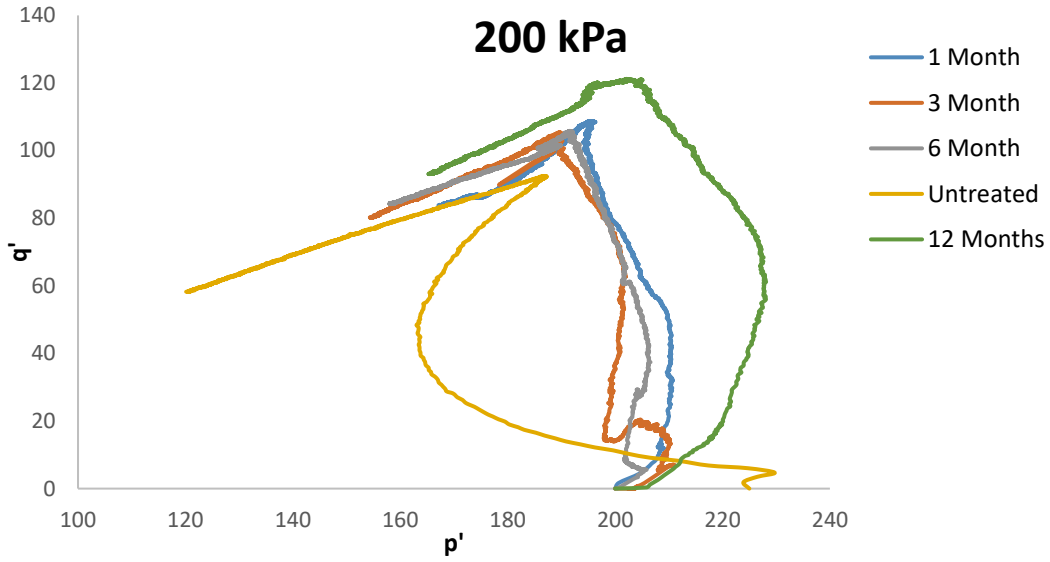

Figure 6.21. Stress paths for samples tested at the 200 kPa confining stress. The untreated (gold) shows quite different behaviour to that of the treated samples, with a strong loop to the left in the early stages of shear before reverting right prior to failure. For 6 and 3 months (grey, orange) some initial loading effects from loading ram seating corrections can be seen. Treated samples show relatively consistent behaviour, though 1 month (blue) and 12 month (green) soaked samples showed the largest moves to the right prior to failure.

6.2.6 Mohr Coulomb Failure Criterion

Mohr coulomb failure criterion was used to determine peak effective cohesion (c') and peak effective friction angles (Φ') for all samples untreated and treated. Mohr circles representing differing confining stresses presented on the same axes were plotted. The summary for these values is shown in Table 6.7, and is plotted in Figure 6.22. The impact of treatment can be seen with all effective cohesions for treated samples larger than that of untreated samples. However, this increase was not consistent throughout treatment.

Table 6.7. A summary table showing the effective cohesion and friction angles calculated for both untreated and treated samples. Following treatment a large increase in cohesion is noted, with the 12 month sample showing a large jump again in effective cohesion. Effective friction angles showed some minor reductions over the 12 months, though the 3 and 6 month samples were relatively similar to the untreated.

Sample	Effective Cohesion (c') (kPa)	Effective Friction Angle (Φ')(º)
Untreated	4.2	29.8
1 Month	26.13	25.93
3 Month	12.29	31.24
6 Month	16.05	30.18
12 Month	40.92	25.29

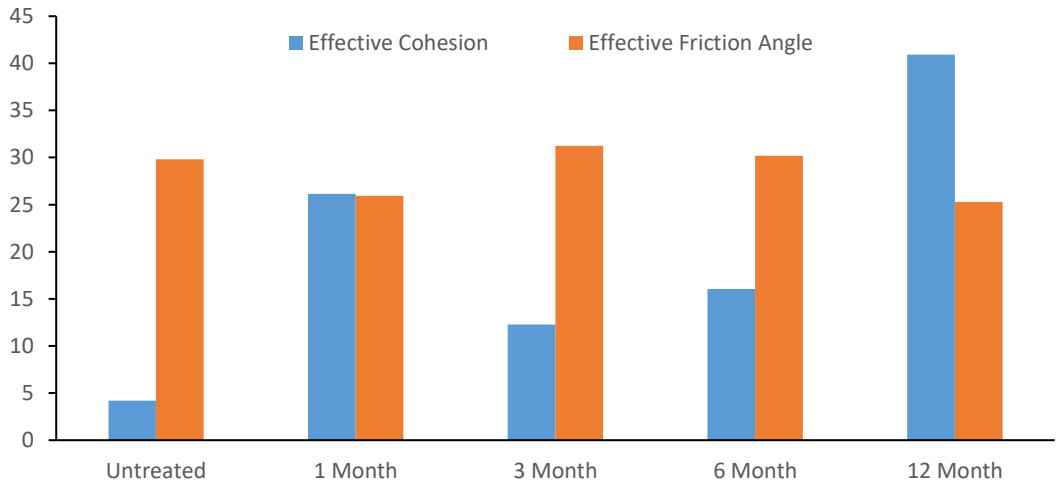

Figure 6.22. A bar chart showing the effective cohesion (blue) and effective friction angle (orange) for treated and untreated samples. Note the y-axis does not have a specific value attributed to it as it is showing the changes in both cohesion (kPa) and friction angle (º)

6.3 Post Triaxial Sample Conditions

Post-failure sample conditions provide an indication as to the type of deformation that contributed to failure. Images of failed samples as well as sketches of visible deformation are presented below. It is worth noting the natural sample tested at 120 kPa is not presented due to triaxial machine error compressing the sample to beyond 20 % resulting in sample destruction.

Modes of failure used in this study are modified from the failure types in soil under triaxial loading as specified by Selby (1993) and further refined by Tang *et al.* (2022). These are consistent with failure types specified in Mills (2016) and Robertson (2017). These consist of four failure modes. Shear failure (Figure 6.23a), wedge failure (Figure 6.23b), intermediate failure (Figure 6.23c) and barrel failure (Figure 6.23d) as per Tang *et al. (*2022). Shear failure (S), indicative of brittle failure, is determined where the specimen has failed along a single sliding plane. Wedge failure (W) indicates a sample undergoing brittle–ductile deformation, characterised by two sliding planes intersecting at an approximate perpendicular angle. Intermediate (I) failure is a combination of shear and barrel failure, indicating ductile deformation. Ductile deformation may also in some instances result in barrel failure (B), where the sides of a sample bulge evenly outwards (Tang *et al.* (2022)).

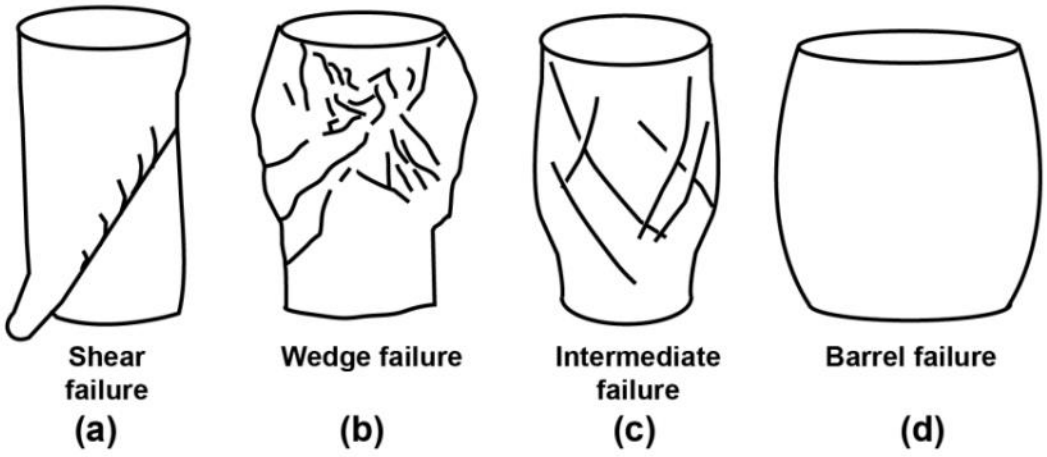

Figure 6.23. Adapted failure styles for soil cores under triaxial testing conditions. Image is sourced from Tang et al. (2022)

Brittle, as well as brittle-ductile deformation can result in shear zones which accommodate the bulk of deformation within samples, known as Primary Shear Zones (PSZ). In some cases, Secondary Shear Zones (SSZ) may be present. These zones allow for the accommodation of less deformation than the PSZ. Samples also may exhibit minor shears, shallower structures, that also allow for the accommodation of some of these shear strains. Inclination, spacing and thickness of PSZ, SSZ and minor shears are described.

Samples are presented with the two faces (anterior and posterior). This provides a '2d' snapshot of the sample shear zone. Samples are shown as both annotated images as well as the outlines of the key features. Table 6.8 summarises the key information of the cores related to failure type and angle of shear plane (from a horizontal origin). Samples are specified by a letter (for untreated) and a number (1, 3, 6, 12) corresponding to the length of treatment combined with the confining pressure at which the sample was tested. Failure types are shortened versions of those specified previously (Shear = S, Wedge = W, Intermediate = I, Barrel = B). Where combinations of failure are observed, these notations are combined (I.e. Shear Wedge failure = SW).

The dark grey shaded regions represent PSZ, while blue represents SSZ. Orientation angles are shaded black with average angles of the adjacent PSZ shown. Red lines represent minor shears, while black boxes show surface deformations.

Table 6.8. Summary of failure types for samples at their respective confining pressures. Where SW = Shear Wedge failure, IW = Intermediate Wedge, I= intermediate and B= Barrel failure. Included are average primary shear zone angles, as well as secondary shear zone average angles

Sample	Failure Type	PSZ Average Angle	SSZ Angle
U120	N/A (SW)*	N/A	N/A
U150	SW	57,63	N/A
U225	SW	56	17
1-120	SW	68	40
1-160	SW	67	N/A
1-200	IW	69,60	N/A
3-120	SW-Minor I	54,21,48	N/A
3-160	SW	62,59	N/A
3-200	B	N/A	N/A
6-120	SW	58,57	N/A
6-160	B	N/A	N/A
6-200	B	N/A	N/A
12-120	B	N/A	N/A
12-160	IW	54	N/A
12-200	SW	54,74	N/A

6.3.1 Untreated Samples

Within untreated samples wedge, shear and intermediate failure modes appear to have occurred for samples tested at 150 and 225 kPa.

150 kPa

At 150 kPa (Figure 6.24) the PSZ appears to have progressed along 2 paths resulting in an intermediate-wedge style failure, with 2 blocks measuring around 70 mm (left block Figure 6.24a and c) and 85 mm (right block Figure 6.24b and d) displaced. Blocks were displaced along the two PSZ, with one stretching from the top right of the sample (Figure 6.24a) to around 8.5 mm above the base of the sample on the left at an average angle of 57^{o}, while the other from 11 mm below the top of the left side of the sample to 13 mm above the bottom right of the sample at an angle of 63^{o}. On the reverse side of the sample the smaller displaced block, had a PSZ that appeared shallower (44^{o},r-l) starting 19 mm below the top of the sample and finishing 19 mm above the bottom left. While the larger displaced block was slightly steeper than the reverse side (64^{o} l-r), finishing approximately 12.5 mm above the sample base. The 'top' block of the sample also exhibited a slightly larger post failure diameter than the base (52 mm top, 45 mm base). Minor shears for the most part remained relatively radial with little inclination along PSZ's. The exception being some slight dragging in the PSZ direction at the very tops of samples along the larger displaced block

225 kPa

At 225 kPa (Figure 6.25) the failure style was less clear, with failure shear-wedge failure, with little consistency shown across the entire failed sample. On side A a single dominant PSZ was present running right to left at around 56^{o}, starting 14 mm below the top of the sample and descending to the base of the sample, with shear wedge displaced over the base of the sample. A shallow SSZ does form 12 mm below the sample top, running l-r at 17^{o}, though this terminates 23 mm below the sample top upon intersection with the PSZ. Minor shears ran along the PSZ orientated at 6–17^{o} anticlockwise. As observed at 150 kPa, the 225 kPa sample exhibited a slightly thicker top block when compared to the base (52 mm top – 46.8 mm base). A slight bulge is noted 45 mm below the top of the sample on the right side. In contrast on the reverse of the sample (side B), a much more distinct SSZ progressing L-R at an angle of 57^{o} is noted, though there are very few minor shears accompanying this deformation. The PSZ descends r-l at 56^{o} with the shear surface terminating 10 mm above the base due to the sheared right-side block. Minor shears are

less oriented along the PSZ on side B with shears generally appearing radially between 0 – 5^{o} in a clockwise orientation

(a)

(b)

(c)

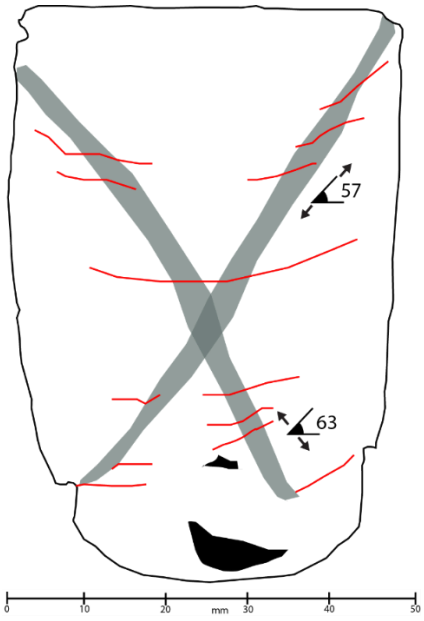

(d)

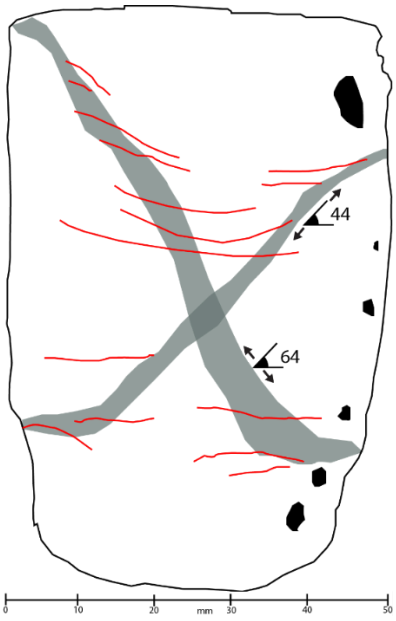

Figure 6.24(a)The sheared core for an untreated 150 kPa sample, primary shear zone's (shaded grey areas) stretch at 57 and 63º angles in an x style failure. Various minor shears are present throughout, generally associated with the primary shear zone. (b) The sheared core for an untreated 150 kPa sample, primary shear zone's (shaded grey areas) stretch at 44 and 64º angles in an x style failure. Various minor shears are present throughout, generally associated with the primary shear zone. (c) the outline of the sheared core in 6.23 (a). (d) The outline of the sheared core in 6.23 (b)

(a)

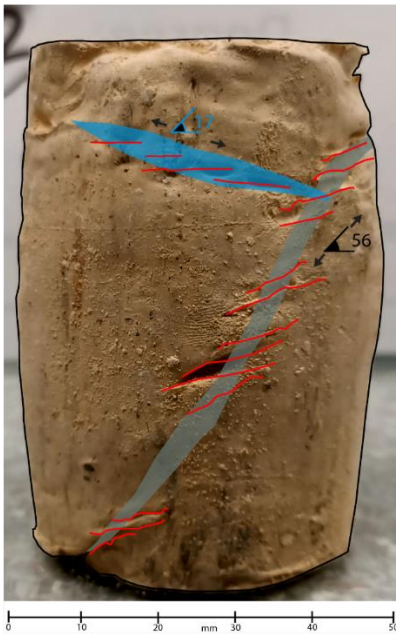

(b)

(c)

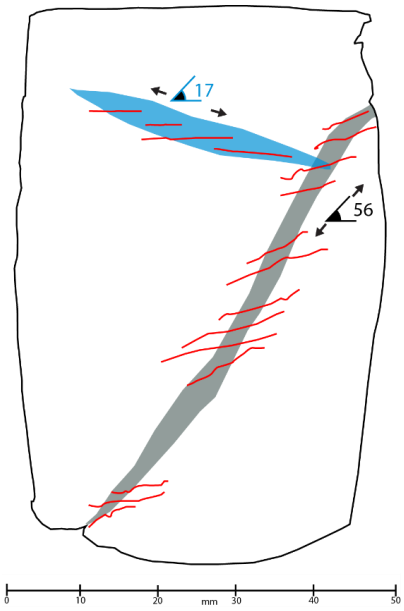

(d)

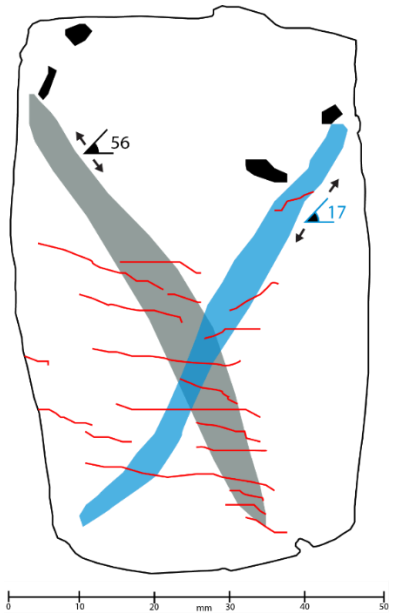

Figure 6.25(a)The sheared core for an untreated 225 kPa sample, primary shear zone's (shaded grey areas) stretch at 56º from right to left. A secondary shear zone extends from right to left as well. Various minor shears are present throughout, generally associated with the primary shear zone. (b) The sheared core for an untreated 225 kPa sample, primary shear zone's (shaded grey area) stretch at a 56º angle. A secondary shear zone intersects at 17º Various minor shears are present throughout, generally associated with the primary shear zone. (c) the outline of the shear features in 6.24 (a). (d) The outline of the sheared core in 6.24 (b).

6.3.2 1 Month Soaked Samples

120 kPa

Samples sheared at 1month treatment (Figure 6.26) exhibit shear and wedge failure, with PSZ's becoming more distinct as confining stress increases. At 120 kPa only one side was able to be photographed due to damage to the reverse side of the sample occurring during removal of membrane. With a shear-wedge failure style, the PSZ at 120 kPa descends r-l at an orientation of 68^{o}, terminating 21 mm above the base. The PSZ itself is thick and relatively undistinguished, with a slight bulging block forming at the base of the PSZ. Minor shears are present, trending along the PSZ at angles 5–25^{o} anticlockwise. An SSZ is present, intersecting around 14 mm above the PSZ termination running at an angle of 40^{o} l-r. This SSZ isn't clear throughout the sample though occurring approximately 15 mm and terminating 15 mm from the edges of the sample. As per the untreated samples, the top of the sample following failure was thicker than the base.

160 kPa

At 160kPa (Figure 6.27) a shear-wedge failure is seen, with side A showing a steep PSZ at an angle of 74^{o}, with the top edge of the PSZ daylighting approximately 20 mm from the very left edge of the sample, extending l-r, terminating 15 mm above the bottom of the samples. The wedge is displaced outwards in a bulge, but hasn't sheared over the base of the sample, failing outwards as opposed to both out and down. Side B has the PSZ descending right to left, 10 mm in from the right edge, terminating at a similar height above the sample base on a slightly shallower 65^{o} inclination. Minor shear structures are observed in both side a and b extending across the PSZ at angles between 10 – 20^{o}. On side A the minor shear structures are relatively evenly spaced, while side b has a concentration of around 20 – 50% of the full length of the PSZ. The top of the sample was slightly greater in diameter than the base following shear. The sample also appears to have buckled slightly during the shear formation, with the sample no longer vertical, instead exhibiting just over 4^{o} of deformation towards the wedge side of the sample

200 kPa

At 200 kPa a shear-wedge failure (Figure 6.28), with some intermediate failure is seen. The PSZ on side a stretching 4 mm below the top r-l, terminating 12.5 mm above the sample base on a 69^{o} angle. The reverse, side b, exhibited a failure surface daylighting 5 mm from the top left edge of the sample, terminating 16 mm above the sample base l-r at a shallower 60^{o} angle. The sample had minor shears observed along the failure surfaces

running in inclination with the PSZ. Some features worth noting are a slight kink in the PSZ on side b approximately halfway down the sample, as well as a slight bulge on the side opposite to the PSZ wedge indicating a degree of intermediate failure. As with the 150 kPa sample, the failed wedge did not descend over the base of the sample and instead bulged outwards.

(a) (b)

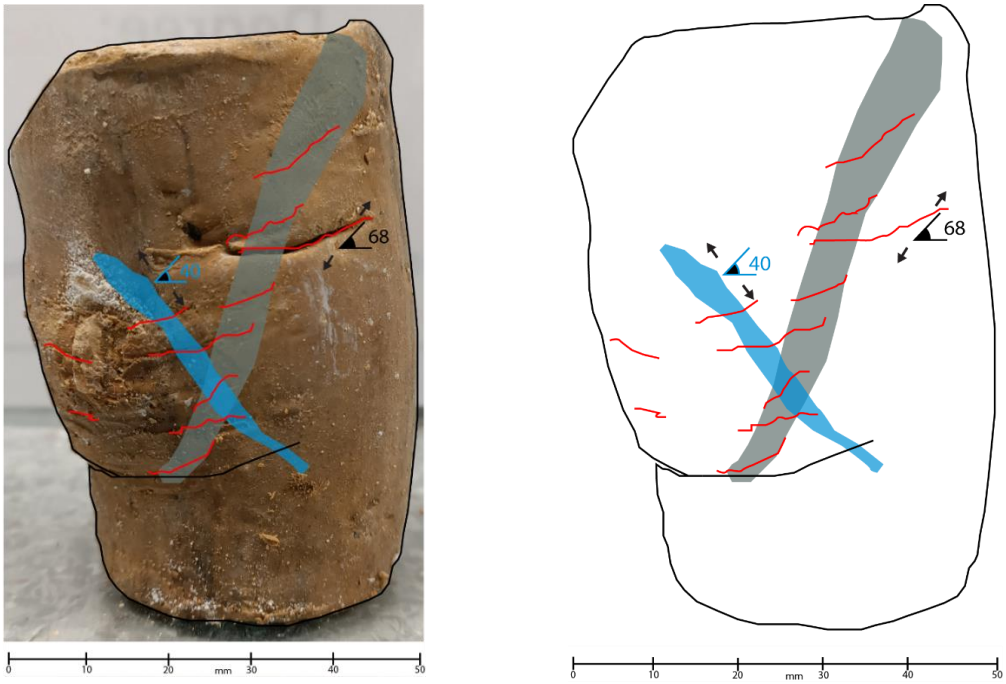

Figure 6.26. (a) the sheared core for the 120 kPa confining stress 1 month sample. A primary shear zone extends from the top right of the sample to the bottom left at 68°. A secondary shear zone is present, with shearing occurring at a 40° angle. (b) the outline of the major shear features.

(a)

(b)

(c)

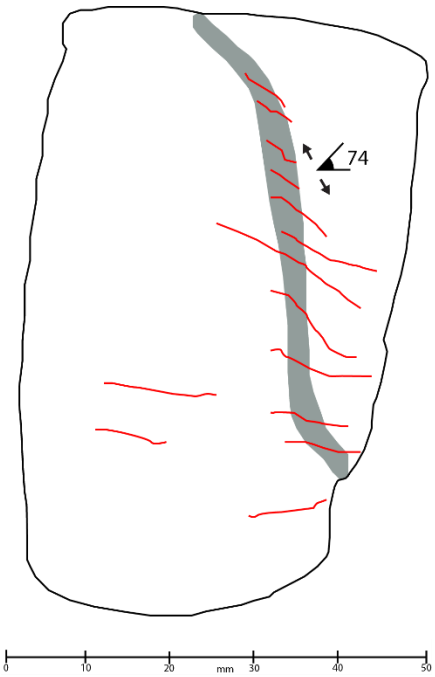

(d)

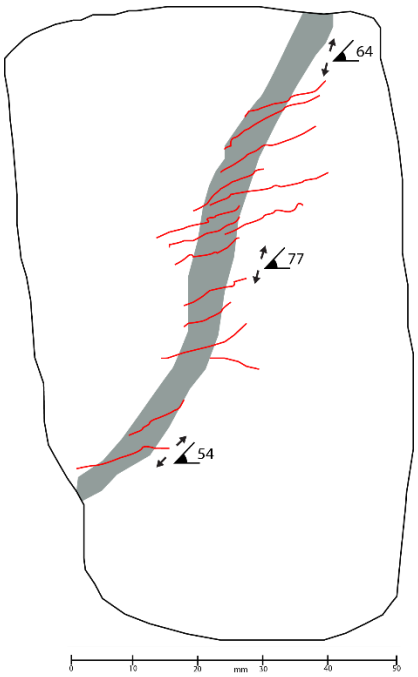

Figure 6.27(a,c)(a)The major shear features present in the 1 month treated 160 kPa confining stress sample. A primary shear zone stretches from left to right at 74º, with minor shears generally associated with the shear zone. The outline of the shear features are shown in (c). (b,d) The major shear features on the revers side of the 1 month 160 kPa treated core. The primary shear zone has 3 differing angles noted as these change throughout failure. Minor shears are associated with the primary shear zone. The outline of shear features is shown in (d).

(a) (b)

(c) (d)

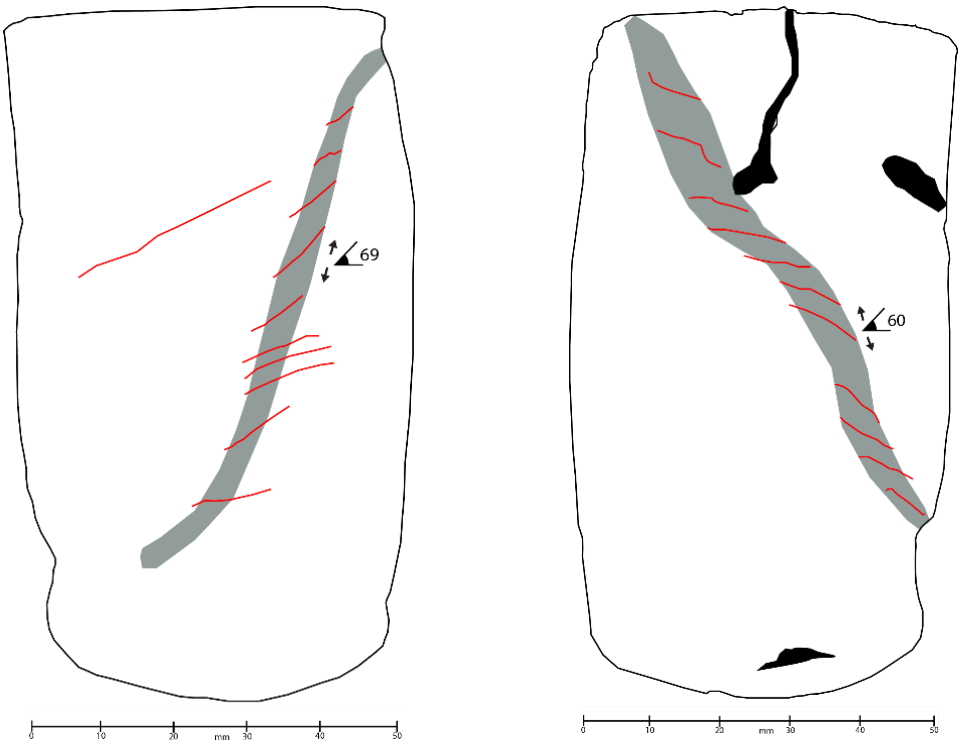

Figure 6.28(a,c)An annotated image of the 200 kPa confining stress, 1 month treated, soil core. A singular primary shear zone is present, with shear seen to occur at an angle of 69º. Minor shears are associated with the primary shear zone. The outline of the shear features are shown in (c). (b,d) The reverse side of the failed 200 kPa, 1 month, core. The primary shear zone has a shallower angle (60º), with some pieces of the sample noted as missing (black zones).

6.3.3 3 Month Soaked Samples

120 kPa

Samples treated for 3 months (Figure 6.29) exhibited all four major failure modes, with 120 kPa samples showing shear-wedge failure, some intermediate, with side a exhibiting a PSZ and SSZ, with the PSZ descending from r-l at 54^{o} in the upper portion, before shallowing out to 21^{o} halfway through the PSZ. This PSZ occurring 12 mm below the top of the sample, terminating 25 mm above the base, with an SSZ occurring radially 8 – 12 mm above the sample base. The reverse, side B exhibits just the PSZ on a shallower 48^{o} inclination extending l-r 8 mm from the top, terminating 14 mm above the base. Side B displays no SSZ, but has much larger minor shears present, with these exhibiting a 15 – 25^{o} inclination in the clockwise direction. Samples show a slight intermediate failure with a slight bulging 1/3 of the way down the sample.

160 kPa

At 160kPa confining stress samples (Figure 6.30) showed shear-wedge failure, with the core appearing to stretch and bulge in certain orientations. A single PSZ is present on both side A and B of the sample with it stretching roughly 10 mm from the top to the base of the sample at angles of 62^{o} and 59^{o} respectively. Extensive minor shears are observed either on, or close to the PSZ indicating clear localisation of stresses during shear. As observed with previous treated samples, the failed wedge did not extend over the edge of the sample, instead the wedge above the shear zone has bulged outwards with the resultant top edge closest to the shear zone dropping lower to accommodate the bulging of the sample outwards.

200 kPa

Barrel failure is seen at the highest confining pressure (Figure 6.31), with two PSZs seen denoting the boundaries of the sample bulging. A number of minor shears are present throughout the sample though these seem to extend radially around the sample with no significant directional inclination, though side A has these concentrated along the PSZ. Due to sample damage the top of the sample is too damaged to make a clear judgement on whether it is larger than the base, though the base appears to have remained a size similar to that of which it started.

(a) (b)

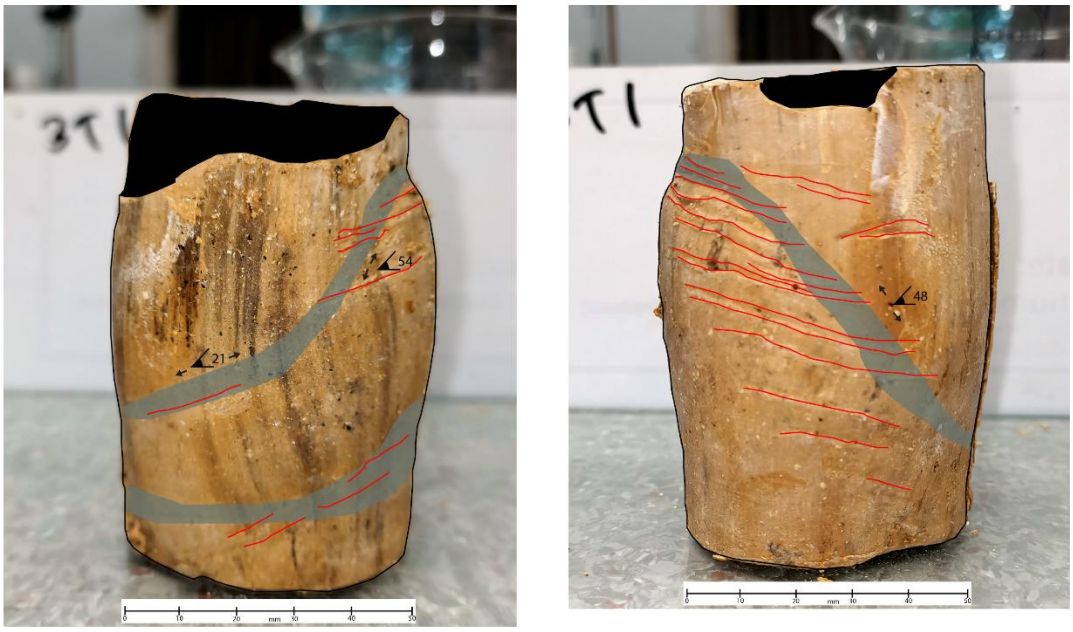

(c) (d)

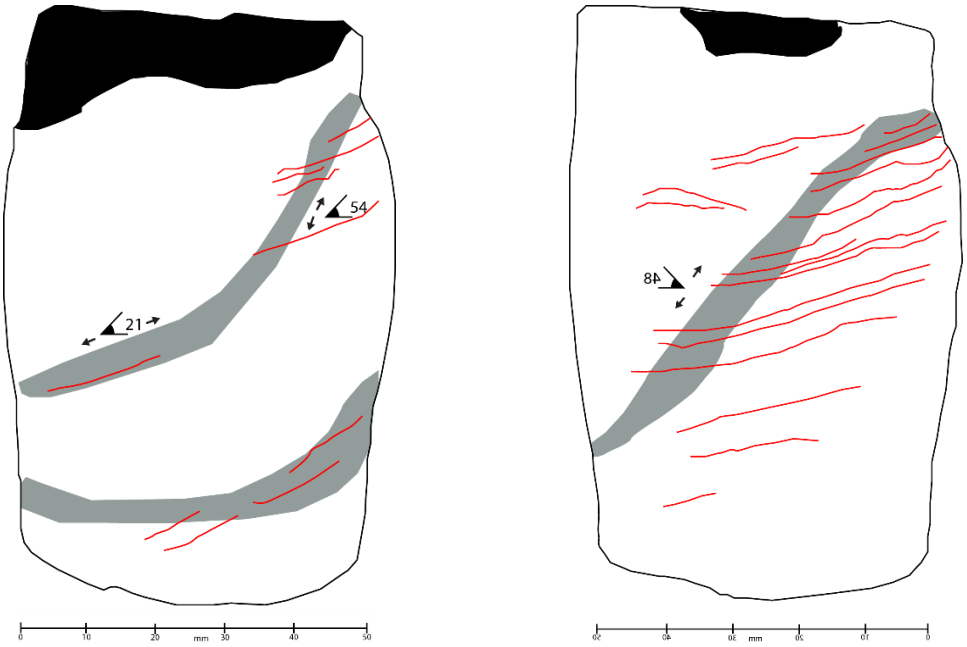

Figure 6.29. (a,c)An annotated image of the 3 month treated, 120 kPa, soil core. Two primary shear zones appear to be present in an apparent barrel/wedge failure style. Some of the damage to the core is noted (black area). The outline of shear features is shown in (c). (b,d) The reverse of the 3 month treated sample, with a singular, 48º primary shear zone noted, minor shears are present throughout. The outline of shear features are shown in (d).

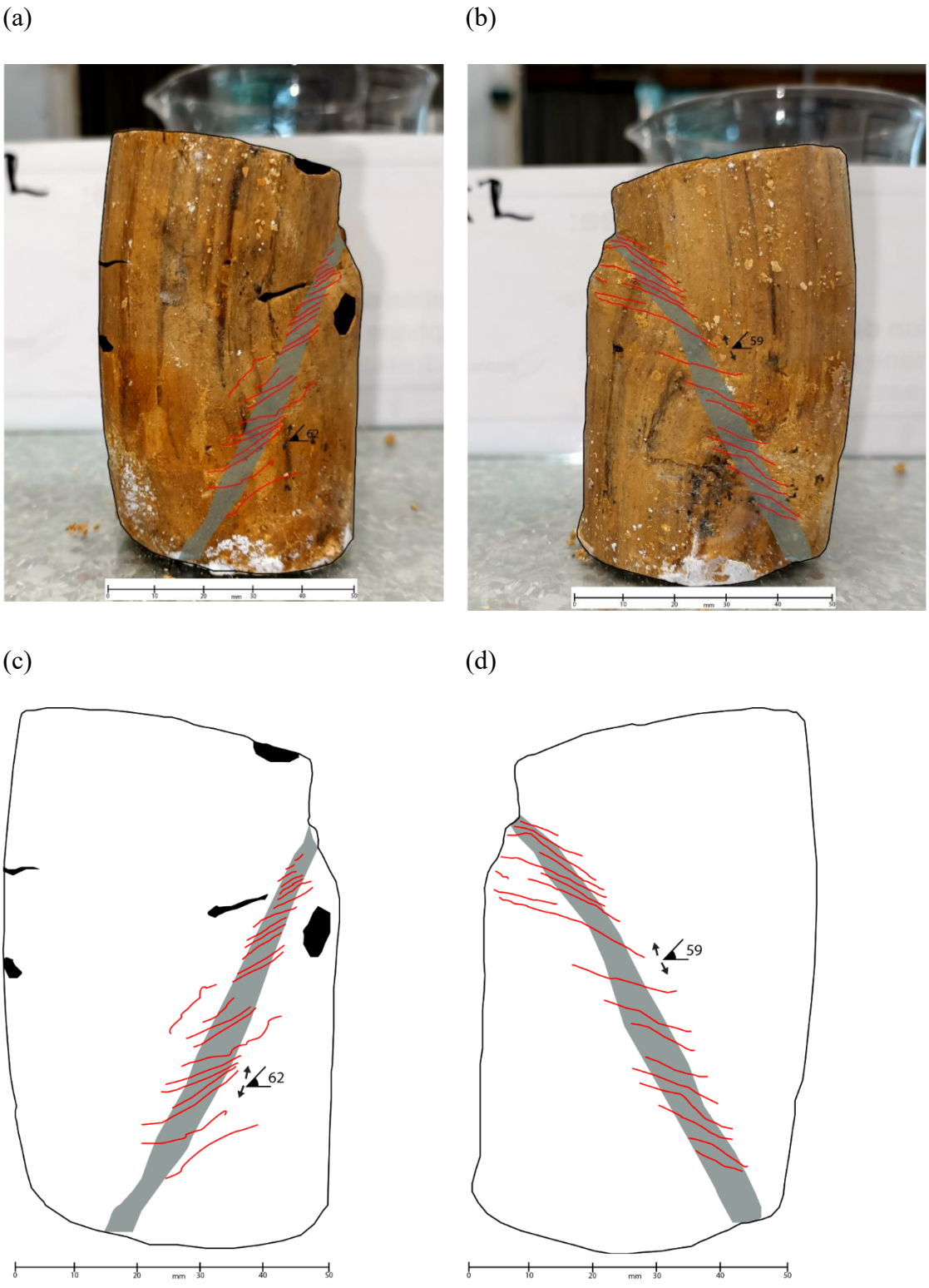

Figure 6.30. (a,c)The annotated image of the 160 kPa, 3 month treated, soil cores. A singular primary shear zone exists with failure occurring at 62º. Minor shears are present along the primary shear zone. The outline of shear features is shown in (c). (b,d) The reverse of the failed core, with the same singular primary shear zone noted, though the angle of failure was slightly shallower (59º). The outline of the image is shown in (d).

(a)

(b)

(c)

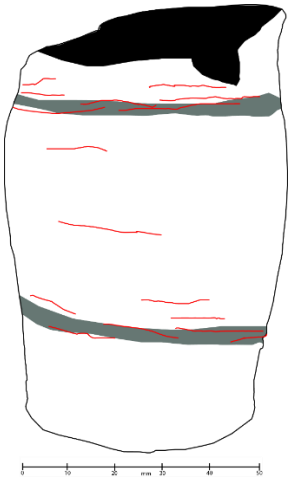

(d)

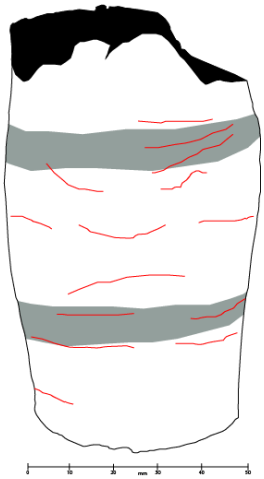

Figure 6.31(a,c) An annotated image of the 12 month treated, 200 kPa, soil cores following failure. Note in this instance barrel failure with a bulging of the material between the two primary shear zones. Some damage to the core has occurred and is shown by the black shaded area. The outline of the features is shown in (c) (b,d) The reverse side of the failed soil core with similar features noted as in (a). Note outlines of the failed core are shown in (d).

6.3.4 6 Month Soaked Samples

120 kPa

Shear failure is seen at 120kPa (Figure 6.32) for samples treated for 6 months, with a relatively thick PSZ, descending at inclinations of 53^{o} and 57^{o} (Side A and B, respectively). The PSZ is concentrated noticeably below the top of the sample, similar to the failure seen for 120 and 160kPa samples treated for 3 months. Minor shears concentrate along the PSZ inclined between 15 – 35^{o}. As observed with previous treated samples instead of a brittle failure, and the entire upper wedge clearly descending over the bottom wedge, as occurred for untreated samples, the upper wedge has bulged outwards to accommodate the movement.

160 kPa and 200 kPa

Barrel failure is seen at 160 kPa (Figure 6.33) and 200 kPa(Figure 6.34) , with two key PSZ's observed demarking the boundaries of the failed material. Both samples showed that the upper portion of the sample above the PSZ had larger diameters than the material below the bottom PSZ. Barrelling at the 160 kPa confining pressure was more pronounced, with much smaller, more localised, minor shears observed, with a peak diameter of 83 mm measured. At 200 kPa, barrelling was smaller by comparison, peaking at 74 mm, though minor shears for the 200 kPa sample were much larger.

(a) (b)

(c) (d)

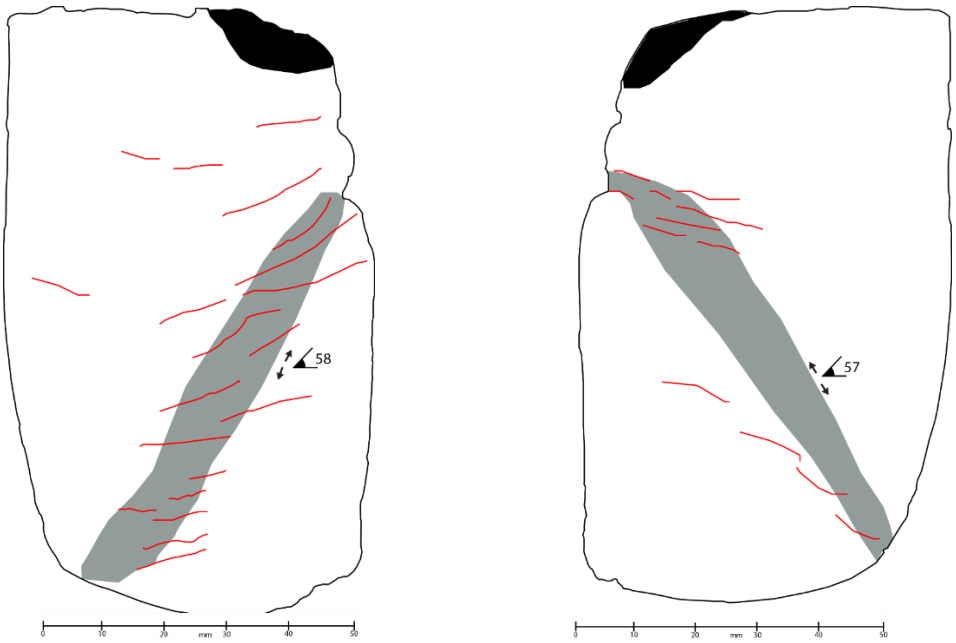

Figure 6.32(a,c) An annotated image of the 120 kPa confining stress, 6 month treated, soil core. A singular primary shear zone, of wedge failure style is shown with a shear angle of 58°. The outline of major features is shown in (c). (b,d) The reverse of the 120 kPa, 6 month, soil core. Similar features are noted with a 1° difference in shear angle (57°) noted. As previous the outline of features is shown in (d).

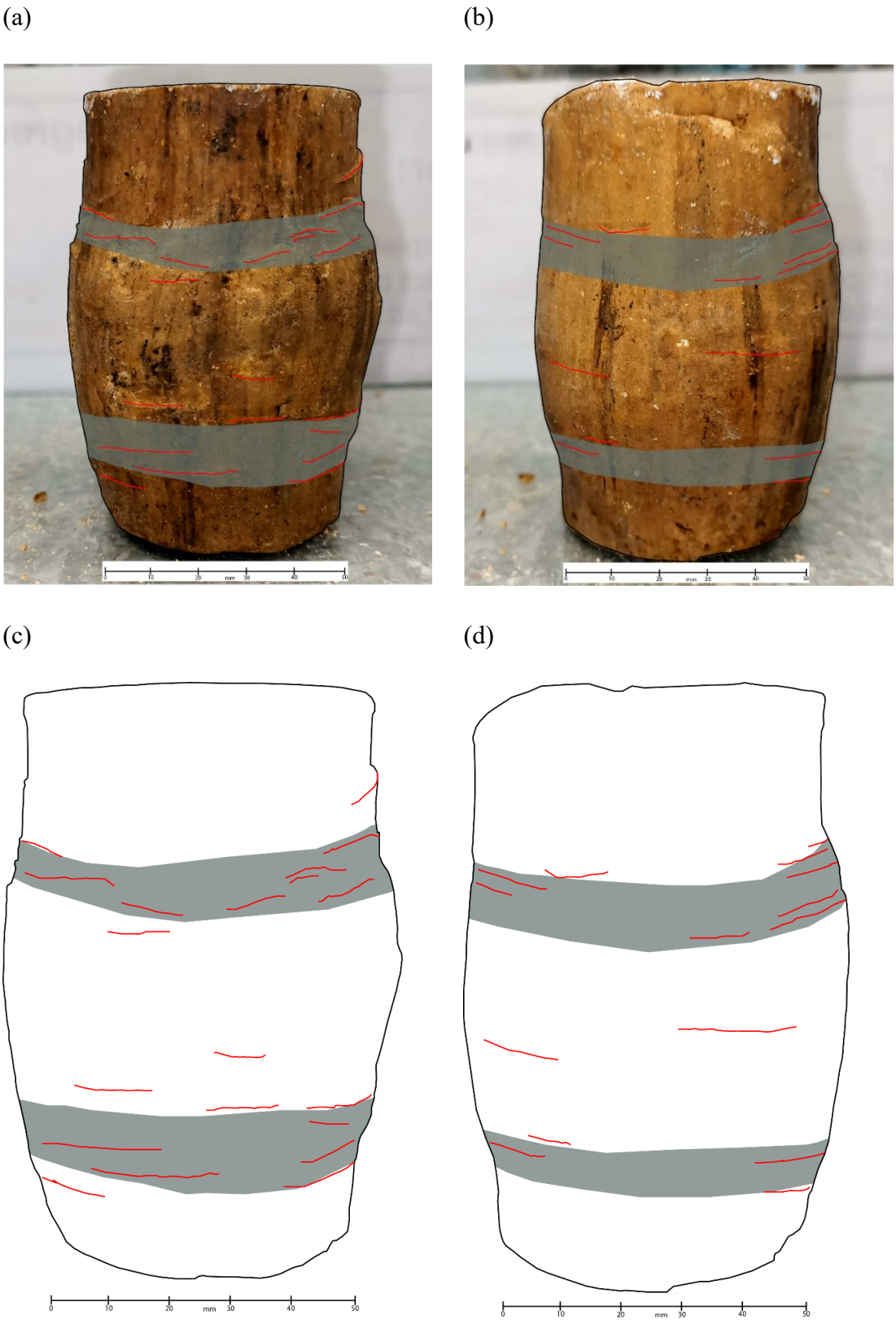

Figure 6.33 a,c) Annotated images for the 6 month, 160 kPa confining stress sample, with a barrel failure style noted. Minor shears also appear to stretch along the sample in a similar barrel style. Outline of major features is shown in (c). (b,d) the reverse of the 160 kPa failed core, with outline of major features shown in (d).

(a)

(b)

(c)

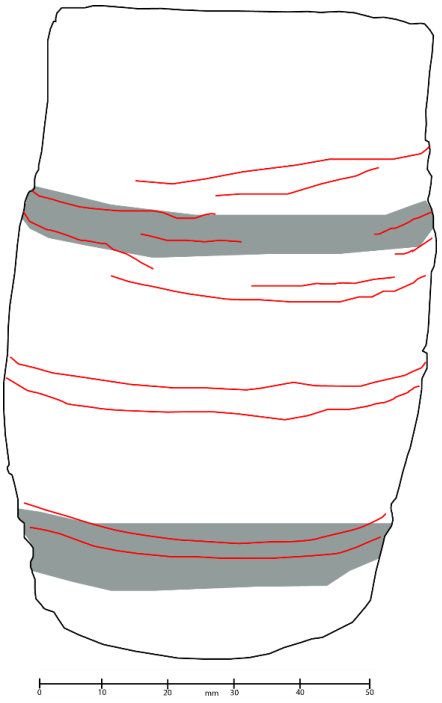

(d)

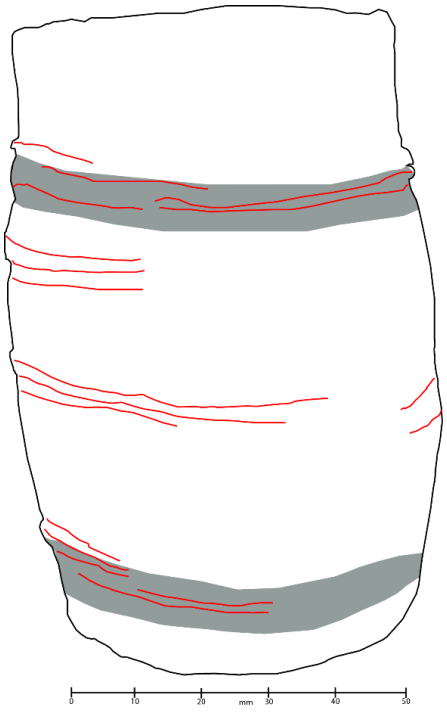

Figure 6.34 .(a, c) the annotated image of the 200 kpa failed cores, failure style is similar to 160 kPa with barrel failure style noted, the outline of the failure features are shown in (c). (b, d) the reverse of the 200 kPa barrel failure, with the outline shown in (d).

6.3.5 12 Month Soaked Samples

120 kPa

Samples tested at 12 months treatment time exhibited barrel, intermediate as well as shear/wedge failures. At 120 kPa confining stress (Figure 6.35) barrel failure is apparent, with two PSZ bands observed 30 mm from the top of the sample and 12 mm from the bottom of the sample. These were accompanied by minor shears extending radially around the sample. These minor shears were found throughout the barrelled portion of the material, with a slight concentration of shears at the top of the sample compared to the bottom. Similar to other treated samples, the base below the shear zone was slightly smaller in diameter than the material above the sheared zone.

160 kPa

Wedge-intermediate failure was observed on samples at 160 kPa confining stress (Figure 6.36), with irregular PSZ's noted for side A and B. For side A the PSZ descended in a semi-circle from 3 mm below the top right edge, descending to 40 % of the sample, before ascending to the left edge 28 mm below the top edge. This PSZ does not descend into the lower portion of the sample, instead creating an intermediate style failure. Minor shears are present throughout, though these for the most part are concentrated along the PSZ. Side B on the other hand displays wedge-intermediate failure, with the samples divided into three portions by the PSZ. The PSZ descends from 12 mm below the top of the sample on the left edge at a 54^{o} angle, descending to 4 mm above the base. The PSZ intersects at around the halfway point of the sample with another PSZ descending from the right edge of the sample, starting 24 mm below the top edge on a shallower 47^{o} inclination. Minor shears are present throughout both sides A and B, with the bulk of these concentrated within the PSZ.

200 kPa

At 200 kPa confining stress (Figure 6.37) the sample exhibits shear-wedge failure with a distinctive PSZ descending from 8 mm below the top edge on both samples at angles of 54^{o} (side A) and 74^{o} (side B). The sample appears to have sheared with an edge visible in sheared material of side B. It is worth noting though that the sample appears to have slightly bulged as seen in previous treated sample cores, as well as a clear lean is present on the samples. Minor shears are concentrated along the PSZ tending on a slightly shallower angle (25 – 37^{o})

(a)

(b)

(c)

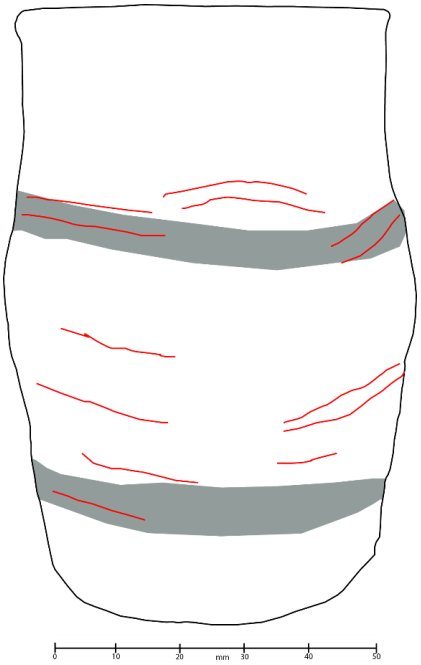

(d)

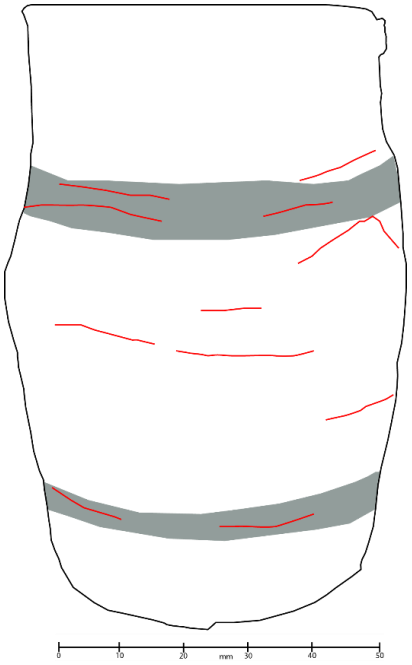

Figure 6.35. (a,c)An annotated image of the 120 kPa, 12 month treated, soil cores. Barrel style failure is observed , with the outline of shear features shown in (c). (b,d) the reverse side of the 120 kPa sample, with the outline shown in (d).

(a)

(b)

(c)

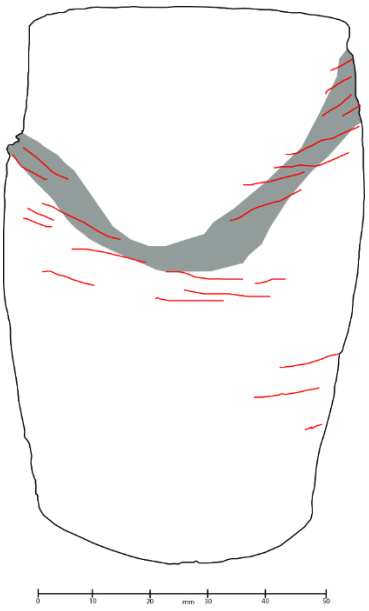

(d)

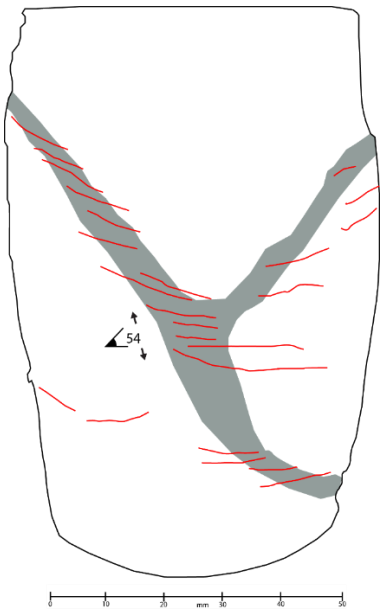

Figure 6.36 (a,c) An annotated image of the wedge style failure observed for the 160 kPa confining stress, 12 month treated soil cores. An outline of shear features is shown in (c). (b) The reverse side of the 160 kPa core, with a 54º angle of failure measured. An outline of shear features is shown in (d).

(a) (b)

(c) (d)

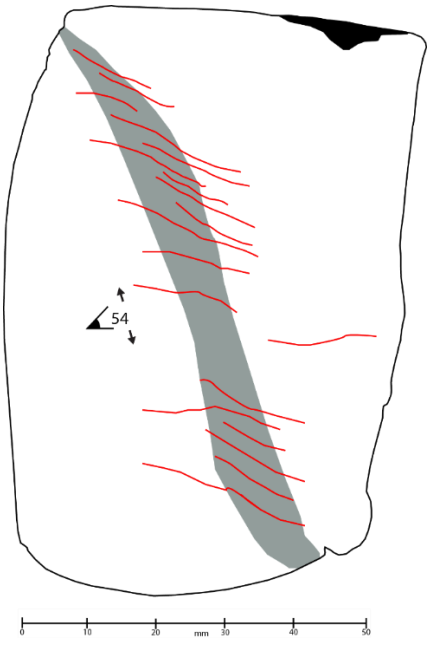

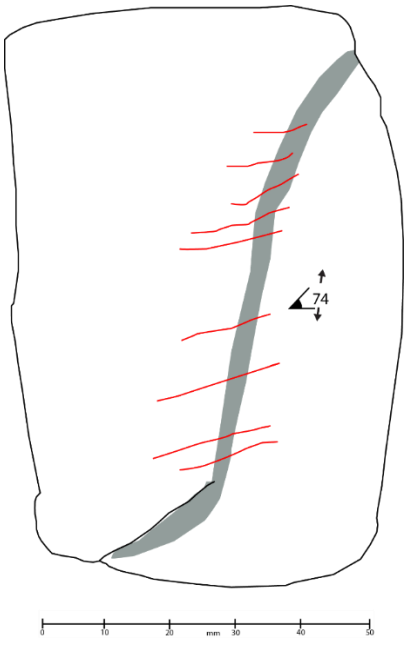

Figure 6.37 . (a,c) An annotated image of the 200 kPa confining stress, 12 month treated soil core. A singular primary shear zone, at an angle of 54º is observed. Minor shears are generally associated with the primary shear zone. The outline of shear features is shown in (c). (b,d) The reverse side of the 200 kPa soil core, with a singular primary shear zone, at an angle of 74º noted. Outlines of the shear features are shown in (d).

Chapter 7

Part I — Discussion

7.1 Bulk Density, Porosity, Void Ratio, and Permeability

7.1.1 Bulk Density

Bulk density in soils is a term given to the general or apparent density from the mass of particles of the material within a given volume. Generally, soils exhibit wet bulk densities that decrease with increasing moisture content (Selby 1993). This relates to soils of lower wet bulk densities having larger and/or greater pore spaces available for water to accommodate. This is due to water having a lower density than soil, reducing the soil's subsequent bulk density. Figure 7.1 shows various soils that are known to exhibit sensitive responses found within the Tauranga region (Wyatt, 2009; Cunningham, 2012; Mills, 2016), as well as plots from Scandinavian sensitive material (Pusch & Söderblom, 1967; Gylland, 2012) and some non-sensitive and slightly sensitive clays from the Hamilton Ash bed formations from within New Zealand (Lowe, 2023).

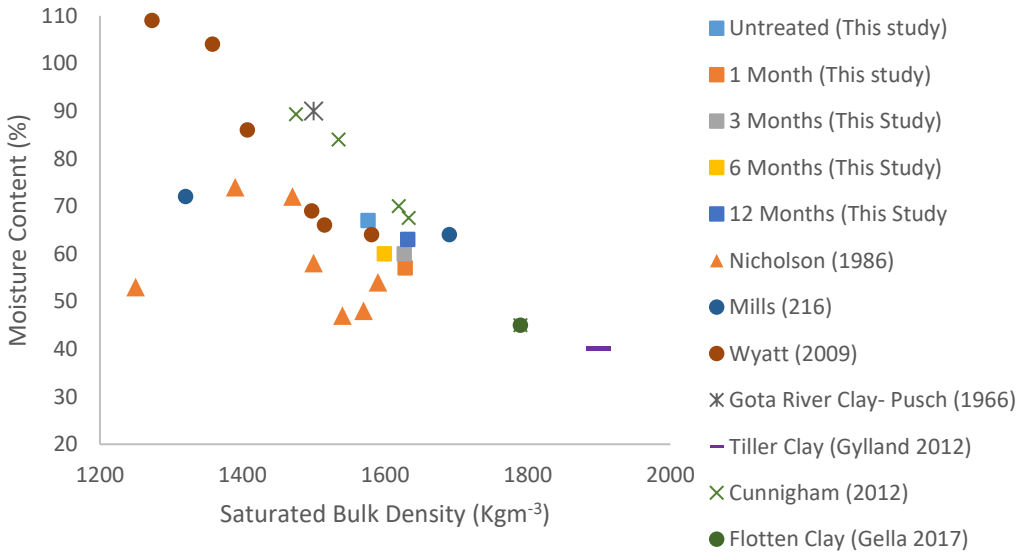

Figure 7.1. Plotted are the saturated bulk densities for various sensitive clay soils both in New Zealand (Nicholson (1986), Wyatt (2009), Cunningham (2012), Mills (2016), this study), as well as overseas (Pusch (1966), Gylland (2012), Gella (2017)) against the respective *in situ* moisture content of that soil. Note the general trend of increasing saturated bulk density with reducing moisture content.

Soils from this research show good agreement with other Tauranga extra-sensitive soils, plotting high bulk densities for the relative moisture contents. When compared to insensitive tephritic material from elsewhere in New Zealand, Tauranga's extra-sensitive soils show much higher bulk densities at similar moisture contents. Compared to overseas sensitive clays, the Tauranga material plots in a similar manner to the Swedish Gota River clay with regards to moisture content and density but exhibits much higher *in situ* moisture contents and lower bulk densities than Norwegian clays, especially the Tiller and Flotten Clays (Gylland, 2012; Gella, 2017).

Bulk densities for treated samples, when corrected for the presence of salt within the soil, showed higher bulk densities than the untreated samples. This increase in bulk density and decrease in moisture content is expected and has been observed in other salt-treated sensitive clays overseas (Helle et al., 2017). The decrease in moisture content is likely related to the increase in salt content within the soil, causing an increase in total salt solids in the soil volume and consequently reducing moisture content due to the lack of available pore space for water.

7.1.2 Porosity and Void Ratio

Soil porosity and void ratio are key aspects of sensitive materials. A pre-requisite in the formation of quick and extra sensitive clays, particularly in Scandinavian quick clays, is the presence of high porosity and, subsequently, high void ratios (Pusch, 1970; Rosenqvist, 1977; Quigley, 1980). These high void ratios and porosity rely on characteristic conditions for forming quick and extra-sensitive clays.

Extra-sensitive soils from Tauranga meet the criteria for the development of such deposits. Those soils are generally dominated by low activity, non-swelling halloysite. Moon *et al.* (2015) showed that these materials also exhibit high porosity and large void ratios due to loosely packed clay minerals and point-to-point contacts. Kluger *et al*. (2017) determined that sensitivity within these halloysite-dominated beds is heavily controlled by the morphology of said clay. In their instance, semi-spheroidal mushroom caps were observed, and their dominance within the halloysite fraction was linked to being the primary control of sensitivity. This significant increase in sensitivity related to morphology was likely observed previously by Smalley (1980), in which he commented on the dominance of "spheroidal halloysite" within samples taken from the 1979 Bramley Drive (Ōmokoroa) slip surface.

Soils from this study exhibited high porosities (63 – 71 %), as well as high void ratios (1.75 (treated) – 2.83 (untreated)), fitting within the range found for Tauranga extra-sensitive soils (porosity= 61 – 78%, void ratio= 1.59 – 3.4(Wyatt, 2009; Arthurs, 2010; Cunningham, 2012; Moon et al., 2013; Mills, 2016; Robertson, 2017). Treated samples showed a marked reduction in both porosity and void ratio, with a 38 % decrease in void ratio (Δe= 0.65) and an 8 % decrease in porosity (Δn= 6 %) seen over the 12 months of treatment. This reduction in void ratio and porosity indicates a potential loss of pore space following the treatment of the soil after 12 months. Previous studies (Wyatt, 2009) found these spaces to be dominated by ultra pores (< 0.1 μm) and micropores (< 1 μm), with dominant pores being <1 μm, though these micropores are poor at transmitting water. This trait is explored in a later chapter.

7.1.3 Permeability

While pore size and its relation to porosity and change following treatment are not addressed in this chapter, one aspect that can be explored is the relationship between permeability, porosity and void ratio. While permeability is conventionally determined via consolidation tests for clay samples, it can also be determined during CU and CD tests for triaxial testing, with permeability calculated from Equation 7.1 derived from Kluger *et al.* (2022). Equations to determine c_{vi} (coefficient of consolidation) and m_{vi} (coefficient of volume of compressibility) are also shown in Equation 7.2 and Equation 7.3. It is worth noting, though (Head & Epps, 2011), that permeability values, if lower than $>10^{-8}$ ms^{-1}, may not be accurate due to errors related to the calculation of C_{vi} when derived from a triaxial as such future tests should refer to AS 1289.6.7.3:2016 to determine the permeability of undisturbed clay samples through triaxial methodology. While permeability values for this study are in excess of 10^{-8} ms^{-1} (Figure 6.9 in the results), and values may have a certain degree of error, there is still value in discussing these results.

$$k = c_{vi} m_{vi} \times 0.31 \times 10^{-9} m/s \tag{7.1}$$

$$c_{vi} = \frac{\pi D_c^2}{\lambda t_{100}} \tag{7.2}$$

$$m_{vi} = \frac{\Delta V_c}{V} \times \frac{1000}{\Delta \sigma^1} m^2/MN \quad (7.3)$$

Expected permeabilities for clay-to-silt soils fall in the range of $<10^{-7} – 10^{-9}$ ms^{-1} for clay-silt mixtures and $<10^{-10}$ ms^{-1} for pure clays (Mitchell et al., 2005). Permeability for untreated soil from this study was calculated to be, on average, $1.82x10^{-9}$ ms^{-1}, placing the soil at the lower end of permeabilities, with the soil acting more as a pure clay than a clay-silt mixture. Compared to similar extra-sensitive Tauranga soils, this soil plots comfortably within the expected range for permeabilities measured for sensitive tephra deposits ($10^{-11} – 10^{-7}$ ms^{-1}) (Kluger et al., 2022). Estimating permeability can be achieved by utilising known empirical relationships between permeability and grain size parameters (Slichter, 1899; Beyer, 1964; Alyamani & Şen, 1993; Barr, 2001; Chapuis, 2004).

These yielded permeability coefficients in the magnitude of $10^{-10} – 10^{-7}$ ms^{-1}, with the average predicted permeability sitting around 10^{-8} ms^{-1}, slightly faster than the untreated measured in this study. As treatment time increases, permeabilities gradually increase in speed, though by a small margin. Permeability increases from $1.82x10^{-9}$ ms^{-1} before treatment to an average permeability of $5.72x10^{-9}$ ms^{-1} after 12 months. This is quite an increase (5x increase) and indicates a clear trend that, on average, soil permeability increases with the length of treatment. This correlation is also clear in the R^2 values of each soil (Figure 7.2), with R^2 for 160 and 200 and averages of 0.92, 0.97, and 0.84, respectively, indicating a clear and direct link between length of treatment and permeability. It is worth noting things are less correlated at 120 kPa, with an R^2 of only 0.61 recorded.

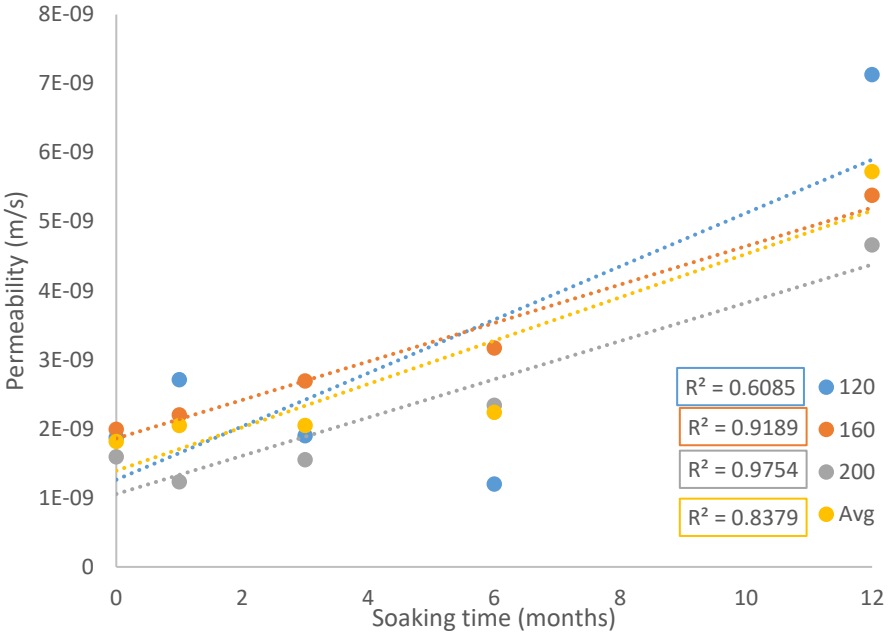

Figure 7.2. A scatter plot showing permeability of samples plotted against soaking time. The average permeability at each testing point is also shown (yellow). The major trend across all samples is an increase in permeability with increasing length of treatment. Strong correlations are observed for all but the 120 kPa sample, which is only moderately correlated.

The relationship between the characteristics of soil pores and permeability can be traced back to the late 1800s. Seelheim (1880) proposed permeability "being related to the squared value of some characteristic pore diameter". Since then, numerous attempts to relate the relationship between the pairs have been made, with one of the most frequently quoted relationships being traced back to Kozeny (1927), later modified by Carman (1937,1956) with the resulting equation known as the Kozeny-Carman (KC) equation. The KC equation states that for a given soil, there should be a linear relationship between permeability and void ratio, where increasing void ratio results in increasing permeability (Carman, 1937). While some authors state that the KC equation is inappropriate for usage on clays (Lambe & Whitman, 1991; Domenico & Schwartz, 1997), more recent studies have indicated the validity of the equation and the relationship it highlights for natural, undisturbed clays (Chapuis & Aubertin, 2003). This relationship of increasing permeability with increasing void ratio, as well as decreasing T_{100} for clays, was further shown by Kluger et al. (2022), where sensitive materials from Tauranga exhibited increasing permeability as the void ratio increased.

This relationship, however, is not observed across both treated and untreated samples (Figure 7.3**)**. This is likely related to the reduction in the void ratio following the treatment of the soil. It can be observed that the opposite of the relationship is exhibited in the

literature, with a drop in void ratio increasing permeability. As a result, direct proportional changes do not appear to exist for treated soils.

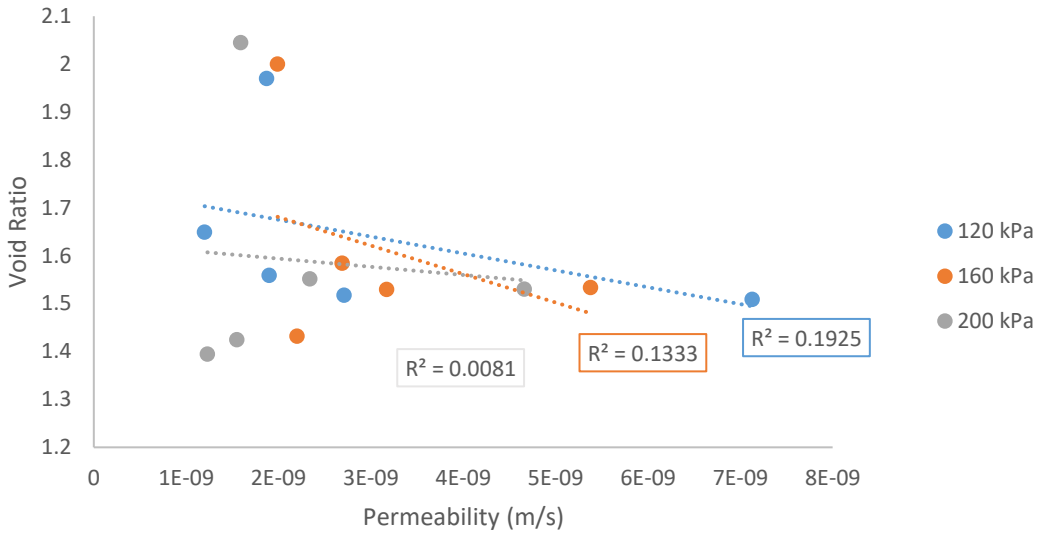

Figure 7.3 .Void ratio following consolidation for samples at their confining stress (i.e. 120 kPa, 160 kPa, 200 kPa) plotted against the specific permeability of the sample. The data for this indicates little to no correlation between the two parameters.

With this said, when examining the changes at respective confining stress for just treated soil (Figure 7.4), this linear relationship appears to become apparent at the highest confining pressure. However, data is only somewhat correlated (R^2= 0.59). The inverse relationship is present, with increased permeability as the void ratio decreases for samples at 120 and 160 kPa, though these values show little to no correlation at all (R^2= 0.10 and 0.06, respectively).

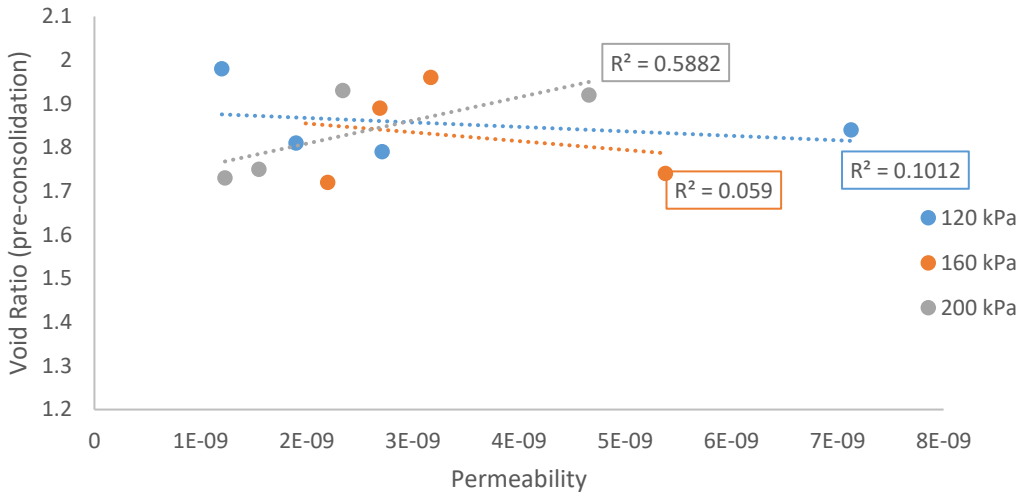

Figure 7.4. Void ratio of samples before consolidation plotted against permeability measured during consolidation for samples at their respective confining stresses. Little to no correlation between initial void ratio and permeability is noted for the 120 and 160 kPa samples, while a reasonable correlation is noted for the 200 kPa samples.

While no clear linear trend exists between void ratio and permeability, what is evident is that, overall, following treatment, increasing permeability coincides with lower void ratios, with an average increase in permeability of 3.91×10^{-9} ms^{-1} noted for an average decrease in void ratio of 0.65 between untreated samples and samples left for 12 months (68 % increase in permeability, with a 38 % decrease in void ratio). The cause of an increase in permeability with an overall decrease in the void ratio is a factor that needs to be explored, with small changes in permeability having a large impact on consolidation (Pane et al., 1983) due to the fact that increasing permeability allows for easier dissipation of excess pore pressures (Mesri & Rokhsar, 1974), a beneficial behaviour for our sensitive clays.

Permeability in clays is expected to be lower than in other soils, even in those clays with larger void ratios. The reduction in permeability may be linked to the smaller particle size of the clays and subsequent reduction in the size of flow channels between pores (interpore space) as well as an increase in tortuosity of flow paths (distance, change of direction of water within the soil) (Mesri & Olson, 1971). Other controls on permeability in clays are often linked to mechanical variables (clay particle size, shape, arrangement, surface area) and physiochemical variables (polarity of fluid, valency of adsorbed cations). The introduction of potassium acetate into the clay certainly impacts the physiochemical aspects of the clay and may, in some way, affect mechanical variables.

For the latter, while the halloysite particle shape will be unaffected, in the short term, the presence of K-acetate will affect particle size. However, this may not necessarily be explained by grain size analysis alone.

7.2 Particle Density and Grain Size

Soil from this study showed a reasonably high clay fraction (25.4 %), though it is dominated by the silt fraction (70.1 %) with a small amount of sand present within the soil (4.5 %). Compared to previous studies on Tauranga-sensitive soils, this soil had much lower clay content than those presented by Mills (2016) but was kept within the high silt proportions found by Wyatt (2009) and Cunningham (2012).

Particle density is the term attributed to the density of solid particles collectively, a summary of the grain density of the individual particles within a soil. In some instances, particle density is referred to as specific gravity, where the ratio of particle density to water at 4ºC is given, thus providing specific gravity as a unitless value (Flint & Flint, 2002). Particle density ranges for soils are usually between 2000 – 3000 kg m^{-3}. Particle densities usually are influenced by the makeup of minerals present within the soils, with examples (not including clays) including feldspars (2500 – 2800 kg m^{-3}), micas(2700 – 3300 kg m^{-3}) and apatite (3100 – 3300 kg m^{-3}) (Blake, 2008; Haynes, 2016).

Particle densities from this study were noticeably high, with untreated soil found to be in excess of 3000 kg m^{-3} (Table 6.1), with a particle density of 3300 kg m^{-3} recorded. Treatment of the soil reduced the particle density noticeably to between 2800 – 2900 kg m^{-3} (13 % decrease) but placed it on the upper end of the expected range for clays. Compared to previous studies on Tauranga extra-sensitive soils, densities for this study were significantly higher, with previous studies showing soils to sit within 2300 – 2600 kg m^{-3} (Wyatt, 2009; Cunningham, 2012; Mills, 2016). The highest recorded of these, sitting at 2777 kg m^{-3}, was observed by Mills (2016) for soil tested from the Matua peninsula in Tauranga. Higher particle densities, of the 'upper' range (>2700 kg m^{-3}) have been observed in New Zealand sensitive materials (Jacquet, 1990), while internationally reports of 2730 – 2840 kg m^{-3} for Indonesian latsol and andosols dominated by halloysite have been recorded (Wesley, 1973). Jacquet (1990) attributed a greater concentration of heavy iron minerals in the sand fraction to the elevated particle densities. However, it must be noted that the material tested by Jacquet did not exceed densities of 2900 kg m^{-3}.

7.3 Atterberg Limits

Atterberg limits of the soil showed properties typically observed in volcanic ash-derived soils rich in halloysite, i.e. relatively high liquid and plastic limits, as well as low activity with high natural moisture content, plotting well below the Casagrande A-line.

7.3.1 Liquid and Plastic Limits and Indexes

Treatment of the soils showed a clear increase in the liquid limit (57 – ~63) and an increase in the soil working range (plasticity index). R^2 values showed good correlativity throughout the data, with R^2 generally being more than 0.95. Overall, most Atterberg limits for the soil treated for 18 months remained almost identical to those measured after initial treatment, with the only difference being the liquidity index.

With the introduction of treatment to the soil, the LI is noticeably reduced, with initial treatments showing a drop in the LI on average of around 0.68 following treatment. It is important to note that the liquidity index is a ratio of natural water content to the soil's liquid limit. Where LI exceeds one (i.e. natural water content of soil is higher than liquid limit), soil sensitivity is likely to be present (Bjerrum, 1954). The soil immersed and treated for 18 months, while not showing a noticeable change in liquid limit or plastic limit, showed a drastic reduction in LI, with a drop to 0.57, below the LI threshold for sensitive soils (LI = 1.1) (Larsson & Åhnberg, 2003). This was achieved through a drop in the initial moisture content of the soil following treatment while maintaining higher liquid limits for the soil. Initial moisture content dropped from 68 % for the natural, untreated soil to 55 % for the 18-month core.

This drop in moisture content is likely related to the drop in porosity and void ratio of treated cores, resulting in less water being able to occupy the available pore space. While there is the potential that less overall water will be able to occupy the soil due to the presence of precipitated salt within the pores, all weight measurements account for the presence of salt within the soil. As such, values represent the soil's 'pure' water content. (Rankka et al., 2004; Andersson-Sköld et al., 2005).

Liquid Limit Variation Source

While the reduction in LL required a longer period, changes in liquid limit occurred relatively rapidly within the first few hours of treatment. This rapid action is likely due to two key interactions between K^+ within the soil and the clay particles. Liquid limits of soils are controlled by a balance of interparticle forces, Diffuse Double-Layer (DDL)

thickness and their relation to the dielectric constant of the pore fluid, with one of these aspects generally overriding the other. Typically, as the dielectric constants increase, interparticle resistances decrease, causing a decrease in liquid limit and, thus, in contrast to this as the DDL decreases, the liquid limit increases (Sridharan & Rao, 1975a).

As K-acetate has been used at 2 mol L^{-1}, K^{+} will be present. As such, the DDL should be heavily suppressed, potentially resulting in a single layer of ions on the clay surface (Appelo & Postma, 2005). It should be noted, though, that while the DDL is inferred to reduce significantly following the introduction of treatment, interparticle shearing forces should increase, resulting in the potential for an increase in the liquid limit. While most major research into these controls has been conducted on soils regarded as the 'extremes' (i.e. kaolinite vs bentonite/montmorillonite), general observations suggest that for kaolin group minerals, due to the larger sizes of the clay particles themselves, interparticle shear forces are the largest controls on liquid limit (Sridharan & Rao, 1975; Sridharan et al., 1988; Widjaja & Setianto, 2019).

Thus, the increase in liquid limit, which is affected by a potential reduction in the dielectric constant from the K-acetate, is likely related to this increase in interparticle friction. The slight drop in liquid limit at 4 molL^{-1} is also documented within kaolinite, with increasing concentrations of metal solutes relating to a negative response in liquid limits (Schmitz & Van Paassen, 2003). The rapidity of the influence of K-acetate following introduction into the soil is likely related to the almost instantaneous rate of exchange of ions within the clay surfaces observed with kaolin group clays (Mitchell et al., 2005).

7.3.2 Comparisons of LI to other Tauranga Extra Sensitives

High field sensitivities often place soils from the Tauranga region in the extra-sensitive range. While some sensitivities reported in literature place them well within the 'quick' range, most notably Smalley et al. (1980) for the Bramley Drive landslide (St = 140), and others ranging between St = 40 – 60 (Wyatt 2009, Gulliver & Houghton 1980), most Tauranga extra sensitive soils did not meet the criteria to be defined as quick (i.e remoulded shear strength < 0.5 kPa).

To address this discrepancy, Wyatt (2009) utilised a novel method to determine the adapted sensitivity of soil, resulting in significantly higher sensitivity values than those derived from conventional direct shear vanes. Variations of 1 – 32 kPa were noted when

compared to conventional techniques. Throughout literature, numerous relationships exist utilising fall cone data to establish the link between remoulded shear strength in the soil to soil liquid index. two key of these are derived from Lerouil et al. (1983) and Locat and Demers (1988) shown as Equations 7.4 and 7.5 below respectively along with the valid working ranges. Note that LI has replaced the original notation of $I_L$in these equations.

$$c_{ur} = \frac{1}{(LI - 0.21)^2}\ (kPa)\ 0.5 < LI < 2.5 \tag{7.4}$$

$$c_{ur} = (\frac{1.167}{LI})^{2.44}\ (kPa) 1.5 > LI > 6.0 \tag{7.5}$$

When applying these equations to this study's soils, significant discrepancies appear between the actual recorded field values derived from *in situ* shear vanes and predicted values for remoulded shear strength. For the soil of this study, expected remoulded shear strengths are predicted to be 0.3 and 0.35 kPa, respectively (field measured = 5kPa). Consequently, this directly impacts sensitivity, with sensitivity plotting, when considering these predicted values, in excess of 150 in both cases. Based on correlations established by Kenney (1977), Mills (2016) plotted data on Tauranga's extra-sensitive material to observe where the New Zealand soil plot compared to Canadian varved and Norwegian quick clays. Mills determined a very weak correlation (R^2=0.24). A recreation of this can be observed in Figure 7.5 (this study's data included). No correlation appears to exist between liquidity and sensitivity (shown as log sensitivity) with R^2=0.0003, with most samples falling well outside the predicted range of LI to sensitivity. With this said, some determined values do fall within the expected range for Norwegian quick clays, with two samples measured by Arthurs (2010) and one by Mills (2016) falling within expected ranges; these were samples from Ōmokoroa (St=22.6, LI=1.45) and Pahoia (St=41, LI=1.45) (Arthurs, 2010), as well as Mills (2016) Om1 sample. Some key features of the figure are the y-axis using a log (base 2) axis and the constraining dashed lines indicative of ‘expected’ ranges for soils based on Northern hemispheric data as derived by Kenney (1977).

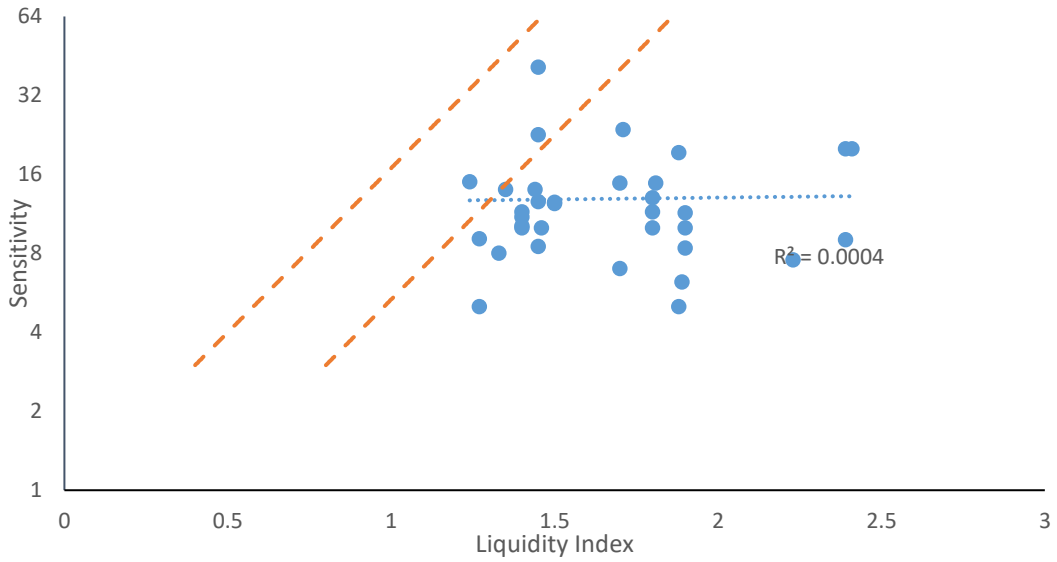

Figure 7.5. Samples of the Tauranga extra sensitive group plotted on an scatter plot adapted from Kenney (1977), with typical ranges expected for extra-sensitive to quick soils (for Scandinavian and Canadian clays) is shown by the dashed orange lines. Few data points appear to fall within this range. When plotting a correlation of sensitivity to liquidity index, no correlation appears going against expectations that, an increasing sensitivity should coincide with an increasing liquidity index.

The significant variation in expected remoulded shear strength from literature expectations and deviation from the ranges specified by Kenney (1977) for sensitive clays are a noticeable concern. The equations above suggest that remoulded shear strengths derived in the field significantly over-predict strength compared to actual ones. In that case, this suggests a potential fundamental issue that needs to be addressed in New Zealand. The causes and variances do pose an interesting question of where the root cause may lie. Two possible cases here may exist. The first option is that the empirical equation presented by Kenney (1977), while appropriate for northern hemispheric soils, is not appropriate for applying to New Zealand extra sensitive soils. This would suggest that New Zealand soils are completely out of step with those in the Northern Hemisphere and act in a unique manner that is not observed anywhere across the globe. This seems unlikely, especially with halloysite-rich Japanese volcanic soils plotting appropriately within the range (Kameda & Morisaki, 2022). The second points to a systemic issue in how remoulded shear strength is calculated in New Zealand. To which I would suggest the latter. When plotting Wyatts adapted remoulded data, an exponential equation is present with an R^2 of 0.98 (when plotting remoulded shear strength against liquidity index) (Figure 7.6).

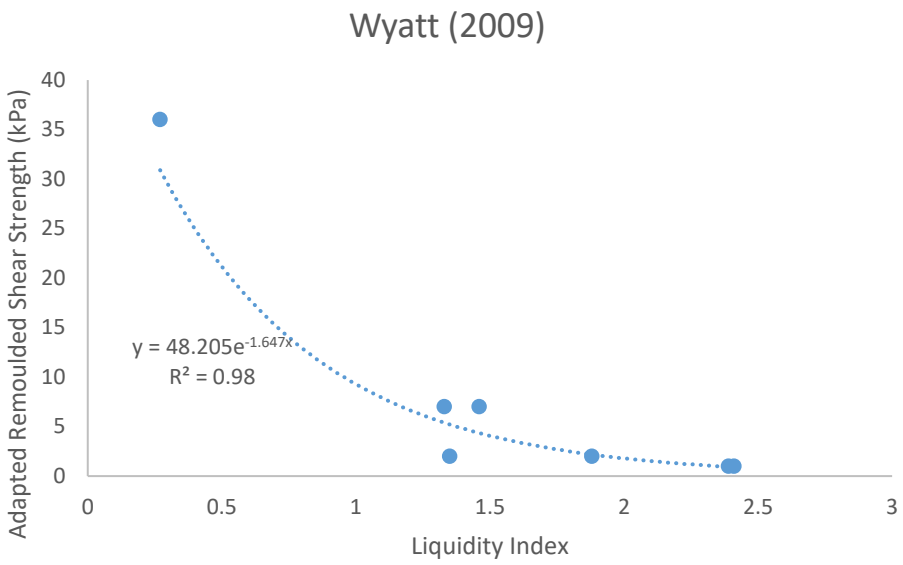

Figure 7.6. Data from Wyatt (2009)'s adapted remoulded shear strength calculations plotted against liquidity index. An exponential regression is applied (as per Leroueil et al. (1985)) to observe whether a more consistent data set is produced. The exponential regression appears to show an incredibly strong correltaion (R^2=0.98) suggesting potential room for further investigation.

When this remoulded exponential is subsequently applied to determine the New Zealand soils remoulded shear strength shown in Figure 7.7a, the original Kenney 1977 plot, as well as a comparison for both (Figure 7.7b), we can see quite the shift in the data, with a large number of data points now plotting within the expected range, and outliers to the data being much closer to the expected range than previous. While not perfect, it provides a good initial indication that the method by which remoulded shear strength is determined in New Zealand may not be appropriate when dealing with sensitive soils.

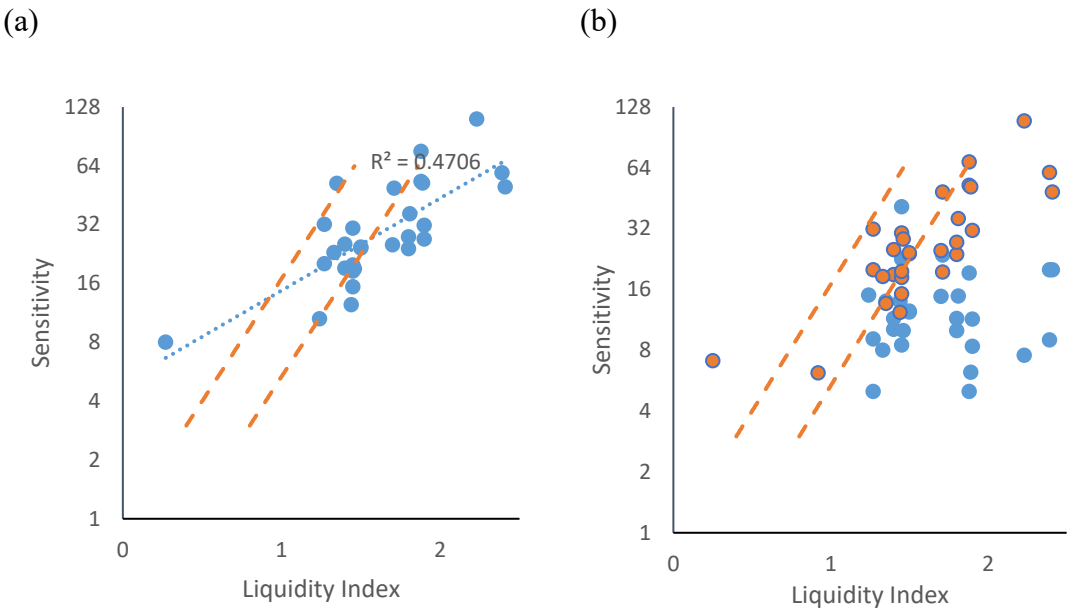

Figure 7.7. (a)Data from the Tauranga extra sensitives with the sensitivity recalculated using the exponential regression equation derived from Wyatt (2009)'s adapted remoulded shear strength calculations plotted onto the Kenney (1977) comparison. What can be found is a drastic increase in correlation with the data showing a loose correlation now between Liquidity index and sensitivity, with a significant increase in the number of data points falling within the expected range. (b) The data from (a) shown as orange with a blue outline plotted with the original values (blue) for sensitivity of the same soils. Illustrating the stark change in soils position following application of the new adapted remoulded shear strength equation.

If we then apply the predictive shear strength equations above to the treated soil, we can get a further indication of potential strength increases in the soil. While these strength indicators do not give insight as to the potential undisturbed strength increases, which are pivotal in preventing failure, they do indicate remoulded shear strength and, thus, the possible behaviour of failed material. It is worth applying a further predictive strength equation in this instance, taken from Wood (1990), where remoulded shear strength is calculated as a value from the resistance to a standard fall cone as a function of the penetration into a sample (Equation 7.6).

$$S_{ur} = k_{\alpha} \frac{(mg)}{d^2} \qquad (7.6)$$

Where k_{α} is a constant based on the angle and weight of the drop cone used, m is mass of the cone, g acceleration due to gravity and d the penetration of the cone into a soil. Wood's

(1990) equation looks at the amount of penetration for a soil remoulded at the natural water content.

For short-term treatment of the soil, shifts in strength have occurred (Table 7.1) with a S_{ur} value of 1.34 and 1.18 kPa derived when plotting in values against Wood (1990) and Lerouil et al. (1983) equations. Locat and Demers strength prediction was not used as I_L for treated samples was below 1.5. A discrepancy emerges here, with Wood (1990) showing a higher shear strength than Lerouil's equation. Still, both show drastic increases over the values calculated for the untreated soil (0.62 kPa and 0.44 kPa, respectively), showing a roughly similar increase in strength (0.72 kPa and 0.74 kPa, respectively) across the two calculations, a positive indication overall. For longer-term strength increases, much larger strength increases are observed (4.42 kPa and 7.72 kPa, respectively). The difference between the two equations does increase, with Lerouil's equation potentially overpredicting shear strength at the lower liquid limit (I_L=0.57). Still, the significant increase in strength across both shows positive signs of a much stronger remoulded soil following treatment.

Table 7.1. A summary table of predicted remoulded shear strengths when applying the equations derived for determining remoulded shear strength from Wood (1990) nd Lerouil et al. (1983), as well as the changes for treated soils respective to the calculated remoulded shear strengths for untreated soil.

Samples	Remoulded Prediction (Wood) (kPa)	Remoulded Prediction (Leroueil) (kPa)	Change in strength respective to Untreated (kPa)
Untreated	0.62	0.44	
Two $molL^{-1}$ (Initial)	1.34	1.18	0.72, 0.74
2 $molL^{-1}$(18 months)	4.42	7.72	3.8,7.28

7.3.3 A-Line Chart Plotting

Soils from this study plotted below the A-line on the Casagrande plasticity chart, placing the soil as a silt of high plasticity (MH), with treatments having the main effect of shifting the soil closer to the A-line but still plotting it below the A-line. Compared to other soils of the Tauranga extra sensitive nature (Figure 7.8), almost all soils plot below the A-line, with two exceptions observed from Arthurs (2010), where one sample plotted slightly above the A-line and one directly on the A-line. This fits with general expectations of volcanic ash-derived soils, with high liquid limits and plastic limits, low activity, high natural moisture content, and plotting below the A-line even while containing relatively sizeable clay fractions.

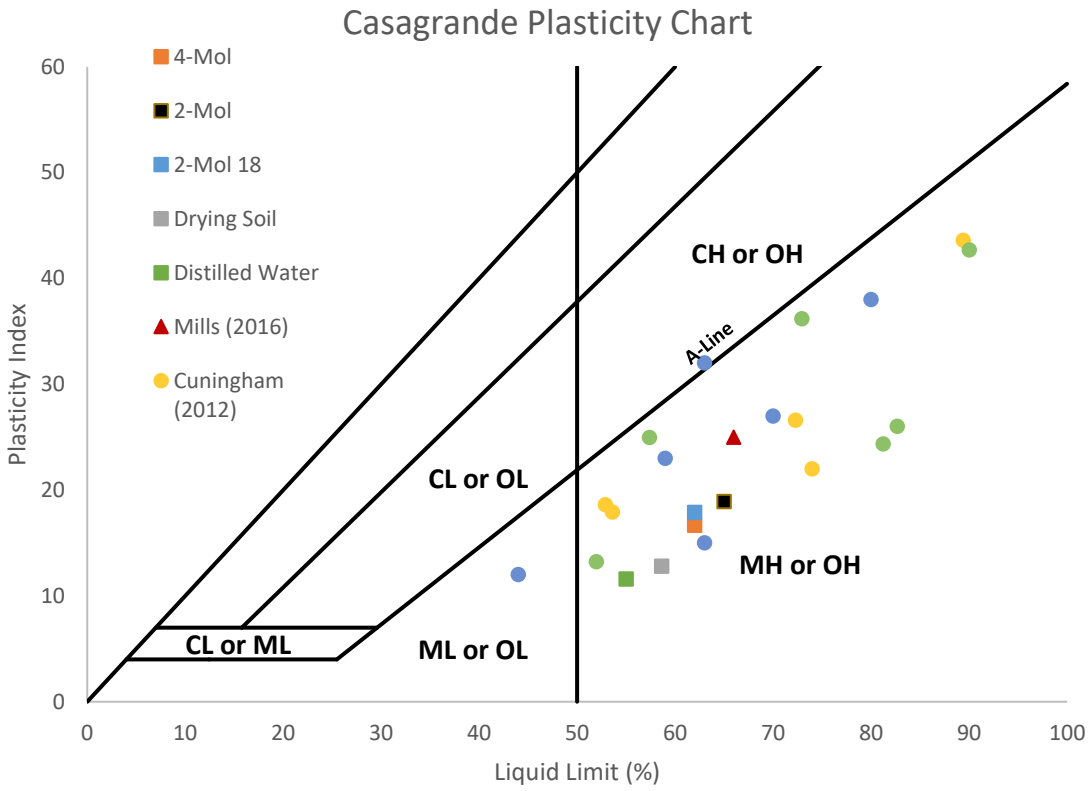

Figure 7.8. Casagrande plasticity chart with data from this study, as well as values from other Tauranga extra sensitive soils. Note nearly all samples plot as MH, with two exceptions from Arthurs (2010).

Over time, several improvements to soil classification have been made, with multiple soil classification systems developed and produced since Casagrande's first plasticity charts. Key reviews of these systems have shown that, while Casagrande's 1947 plasticity chart certainly has its uses, more suitable classification systems have subsequently been developed. An example of this is the Moreno-Maroto and Alonso-Azcarate charts (Figure 7.9) (henceforth referred to as the MM-AA system), the most suitable (Moreno-Maroto et al., 2021).

The MM-AA system applies an objective criterion on quantitative soil properties while allowing for correlation to conventional testing methods for plotting soil properties. This MM-AA system allows for the classification of soils that exhibit 'intermediate' characteristics, defined as such due to a high proportion of silt and sand compared to the clay fraction of the soil as well as potentially low activity from the clay minerals present (Moreno-Maroto & Alonso-Azcárate, 2018). When plotting the data previously plotted on the Casagrande chart, there is far less consistency in classification. Half the data

plotted above the M-line, suggesting soil with intermediate characteristics, a third sitting comfortably below the M-line acting more as a silt of high compressibility, and an increase of 3 samples now classified as clays of high compressibility. While this plot fits with the general trend observed across halloysite dominated clays of plotting below the A-line as generally high compressibility silts, it also shows that for half of those soils, in a remoulded state, they act more as an intermediate soil as opposed to a silt.

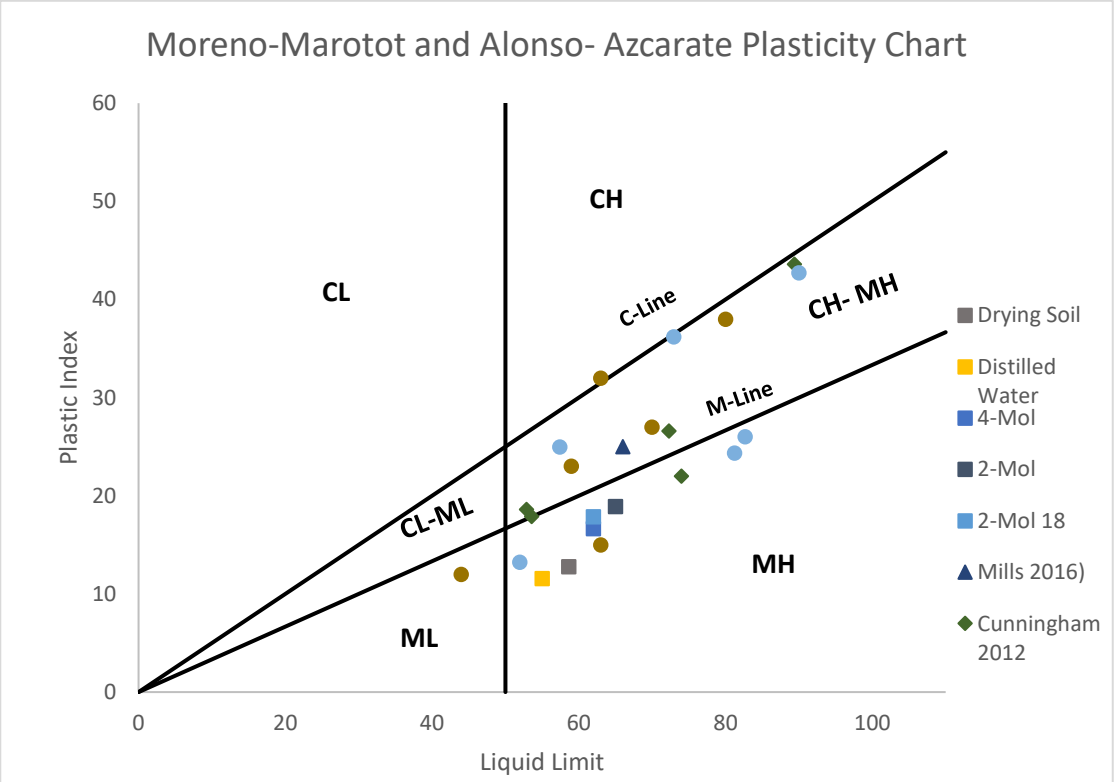

Figure 7.9. Atterberg data from this study, as well as other Tauranga extra sensitives plotted onto the Moreno-Marotot and Alsonso-Azcarate plasticity chart. The inclusion of an intermediate classification (CH-MH), has resulted in a number of re-classifications of soils from MH to CH-MH.

7.3.4 Liquid Limit / Plastic Index Ratio to Sensitivity

One method of 'predicting' a soil's potential sensitivity is its comparison to the LL/PI ratio (Spagnoli & Feinendegen, 2017). While across all data sets, no clear correlation seems to exist between the soil classification (LL/PI) and sensitivity (Figure 7.10), in contradiction to published literature, a reasonably strong correlation ($R^2 = 0.83$) appears to exist for classification versus sensitivity for soils utilising the 'adapted' sensitivity from Wyatt's (2009) research on extra sensitive Tauranga material.

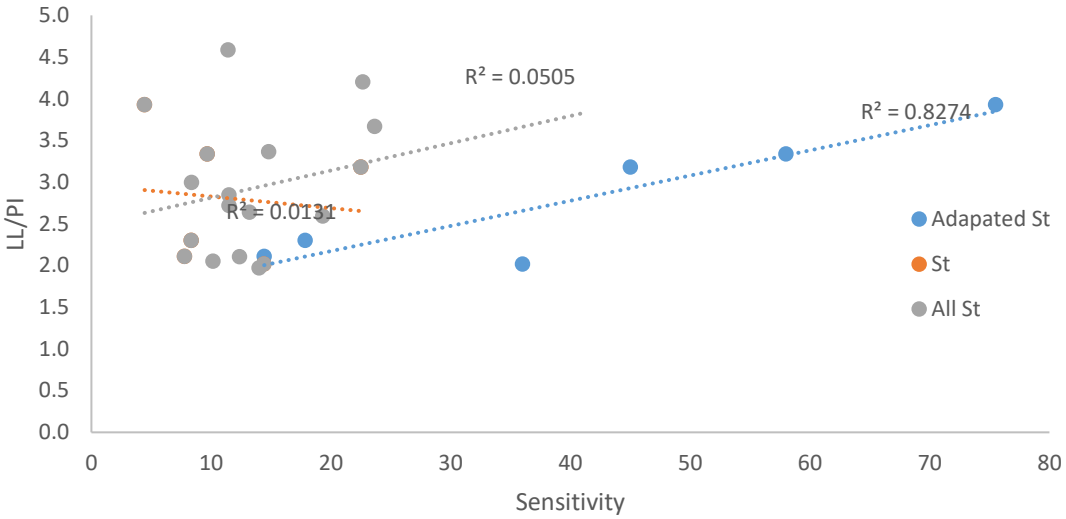

Figure 7.10. Soils from this study (orange), other Tauranga extra sensitives, and values derived from Wyatt's (2009) adapted sensitivity plotted as the liquid limit/plastic index ratio against sensitivity. General expectations from literature (Spagnoli and Feinendegen, 2017) are that LL/PI and sensitivity are directly correlated.

With this said, a noticeable outlier does appear to exist for Wyatt's data. This variation could be related to two key factors. One is discrepancies in the LL/PI ratio, with variations in PL due to differing methodologies, variations in techniques and user error. This error is observed throughout the literature, with variations of PL measuring between 8 – 12% (Sherwood, 1970; Sherwood & Ryley, 1970; Sivakumar et al., 2009; O'Kelly et al., 2018). Shifts of 8 – 12% in PL would significantly impact both the PI and LI, resulting in a possible shift in classification both on the MM-AA plasticity chart and similarly on plotted correlations.

The second is potential problems with the sensitivity calculation, highlighted by Figure 7.10 with a strong R^2 (0.83) for adapted sensitivity, while sensitivity determined from conventional hand shear vane produced an R^2 of 0.01. Similarly, it is well established in the literature that sensitivity and liquid index are directly related (Bjerrum, 1954, 1955; Wood, 1990), with soils generally plotting in a clear, relatively strongly correlated fashion. For soils from the Tauranga region, this correlation is not present. Issues around the calculation of sensitivity determined from various methods have been highlighted in research on Japanese clays, with certain authors finding significant variations in sensitivity across different methodologies (Tanaka et al., 2012), and these issues are evident for Tauranga extra-sensitive soils. While not necessarily directly related to the aims of this study, these issues are important to highlight as, if the methodology used in this research is to be applied in the field; it is targeted for application to extra-sensitive

soils. What has been observed here is an inadequacy in the current methodologies outlined in the NZGS field handbook and guidelines for best practice in identifying extra sensitive soils, meaning areas that contain soils that may have a significant impact on the environment through triggering landslides are unidentified due to over-estimations in remoulded strength.

7.4 Triaxials

7.4.1 Strength Characteristics

Triaxial test results showed strong consistency at all confining stresses, with peak deviator stress increasing with increasing length of treatment. For untreated soil, values plot within the ranges expected for Tauranga extra-sensitive soils derived from previous studies (Wyatt, 2009; Arthurs, 2010; Cunningham, 2012; Mills, 2016). The high friction angle and low cohesions similarly display consistency with the ranges observed in previous studies. The higher friction angle also fits well with trends stated by Wesley (2010), with soils with higher friction angles plotting below the A-line in a typical Casagrande plasticity chart and further fits with indications from Tauranga-sensitive soils as specified by (Moon, 2016)

The impact of treatment on the soil is evident, with a significant increase in peak deviator stress observed across the length of the soil treatment, with an average increase of 65 kPa across the 12 months at the three confining pressures noted. This is related to an average increase of 47 % in peak deviator stress, a 66 % increase at 120 kPa, 43 % at 160 kPa and a 31 % increase at 200 kPa. However, this drastic increase in strength was not followed by a clear trend in strain at failure, with failure occurring slightly earlier for 120 and 160 kPa samples but around 0.6 % later after 12 months at 200 kPa.

This shift in strength change is similarly reflected in changes to the effective cohesion and effective internal friction angle determined from results, with a drastic increase (36.7 kPa) in cohesion over the 12 months of treatment and a 4.51^{o} decrease in internal friction angle. The drastic shift over the 12 months indicates a starkly different shift in failure style within the soil. The change favouring a high cohesion over friction angle suggests a shift in soil behaviour, with the soil initially acting predominantly as a silt under shear to one acting as a normally consolidated clay (Waltham, 2009). The behavioural shift suggests that apparent strength within the soil is, following treatment, favoured towards

the clay fraction, with the high level of cohesion likely influencing the higher peak deviatoric stress recorded.

This increase, at a clay level, indicates a noticeable increase in the intraparticle attraction of clay particles. The potential increase in attraction within the clay fraction particles is likely related to the charging and potential de-protonation of the clay surface. This results in negative charging of the clay surface and a subsequent increase in soil pH following treatment. While northern hemispheric clays from Scandinavia have shown increases in shear strength following treatment with potassium salts, the dominant clay fractions in these studies are often illite and smectite, with an increase in edge–face interactions allowing for significant increases in strength within the soil as a result (Helle et al., 2017). Halloysitic-rich soils of the Tauranga extra-sensitive group are unlikely to follow similar behaviours to those of the northern hemisphere due to the differing clay morphology, with sensitive halloysite materials often exhibiting a dominance of spheroidal and 'mushroom cap' morphology (Moon, 2016; Kluger et al., 2017, 2022). Ultimately, the cause of this strength increase is likely to be better explained following further investigation into changes to the clay chemistry (Chapters 8-13).

7.4.2 Pore Pressure Changes

Pore pressure generation showed an increase in excess pore pressures generated at failure over 12 months for the lower (120 kPa and 160 kPa) confining pressures, with increases of 4.8 kPa (12.7 %) and 11.7 kPa (13.3%), respectively. A drop in pore pressure was observed at the highest confining stress, with a 6.3 kPa (4.8 %) reduction across the 12 months. At the highest confining pressure, though, pore pressure at 12 months was higher than the previous treated months. One metric that can be utilised with excess pore pressures is the Skemptons A-bar value (Ā). Ā is a useful metric, the pore pressure coefficient of pore pressure to deviator stress, where if Ā exceeds 0.75, it can indicate high soil sensitivity (Skempton, 1954; Head, 1998). Compared to overseas soil values, Tauranga extra-sensitive soils report Ā values around 1.09 (Wyatt, 2009), while some overseas glaciomarine quick clays often report Ā values two and up. Values of Ā are detailed in Table 7.2

.

Table 7.2. A summary table showing Ā at failure for both untreated and treated samples at their respective confining pressures. Note no soil exhibits an Ā greater than 0.75, the marker value of indicating high soil sensitivity.

	120 kPa	160 kPa	200 kPa
Untreated	0.42	0.59	0.70
1 Month	0.36	0.43	0.52
3 Month	0.37	0.46	0.53
6 Month	0.33	0.43	0.51
12 Month	0.28	0.42	0.51

A noticeable reduction in Ā at failure is noted following the soil treatment, with almost all reductions occurring within the first month. With this said, for untreated soil, Ā values at failure indicate that soil, at least at failure, is not acting in a highly sensitive manner. The highest Ā exhibited is 0.7, below the 0.75 value expected for sensitive soils.

When looking at the pre-failure behaviour of the soil, though a different story begins to emerge. Figure 7.11 show the Ā path during shear. At the lowest confining pressure, relatively similar behaviour is exhibited, with all samples showing a relatively rapid rise in Ā before dropping off.

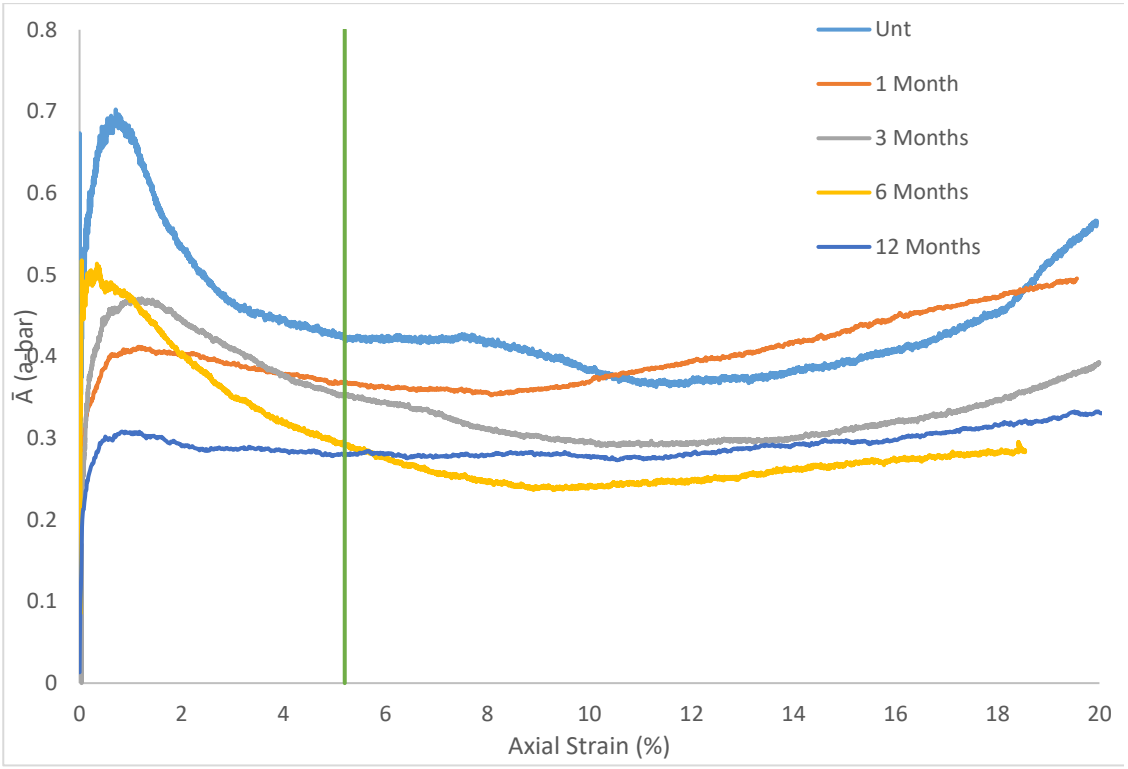

Figure 7.11. Ā paths for soils under shear at 120 kPa confining stress. No samples show an Ā in excess of 0.75 at any point during the stress path. It is worth noting Ā increases as the soils strain soften following failure. The solid green vertical line represents the average axial strain at failure across all samples.

At 160 and 200 kPa confining stresses (Figure 7.12), though, treated samples all exhibited consistent Ā behaviour, with samples showing a gradual increase in Ā up to failure, with the bulk of deviance across samples occurring in the post-failure strain softening phase from ~10 % axial strain and onwards.

(a) (b)

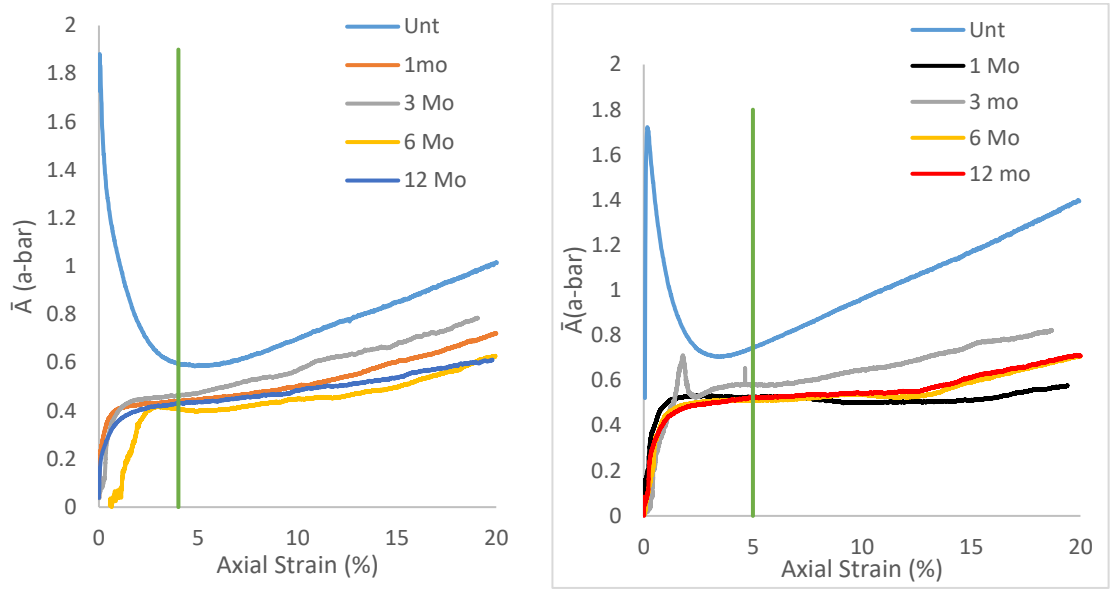

Figure 7.12(a) the Ā paths for soils sheared at 160 kPa confining pressure. Untreated soil shows a drastically different pre-failure behaviour when compared to treated soils, with a peak Ā of 1.89 recorded. The solid green vertical line represents the average axial strain at failure across all samples. (b) Ā paths for soils sheared at 200 kPa confining stress. A peak of 1.72 Ā was recorded for untreated, while untreated samples showed distinctly differing behaviour. The solid green vertical line represents the average axial strain at failure across all samples.

Untreated samples, on the other hand, exhibit large variance in Ā leading up to failure, with peak Ā's recorded of 1.89 and 1.72, respectively, before dropping to the values recorded in Table 7.3 at failure. While Ā at failure does not suggest high sensitivity in the soil, as laid out by Head (1998), the rapid generation of excess pore pressures compared to deviator stresses upon initial loading with high Ā may suggest otherwise. This rapid pore pressure generation in the early loading stages is similarly reflected in the PQ plots, with soils showing a high degree of contraction upon initial loading. The drop in pore pressures before failure is not entirely unexpected, with previous studies in some clays noting a similar Ā drop before failure, relating it to changes in volumetric strain as a result (Holt et al., 2018).

When compared to Ā values for other Tauranga extra-sensitive soils (Table 7.3), all but one tested series of samples from Wyatt (2009) are below the 0.75 marker value for a high sensitivity response from the soils at failure, with the one sample exhibiting an excess of 0.75 recording the second highest normal and adapted sensitivity.

Table 7.3. A summary table with Ā values for soils from this study as well as others derived from various Tauranga extra sensitive soils. All but one sample did not show an Ā value at failure in excess of 0.75. In fact the sample that did show an excess of 0.75 (Wyatt (2009) TS1), had a measured sensitivity of only 9.

	Ā at failure	**Sensitivity**
Untreated (This Study)	0.57	11.4
Mills (2016) Om1b	0.65	13.2
Mills (2016) M1	0.58	10
Wyatt (2009) TS1	0.86	9 (59)
Wyatt (2009) TS3	0.48	5 (76)
Wyatt (2009) OS1	0.43	8 (23)
Wyatt (2009) OS2	0.38	10 (19)
Wyatt (2009) OS3	0.06	6 (8)
Wyatt (2009) OS4	0.40	14 (52)

Based on sensitivities of the soil from this study determined both in the field, as well as the remoulded shear strength derived from Wood (1990), it would be expected that Ā be more than 0.75 at the point of failure as the soil presents as sensitive in all other facets, yet this is not reflected at failure. On the other hand, a sensitive response is noted in the pre and post-failure stages.

Skempton (1958) provides another derivation to evaluate the pore pressure response and whether the pore pressure response is reliant solely on the mean principle stress or the pure shear stress represented by the signifier A (Equation 7.7) Note in this instance Δu also represents the signifier A. Skempton (1958) states that where A=1/3, pore pressure depends solely on mean principal stress. In contrast, if A≠1/3, pore pressure is markedly influenced by pure shear stress in the case of a material behaving in accordance with elastic theory. This is taken with the expectation that B=1 following saturation and consolidation of a sample during the triaxial shear process.

$$\Delta u = B\left[\frac{1}{3}(\Delta\sigma_1 + 2\Delta\sigma_3) + \frac{3A-1}{3}(\Delta\sigma_1 - \Delta\sigma_3)\right] \qquad (7.7)$$

More recent authors have refined the equation to look at the coefficient A with reference to Δp’ and Δq and soil stress states (Wei et al., 2022) (Equation 7.8).

$$A = \frac{1}{3} - \frac{\Delta p'}{\Delta q} \tag{7.8}$$

When applied to untreated soil from this study, A ends up, on average, as A=-0.68, suggesting, based on Skempton parameters, that shear stress has a marked influence on our system, and the mean principle stress is not solely responsible for pore pressure generation. Similarly, A<1/3 suggests a high degree of contraction at the point of failure for untreated soils. This is reflected within the P Q plots of the soil, where a high degree of contraction is noted throughout. While all samples show contraction during failure, the paths taken differ. Untreated soil exhibits large contraction in the initial strain phase, accompanied by a rapid rise in excess pore pressures and the high Ā values observed before tending more to the right as the soil reaches the critical state line. This rapid generation of pore pressure and rapid contraction may indicate a rapidly forming progressive failure shear band (Thakur et al., 2018), with pore pressure rapidly concentrating in the initial loading phase within the shear band. This shear band may form, and the pressure begins to 'dissipate' respective to the strain, with the stress path tending more to the right. This behaviour is not noted in the treated soil cores, with stress paths progressing straight upwards towards the CSL or tending slightly to the right during the initial shearing phase. This suggests a significant shift in the soil behaviour following treatment.

7.4.3 Sample Core Failure Styles

Sample failure style for untreated soils was dominated by shear wedge failure, creating a distinctive PSZ clear for all samples. PSZ angles ranged between 56 – 63°. For treated samples, shear and intermediate wedge failures dominated until the 200 kPa sample was treated for three months. After this point, failure styles were dominated by barrelling, with some intermediate and shear wedge failures occurring.

For untreated samples, soil cores showed buckling, brittle style failures, with an X-mode failure observed at the 160 kPa mark and an intermediate between the X-mode and two symmetrical plane style failures noted at 225 kPa, though is likely a 'brittle' failure with no clear indication of plastic deformation (Kodaka et al., 2007). When examined in conjunction with excess pore pressure generation and its bias, favouring excess pore pressures to the top of samples is indeed reflected in the failure soil cores. Following treatment, after three months, samples begin to shear in a more plastic manner, with

samples yielding as opposed to shearing more frequently, indicating a shift in failure from brittle style failure to ductile failure following treatment (Li et al., 2022). Similarly, after three months, there is a distinctive shift in excess pore pressure bias, with an initial bias during generation to the base of the sample before shifting to the top of the sample following failure.

Mills (2016) proposed that within the Tauranga extra sensitive soil, during shear, soils will undergo progressive failure. A failure mechanism derived from Scandinavian quick clays, where, upon a change in load or conditions to the soil, the strain begins to localise within the sensitive material, and a distinctive shear band begins to form. Within this shear band, excess pore pressures begin to generate, reducing the effective stress within the shear band and subsequently accelerating the speed at which the soil is likely to reach its residual strength as it is forced down the Mohr coulomb line. Excess pore pressure biases may also be present based on the location of the shear band, with excess pore pressure generally migrating more heavily in one direction as a result (Gylland et al., 2013, 2014; Andresen & Jostad, 2017; Thakur et al., 2018). A progressive failure mechanism appears to be present within the untreated soil of this research, with consistent features of progressive failure noted, with heavy bias in pore pressure generation favouring the upper part of samples, resulting in an internal gradient of excess pore pressures. Shear band orientation (55 – 63^{o}) fits within the ranges observed in other studies due to the lower strain rate applied (Gylland et al., 2013).

Excess pore pressures for untreated samples, as discussed previously, while showing clear bias to the top of the sample, show little in the way of stabilising following failure, other than the 160 kPa sample, which exhibited relative stable bias throughout the sample. For both 120 kPs and 200 kPa samples, growth in excess pressure direction appears to occur after the 10 % axial strain region as the soil begins to enter the pore pressure induced shear zone, with, during this area, shear bands likely growing as the sample begins to undergo significant declines in residual strength as a result of increasing excesses in pore pressure (Thakur et al., 2018).

Treated samples, on the other hand, while exhibiting a shift to more plastic deformation, as well as yielding of soil (barrelling) as opposed to shearing, also exhibit a pressure bias to the base of the sample, as opposed to the top of the sample, likely as a result in the shift in strain localisation being less distinct and clear. Further, excess pore pressure growth following failure, for the three and 6-month samples at least, shows relative stability following soil failure, indicating any shear zones present have fully propagated and the

soil is unlikely to grow shear bands (Yuan et al., 2013). Excess pressures for samples after 12 months seem to deviate from this stability, with growth in the bias noted following the failure of samples. This growth indicates that the strain localised shear surfaces noted for samples at the 160 kPa and 200 kPa samples likely have not finished developing, indicating residual shear stress was far from achieved. However, excess pressures did seemingly bias towards the base of the sample as opposed to the top of the sample.

This shift in behaviour and increase in post-peak residual strength is further made clear by the total percentage of strain softening exhibited by the soil decreasing with the treatment time. With soil at the natural confining stress, there was a decrease of 23 % in strain softening following treatment, which was a huge reduction, especially considering a similar failure style exhibited by the soil core. Reductions of around 5 % were noted for the lower confining pressures, which, while not as high as these, were generally accompanied by a shift in failure style from Shear-wedge brittle failure to plastic barrelling and plastic intermediate wedge failures. Overall, these decreases in strain softening indicate the soil either shows a significantly increased residual or, more likely, a much larger strain range required to achieve a similar residual strength.

Implications of this shift in the behaviour of the soil under strain following treatment, as well as increases in the potential residual, indicate that the K-Acetate treatment may be an effective method of both reducing sensitivity as well as increasing shear strength high enough to successfully stabilise the soil. The positive impact of the treatment can be observed across several different geomechanical aspects, including an increase in the liquid limit of the soil, reduction of liquidity index, increase in peak deviator stress along with increases to cohesion, as well as a shift in shear behaviour under strain from brittle to plastic.

Chapter 8
Part I — Conclusion

The aim of this part (Part I) of this thesis was to examine the various geomechancial characteristics and triaxial parameters for an untreated Pahoia Tephra, as well as a K-Acetate treated Pahoia Tephra. In particular, the primary aim was to see whether a positive response could be elucidated from Pahoia Tephra following treatment over a 12-month time frame. In this instance a positive response is one where the strength of the soil (either as peak deviator stress or effective cohesion) is increased, as well as a producing a reduction in sensitivity (measured in this instance through LI).

For the untreated Pahoia Tephra soil, a number of interesting parameters were observed during testing. Specifically, the soil produced a particle density far higher than those gathered from Tauranga extra-sensitives, as well as a natural moisture content far in excess of the liquid limit (as would be expected for an extra-sensitive soil). It was noted that remoulded shear strengths for the soil, when derived in the lab from fall cone parameters, were lower than those measured in the field by a considerable margin suggesting potential issues with current standard methodology for deriving remoulded shear strength in the field in New Zealand. Similarly, the soils from this study (as well as other extra-sensitives) did not plot within the expected range of sensitivity to LI, further supporting these concerns. On a positive note, though, treatment with K-acetate (over an 18-month period) reduced liquidity index to below one, the marker value for inferring sensitivity within a soil.

In a similar vein, shear strength of the soil was drastically increased following treatment by K-acetate, with an increase in effective cohesion by 36 kPa, with a 47 % increase in peak deviator stress at failure for the soils following treatment. This suggested that on a clay level, the K-acetate is interacting with the halloysite (expected to be present within the sample) and producing an increase in strength. The mechanism of which will be further explored in Part II. In further support of the sensitivity reduction, pore pressure parameters $\bar{A}$ during shear showed a drop overall, in particular with $\bar{A}$ not exceeding 0.75 at any point during the shear path for treated soils, a trait not observed for the untreated soils. This is of particular value due to the expectation of where $\bar{A}<0.75$, there is an expectation of high sensitivity within the soil.

Part II

Clay Chemistry

Chapter 9
Part II — Introduction

This chapter encompasses all the testing undertaken, both in lab and externally, to assist in determining various factors relating to the specific clay chemistry for both untreated and treated Pahoia Tephra samples obtained throughout this research. This part is broken down into this initial introductory chapter, methods, results and the discussion/conclusion. Covered within this chapter are tests ranging from X-ray diffraction analysis to point zero charge analysis. Where possible tests were undertaken internally at the University of Waikato, though some required external sources to provide the data.

Chapter 10

Part II — Methods

10.1 X-Ray Diffraction (XRD) Analysis

XRD analysis was undertaken to provide data on the basal spacing of minerals present within the soil samples of this research. Testing was conducted using a Panalytical Empyrean X-Ray Diffraction machine and was undertaken using the Waikato University XRD Standard Operating Procedure (SOP). Analysis was undertaken using a Cu (Ka) source with a 2θ set from 0° to 80°. A minor variation from conventional testing was employed: bulk samples were smeared directly onto glass plates and tested directly with no extra preparation instead of solely analysing the titrated clay fraction. In addition, the formamide treatment (Churchman et al., 1984) was employed for the clay fraction to assist in distinguishing whether kaolinite or halloysite was present.

10.2 Differential Scanning Calorimetry, Differential Thermal Analysis and Thermogravimetric Analysis (DSC/DTA/TGA)

Thermogravimetric Analysis (TGA), Differential Thermal Analysis (DTA) and Differential Scanning Calorimetry (DSC) were undertaken to determine the response of soils used within this study to continuous heating and examine the decomposition behaviour of the various bonds found within the soils used. Testing was conducted on a Perkin Elmer STA8000 machine. Three potential methods were identified from the literature. These include methods found in Churchman and Theng (1984), Johnson *et al.* (1990) and Cheng *et al*. (2010). Cheng *et al*.'s (2010) approach was discounted as an option due to the requirement for testing in a constant flow (60cm^3/min) of nitrogen, which was incompatible with the Perkin Elmer setup. Johnson *et al*.'s (1990) method was also dismissed due to the narrower testing range (30–700°C), which could potentially result in upper exothermic peaks (885–1000°C) not being achieved. Therefore, it was determined that Churchman and Theng (1984) provided the most appropriate and relevant methodology, especially as this approach was undertaken on soils similar to those from this study(halloysite samples from the upper North Island). Also integrated into the methods used were those laid out by Lowe and Nelson (1983).

Samples were heated in air from 40 to 1100ºC at 10ºC per minute. Prior to testing, samples were dried in an oven at 110ºC for a minimum period of 48 hours, before cooling to room temperature in a humidity-controlled silicon bead desiccator. Values are reported as degrees celsius (ºC) for temperature, millijoules (mJ) for energy release, joules per gram (J/g) for the enthalpy change (delta H) and percentage weight lost (%).

10.3 Fourier Transform Infrared (FTIR) Spectroscopy

Fourier Transform Infrared (FTIR) analysis was undertaken on both untreated and treated soil to explore and examine the various bonds found on the clay particles themselves, as well as explore the bonds that may have formed between the clay and the potassium acetate treatment. Samples were tested using a Perkin Elmer Spectrum 400 FT-IR spectrometer. A number of specifications for methods existin the literature, presenting various resolutions and monitoring lengths. Ultimately, it was decided that a variation of the methods proposed by Frost and Kloprogge (1999), which are based on those of Frost and Kristof (1997), should be used.

Dried clay powder samples were pressed with potassium bromide (KBr) into small discs at a ratio of 9:1 (KBr:Soil) and tested at a resolution of 2 cm^{-1} between 450–4000 cm^{-1}. The testing resolution of 2 cm^{-1} spacing was consistent with the previous methods set out by Frost and Kloprogge (1999) and Frost & Kristof (1997). However, deviations from these studies were employed with the preceding studies having a wider range of 150–4000 cm^{-1}. Samples were run for a minimum of three scans, and the average transmittance was recorded.

10.4 X-Ray Fluorescence (XRF) Analysis

XRF was undertaken to determine the elemental composition of the soils used in this study. Testing was conducted on a Bruker WDXRF S8 Tiger machine. Samples were prepared following UoW's SOP. Prior to XRF being undertaken, Loss On Ignition (LOI) testing was undertaken with samples heated to 1300ºC for five hours, before being cooled in a desiccator for 24 hours prior to weighing. Samples were tested in disc form, with preparation undertaken through mixing and fusion of soil samples with a 12:22 alumina flux and ammonium iodide. Discs were then cooled and tested in the Bruker WDXRF S8 Tiger machine, with the major elements monitored. Settings used were the in-house protocols employed by UoW for clay soils

10.5 Crystallinity Index and Hydration Status

Crystallinity, or the stacking order and internal variability, of clays in this instance were calculated using the data measured during FTIR testing, as per the methodology laid out by Parker (1969). This method looks at the specific ratio of the two reflectance peaks around 3696 cm^{-1} (A) and 3620 cm^{-1} (B), where A/B provides the crystallinity index. While it is possible to calculate crystallinity using the XRD ratio derived from the counts of the 4.4 and 2.4 Å peaks, as per Hughes and Brown (1979), the lack of a consistent clear peak at 2.4 Å meant this was not realistically feasible. The third method utilising the DTA patterns of halloysite, as per Smykatz-Kloss (1974), was also not used in this instance due to the large variation and errors that may occur when applying this method to halloysite as observed by Churchman and Theng (1984).

The hydration status (R_w) of the tested soil was determined using the methodology specified by Churchman and Theng (1984), using the ratio of the 10.1 Å (H_{10}) peak to the 7 Å (H_7) peak observed in the XRD pattern. This is shown in equation 10.1.

$$R_w = \frac{H_{10}}{(H_7 + H_{10})} \tag{10.1}$$

10.6 Cation Exchange Capacity (CEC) and Base Saturation Analysis

Cation Exchange Capacity (CEC), base saturation analysis and major cations testing were undertaken by an IANZ accredited external lab, specifically Hill Laboratories (Hamilton). This was undertaken to examine the changes to the clays themselves following treatment, and to whether remnant ions are present on the soil. Samples were dried at 110ºC for 24 hours, and subsequently crushed in a mortar and pestle to a fine powder before 50 g were separated and sent to Hill Laboratories for analysis, where samples were tested in line with their 'Basic Soil Analysis' accredited testing regimen. This testing included pre-drying the sample in a forced air convection drier at 35ºC, before being passed through a 2 mm sieve (i.e. the <2 mm fine earth fraction was analysed). Major cations for the soil were then determined through a 1 M neutral ammonium acetate extraction, followed by ICP-OES (Inductively Coupled Plasma Optical Emission Spectroscopy) on the subsequent extractant. Detection limits for the cations include 0.01 meq/100 g for potassium (K), 0.04 meq/100 g for magnesium, 0.05 meq/100 g for sodium and 0.5

meq/100 g for calcium. CEC was measured through a summation of the extractable cations and extractable acidity. It should be noted, though, that overestimates of the CEC may occur due to the presence of soluble salts within the soil, which, in the case of the potassium acetate treated soil is expected. Total Base Saturation (BS) was calculated from the extractable cations and CEC of the soil, providing an indication of the total exchange capacity of the soil taken up by cations within the soil. The report from Hill Laboratories reported major cations and CEC in meq/100 g. This is an in-house reference equivalent to meq/100 g or cmol/kg (where 1 meq/100 g = 1 cMol/kg), and thus will be referred to as cmol/kg within this chapter.

10.7 Zeta Potential Analysis

As for the CEC/major cations analysis, zeta potential analysis of the soil was undertaken by an external laboratory, specifically the University of Canterbury, on a Malvern Zetasizer Nano ZS. Samples for zeta potential analysis were made up from both untreated and treated soil samples. This was to examine the zeta potential of the clay particles, and to examine whether treatment has led to any changes of the soil itself. Samples were first dried in a convection oven at 110^{o}C for 24 hours before being crushed in a mortar and pestle to break up the soil aggregates into a fine powder. The powder was then re-dried at 110^{o}C for 24 hours before being cooled for 24 hours in a silica bead desiccator. Following cooling, a small sample of soil was mixed with of de-ionised water. This suspension was then shaken for a minute and placed in a sonic bath for five to ten minutes to allow for the further break up of any aggregates in the suspension. After sonification, samples were then shaken once more before being allowed to settle for one to two minutes. This settling was to ensure the separation of the sand from the silt/clay fraction. Twenty millilitres of suspension from the top of the sample was then decanted, and couriered to the University of Canterbury for anlaysis. Samples were run for 12 runs at a 2 mm measurement position within water dispersant at 25^{o}C. In cases where a ‘good’ result was not obtainable, samples were diluted at a 1:10 and 1:100 dilution where required

10.8 Point Zero Charge (PZC) Analysis

Point Zero Charge (PZC) analysis was undertaken on a BTG Mütek GmbH PCD03. Testing was undertaken to examine the streaming potential of samples, as well as to examine whether treatment of the soil has affected the clay's PZC. Samples were prepared according to the manufacturer’s specifications, with suspensions of dried, powdered soil

prepared with de-ionised water. When placed into the machine and run, samples were left until a stable initial streaming potential value was achieved; this was, on average, around 1 ½ minutes from the start. In deviation from manufacturer specifications, the titrant, in this case a saturated alum solution, was added stepwise via a 0.1 ml digi-pipette, as opposed to a glass pipette, due to the length of time required for potential values to stabilise (2–3 minutes on average). Titrant was added until a potential value of 0 was achieved. Approximately 0.5 g of sample was tested for each sample.

10.9 Pore Volume, Size, and Surface Area Analysis

Surface area, pore size and volume were obtained using a Quantachrome Nova 2000e through nitrogen adsorption. The specific surface area was measured using the Brunauer Emmet Teller (BET) method, using multi-point analysis, along with a Langmuir isotherm using the adsorption data.

Total pore volume and pore size distributions were computed by applying the Barrett-Joyner-Halenda (BJH) method. The micropore range was determined using the Horvath-Kawazoe (HK) method. Pressure ranges for BJH were run between 0.01–0.95 P_o/P, and HK was run at 0.01–0.35 P_o/P. Pre-dried (110°C for 24 hours) crushed clay powders were first run through the Quantachrome degas cycle, with samples degassed to 200 µm Hg, with an evacuation rate of 5mm Hg s^{-1} while the sample was heated to 80°C at a rate of 10°C per minute. The sample was then held at 200 µm Hg pressure and 80°C temperature for a minimum of 8 hours, with a longer evacuation time applied as opposed to high temperatures due to the relatively low decomposition temperature of the halloysite crystal structure.

10.10 Scanning Electron Microscopy (SEM) and Energy Dispersive Spectroscopy (EDS)

Scanning Electron Microscopy (SEM) was undertaken on a Hitchachi Regulus SV 8230 at 5 kV for untreated samples and 3 kV for treated samples. This was undertaken to allow for visual inspection of the clay spheroids, as well as how the spheroids interact with each other. The drop in energy used was due to extensive charging on the clay surface of treated samples at 5 kV. This charging was also present at 3 kV, and a lower charge was attempted, but this was ultimately not used due to loss of image quality on capture. Clay morphology percentages, determined from the three forms of halloysite (spheroid, tubes

and books), were determined via clay counting on bulk images across all treatment times, with a minimum of 100 clay particles counted per image on three individual images.

Images were selected randomly. Morphology counts were then averaged to provide clay morphology percentage. Clay samples were made up from samples dried in an oven at 110^{o}C for 24 hours, crushed in a pestle and mortar until a fine powder was made, re-dried at 110^{o}C for 24 hours, then spread onto a slide and covered with a platinum coating prior to further analysis.

Energy Dispersive Spectroscopy (SEM-EDS) was run at 15 kV through the Hitachi Energy Dispersive Spectroscopy elemental analysis software. Clays within a 5 μm scale area were scanned and the K-series response was obtained and displayed as both graphs and tabulated outputs. This process was repeated on ten differing sites within each slide to provide average elemental compositions. Before analysis, a minimum scanning response value of 8000 counts per second was used. Due to the higher charging voltage and 'zoomed out' nature of the scanning at a 5 μm scale, results produced are qualitative due to the large amount of clay within a respective scanning area.

Chapter 11

Part II — Results

11.1 XRD

11.1.1 Clay Fraction Analysis

Untreated

XRD reflections for untreated soil are displayed in Figure 11.1, with four differing runs undertaken. The first run (red line) was representative of the sample run at ambient (standard room temperature) conditions. This showed a large reflection at 10.1 Å. Less intense but notable reflections were also observed at 4.4 Å and 3.4 Å.

The second run (blue line) for the samples treated with ethylene glycol for 24 hours shows the beginnings of an upshift (expansion) in the sample to 11 Å, though this is a minor peak. Instead, there was a decrease in the overall count at 10.1 Å, with responses falling between the 11–10.1 Å range. The 4.4 Å reflection was maintained, but the 3.4 Å peak appears to be in the process of collapsing following the introduction of ethylene glycol.

The third run (green line) for the samples heated at 110 ºC for four hours shows an upshift in the 10.1 Å with a clear 11 Å peak shown. There is also the evolution of a distinctive 7.2 Å peak not previously present in the ambient and ethylene glycol treatment. The 4.4 Å peak remains, although the 3.4 Å peak has shifted up to 3.6 Å.

The final run (fuchsia) for the sample heated at 550°C shows a complete loss of almost all peaks, with the only changes from baseline being a slight rise at around 4 Å. Outside of this, all peaks have disappeared in their entirety.

The 10.1Å peak found in the ambient soil is typically ascribed to the presence of halloysite within the clay fraction of the soil. This sharp distinctive 10.1Å peak is typical of both New Zealand soils and those sampled within the Pahoia Tephra/Tuff unit (Lowe & Nelson, 1983; Churchman & Theng, 1984; Lowe, 1986; Lowe & Percival, 1993; Joussein et al., 2005, 2006; Wyatt, 2009; Arthurs, 2010; Cunningham, 2012; Cunningham et al., 2016; Churchman et al., 2016). The collapse of this peak to 7.2 Å upon heating to 110°C is also typical of halloysite clays (e.g., Churchman et al., 2016). The complete loss of all peaks at 550°C is a phenomenon explored and explained with the DSC testing.

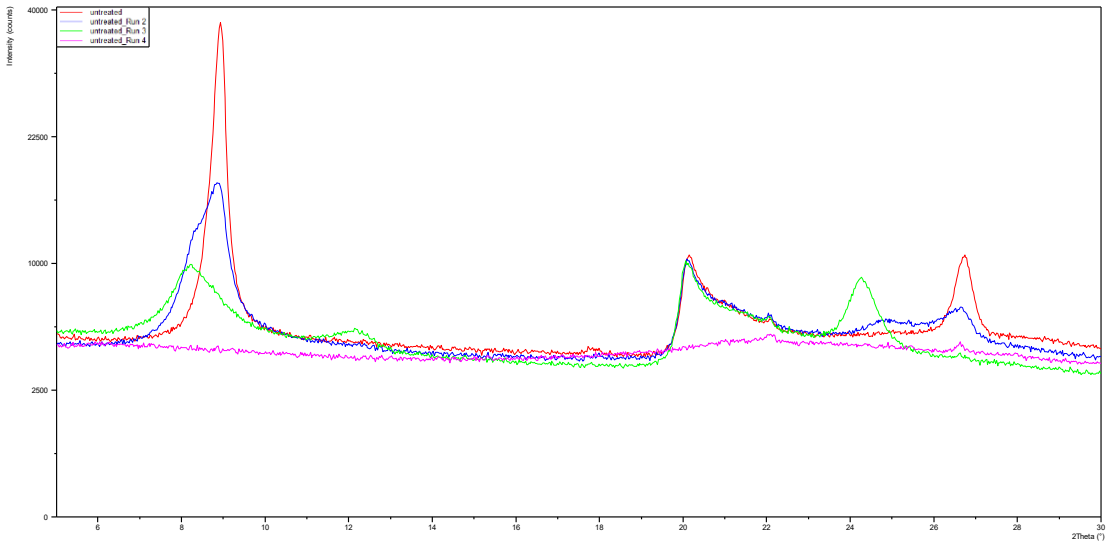

Figure 11.1 An XRD diffractogram showing the peaks for the untreated soil where the following treatments were employed: ambient (red line), ethylene glycol treatment (blue), sample heating to 110°C for 24 hours (green) and sample heating to 550°C for 24 hours (fuchsia).

Figure 11.2 shows the untreated soils tested with formamide to distinguish between kaolinite and 7 Å halloysite. In this instance, the blue 2 theta line represents the natural soil before pre-formamide treatment, while the red line shows the post-formamide treatment of the clay. Although the pre-formamide-treated line shows near identical results to those shown in the ambient run (Figure 11.1), the formamide-treated soil shows good agreement with most peaks. A small dip in intensity at the 10.1 Å is seen, with a small upshift (expansion) to around 10.2 Å as well as a slight upshift in the 3.4 Å peak, but otherwise the two curves are in good agreement, confirming the presence of halloysite within the sample. The general expectation following formamide treatment is a slight increase in the 001 basal spacing peak, with the clay expanding from 10 Å to around 10.2 Å (Joussein, 2007), which is indeed reflected with a 0.15 Å increase noted in the formamide treated soil. Further to this, the showing of an increase in disorder with the 02,11, and 003 peaks, with the sharp, distinctive peaks observed in the initial testing becoming more disordered as the reflections in the 003 peak undergo a slight increase in basal spacing, confirms the presence of halloysite.

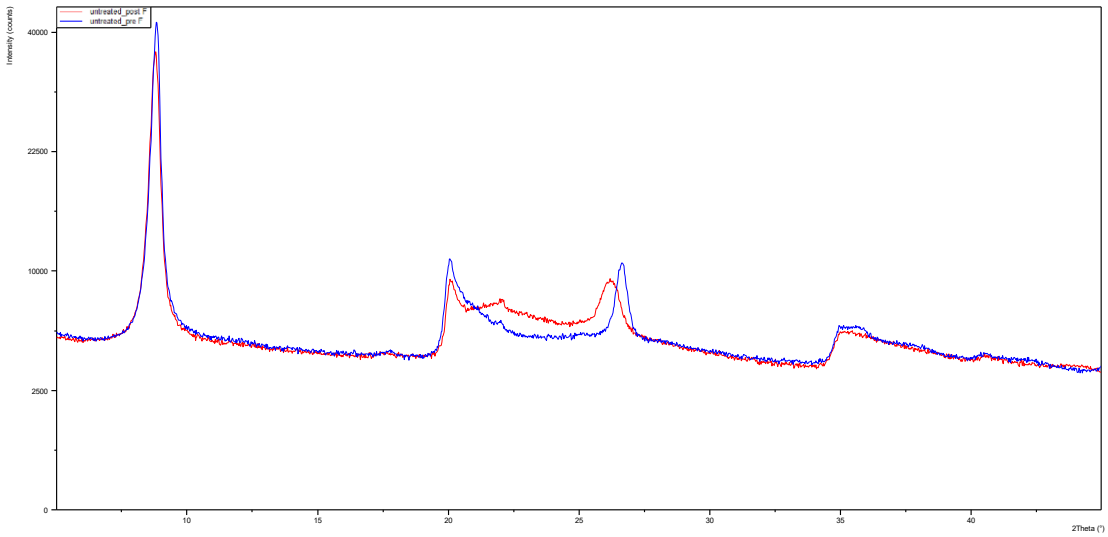

Figure 11.2. An XRD diffractogram showing peaks for the untreated soil prior to formamide treatment (blue line) and after formamide treatment (red line).

1 Month Soaked Samples

For the soil treated with K-acetate for one month (Figure 11.3), XRD reflections for the initial run show a strong 10.1 Å peak, with similarly intense peaks noted at 4.4 Å and 3.4 Å. A new, smaller peak at 3.1 Å, not present in untreated samples, is also noted. Run two with ethylene glycol shows two distinctive peaks at 10.8 Å and 10.1 Å as the sample begins to upshift, with total counts between in this region halved, likely due to the split in spacing between 10.8 Å and 10.1 Å.

The rest of the reflection curve shows relatively good agreement with the original run, though a small peak at 3.6 Å is observed. Upon heating to 110 °C, there is a reduction in the 11 Å peak height, with a complete loss of the 10.1 Å peak. The only other differing peak is seen at 3.7 Å. The collapsed 7 Å peak is present, though it is incredibly small. Heating to 550 °C shows a collapse in almost all major peaks, bar the small peaks present at 4.2 Å, 4 Å, and 3.1 Å.

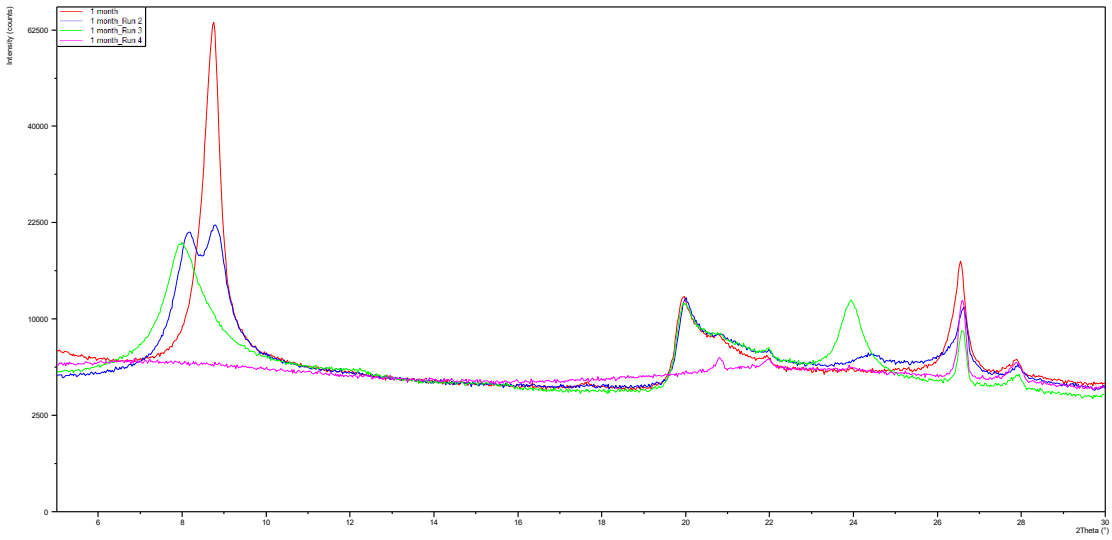

Figure 11.3 An XRD diffractogram showing the peaks for the 1 month-treated soil where the following treatments were employed: ambient (red line), ethylene glycol treatment (blue), sample heating to 110° C for 24 hours (green) and sample heating to 550° C for 24 hours (fuchsia).

Formamide treatment (Figure 11.4) of the clay shows an upshift from 10.1 Å to 10.4 Å, as well as the development of a new peak between 3.4–3.5 Å. This expansion provides additional confirmation of the presence of halloysite (Churchman et al., 2016).

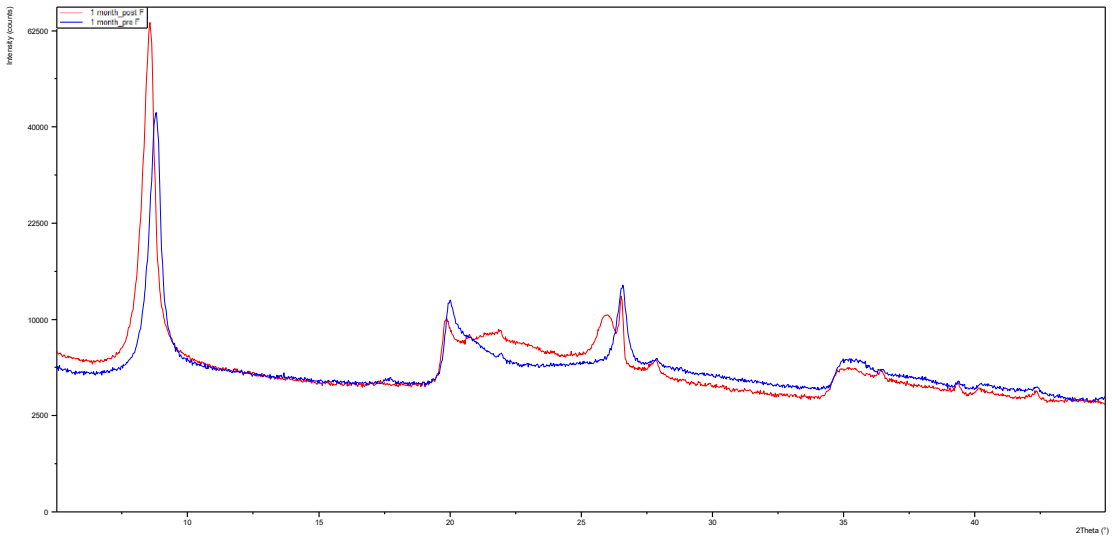

Figure 11.4: An XRD diffractogram showing peaks for the 1 month treated soil prior to formamide treatment(blue line) and after formamide treatment (red line).

3 Month Soaked Samples

The clay tested for soil that had undergone three months of treatment (Figure 11.5) shows strong peaks for the initial run at 10.1 Å, 4.4 Å, and 3.3 Å. Treatment with ethylene glycol of the sample presented similar peaks spread across 10.8–10.1 Å as observed in the untreated natural soil. The peak at 4.4 Å remained present following the ethylene glycol treatment, but the 3.3 Å peak disappeared. This peak provided a more gradual rise between 3.6–3.3 Å, although proportionally this rise does not account for the loss in the 3.3 Å peak. Heating to 110 °C resulted in an upshift in the clay to 11 Å, with the peak at 10 Å disappearing. As seen in the 1-month soil treatment, a very minor increase in 7 Å is observed, with the only other major change being the upshift in the 3.3 Å to 3.7 Å. Heating of the soil to 550 °C led to the collapse in all peaks, though a small increase at 3.3 Å is noted, although the increase is nowhere near the level of intensity seen for the original run of the soil.

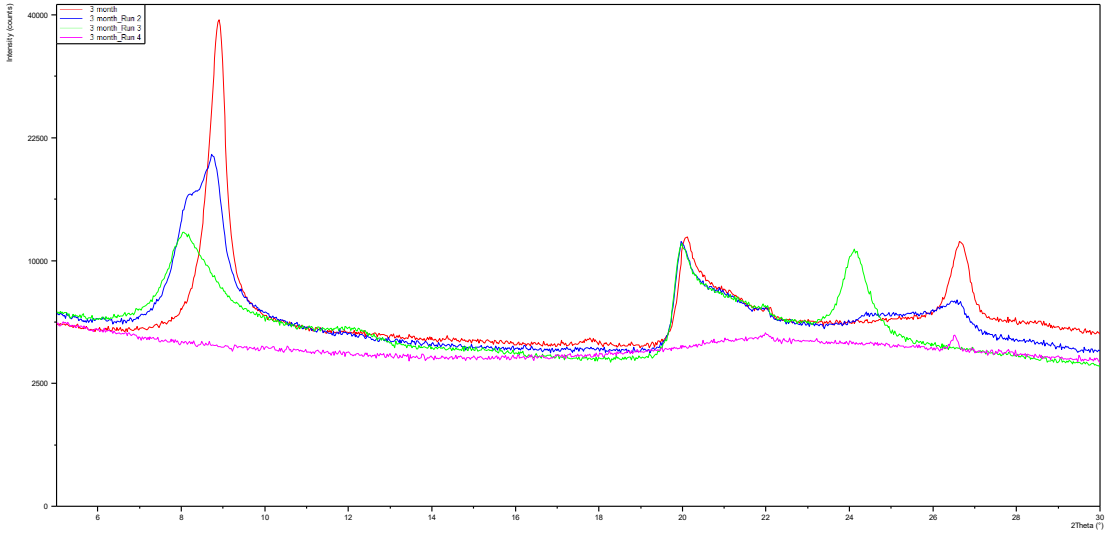

Figure 11.5 An XRD diffractogram showing the peaks for the 3 month-treated soil where the following treatments were employed: ambient (red line), ethylene glycol treatment (blue), sample heating to 110° C for 24 hours (green) and sample heating to 550° C for 24 hours (fuchsia).

Treatment of the soil with formamide (Figure 11.6) shows a small upshift in the 10.1 Å peak to 10.2 Å, as well as an upshift of the 3.3 Å peak to between 3.3 and 3.4 Å, showing, again, good agreement with the presence of halloysite within the sample analysed.

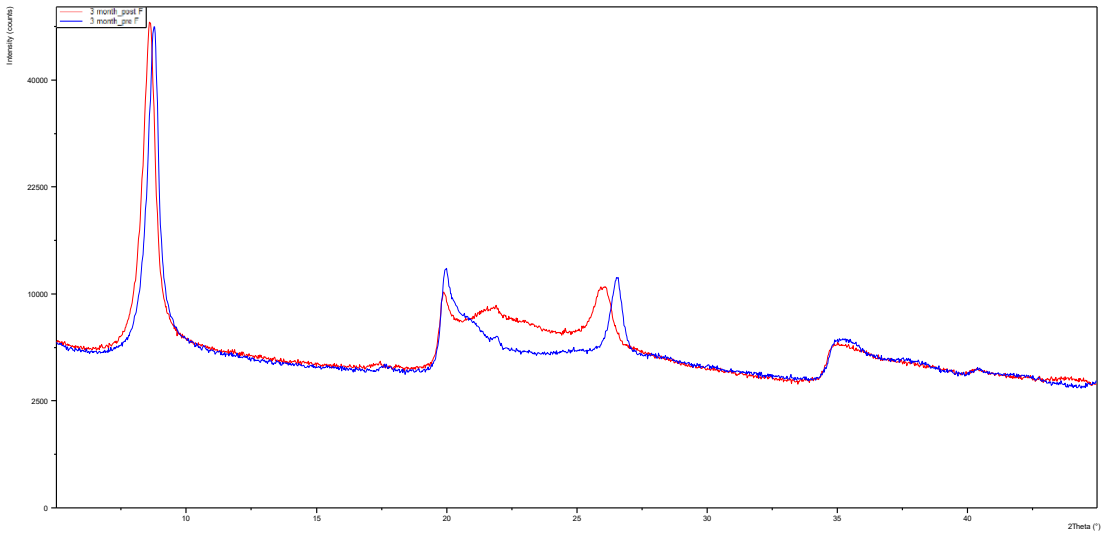

Figure 11.6: An XRD diffractogram showing peaks for the 3 month-treated soil prior to formamide treatment (blue line) and after formamide treatment (red line).

6 Month Soaked Samples

Samples treated for six months with potassium acetate show three distinctive peaks on the initial XRD run with reflection peaks at 10.1 Å, 4.4 Å, and 3.3 Å (Figure 11.7). Treatment with ethylene glycol resulted in an upshift from 10.1 Å to 10.8 Å, as well as a slight upshift in the 3.3 Å peak to 3.4 Å. Heating at 110°C produced a final clear upshift to 11 Å from the initial 10.1 Å peak. No clear 7 Å peak was present following heating, although a drop in the amount of expansion from 3.3 Å to 3.6 Å was evident in this instance. In contrast to the 1- and 3-month samples, the peak at 3.3 Å did not completely disappear upon heating; instead, a small peak persisted. Heating at 550°C resulted in a total collapse of the 11 Å, 4.4 Å, and 3.6 Å peaks, although a much larger 3.3 Å peak was still present.

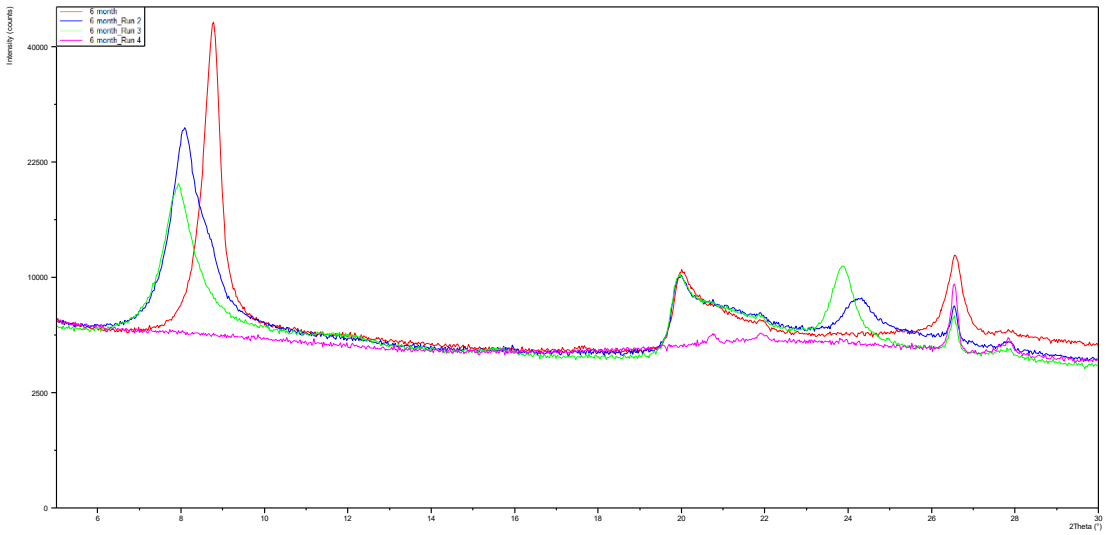

Figure 11.7 An XRD diffractogram showing the peaks for the 6 month-treated soil where the following treatments were employed: ambient (red line), ethylene glycol treatment (blue), sample heating to 110° C for 24 hours (green) and sample heating to 550° C for 24 hours (fuchsia).

Treatment with formamide (Figure 11.8) led to a very different result than those collected for the untreated samples, as well as for the 1- and 3-month treatments. There was a loss in intensity in the 10.1 Å peak, although it was still present, and there was a significant growth in reflections observed between 4.2 and 2.6 Å, with a gentle, gradual peak observed across the 1.8 Å region, although no distinctive peaks were seen in this region. This result was validated with a secondary run of the formamide treatment, and a near-identical peak was generated. While it does indicate the presence of halloysite in this sample with the 10.1Å peak remaining, the large, gentle peak region is certainly a noticeable difference.

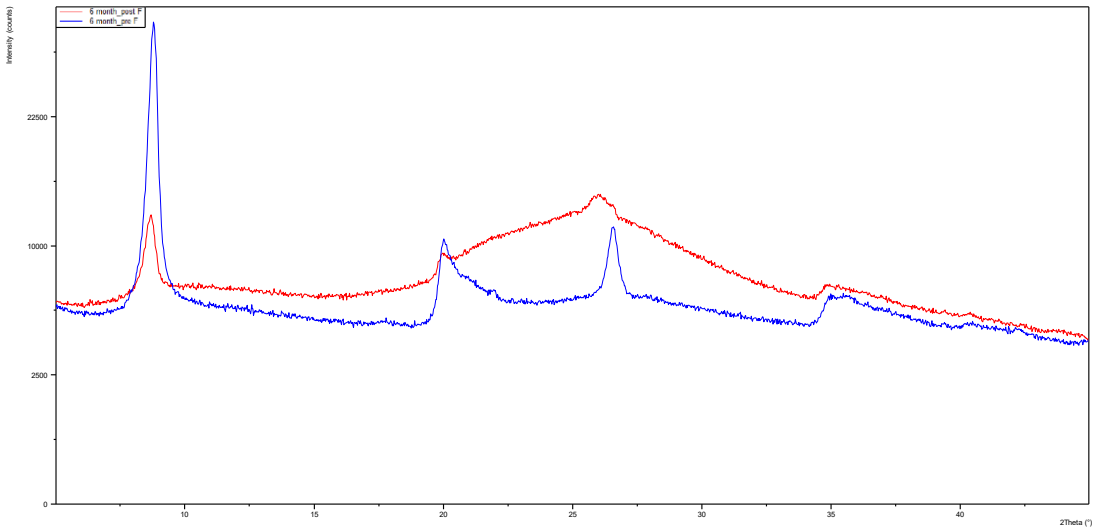

Figure 11.8: An XRD diffractogram showing peaks for the 6 month-treated soil prior to formamide treatment (blue line) and after formamide treatment (red line).

12 Month Soaked Samples

Peaks for the 12-month treated samples are shown in Figure 11.9. The initial runs showed similar results to those of previous treated soils with an initial 10.1 Å peak, with further peaks seen at 4.4 Å and 3.3 Å. Treatment with ethylene glycol showed a clear, distinctive upshift to 10.9 Å with a narrow band peak of somewhat less intensity than the initial run, though not a large drop-off. Peaks at 4.4 Å and 3.3 Å remained, although the 3.3 Å peak was slightly less intense than for the initial run. A new upshifted peak at 3.5 Å is observed with a flat top to the peak running between 3.5 and 3.4 Å. Heating to 110°C shows a complete upshift to 11 Å with a drop in intensity. A small 7 Å peak is noted, although the 4.4 Å and 3.3 Å peaks remained. The 3.4 – 3.5 Å peaks have narrowed in band intensity, with a single sharp peak at 3.6 Å observed in the 110°C-treated curve. Heating the sample to 550 °C led to the loss of the 11 Å, 7 Å, 4.4 Å, and 3.6 Å peaks. However, a sharp peak in responses is seen at 3.3 Å as well as a smaller increase and peak at 3.1 Å

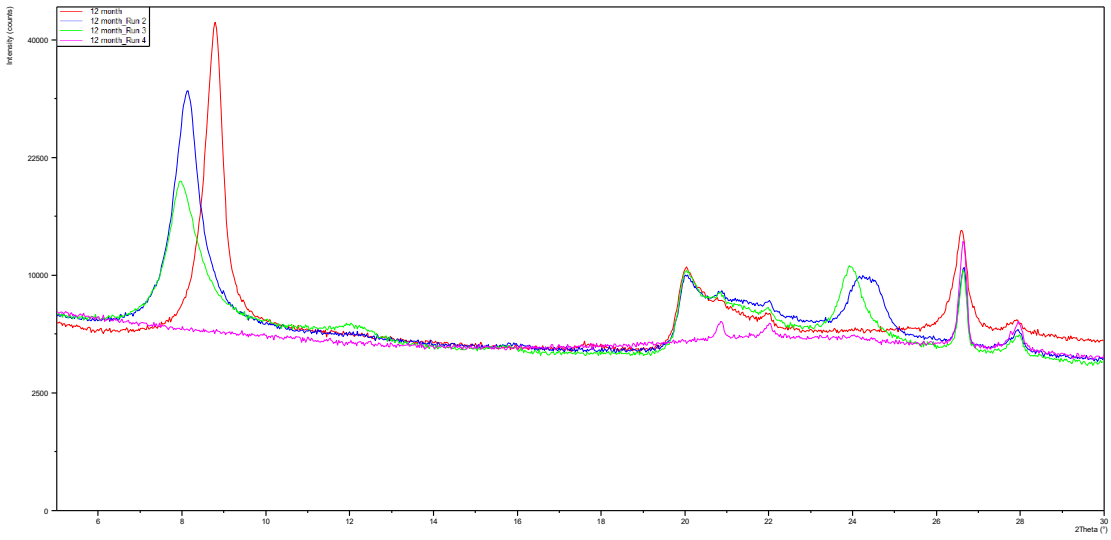

Figure 11.9 XRD traces showing the peaks for the 12 month-treated soil where the following treatments were employed on the soil during testing. ambient (red line), ethylene glycol treatment (blue), sample heating to 110°C for 24 hours (green) and sample heating to 550°C for 24 hours (fuchsia).

Treatment with formamide (Figure 11.10) shows good agreement with almost all other samples with a clear peak at 10.3 Å following treatment, which provides confirmation of the presence of halloysite.

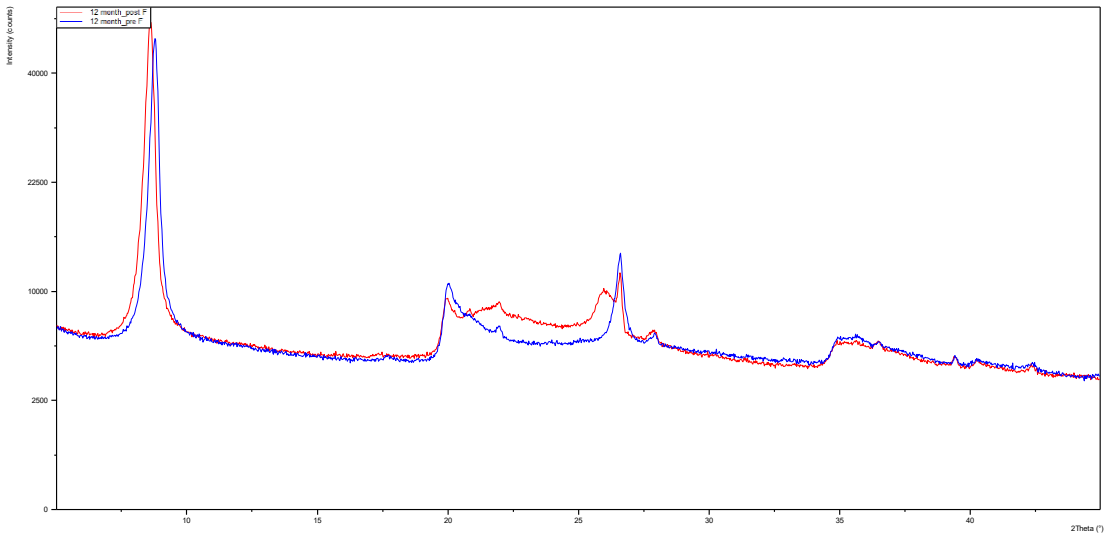

Figure 11.10: An XRD diffractogram showing peaks for the 12 month-treated soil prior to formamide treatment (blue line) and after formamide treatment (red line).

10 MolL^{-1} samples

The samples treated with 10 molL^{-1} K-acetate showed no clear increase in basal spacing after the initial run, with a peak at 10 Å observed. Further peaks were noted at 4.4 Å, 4 Å, and 3.3 Å (Figure 11.11). Treatment with ethylene glycol shifted the 10 Å peak to 11 Å, as well as shifting the 3.3 Å peak to 3.5 Å, although the 3.3 Å peak did not collapse. Heating to 110°C produced an 11 Å peak, as well as a slight upshift of the glycol-treated 3.5 Å peak to 3.5 – 3.6 Å. No increase in the 7 Å peak was observed following the heat treatment. Heating to 550°C produced a loss of all but the 4 Å and 3.3 Å peaks

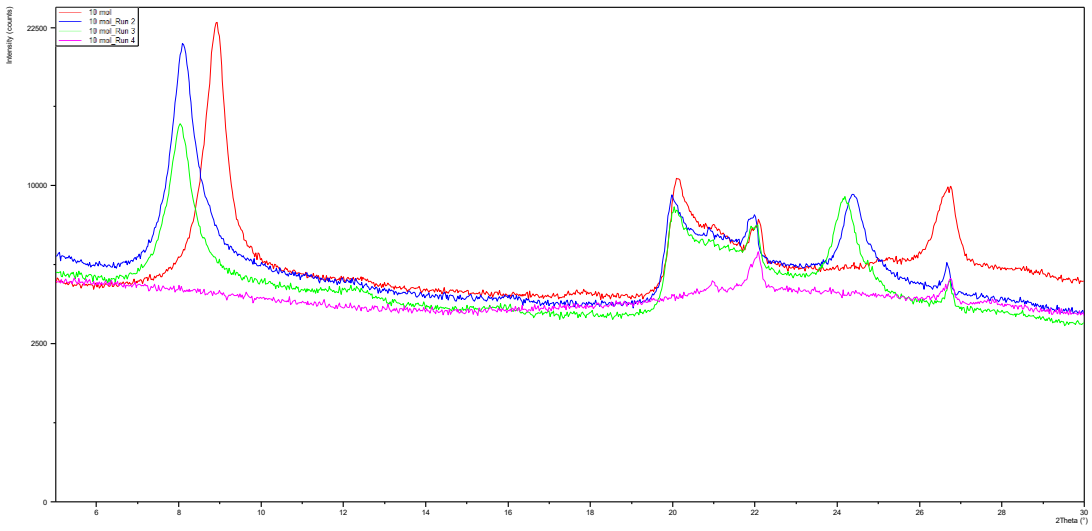

Figure 11.11 XRD traces showing the peaks for the 10 molL^{-1} treated soil where the following treatments were employed: ambient (red line), ethylene glycol treatment (blue), sample heating to 110^{o} C for 24 hours (green) and sample heating to 550^{o} C for 24 hours (fuchsia).

Formamide treatment of the resultant clay (Figure 11.12) produced an upshifted (10.3 Å) peak confirming the presence of halloysite within the samples.

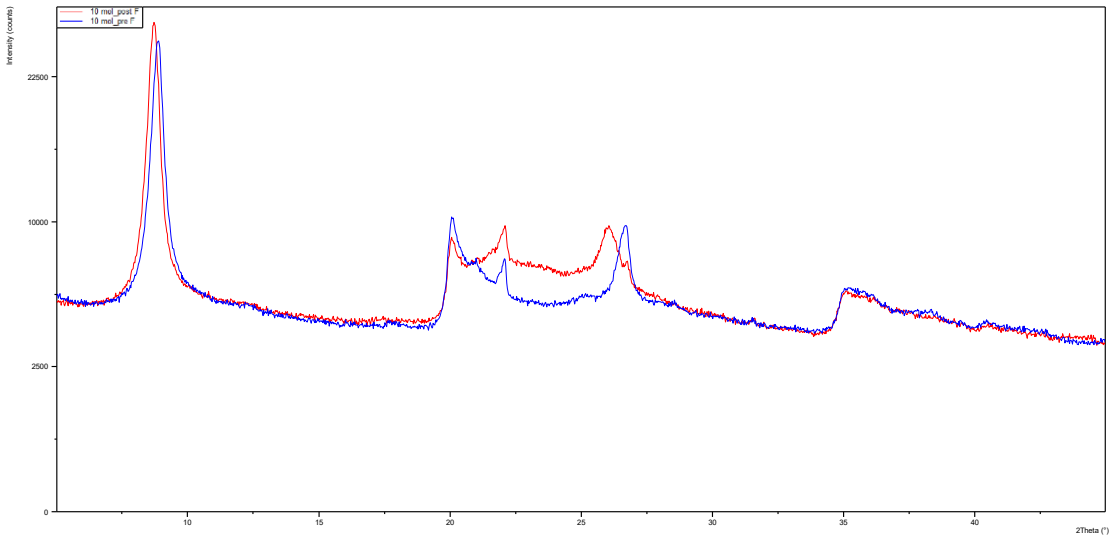

Figure 11.12: An XRD diffractogram showing peaks for the 10 molL^{-1} treated soil prior to formamide treatment (blue line) and after formamide treatment (red line).

11.1.2 Bulk Sample Analysis

Reflection peaks for both untreated and treated soil samples are shown in an composite graph below (Figure 11.13). Samples showed a consistent response, with all samples showing the largest peak at ~10.1 Å (7º 2θ) consistent with that of the 001 peak of hydrated halloysite. No peaks prior to 10.1 Å were noted, providing a strong indication that the potassium acetate has not intercalated into the halloysite basal space. Further peaks for halloysite in the 02,11 bands were noted at ~4.4 Å as well as the 003 hydrated halloysite peak noted at 3.4 Å (~27º2θ).

The expectation for the halloysite K-acetate complex would be a significant increase in the 001 spacing to 14.3 Å, on top of a decrease in the 02,11 band with a 4.33 Å response on top of a new 002 band forming at 7.4 Å. A small increase in count was noted at 7.36 Å, with this likely representing a small amount of dehydrated halloysite. With this said, no subsequent secondary peaks were observed.

Kaolinite was likely not present, though a peak at 1.47 – 1.49 Å was noted, potentially indicating the presence of kaolinite. However, such kaolinite was not detected in previous analyses and, based on the amount of iron found within the sample, it is more likely that this peak corresponds to the D_2 orientation of magnetite, with the first peak noted in its D_1 orientation observed at 2.5 – 2.6 Å.

Peaks for low-temperature cristobalite and low-temperature quartz are also noted, with peaks at 4.06 Å and 3.37 Å, respectively (e.g., Lowe and Nelson, 1994). However, this peak is close to the 3.4 Å hydrated halloysite 003 peak and is thus in low quantities. Pyroxene may also be present, with a noticeable peak at 2.58 Å noted. When comparing the untreated trace to that of the treated traces, three main discrepancies were noted.

The first discrepancy is the lack of an initial peak for the 3.4 Å hydrated halloysite for the untreated sample; this is instead shifted slightly lower to around 3.35 Å, whereas the hydrated halloysite shows a 2-step peak in this instance. The second discrepancy is for the 6-month-trated sample with a small peak at 3.2 Å observed, a peak not reflected in the other samples. The last discrepancy is the large peak observed in the untreated soil at 1.97 Å, which is not observed in any capacity for the treated soil, this is speculated to be attributed to ferrihydrite (e.g., see Childs, 1992).

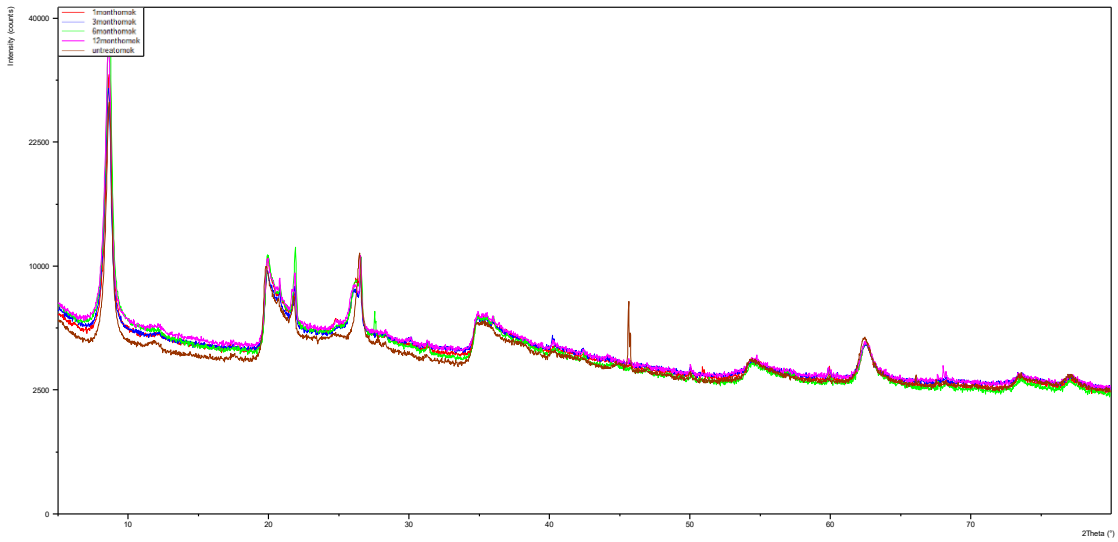

Figure 11.13. XRD traces depicting the 2-theta peaks for the bulk soil samples of various soils, with untreated shown by the brown line, 1-month treatment by the red line, 3-month treatment by the blue line, 6-month treatment by the green line, and 12-months' treatment by the fuchsia line.

11.1.3 Rehydration Peaks

In order to prepare a rehydrated soil paste, both the treated and untreated soils were dehydrated in an oven at 110°C for a minimum of 48 hours, cooled in a silica bead desiccator for a minimum of 48 hours, and then mixed with de-ionised water. This process was undertaken to examine the post-rehydration state of the halloysite within the clay.

These rehydrated soil pastes were then run through the XRD in a similar fashion to that of the bulk sample, with the diffractogram traces (and peaks) shown in Figure 11.14.

Most samples had the characteristic dehydrated (7 Å) halloysite present (7.4 – 7.6 Å), while all had the 02,11 bands and 003 peaks observed at 4.5 Å and 3.4 Å, respectively, across all samples. Samples soaked for 6 and 12 months produced interesting rehydration peaks, with a small peak present at 10.2 Å for the 6-month sample. On the other hand, the peak for 12 months was very different, with a broad shoulder from 9.7 Å to around 7.5 Å present. Additional peaks at 4.1 Å and 3.7 Å were also noted. In addition, the 10 mol samples (not shown) showed a clear expansion of the 001 reflection to 14.3 Å, indicative of the development of an intercalated complex (Lowe & Nelson, 1994).

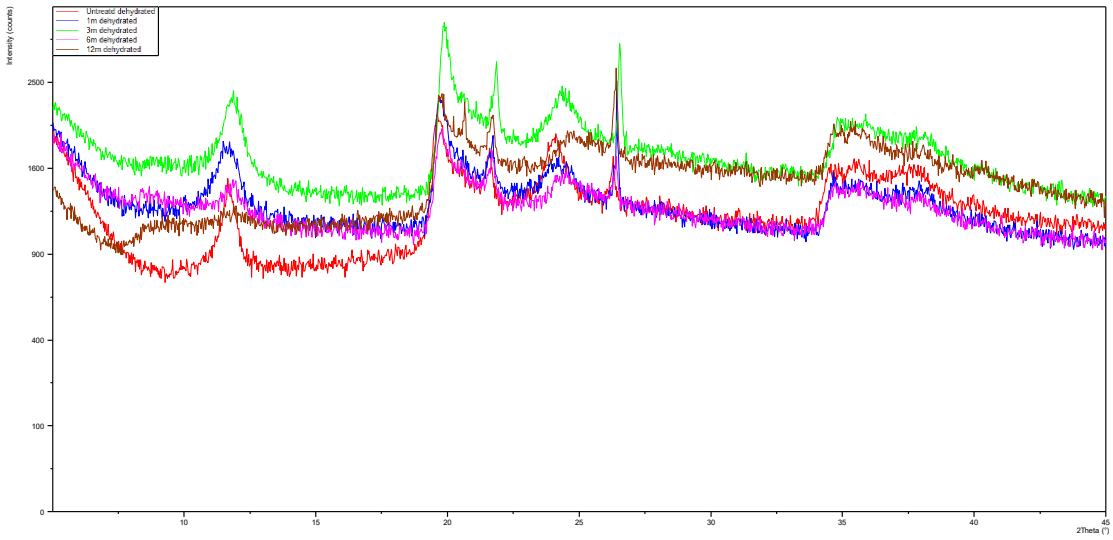

Figure 11.14. XRD traces depicting the 2-theta peaks for the rehydrated untreated and treated soils, with untreated shown by the red line, 1 month by the blue line, 3 months by the green line, 6 months by the fuschia line, and 12 months by the brown line.

When rehydrated samples were subsequently placed in the oven for 1 hour (at 110°C) and run in the XRD (Figure 11.15), there was little change for the untreated, 1- and 3-month samples, whereas 6- and 12-month samples show a complete collapse in any peaks in the hydrated (10 Å) halloysite range, and show a consistent collapse to 7.3 Å. Interestingly the 10 molL^{-1} sample did not collapse and retained its 14.3 Å peak.

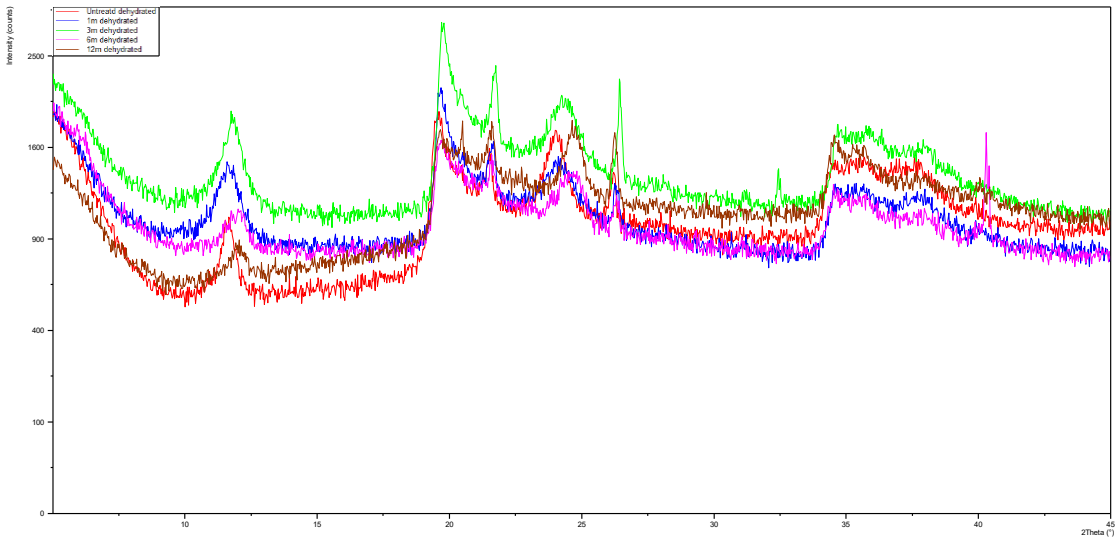

Figure 11.15. XRD traces depicting the 2-theta peaks for the rehydrated soils (following initial rehydration), with untreated shown by the red line, 1 month by the blue line, 3 months by the green line, 6 months by the fuchsia line, and 12 months by the brown line.

11.1.4 Summary Table

The summary of the peaks observed, and their interaction at each stage of the XRD process, are shown in Table 11.1. The table has divided the soil samples on the basis of their treatment. These are subsequently then split off with the main identified peaks reported for each of the stages of the XRD process (i.e. ambient, ethylene glycol treatment, etc). These were undertaken to show how, if at all, peaks may have changed.

Table 11.1. A summary of the XRD clay fraction analyses, with notes made of the major peak lengths observed at each of the five differing conditions the soils were exposed to during the XRD process as well as an inference of the minerals potentially present within the clay fraction.

Soil sample type	Ambient Peaks (Å)	Ethylene Glycol Peaks (Å)	Heating at 110°C (Å)	Heating at 550°C (Å)	Formamide Treatment (Post Treatment)	Potential Identified Minerals
Untreated	• 10.1Å • 4.4 Å • 3.4 Å	• Broad shoulder from 11-10.1 Å • 4.4 Å • 3.4 collapsing	• 11 Å fully formed. • 7.2 Å newly present • 4.4 Å • 3.6 Å (upshifted from 3.4 Å)	• 4 Å only peak observable.	• 10.1Å • 3.4Å	• Halloysite (10.1 Å form at ambient)
1 Month	• 10.1 Å • 4.4 Å • 3.4 Å • 3.1 Å peak also observed.	• 10.8 Å peak formed as well as 10.1 Å • 4.4 Å • 3.6 Å peak forming • 3.4 Å peak collapsing	• Drop in overall counts. • 11 Å fully formed • small 7 Å peak • 4.4 Å • 3.7 Å peak formed.	• Small peaks present at 4.2 Å, • 4 Å • 3.1 Å	• Small upshift from 10.1 Å to 10.4 Å. • New peak formed between 3.4 and 3.5 Å.	• Halloysite (10.1 Å) • no halloysite intercalate present (expected peak to be <10.1 Å at ambient)
3 Months	• 10.1 Å • 4.4 Å • 3.3 Å	• 10.8 Å-10.1 Å broad peaks • 4.4 Å • 3.3 Å peak disappeared. • Small rise between 3.6-3.3 Å	• 11 Å peak. • Minor 7 Å • 3.7 Å peak formed • 4.4 Å peak.	• 3.3 Å small peak but no others present.	• Small upshift in 10.1 Å peak to 10.2 Å. • Small upshift in 3.3 Å to 3.4 Å.	• Halloysite (10.1 Å) present. • No halloysite intercalate present.

Soil sample type	Ambient Peaks • (Å)	Ethylene Glycol Peaks • (Å)	Heating at 110ºC • (Å)	Heating at 550ºC • (Å)	• Formamide Treatment (Post Treatment)	• Potential identified minerals
6 Months	• 10.1 Å, • 4.4 Å • 3.3 Å	• 10.8 Å peak (uspshifted from 10.1 Å) • 4.4 Å • 3.3 upshift to 3.4 Å	• 11 Å • 3.3 Å upshift to 3.6 Å though 3.3 Å peak still present.	• Large 3.3 Å peak present.	• Drop in 10.1 Å peak intensity (though maintained). • Broad shoulder between 4.2-2.6 Å region.	• Halloysite (10.1 Å). • No intercalate present.
12 Months	• 10.1 Å • 4..4 Å • 3.3 Å	• 10.9Å upshift(from 10.1 Å) • 4.4 Å • 3.3 Å • New 3.5 Å peak present	• 11 Å • new 7 Å peak present • 4.4 Å • new 3.6 Å peak present.	• 3.3 Å • new peak at 3.1 Å observed.	• 10.3 Å peak upshifted from 10.1 Å present	• Halloysite (10.1 Å) present • No halloysite intercalate present.
10 molL^{-1}	• 10.1 Å • 4.4 Å • 4 Å • 3.3 Å	• 11 Å (Upshifted from 10 Å) • 4.4 Å • 3.5 Å (upshifted from 3.3 Å) • 3.3 Å	• 11 Å • 4.4 Å • 3.5-3.6 Å peak (instead of solely 3.5 Å)	• 4 Å • 3.3 Å	• 10.3 Å peak upshifted from 10.1 Å	• Halloysite (10.1 Å) • No halloysite intercalate present.

11.2 DSC-DTA/TGA Analysis

The summarised data for untreated samples, as well as 1, 3, 6, 12 month and 10 molL^{-1} samples can be seen in the Table 11.2 and Table 11.3 at the end of this section. These tables show the individual peak and onset temperatures for both DSC and TGA results for each grouping of samples, as well as area (mJ and %, respectively) and energy (delta/h) per gram of sample required.

11.2.1 Untreated

Figure 11.16 shows the DSC signal for untreated sensitive Pahoia Tephra, sampled from Kowhai Grove, Ōmokoroa. Within the DSC signal two main features are present. The first, a reasonably strong endothermic response, peaking at 506^{o} C, absorbing 6245 mJ of energy at roughly 369 joules per gram of soil. The second feature a 952^{o} C peak, with a small exothermic response (-905mJ) noted, which is accompanied by a 53.5 J/g release of energy.

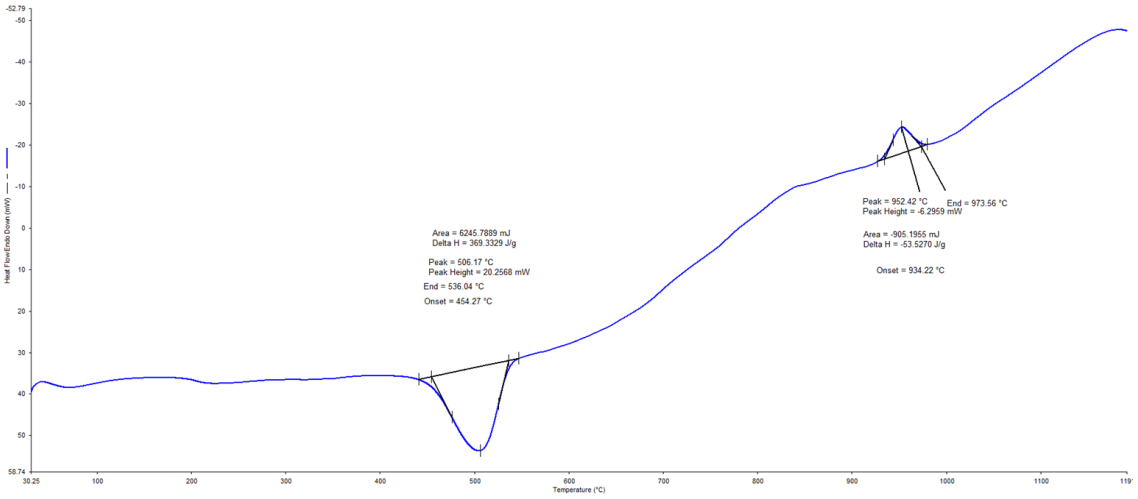

Figure 11.16: A DSC chart showing the enthalpy for an untreated soil sample. The major endo and exothermic events are noted with information including area, peak height, as well as peak, end and onset temperatures for any events.

When examining the TGA curve (Figure 11.17), as well as its first derivative for untreated soil, a total of 14.4 % of mass was lost over the course of the analysis. Unlike the multiple events noted in the DSC signal there was a single, significant mass loss event, occurring at a peak of 504° C, with a mass loss of around 9 %. The remaining 5.4 % mass was lost in the first 466°C of heating, as well as between 520–750°C. The bulk of the mass loss likely relates to the OH bonds breaking.

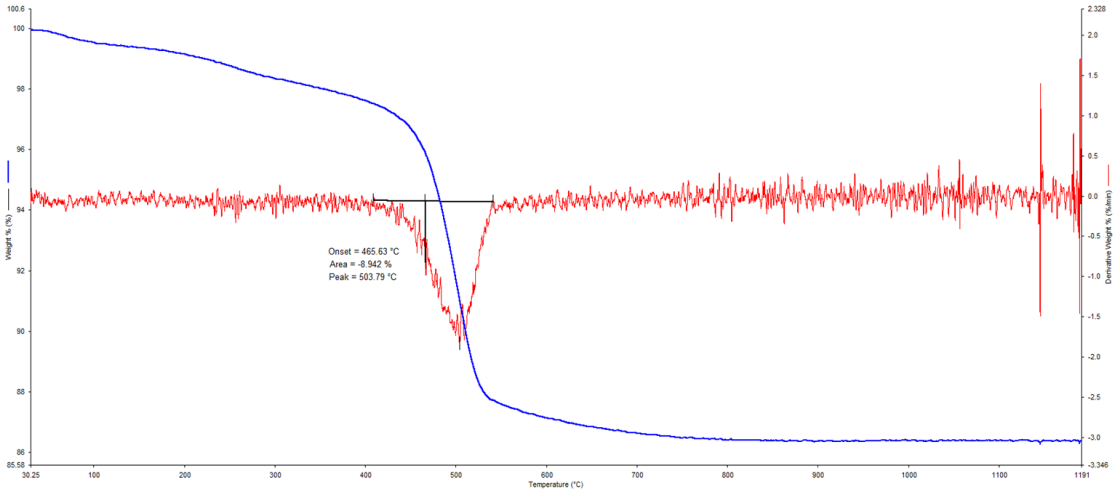

Figure 11.17.A TGA curve (blue line) with the smoothed first derivative (red line) included showing the mass loss events noted for an untreated soil sample.

11.2.2 1 Month Samples

The sample tested following 1 month of treatment (Figure 11.18) showed four peaks across the DSC curve. The first occurring at 60.7°C, with an endothermic response of 568.5 mJ noted ($\Delta H = 38\ Jg^{-1}$). The second response peak was observed at 320°C, with a larger 4699.5 mJ ($\Delta H = 311.6$ J/g) released during the exothermic response. The third was an endothermic response peaking at 473°C, though the response was notably smaller than untreated with only 2655 mJ of energy absorbed during the reaction. The fourth and final peak was noted at 958°C, with a total of 270 mJ of energy released in an exothermic response.

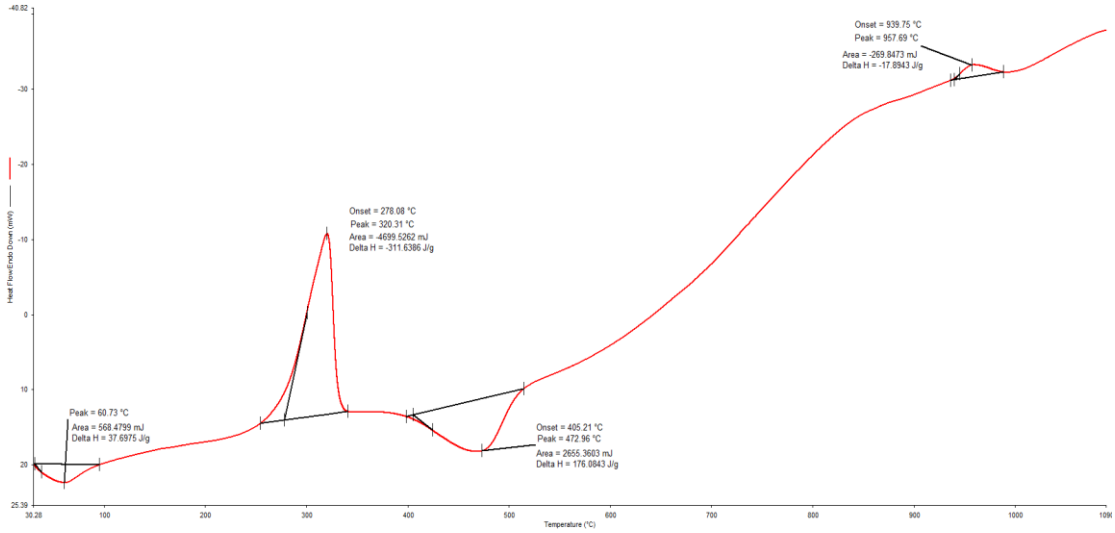

Figure 11.18.A DSC chart showing the enthalpy for an 1 month-treated soil sample. The major endo- and exothermic events are noted. Four major events have been observed at various points during the DSC test.

For the TGA and first derivative signals (Figure 11.19), a total of 18 % of mass was lost over the course of the entire test, with three primary areas of loss noted. The first at 59ºC, with 1.5 % of mass lost up to roughly 100º C. The second was a short sharp loss of 2.5% of mass peaking at 317º C. The third mass loss occurred quite soon after the second mass loss with 163ºC observed between the mass loss responses. This third mass loss was the largest of the three (5.1 %) peaking at 480ºC

.

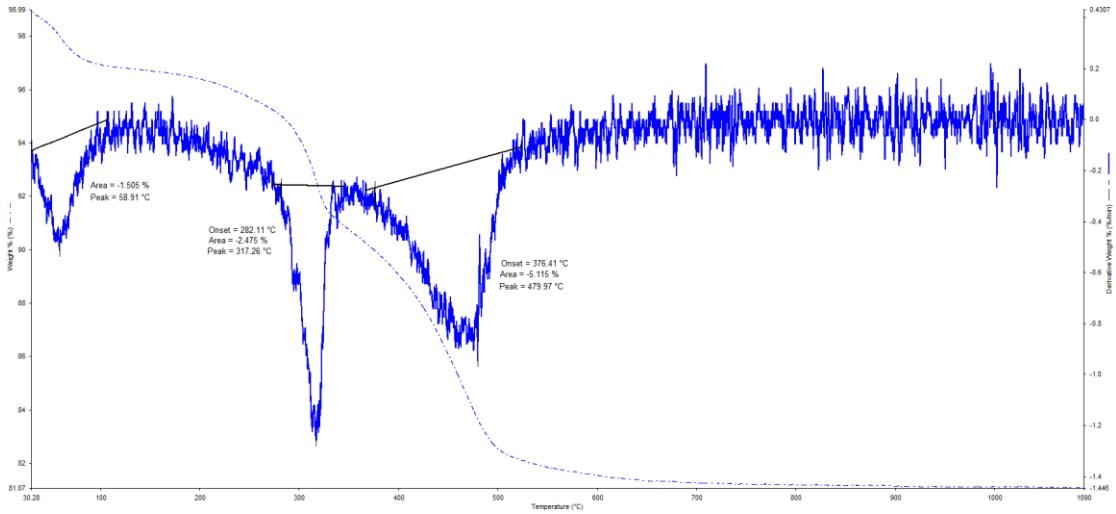

Figure 11.19.A TGA curve (blue line dashed) with the smoothed first derivative (blue line) included showing the mass loss events noted for the 1 month-treated soil sample.

When plotted on a multiple y-axis graph (Figure 11.20) it can be seen more clearly the linkage between the mass loss events observed in the TGA testing (as well as within the first derivative signal) and the major exothermic and endothermic events occurring within the soil. This is particularly significant with the sharp exothermic event occurring at 320°C corresponding to a similar short mass loss event, while the endothermic event occurring at 473°C appears to have a much broader mass loss event as shown by the longer more gradual TGA signal, and much wider first derivative signal.

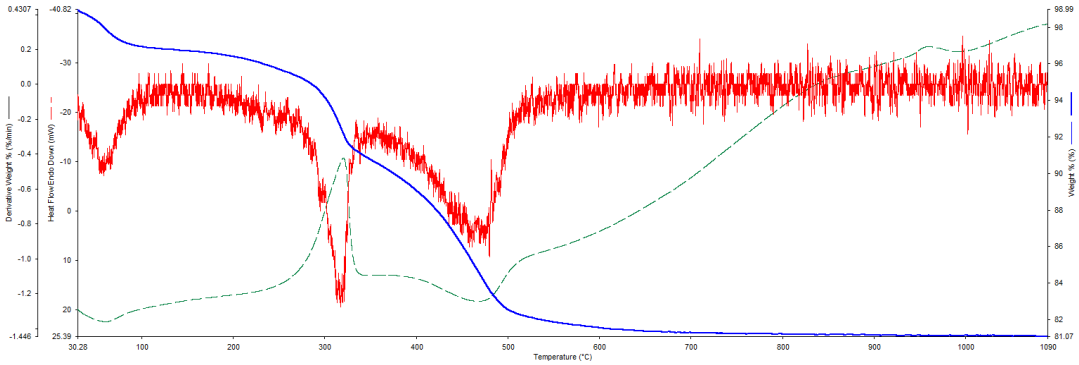

Figure 11.20. A combined DSC (green dashed), TGA (blue) and first derivative (red) signal imposed on a multiple Y-axis, with X axis remaining constant as the temperature range of the testing.

11.2.3 3 Month Samples

At 3 months treatment (Figure 11.21), the sample showed four peaks. The first is an initial peak at 64°C, with 519 mJ of energy taken up in the endothermic response. This was followed by a strong exothermic peak peaking at 327°C, with 5557 mJ of energy being released. The third peak was at 481°C with 2972 mJ being absorbed during an endothermic peak. The fourth and final peak was noted at 955°C, with 224 mJ of energy being released.

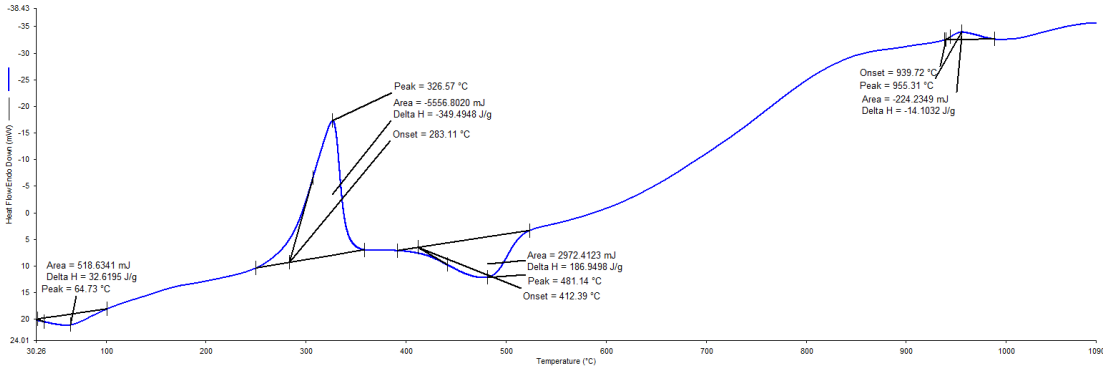

Figure 11.21. A DSC graph showing the enthalpy for an 3 month-treated soil sample. The major endo- and exothermic events are noted with relevant information included on the graph.

The TGA/first derivative curve (Figure 11.22) showed a total 17.6 % of mass lost over the course of the test with mass loss occurring in three main stages. The first loss was at 65.27ºC, with a loss of 1.6 % noted. The next was at 327ºC with a loss of 3 % noted. The final mass loss occurring at 460ºC with a larger 4.5 % lost.

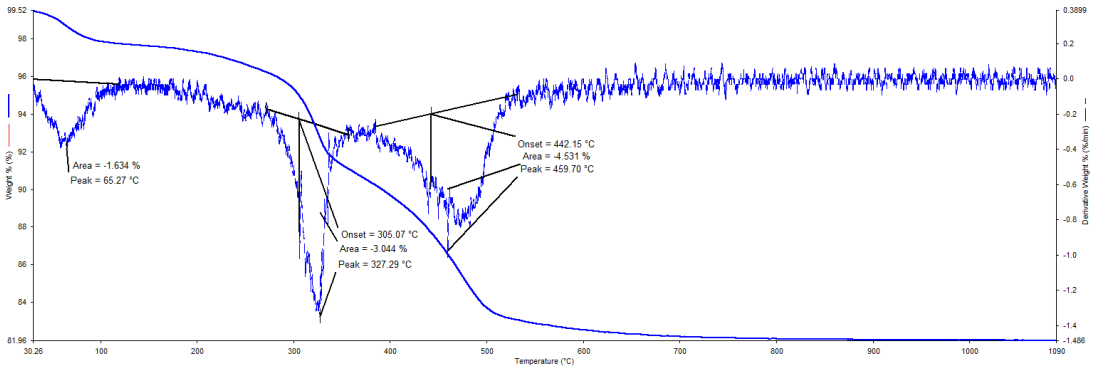

Figure 11.22. A TGA curve (blue line dashed) with the smoothed first derivative (blue line) included showing the mass loss events noted for the 3 month-treated soil sample.

In a similar vein to that of the 1 month-treated sample, the sizes of the first derivative mass loss events seem to fit well with the relative sizes of the endo- and exothermic events (Figure 11.23) noted in the DSC signal, with a slower mass loss occurring during the endothermic event at 460ºC, especially when compared to the size of the exothermic event at 327ºC.

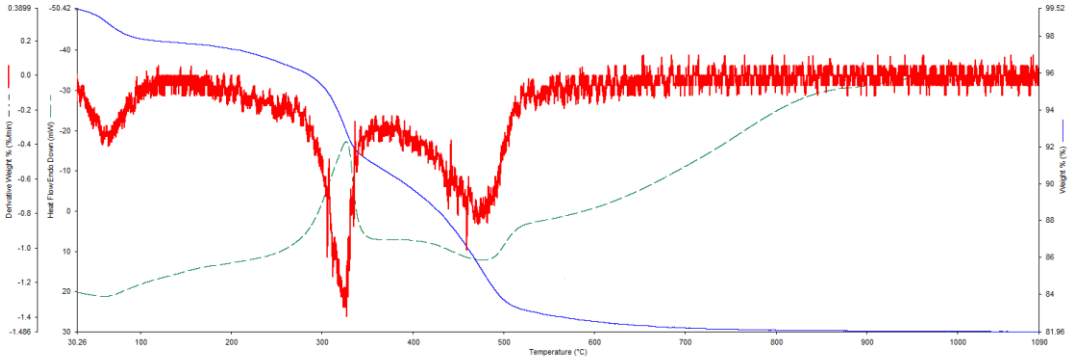

Figure 11.23. A combined DSC, TGA and first derivative signal imposed on a multiple Y-axis, with X axis remaining constant as the temperature range of the testing for the 3 month-treated samples .

11.2.4 6 Month Samples

The sample at 6 months (Figure 11.24) showed four peaks with an initial peak occurring at 64ºC, with an absorption of 531.7 mJ in an endothermic reaction. This was followed by a strong exothermic peak peaking at 324ºC, with 4704 mJ of energy being released. The third peak was at 475ºC with 3264 mJ being absorbed during an endothermic peak. The fourth and final peak was noted at 960.99ºC, with 291 mJ of energy being released.

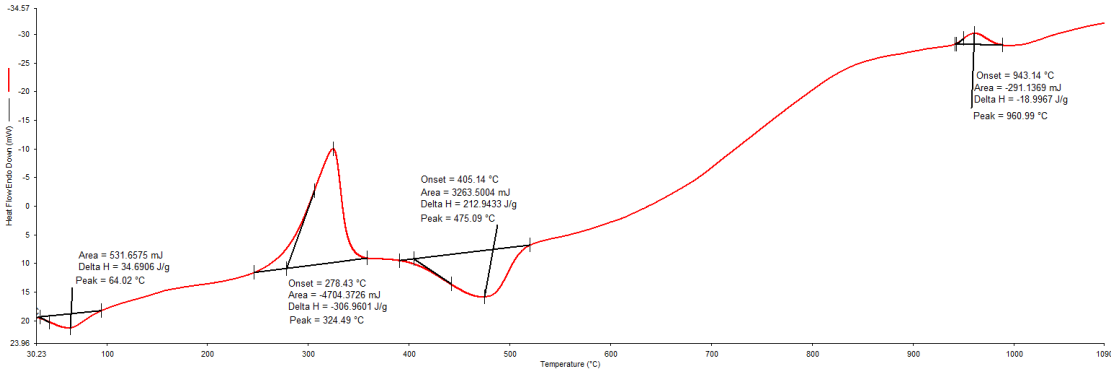

Figure 11.24. A DSC graph showing the enthalpy for an 6 month-treated soil sample. The major endo and exothermic events are noted with relevant information included on the graph.

Total percentage mass loss was around 18 % (Figure 11.25), similar to that for the previous samples, with three stages of significant mass loss noted in the first derivative curve. The first mass loss event occurring at the peak temperature of 30.23°C, with 3.6 % being lost. The second mass loss event was during the first exothermic peak noted in the DSC signal, with 2.7 % of mass lost at a peak temperature of 319°C. The third and final major mass loss event was observed at a peak temperature of 475°C, with 4.3 % of mass lost during this endothermic reaction.

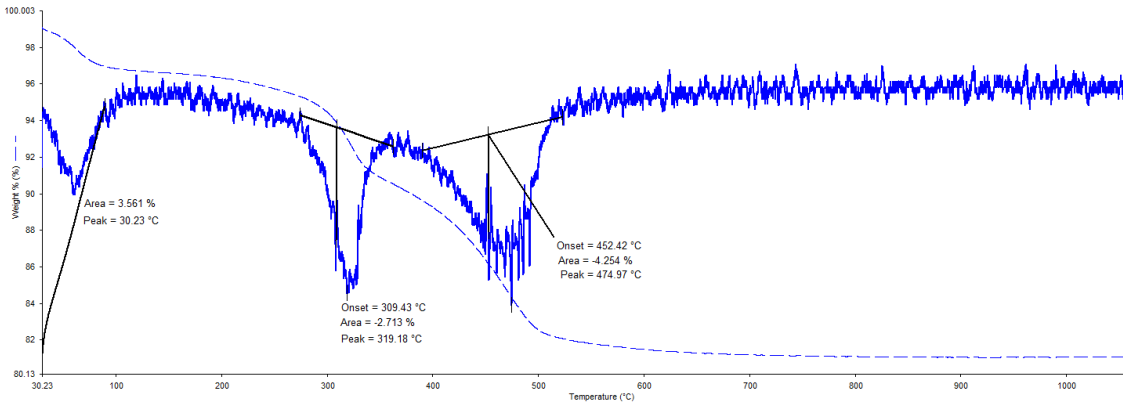

Figure 11.25. A TGA trace (blue line dashed) with the smoothed first derivative (blue line) included showing the mass loss events noted for the 6 month-treated soil sample.

As seen previously, the mass loss events fit well with almost all major endo- and exothermic events (Figure 11.26). The only exception is that of the upper event at around 950°C. A slight change can be seen in comparison to the 3- and 1- month- treated samples with the major endothermic mass loss event being much sharper and shorter than those previous.

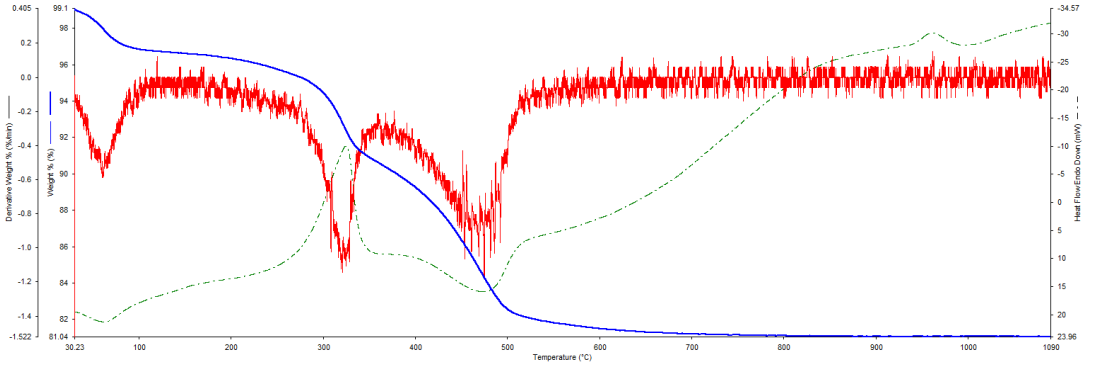

Figure 11.26. A combined DSC, TGA and first derivative signal imposed on a multiple Y-axis, with X axis remaining constant as the temperature range of the testing for the 6 month-treated samples.

11.2.5 12 Month Samples

For the sample analysed after 12 months of treatment, three clear peaks exist within the first 600°C with the potential for two to three further peaks up to 1200°C (Figure 11.27). The first peak was observed at 63.5°C, with 275 mJ of energy absorbed in an endothermic peak. The next response was noted at 330.4°C with 4950.9 mJ of energy released in an exothermic peak. The final clear peak was noted at 492.1°C with 2181.8 mJ of energy absorbed in an endothermic peak. In the final 600°C of heating a small increase and decrease of heat was noted around 700°C, followed by two smaller exothermic releases around 870°C and 960°C.

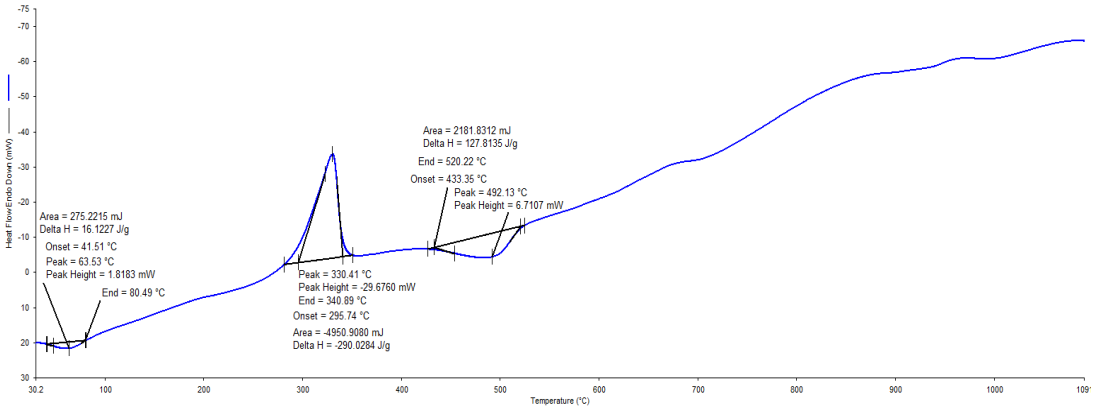

Figure 11.27. A DSC graph showing the enthalpy for an 12 month-treated soil sample. The major endo and exothermic events are noted with relevant information included on the graph.

For the mass changes (Figure 11.28), a total of 20 % of mass was lost over the course of the analysis with three main mass changes were observed. The first occurred between 54.6ºC and 79.4ºC with 1.6 % of mass lost. The second was between 307.1ºC and 337.2ºC with 3.3 % of mass lost in a short, sharp instance. The final major mass loss was between 475.7ºC and 500.9ºC with 3.6 % of mass lost.

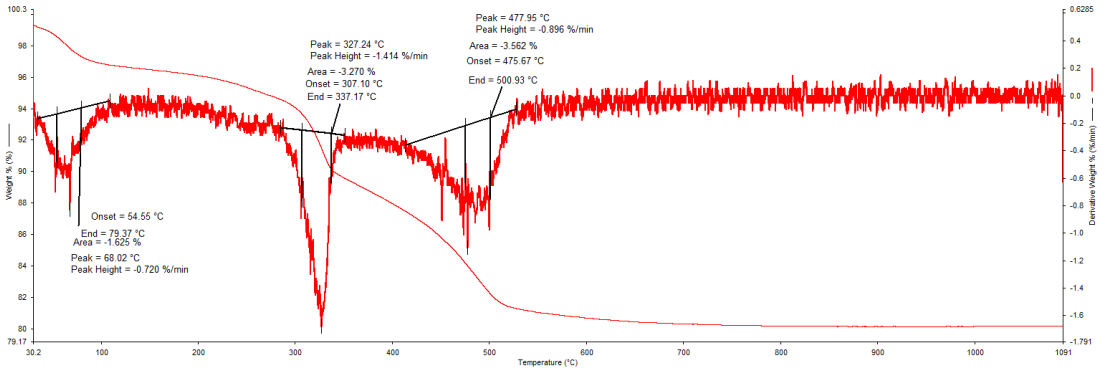

Figure 11.28 A TGA curve (solid red line) with the smoothed first derivative (squiggly red line) included showing the mass loss events noted for the 12 month-treated soil.

When imposed on top of one another (Figure 11.29) there is good agreement between the exo and endothermic events during heating and mass loss events. While the TGA curve does sow the secondary exothermic mass loss event to be relatively quick over a short range of temperatures, the first derivative highlights this much more starkly.

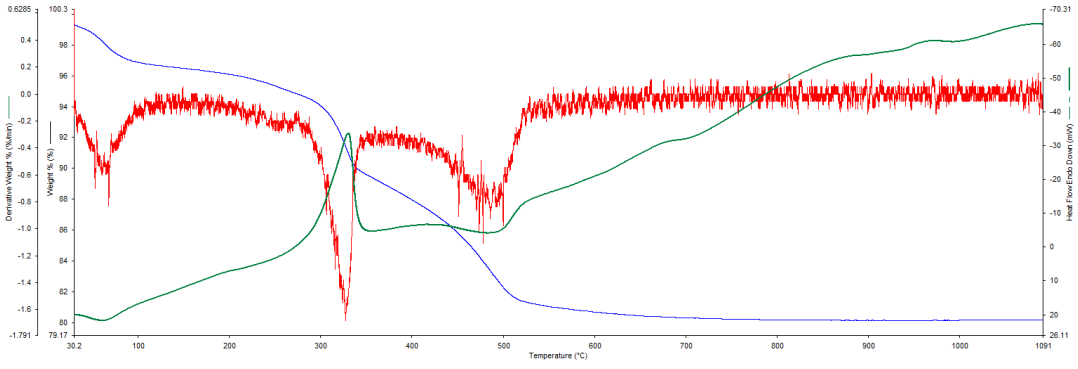

Figure 11.29 . A combined DSC (green), TGA (blue) and first derivative (red) signal imposed on a multiple Y-axis, with X axis remaining constant as the temperature range of the testing for the 12 month-treated samples.

11.2.6 10 MolL^{-1} Samples

Samples that were treated with 10 molL^{-1} showed two small endothermic responses early on in the heating cycle (Figure 11.30), with an endothermic peak noted at 86.5ºC, absorbing 1929 mJ of energy. The second small endothermic response was noted peaking at 303.9ºC with 431.8 mJ of energy absorbed. The third response was a significant short release of energy beginning at 355.8ºC and ending at 387ºC, peaking at 387ºC, with 57433.8 mJ of energy released, a significant drop off noted following peak to the ending of energy release

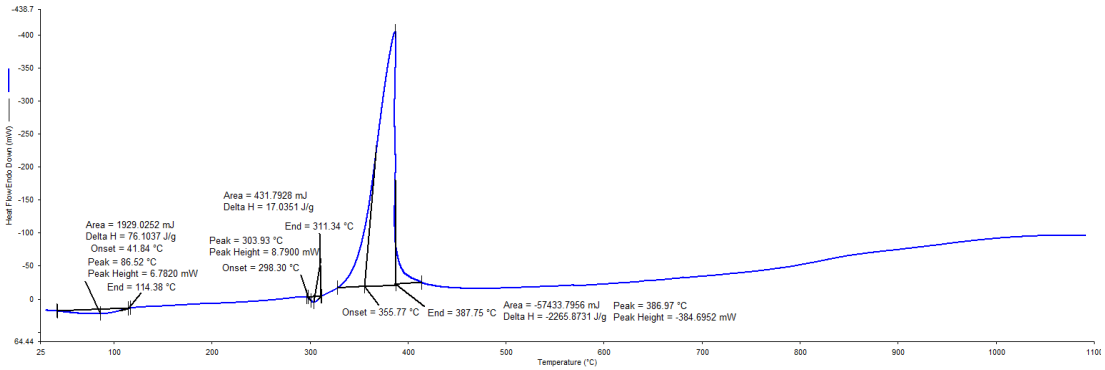

Figure 11.30. A DSC plot showing the enthalpy for a 10 molL^{-1} treated soil sample. The major endo and exothermic events are noted with relevant information included on the graph.

Three mass loss events were noted within 10 mol L^{-1} samples, though these were especially highlighted by the first derivative signal. Initially there was a 3.9 % mass loss event at 80ºC, a second 18.6 % mass loss event at 364ºC and a final, 0.8 % loss at 784.4ºC. It is worth noting though that between 400ºC and 850ºC there was a sharp cessation of the large secondary mass loss event and instead a steady decline was observed

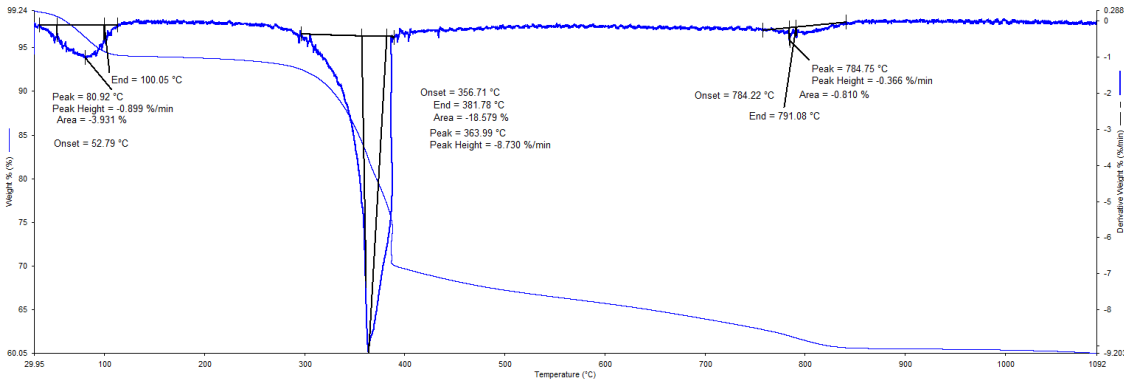

Figure 11.31 . A TGA curve (blue line) with the smoothed first derivative (red line) included showing the mass loss events noted for the 10 molL^{-1} treated soil sample.

When examining the imposed TGA, first derivative and DSC lines on top of one another (Figure 11.32) a few aspects emerge. Two of the three pre-500ºC DSC spikes were observed in the mass loss with 3.9 % lost initially at 80.92ºC, followed by a sharp loss of 18.6 % of mass lost at 364ºC. The TGA mass loss showed a similar response to the DSC signal in that the loss stopped abruptly. A third and final mass loss was noted at 784.8ºC with around 0.8 % of mass lost.

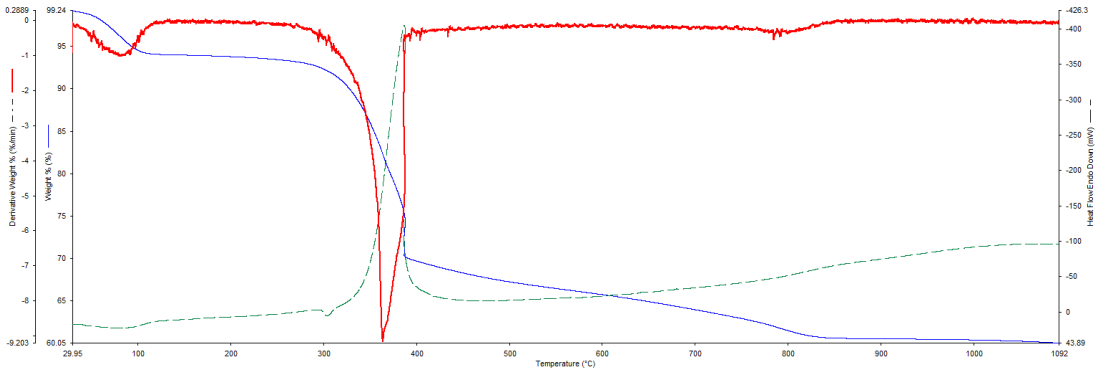

Figure 11.32 C. A combined DSC, TGA and first derivative signal imposed on a multiple Y-axis, with X axis remaining constant as the temperature range of the testing for the 10 molL^{-1} treated samples.

Table 11.2. A summary of key DSC parameters obtained during analyses of soils. Values are split into Peak temperature, onset temperature, area, and delta h. Values recorded are associated with the major enthalpy events. For area and delta H, positive value represents an endothermic event, while negative values are indicative of an exothermic event.

Sample	Peak Temp (°C)				Onset Temp (°C)			Area (mJ)				Delta H (J/g)			
Untreated	N/A	N/A	506	952	N/A	454	934	N/A	N/A	6245	-905	N/A	N/A	369	-535
1 Month	61	320	473	958	278	405	940	568	-4700	2655	-270	38	-312	176	-18
3 Months	65	327	481	955	283	412	940	519	-5557	2972	-224	33	-349	187	-14
6 Months	64	324	475	961	278	405	943	532	-4704	3264	-291	35	-307	213	-19
12 Months	66	330	492	N/A	296	433	N/A	275	-4951	2182	N/A	16	-290	128	N/A
10 MoL-1 sample	87	304	387	N/A	289	356	N/A	1929	432	-57434	N/A.	76	17	-2266	N/A

Table 11.3 A summary of key TGA parameters obtained during analyses of soils. Values are split into onset temperature, peak temperature, area and mass loss.

Sample	Onset Temp (°C)			Peak Temp (°C)			Area (mJ)			Mass Loss Total (%)
Untreated		N/A	466	N/A	N/A	503.8	N/A	N/A	-8.942	14.42
1 Month	NA	282.1	376	58.9	317.3	480	-1.51	-2.475	-5.115	18
3 Months	NA	305.1	442	65.3	327.3	459.7	-1.63	-3.044	-4.531	17.56
6 Months	NA	309.4	452	30.2	319.2	475	3	-2.713	-4.254	18
12 Months	54.55	307.1	476	68	327.2	478	-1.63	-3.27	-3.562	20.83

11.3 FTIR Analysis

Figure 11.33 a and b show the transmittance (%) curves for the samples treated with 2 $molL^{-1}$ K-acetate in comparison with the untreated natural soil, with curves placed in ascending order from untreated at the base followed by 1, 3, 6, and 12 month treatments above. Figure 11.33B shows the same curves, with the major transmittance responses noted by black lines. These lines illustrate new reflectance peaks as well as any potential shifts in reflectance. Responses are divided into two primary sections, the first between 3850–2850 cm^{-1} corresponding to the Al-OH stretching vibrational modes. The second between 1800–650 cm^{-1} corresponding to a variety of structures within the clay including Si-OH vibrational modes, water molecule structures as well as any potential intercalate and acetate reaction structures. Peaks are noted and labelled accordingly.

(a)

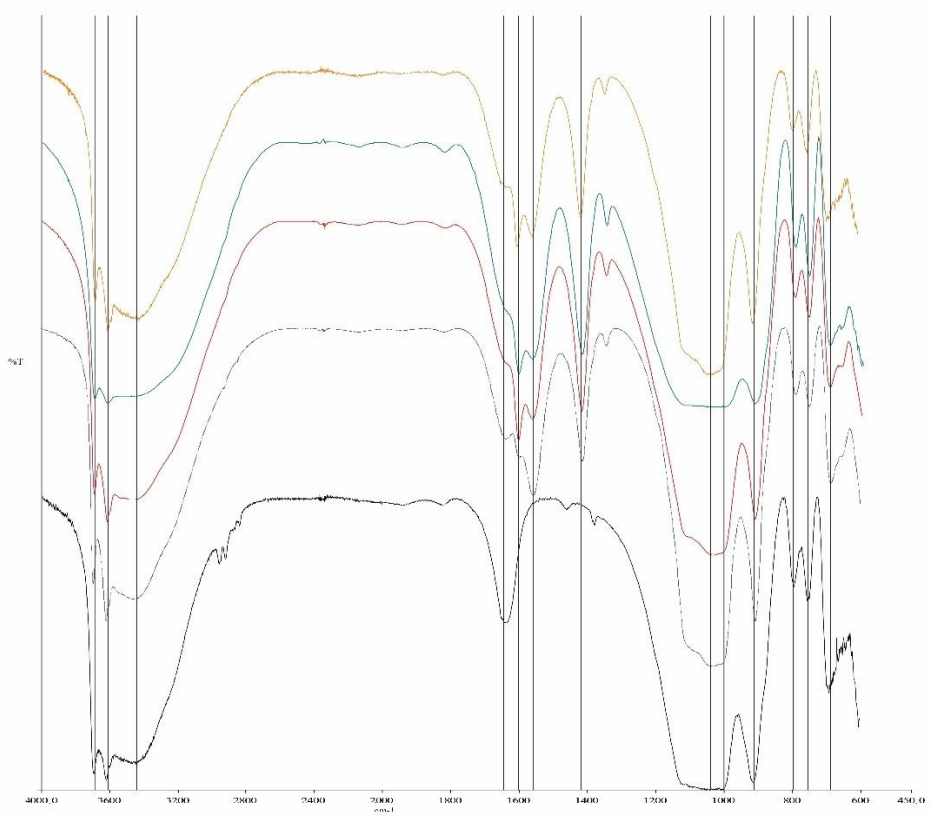

(b)

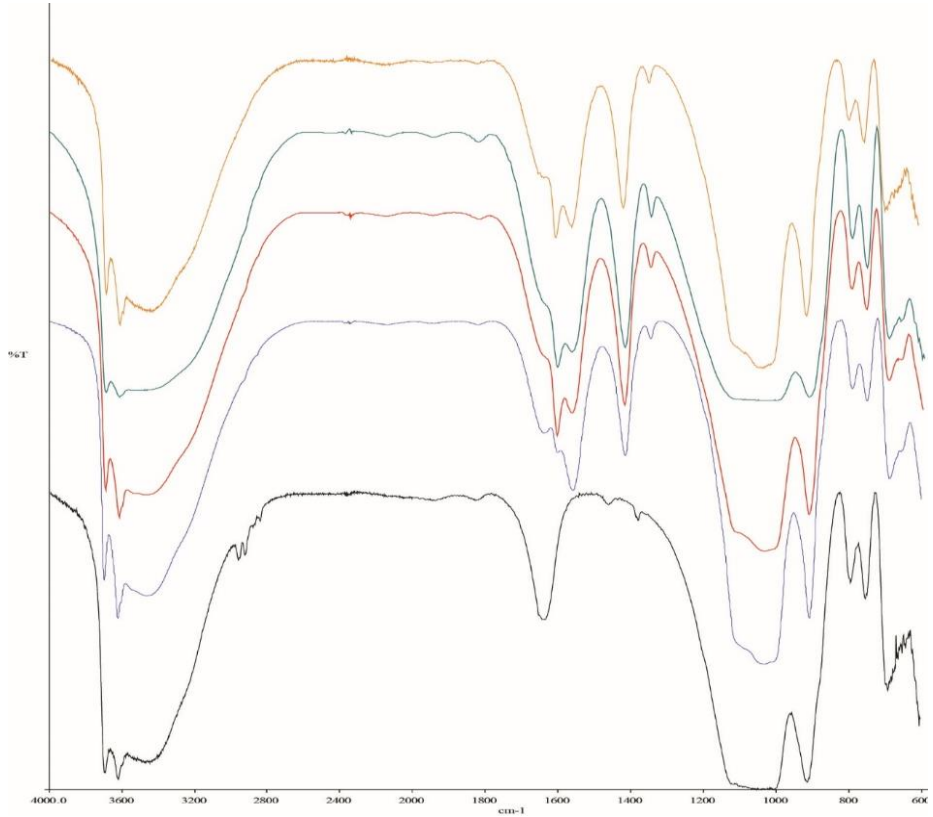

Figure 11.33a. FTIR traces for untreated and treated soil samples, with vertical lines denoting the locations of consistent major peaks observed within treated samples for comparison to untreated soils. B. FTIR curves for treated and untreated soil samples with line correspondence as follows: Black = untreated, Blue = 1 month treated samples, Red = 3 months treated samples, Green = 6 months treated samples, Yellow = 12 months treated samples.

For analysis of FTIR results, peak locations are split into two main sets of wavenumbers. The first section sits between 3850–2850 cm^{-1}, and the second 1750–650 cm^{-1}. It should be noted here that these wavenumber lengths have been selected due to expectations of the location of responses based on values presented in literature (Frost, 1997). The results for both of these can be seen in detail, with some speculated assignments to wavenumbers, in Table 11.4. These speculated wavenumber assignments are made based on values presented elsewhere in various pieces of published literature (Frost, 1997a; Frost, et al., 2000a; Frost, et al., 2000b; Cheng et al., 2014)

Table 11.4. A summary of the various key FTIR peaks for treated and untreated soil samples. Assignments have been made to wavenumber lengths where possible.

	Wavenumber (cm^{-1})				
Assignments	**Untreated**	**1 Month**	**3 Month**	**6 Month**	**12 Month**
Stretching perpendicular surface -O-H (V_1)	3697	3695	3695	3696	3696
O-H stretching of inner hydroxyls V_2	3623	3620	3620	3621	3620
Stretching vibration of OH		3609	3600		3600
Remnant interlayer water	3591				
Remnant interlayer water	3478	3467	3462	3463	3454
Bending of -OH in adsorbed water (hole)	1650				
Water	1635				
		1600	1603	1604	1604
Intercalated double bonded COO ion		1560	1554	1559	1560
O-C-O hydrogen bond to inner OH		1417	1418	1418	1419
CH_3 interaction with Silica sheet		1342	1341	1343	1346
(Broad band) Si-O stretching	1042	1035	1035	1035	1035
O-H deformation of inner hydroxyls	912	912	911	911	910
Symmetric stretching of Si-O	793	795	794	793	793
Perpendicular Si-O stretching	751	753	752	752	751
Perpendicular Si-O stretching	689	691	691	691	694

11.3.13850–2850 cm^{-1} Spectrum

For the untreated soil in the 3850–2850 cm^{-1} spacing the -OH inner surface hydroxyl transmittance peaks were noted, with the -OH groups perpendicular to the surface at 3697 cm^{-1} (V_1 band) observed. There were also transmittance peaks observed at 3623 (v_2 band) observed corresponding to the stretching OH group co-ordinated between the tetrahedral and octahedral halloysite unit sheets. Following from this a small secondary peak at 3591 cm^{-1} likely corresponds to remnant interlayer water within the halloysite crystal lattice. A

much smaller and gradual peak at 3478 cm^{-1} was also noted, probably a potential secondary peak for the remnant interlayer water molecules.

The treated samples showed consistency with several peaks observed in the untreated soil, with the major V_1 and V_2 vibrational bands seen occurring at 3695–3696 cm^{-1} for treated soils and 3620–3621 cm^{-1}. Remnant interlayer water was observed between 3454–3467 cm^{-1} for treated soils, indicating a downshift in location of the peak of the water from the untreated soil peak at 3478 cm^{-1}. For all treated samples no new peaks were observed, indicative of a lack of intercalation by the potassium ions into the halloysite crystal lattice.

11.3.2 1750–650 cm^{-1} Spectrum

The untreated soil showed six peaks in the lower 1750–650 cm^{-1} range. These were the initial peak at 1635 cm^{-1}, representative of the bending -OH of the adsorbed water in the halloysite lattice. A number of smaller peaks were noted between the 1635 cm^{-1} and 1042 cm^{-1} peak, although none of these was significant enough to designate a specific peak. The major peak noted at 1042 cm^{-1} is likely a broad band reflection of the Si-O stretching of the silica sheet within the halloysite crystal structure. This was followed by the OH deformation peak for the inner hydroxyls at 912 cm^{-1}. Symmetric and perpendicular stretching reflections of the Si-O bonding within the silica sheet are also observed in the FTIR curves at 793, 751, and 689 cm^{-1}, respectively.

The treated soil showed reasonable agreement with the values observed for the untreated soil for several reflections in the 1750–650 cm^{-1} range Some variations noted include for the broad band Si-O stretching reflection, with a downshift from 1042–1035 cm^{-1} observed. Three new features and a potential significant downshift were present in the treated transmittance peaks when compared to the untreated soil. The first of these was a possible downshift in the bending of the OH adsorbed water peak, with the peak shifting down from 1635cm^{-1} in the untreated soil samples to around 1603 cm^{-1} for the treated samples. On top of this, three new transmission peaks were observed. The first around the 1560 cm^{-1} mark, indicative of a double bonded COO ion that has intercalated into the halloysite unit. The second occurred around 1418 cm^{-1}, showing an O-C-O ion hydrogen bonded to an inner hydroxyl group of the halloysite crystals. Finally, the third was a peak around 1343 cm^{-1} showing the interaction of the CH_3 unit from the acetate unit interacting with the silica sheet of the halloysite crystal unit.

11.4 XRF

Untreated clay (KGU), shown in Table 11.5 showed good agreement with major element compositions of other halloysitic rich soils of rhyolitic origin within New Zealand, with other studies generally showing SiO_2 and Al_2O_3 compositions ranging between 41–47 % and 32–42 %, respectively (Churchman & Theng, 1984; Lowe & Percival, 1993). Iron (expressed as Fe_2O_3) concentrations were slightly higher than a number of other halloysitic rich deposits within New Zealand (0–1 %) but showed agreement with soils within the upper central North Island, including within the Bay of Plenty and Waikato (3–8%) (Hughes, 1966; Churchman, 1970; Tonkin, 1970; Kirkman, 1977; Marsters, 1978).

Table 11.6 and Figure 11.34 shows the relative proportions of major elements within the treated soils analysed using XRF compared to untreated soil, with loss on ignition (LOI) also included. Treatment of soil cores has notably impacted the element percentages, with a drop in the two major oxides (SiO_2 and Al_2O_3) of halloysite clay of around 7 % silica and 6 % alumina seen. In contrast to this, a 4.3–5.3 % increase in potassium has occurred, with an increase in LOI of 5–8 % noted for samples treated over the 12 months. Minor variations with other elements/oxides were noted, with main variation observed in iron contents (Fe_2O_3) of -0.57%–1.11 % seen. While small overall percentages, most samples (1 month, 3 months, 12 months) all increased in iron content, with 6 month-treated samples slightly declining in iron content.

Table 11.5. Summary results for major elements/oxides measured during XRF analyses of treated and untreated soil samples.

Sample	SiO_2 (%)	Al_2O_3 (%)	TiO_2 (%)	MnO (%)	Fe_2O_3 (%)*	MgO (%)	CaO (%)	Na_2O (%)	K_2O (%)	P_2O_5 (%)	LOI (%)
KG U	44.73	33.09	0.71	0.14	6.22	0.13	0.09	0.07	0.11	0.05	15.34
KG 1 Mo	37.95	27.44	0.73	0.11	6.71	0.09	0.04	0.06	4.56	0.06	22.68
KG 3Mo	37.43	26.87	0.79	0.12	6.94	0.09	0.06	0.10	4.89	0.06	22.94
KG 6Mo	37.73	27.81	0.64	0.09	5.65	0.07	0.04	0.06	4.37	0.05	23.92
KG 12mo	38.18	27.5	0.78	0.05	7.33	0.08	0.04	0.07	5.31	0.07	20.75
KG 10M	18.46	13.33	0.30	0.04	2.56	0	0.04	0.34	25.32	0.03	38.70

Table 11.6. The differences between untreated and treated samples across all major elements/oxides, as well as changes in LOI.

Sample	SiO_2 (%)	Al_2O_3 (%)	TiO_2 (%)	MnO (%)	Fe_2O_3 (%)*	MgO (%)	CaO (%)	Na_2O (%)	K_2O (%)	P_2O_5 (%)	LOI (%)
KG 1	-6.78	-5.65	0.02	-0.03	0.49	-0.04	-0.04	-0.01	4.45	0.01	7.34
KG 3	-7.30	-6.22	0.08	-0.02	0.72	-0.04	-0.03	0.03	4.78	0.01	7.60
KG 6	-7.00	-5.28	-0.07	-0.05	-0.57	-0.06	-0.05	-0.01	4.26	0.00	8.58
KG 12	-6.55	-5.59	0.06	-0.09	1.11	-0.05	-0.05	0.00	5.20	0.02	5.41

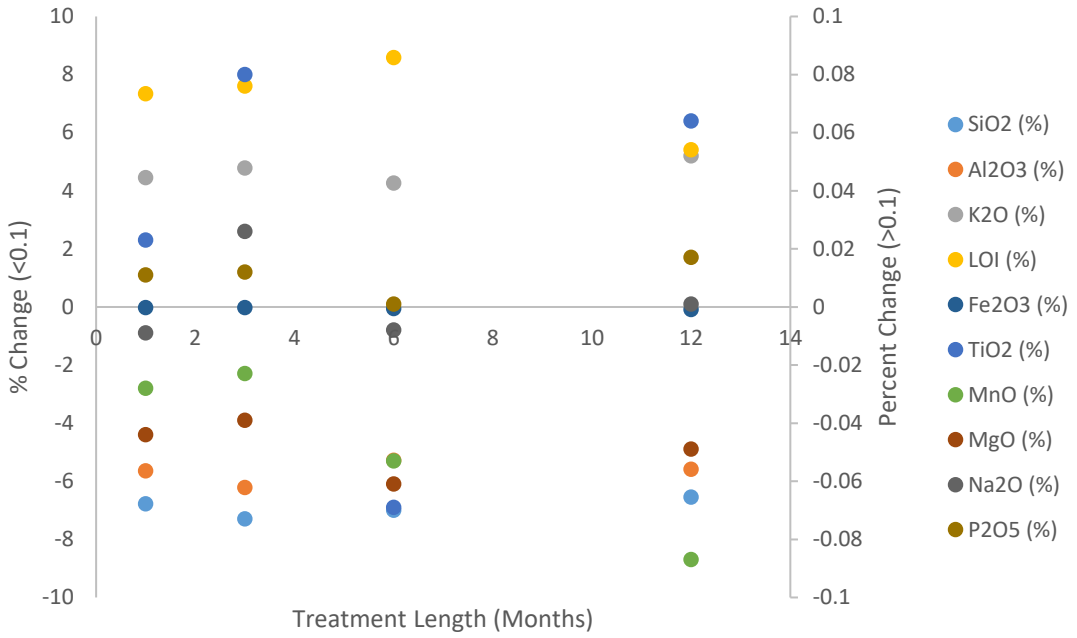

Figure 11.34. Percent changes for the major elements/oxides observed for treated samples. Samples with changes greater than 0.1 % are represented by the left-hand y-axis, while those with changes smaller than 0.1 % are represented by the right-hand axis. Colours for the different elements/oxides can be seen in the legend within the figure.

11.5 Crystallinity Index and Hydration Ratios

Table 11.7 shows the crystallinity indices and hydration ratios for both treated and untreated soils. Crystallinity indices calculated using XRF data showed a relatively high crystallinity for both treated and untreated clay samples, indicating a relatively high-level degree of order and low variability in morphology of the halloysite within the sample. Overall, a very minor (0.001) increase in crystallinity is noted, though no significant changes are observed. Hydration status of the clays indicate that the clays analysed were relatively high with minimal dehydration observed in the bulk samples providing good indication for the presence of a large volume of hydrated halloysite within the sample. Lowe and Nelson (1994) examined crystallinity data for halloysites based on the sharpness of XRD-derived peaks.

Table 11.7. Crystallinity indices and hydration ratio for the untreated and treated soils, with the three methods of calculating crystallinity presented.

Sample	XRD method	FTIR Method	DTA (Slope)	Hydration Ratio
Untreated	4.86	0.97	2	0.85
1 Month	3.13	0.87	1.88	0.85
3 Month	2.90	0.91	1.87	0.84
6 Month	2.83	0.98	1.78	0.88
12 Month	2.76	0.88	1.76	0.86

11.6 CEC, Base Saturation and Major Cations

Testing for major cations and CEC (Table 11.8) of treated soils showed a relatively high base saturation coupled with low CEC for natural untreated soil, with a CEC of 6 cmol/kg reported alongside a 70 % base saturation of the soil. For untreated soil, divalent cations were more dominant than their monovalent counterparts, with 1.5 and 1.17 cmol/kg for Ca^{2+} and Mg^{2+} noted, compared to 0.92 and 0.61 cmol/kg for K^{+} and Na^{+}. Treated soils showed a marked increase in CEC (94–114 meq/100), with a significant increase in base saturation. This increase in base saturation and CEC was not unexpected due to treatment of the clay with K- acetate.

As a result, base saturation may not necessarily reflect the actual saturation, though the increase in pH of the soil does support the likelihood that base saturation was close to 100 %. K^{+} was heavily favoured in the major cation distribution with between 92.2–111 cmol/kg. Ca^{2+} and Mg^{2+} both showed a drop of around 1 cmol/kg following treatment with values measuring < 0.5–0.6 and 0.13–0.31 cmol/kg, respectively. Sodium in contrast showed an increase compared to untreated soil, increasing from 0.61 to 1.57–2.04 cmol/kg. This increase could be related to impurities within the potassium acetate or due to remnant ions within the De-Ionised (DI) water used to makeup treatment solutions. A point to note here is the drop in CEC and base saturations of the 12 month-treated soil (when compared to the 6 month-treated sample prior to that). The cause of this drop is unknown, as it may be due to influences within the extraction process, sub sampling bias or other factors.

Table 11.8. CEC (cmol/kg), base saturation (%) and cation concentrations (cmol/kg) for untreated and treated soil samples as reported by Hill Laboratories.

Soil	CEC cmol/kg	Base Saturation %	Potassium cmol/kg	Calcium cmol/kg	Magnesium cmol/kg	Sodium cmol/kg
Untreated	6	70	0.92	1.5	1.17	0.61
1 Month	104	100	101.1	0.6	0.31	1.89
3 Month	114	100	111	0.6	0.26	2.04
6 Month	110	100	107.3	<0.5	0.18	2
12 Month	94	100	92.2	<0.5	0.13	1.57

11.7 Zeta Potential

Zeta potential measurements (Table 11.9) undertaken have all been derived from a 1:100 dilution of soil/DI water mixtures sent to the University of Canterbury. This high dilution factor was necessary due to poor quality results and inconsistent data produced by the undiluted (untreated, 1- , 6-months) and 1:10 dilution (1- and 12-months) samples. This was speculated to have occurred as a result of a high concentration of salts within the soil likely causing issues with the zeta potential machine, even after calibration.

The zeta potential measurements for the untreated soil were lower than for the accompanying treated samples by between 10–15 mV, with -25 mV measured for untreated samples. Treated samples showed a decrease in zeta potential, with values ranging from -36.1 mV to -40.4 mV across the 12 months of treatment. Conductance shows little consistency outside of conductivity being higher for treated samples when compared to that of the untreated samples, as would be expected due to the potential presence of potassium acetate within the clay. Zeta potential deviation across treated samples ranged between 4–6 mV, with relatively good agreement in zeta potential distribution curves.

Table 11.9. Zeta potential (mV), conductivity (mS/cm) and zeta size (nm, where reportable) for treated and untreated soil as measured by the University of Canterbury. Note ND represents where no data have been recorded.

Sample	Zeta Potential mV	Conductivity mS/cm	Zeta Size nm
Untreated	-25.1	0.00349	410.8
1 Month	-36.1	0.0274	ND
3 Month	-40.4	0.146	ND
6 Month	-38.8	0.0782	ND
12 Month	-39.1	0.149	ND

11.8 PZC Analysis

Table 11.10 shows the various values derived during PZC analysis testing. Overall pH change from initial pH to the PZC pH showed relative consistency across all samples, with between 2.5–2.61 change in pH between the initial pH and subsequent PZC achieved. While the range between the initial pH and PZC pH was relatively consistent, all other aspects measured for untreated versus treated samples showed marked change.

Table 11.10.Streaming potential (mV) measurements for treated and untreated soil, with the pH of the point of zero charge (PZC) and the amount of pH change required to achieve this.

Sample	Streaming Potential (mV)	Initial pH	PZC pH	pH change	Vol added (ml)
Untreated Clay	-618	6.43	3.82	2.61	4.3
1 Month	-180	8.11	5.6	2.51	9.2
3 Month	-137	8.31	5.71	2.6	9.6
6 Month	-121	8.17	5.67	2.5	9.8
12 Month	-120	8.39	5.83	2.56	9.5

Streaming potential on the other hand showed a significant increase for treated samples when compared to the untreated. Starting potentials showed a change of 500 mV between the untreated and 12 month-treated clay. Further, the pH of the treated soil was much higher than the untreated soil, with the treated clay exhibiting a slight alkaline response and mildly acidic PZC and the untreated clay showing a slightly acidic soil, followed by an acidic PZC. Similarly, more than twice the amount of alum titrant was required to achieve the PZC for the treated samples (9.2–9.8ml) when compared to the untreated soil (4.3 ml).

When looking at the correlativity of the streaming potential to the initial and PZC pHs (Figure 11.35), streaming potential is strongly correlated in a linear fashion in both cases ($R^2 = 0.989$ for initial, and $R^2 = 0.994$ for PZC pH).

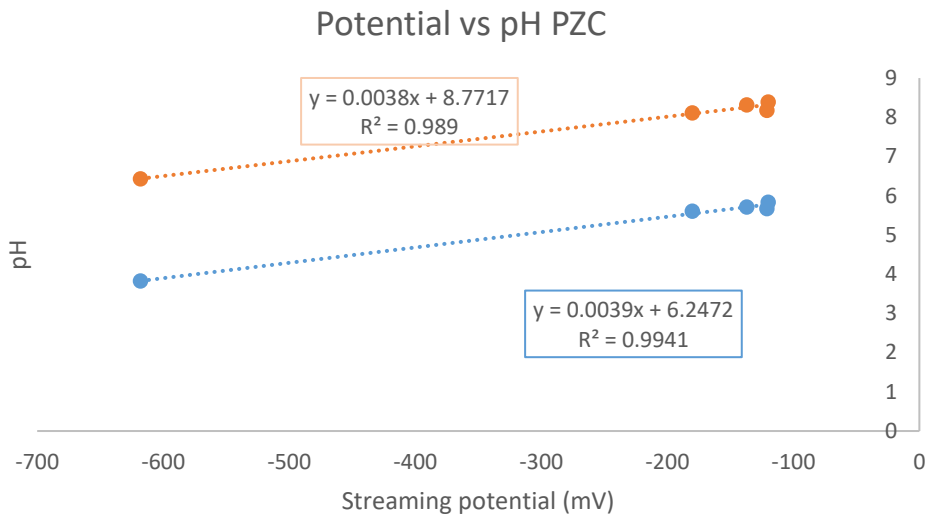

Figure 11.35. Streaming potential and pH for treated and untreated samples from this study with initial pH and initial streaming potential plotted as the orange dots and dashed line, while blue dots and lines represent the final pH and initial streaming potential.

While potentially indicating the possibility of relating pH to streaming potential, when comparing the untreated natural soils to other similar sensitive soil material from the Tauranga region (Figure 11.36), a weaker, negative correlation is still present for the initial pH to streaming potential (R^2 =0 .79) with higher pH's noted for higher streaming potential. For PZC pH, a positive strong positive correlation on the other hand does still exist ($R^2 = 0.91$).

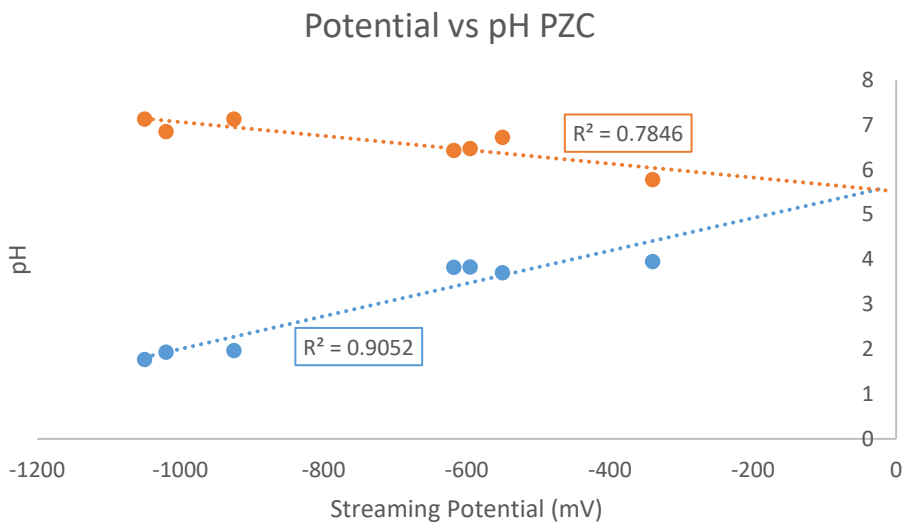

.

Figure 11.36.Streaming potential for Tauranga region clay samples plotted against their pH for the initial pH and streaming potential (orange dots and dashed line), and the final pH and initial streaming potential (blue dots and line).

Figure 11.37 shows the titrant curves for the treated and untreated samples. It is evident from the titrant curves that both the treated and untreated samples reach close to the PZC quite rapidly. Treated samples reached around 20 mV of the PZC after approximately 1 ml of titrant being added; in contrast, the untreated natural soil required around 2.3 ml of titrant to reach a similar streaming potential. To overcome this last 20 mV though, natural soil only required 2 ml of titrant, while all treated soils required over 8 ml of titrant to reach the PZC, with a large pH buffer zone appearing.

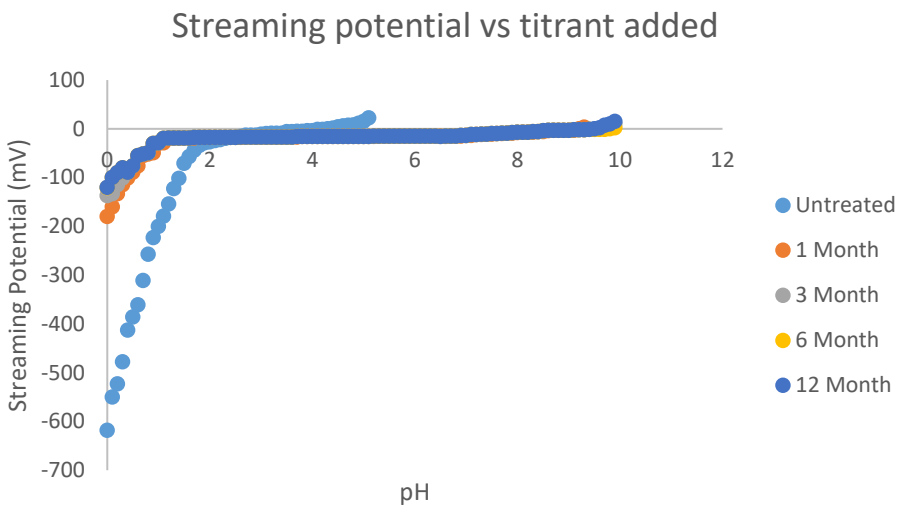

Figure 11.37. Streaming potential versus the pH of the sample at each addition of the alum titrant for treated and untreated soils. The respective colours corresponding to specific samples can be found in the legend within the figure.

11.9 Surface Area, Pore Volume and size analysis

Samples tested in the BET gas analyser to determine the respective values for specific surface area, and pore sizes and volumes are shown in Table 11.11

Table 11.11. Absorption results for treated and untreated soils derived through nitrogen absorption. Results for surface area, pore volume, micro and mesopore size are included.

Sample	Surface Area (BET)	Surface Area (BJH)	Pore Volume (Micropore)	Pore Volume (Mesopore)	Micropore Size (Diameter)	Mesopore size (Diameter)
	m^2g^{-1}	m^2g^{-1}	cm^3g^{-1}	cm^3g^{-1}	Å	Å
Untreated	46.10	25.01	0.019	0.17	7.60	30.64
1 Month	34.84	26.55	0.010	0.15	7.35	34.56
3 Months	45.42	37.61	0.016	0.19	7.27	31.92
6 Months	32.26	28.22	0.012	0.15	8.27	30.44
12 Months	36.12	34.55	0.013	0.27	10.97	32

.

Untreated values for desorption values are shown in Table 11.12**.** Surface area appears to reduce in the micropore range on average, while the surface area in the mesopore range increases over the course of the treatment. This trend seems to continue for pore volume, while both micro and mesopore diameter both increase over the treatment.

Table 11.12. Nitrogen desorption results for the untreated soil. Results for untreated soils are included due to issues with nitrogen desorption testing for pores potentially infilled with metal salt precipitates.

Sample	Surface area (BJH)	Pore volume (Mesopore)	Mesopore Size (Diameter)
Untreated (desorption)	33.7	0.1384	48.58

One aspect to examine is the pore size distribution of the sample in the mesopore range (Figure 11.38). For untreated soil within the mesopore range, two main peaks occur. The first is at 34 Å, the second at 41 Å. After the 50 Å peak there is a smoothing of the curve, indicating consistency in the pore space and a lack of distinct change, hence suggesting few pores of this size.

Samples treated for 3 and 6 months displayed a much smoother response, with 6 months, after repeated tests, showing an unexpected response with pore size increasing after 100 Å at a peak, while the 3 month-treated sample showed a small peak around 35 Å similar to that for the untreated sample. Samples tested for 1 month showed reasonable consistency with the untreated sample with an initial peak at 34 Å, and 52 Å, though the 41Å peak disappeared. The 12 month-treated sample on the other hand showed a small expansion to 36 Å, as well as either a shrinking from the 50 Å peak, or expanding of the 41 Å peak to 44 Å. This pore size distribution in the mesopore range fits well with the general BJH values, with an expansion of mesopores occurring, albeit small.

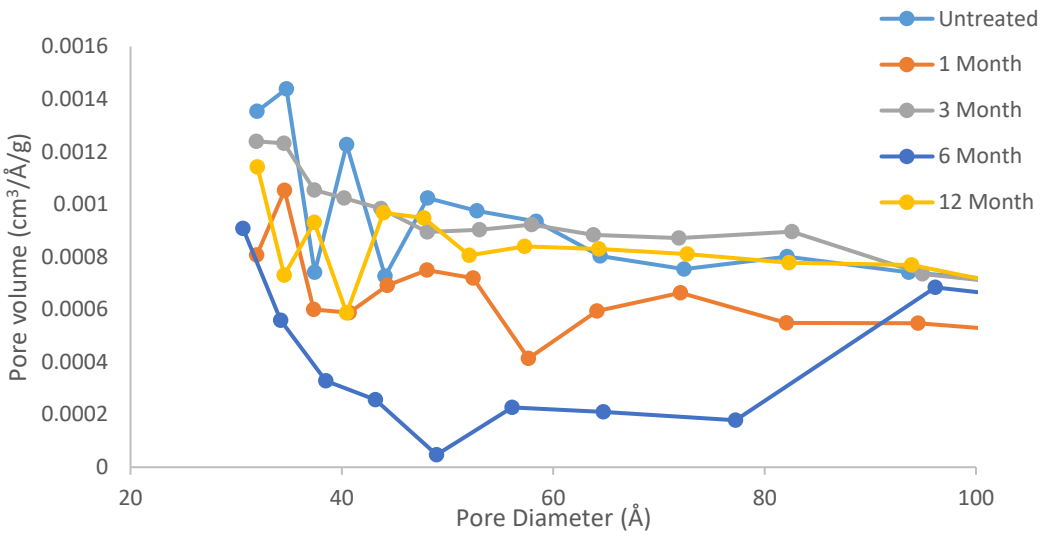

Figure 11.38. Pore volume plotted against pore diameter for treated and untreated soils to show the various size ranges of the pores within the halloysite pre- and post-treatment.

11.10 SEM Analysis

11.10.1 Size and Morphology

Table 11.13 shows the average percentage for halloysite morphologies determined via clay morphology counting across multiple SEM images for the untreated and treated soils. Three primary forms of halloysite were noted in SEM images consistently across all treatments: spheroidal, tubular and halloysitic books.

Spheroidal halloysites have not been distinguished in this instance between the more conventional spheroids and the newly identified mushroom-cap morphology, as reported by Kluger *et al.* (2017). This was due to the difficulty in observing the open cap ends in images, especially within treated samples with open ends often aggregating and appearing to 'bond' with other spheroid surfaces (as shown for natural samples by Kluger et al., (2017)).

Across all samples, around 88.5 % of all halloysite was made up of spheroidal morphology, accompanied by around 11 % of tubes and 0.5 % halloysitic books (as reported by Cunningham et al., (2016)). Spheroid domination ranged between 84–92 %, with tubules ranging from 6–15 % of total morphologies. Books were much less frequent and only observable in three of the five averages.

Table 11.13.Average counts for the clay morphology across 10 images for each of the treated and untreated soil samples, with standard deviations included.

Morphology	Count % (untreated)	Count % (1 Month)	Count % (3 Month)	Count % (6 Month)	Count % (12 Month)	Average %
Spheroidal	92.3 (SD=24)	84.3 (SD=13)	91.3 (SD=10)	86.5 (SD=16)	87.7 (SD=11)	88.4
Tubular	6.2 (SD=4)	15.7 (SD=6)	8.1 (SD=7)	13.5 (SD=5)	11.8 (SD=3)	11.0
Books	1.5 (SD=2)	0.0 (SD=1)	0.6 (SD=2)	0.0 (SD=1)	0.5 (SD=1)	0.5

The average size of the dominant spheroids is shown in Table 11.14 and Figure 11.39. Lengths were determined from measurements taken on 45 individual spheroids across a variety of images. Lengths were determined within the Hitachi image viewing software using a linear measurement tool. Across the 12 months of measurement the average spheroid shrank from 343 nm diameter to 176 nm, a reduction of 167 nm. This shrinkage appears to be consistent as the size and length of the treatment appear to be correlated, with an initial rapid shrinkage in the clay spheroid during the first 3 months (-140 nm), before a much smaller reduction in diameter over the remaining 9 months (-27 nm).

Untreated samples appear to have a much narrower range of sizes compared to those of the first and third months of treatment, although the overall sizes observed for minimum, and maximum were larger than for the treated samples (234 nm untreated; 157 and 100 nm for 1 and 3 months minimum size; 470 nm versus 420/347 nm for maximum). For treated samples, the deviations and range between maximum and minimum sizes reduced over the course of the 12 months of treatment, with samples appearing to be reaching a new diametric equilibrium as the length of time of treatment went on.

Table 11.14. Average size of halloysite spheroids for the untreated and treated soils. Various statistics are included.

	Untreated (nm)	1 Month (nm)	3 Month (nm)	6 Months (nm)	12 Month (nm)
Size (nm)	343	269	203	188	176
Std Dev	57	66.99	51.57	50.87	46.55
Min	234	157	100	90	120
Max	470	420	347	281	303
Range	236	263	247	191	183

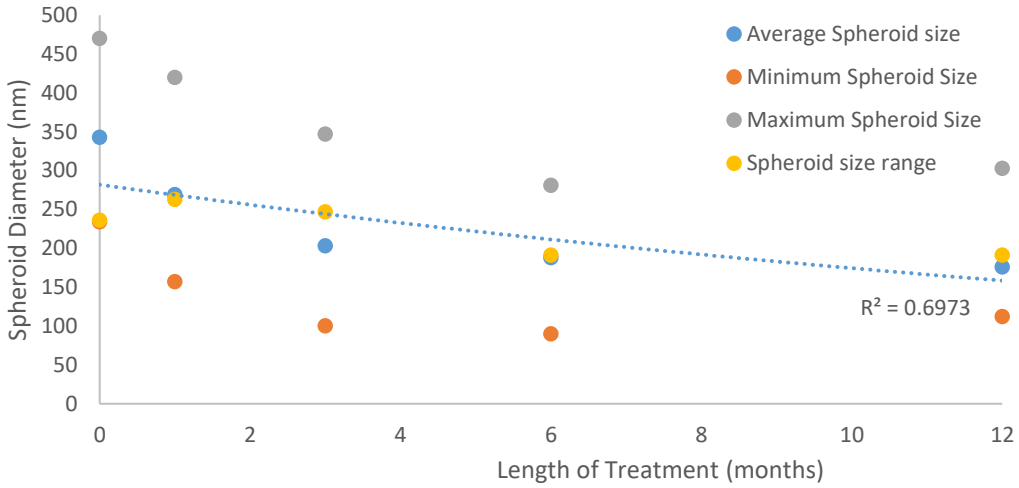

Figure 11.39.Average spheroid size and associated statistics in a scatter plot form. Data derived from Table 11.14.

11.10.2 Untreated Soil

SEM of the clay powder showed dominance throughout the sample of halloysite. Table 11.13 shows the relative proportions of the varying morphologies of halloysite within the samples based on clay counting of the individual halloysite particles. Clay counting of the SEM images indicated that morphology was overwhelmingly dominated by spheroidal mushroom-cap halloysite (92 %), with small amounts of halloysite tubes and books present also (6.2 % and 1.5 %, respectively).

Figure 11.40 and Figure 11.41(a-f) show the overall bulk fabric of the untreated clay at 22,000 times magnification. Bulk fabric showed large quantities of the halloysite of varying morphologies present, with spheroidal mushroom caps dominating. Additional minerals were difficult to distinguish due to the large volume of halloysite covering most aggregate surfaces, though some weathered volcanic glass shards, highlighted by the red circles, were noted within the clay fractions. These glass shards showed classic sharp edges with conchoidal fractures on their surfaces.

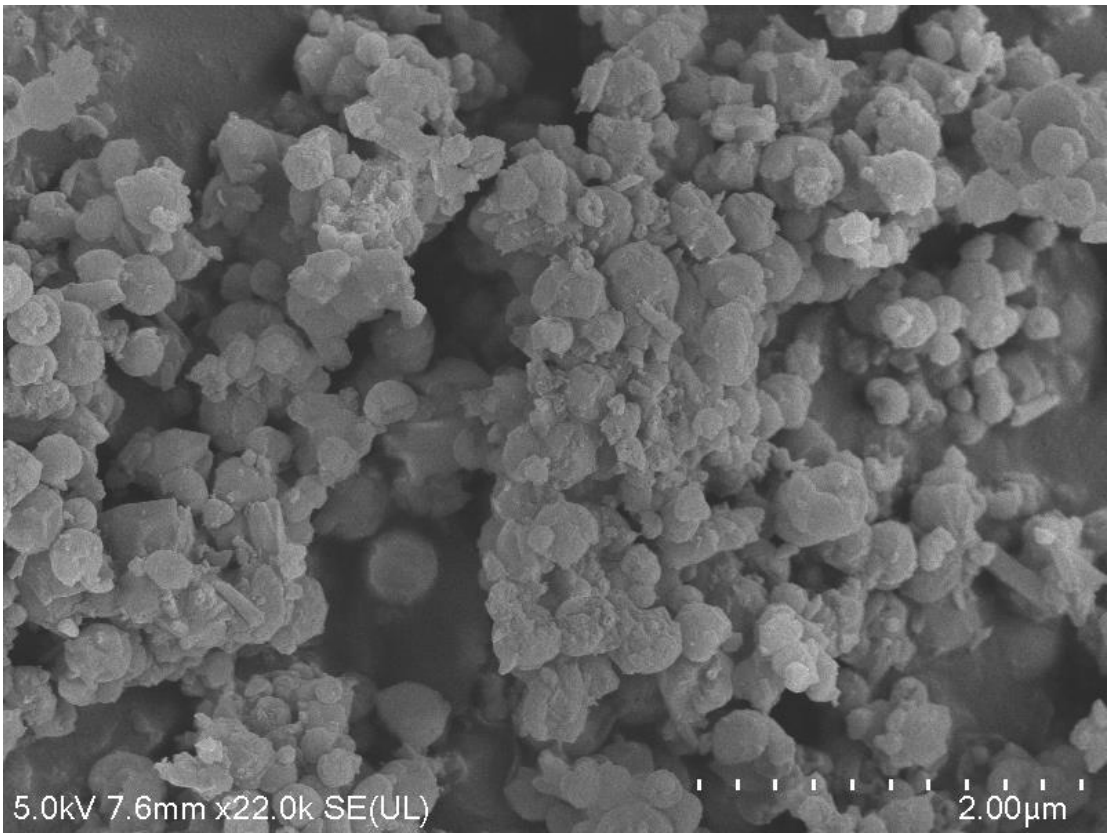

Figure 11.40. SEM image of untreated halloysite at a 2 µm scale..

Untreated halloysite spheroids averaged around 339 nm in diameter, ranging from 234 nm for smaller particles, and up to 470 nm for the largest halloysites (with a standard deviation of 65 nm). Average diameters of the opening on the base of the halloysite spheroid mushroom-cap shaped particles were just over half the diameter of the halloysite spheroid itself. It should be noted though that this average is potentially impacted by the fact that spheroids are desiccated, and openings have potentially shrunk during drying. Further to this there were also significantly fewer openings available to measure, meaning a much smaller sample size was used because of halloysite spheroid orientations within the SEM imagery, with the opening usually facing away from the imager.

Tubular halloysites were, on average, around 440 nm in length and 100 nm in outer diameter. Due to the orientation of the tubes, the opening was rarely facing directly to the imager, which as result meant the inner diameter was unmeasurable.

Halloysitic books had a similar challenge posed in measuring the dimensions of the constituent plates due to the orientation and covering of the plates themselves by other halloysite particles. With this said, it was possible in several instances to measure the

spacing between individual sheets, with an average spacing of 10.2 nm noted. While undertaking the imagery some charging did occur on the clay surfaces, though this charging usually occurred after an extended period of usage (two hours or more), allowing for better quality images to be taken.

(a)

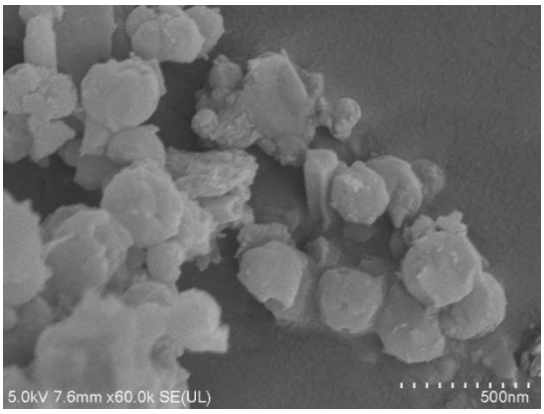

(b)

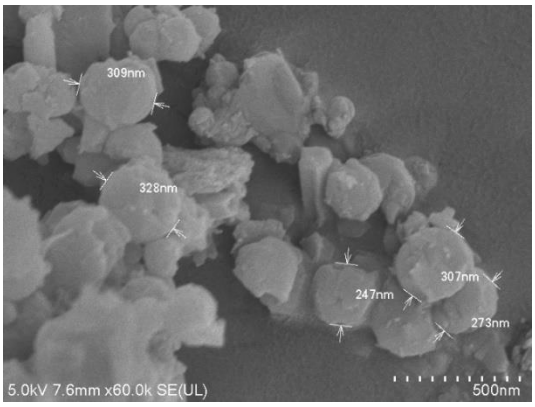

(c)

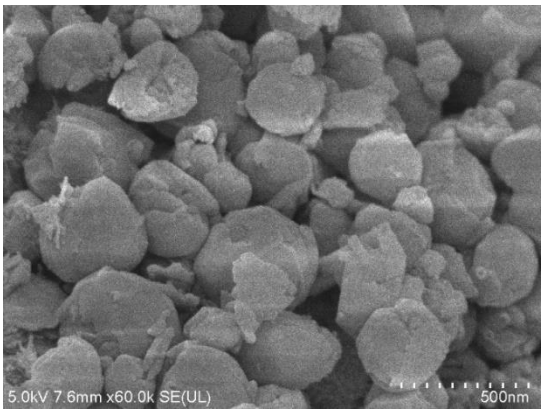

(d)

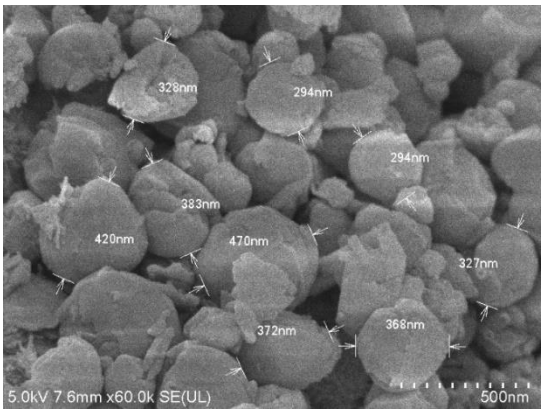

(e)

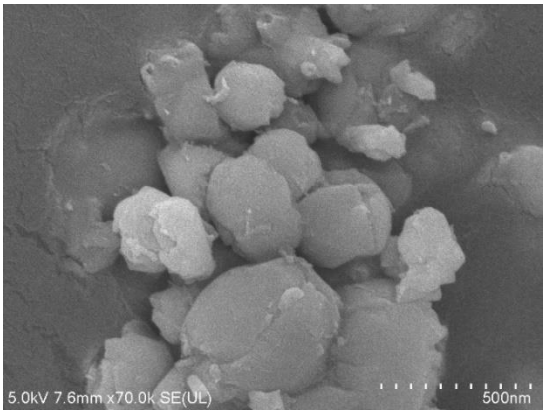

(f)

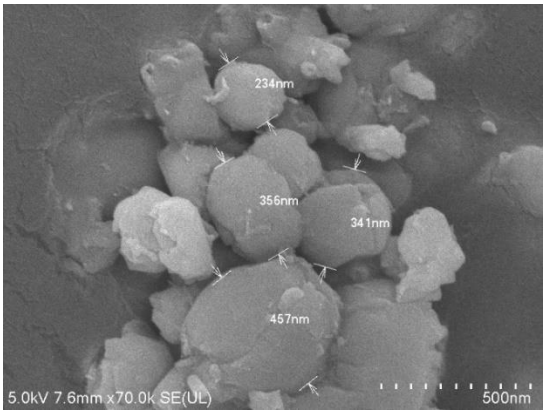

Figure 11.41(a). SEM images at 60,000 magnification of a randomly selected sample of halloysite. Spheroids, books and tubes noted in the images. (b). The same SEM image as 29a, but with several diameters for the spheroids included. (c). An SEM image of halloysite (with some charging) at 60,000 magnification. (d). The same image as 29c though in this instance measurements for halloysite spheroids are included. (e). Images of untreated halloysite spheroids at 70,000 times magnification. (f). The same image as 29e, though this image has spheroid diameter included.

11.10.3 1 Month Treated Soil

Samples treated for one month showed a much larger volume of tubular morphology than untreated, though the spheroidal halloysite still dominated. Issues with charging and tearing within images as a result of the highly charged clay surfaces were present, resulting in loss of quality in some instances (Figure 11.42 a and b). One aspect to note for samples after one month was the tendency for fewer exposed mushroom cap base recesses, with most spheroids congregating and clumping. Figure 11.42c shows the distribution of clay throughout a larger portion of the stage, with all possible soil 'clumps' covered in a large volume of halloysite spheroids. Figure 11.42a also shows the beginning of a precipitate-like substance on top of the clays in some instances, presenting as spots of noted charging when compared to the larger clay surfaces around.

(a)

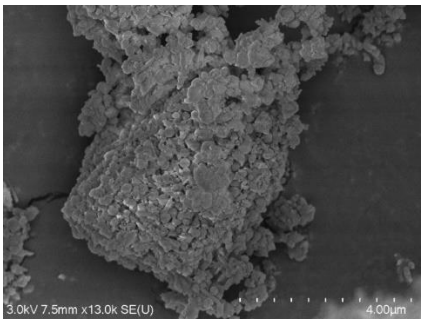

(b)

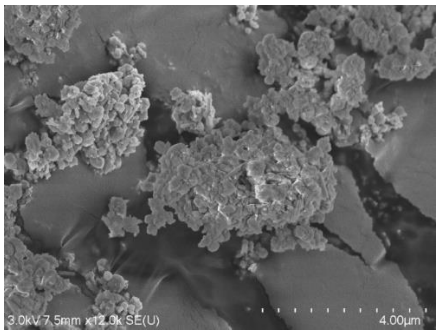

(c)

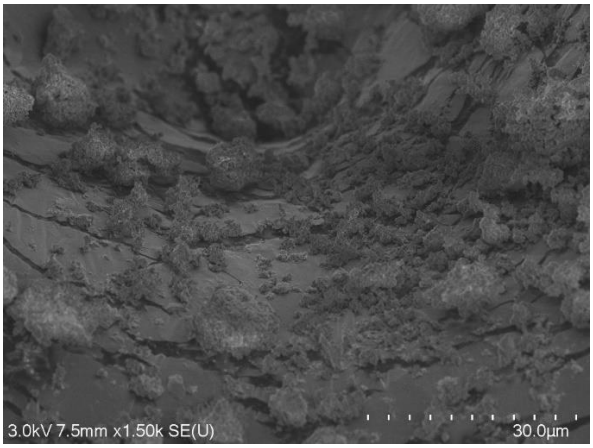

Figure 11.42(a). SEM image at 13,000 times magnification of halloysite covering a larger particle with some charging evident on the image. (b). Similar to figure 30a with halloysite clay covering a larger particle, charging evident on the edges of some halloysite particles. (c). A 'zoomed out' view at the SEM stage (at 1,500 times magnification) showing in detail the 'covering' of all particles with small halloysite clay particles.

11.10.4 3 Month Treated Soil

The samples from three months of soakage showed identical morphologies to those previously encountered in the untreated and 1-month treated soils. Morphology distribution was closer to that of the untreated soil, with spheroids being far more dominant (91 %) than tubules and books in these images.

Figure 11.43a shows the general bulk clay, with a mixture of small and large, onion-like spheroids noted, as well as a number of tubules. In the lower portion of the image, a coating of much smaller material appears. Figure 11.43b and c show the presence of a new, previously unobserved fibrous material coating some of the clays as well as in a large aggregation.

The fibrous like material appears to be incredibly small tubes, ranging between 6 and 15 nm in diameter, with lengths ranging from a few nm to 300 nm. Similar particles are shown in micrographs in Cunningham et al. (2016). The ‘aggregate’ of this unidentified mineral is further shown in Figure 11.43c. While some image tearing is present, the image taken at 90.1 K times magnification shows the tubes clumped together. Figure 11.43d shows this further with the material appearing to coat large portions of the clay minerals. One option may be that this material is imogolite, an Al-rich secondary mineral formed in some weathered volcanic ash deposits (Lowe and Percival, 1993). However, the predominance of silicon in the samples (and relative shortage of aluminium) would tend to negate this identification (Lowe, 2019).

(a)

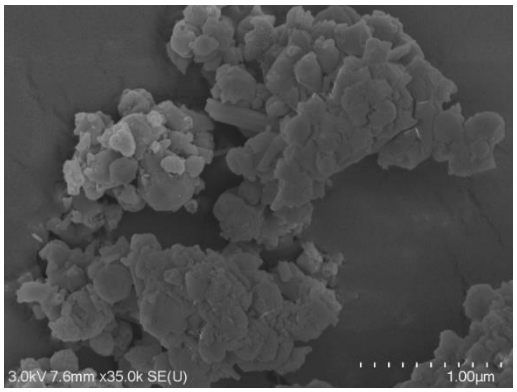

(b)

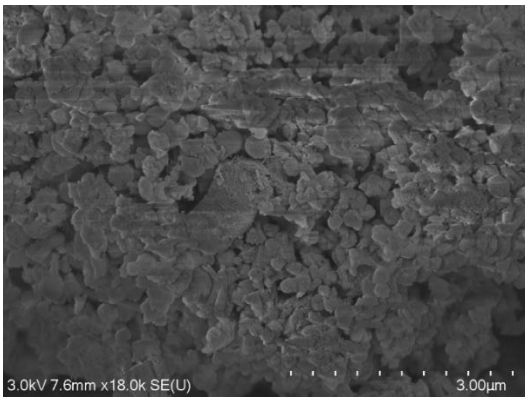

(c)

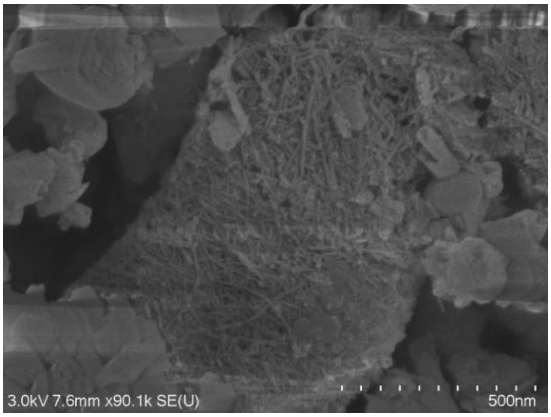

(d)

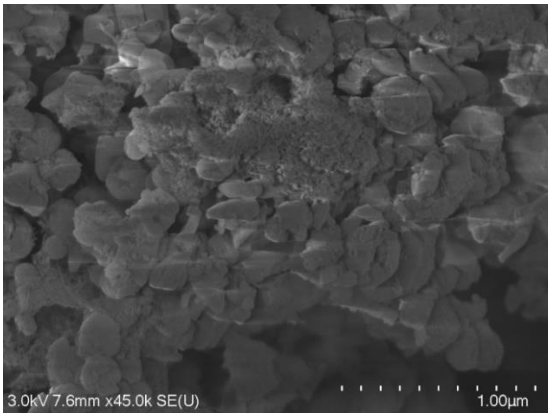

Figure 11.43.(a) bulk mixture of halloysite spheroids and tubules taken at 35,000 times magnification. (b). Fibrous like material found within the halloysite material. (c) A higher magnification (90,100 times magnification) image of the fibrous nanotubes observed on the halloysite clay. (d). Another image of the fibrous material (at 45,000 times magnification) with charging noted within image.

11.10.5 6 Month Treated Soil

Samples from six months of treatment are shown in Figure 11.44a and b. Figure 11.44a shows a small cluster of halloysite minerals, the bulk of which are spheroids with some halloysitic tubes present. A large platy mineral is present in this image, while this could be a singular halloysite plate, the lack of accompanying plates suggests it may be another mineral such as biotite. Some volcanic glass appears to be present in the upper right portion of this image, though the bulk is dominated by halloysite in various morphologies.

Figure 11.44b shows a halloysite conglomerate with more platy minerals, spheroids, and tubes, with the tubes in this image much longer and with a larger diameter. Furthermore, in this image a mixture of round tiny spheroids and more small tubules is evident. Similar to the 3-month SEM images, these appear to coat the clay surfaces in some areas. These may be mixture of allophane and possibly imogolite in small quantities, although the relatively low Al contents would possibly preclude these.

(a) (b)

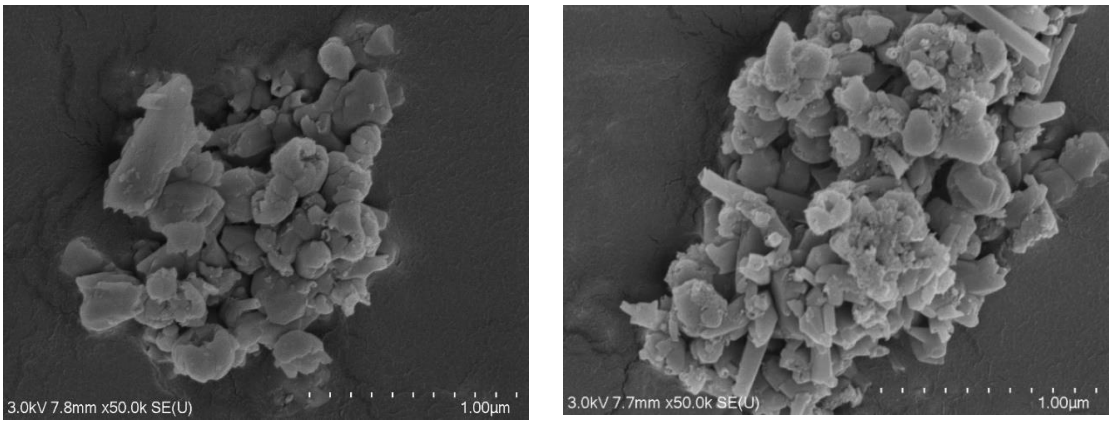

Figure 11.44(a) A small cluster of halloysite mineral with various morphologies present. A large platy mineral is not observed in other SEM images is present for this 6-month treated sample. (b) A halloysite conglomerate, similar to that of 32a with a higher concentration of the platy mineral present.

11.10.6 12 Month Treated Soil

Images of samples from the 12-month period of treatment (Figure 11.45a and b) show similarity with the previous months treated images, with halloysite spheroids dominating and some larger tube morphologies present throughout. The smaller nanotubes observed coating the clays previous are present in both Figure 11.45a and b, though overall during imaging smaller quantities of these nanotube-like materials were noted. One aspect that is worth noting here is the degree in which spheroids are bunched together and appear to have an attraction between mushroom cap base to other spheroids outer surfaces, leading to large, connected chains of spheroids.

(a) (b)

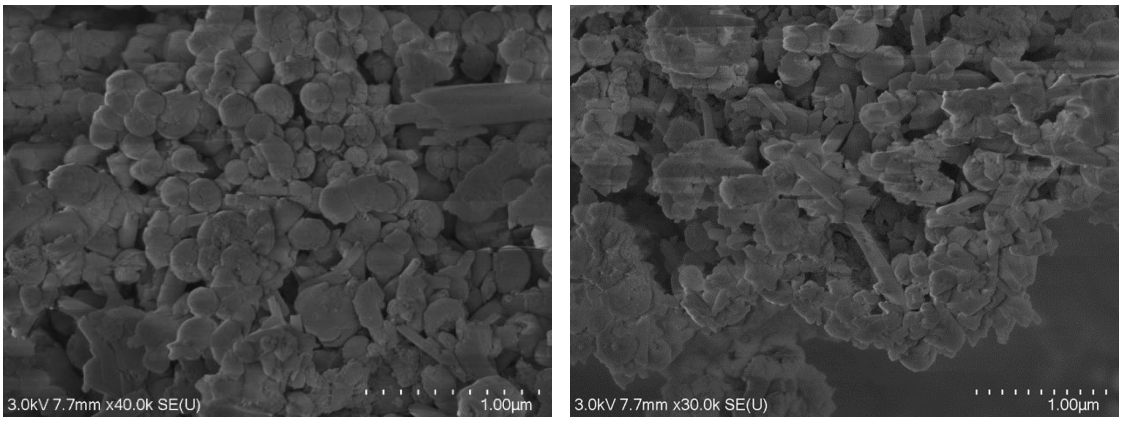

Figure 11.45(a,b). SEM imagery of 12 month treated halloysite clay with charging much more present on figure 33b.

11.10.7 SEM EDS

SEM energy dispersive spectroscopy (EDS) undertaken on soil showed a slow but clear change over the course of the 12 months of treatment of the soil (Table 11.15 and Figure 11.46). Of the major elements observed, O showed the highest response across all treated samples with a narrow variation over the entire duration (57.5−59.6 %). This was followed by Si (17.4-19.3 %), Al (17.3-15.6 %), Fe (4.2-3.7 %) and Ti (<1 %). Treated samples all showed the presence of between 2.5-3.9 % K with the general trend indicating

an increase in the amount of K on the clays surface observed over the 12 months of core soakage.

Table 11.15. SEM EDS elemental proportions for the untreated and treated soils. Elemental compositions are for the clay surface.

Element	Untreated		1-Month		3-Months		6-Months		12-Months	
	(%)	+/-	(%)	+/-	(%)	+/-	(%)	+/-	(%)	+/-
O	59.59	1.87	58.20	0.44	58.61	2.36	57.49	1.73	58.53	2.41
Al	16.79	1.52	15.58	2.20	16.22	0.91	17.28	0.54	15.84	1.08
Si	19.32	1.88	18.57	2.89	17.82	1.06	18.76	0.75	17.40	1.46
K	0.00	N/A	2.99	1.68	3.28	0.58	2.53	0.59	3.93	1.36
Fe	4.05	0.89	4.24	1.73	3.76	0.98	3.72	0.86	4.01	0.88
Ti	0.35	0.11	0.42	0.15	0.34	0.08	0.31	0.08	0.33	0.08

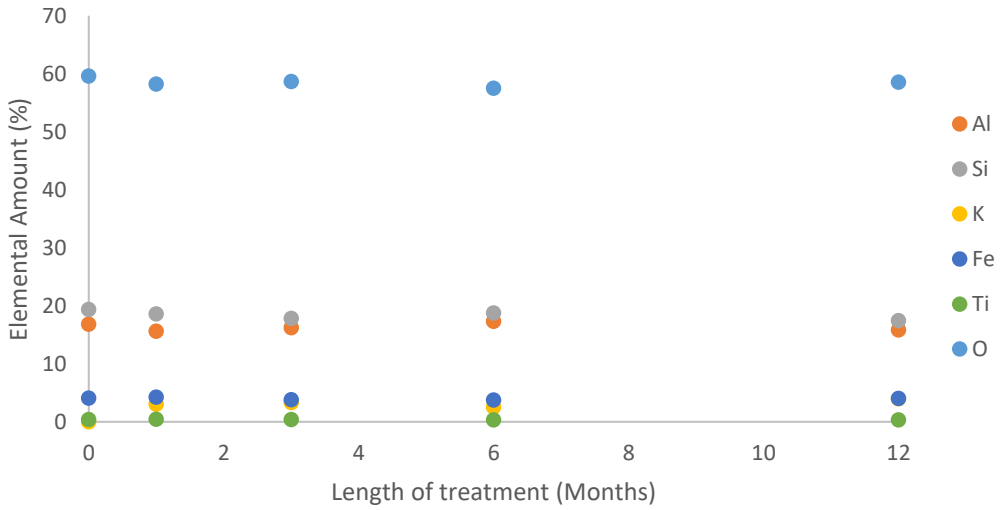

Figure 11.46. Elemental composition for treated and untreated soils as measured using SEM EDS spectroscopy.

Standard deviations of elemental composition were relatively unaffected by length of treatment with no clear trend in deviation over time. Looking at the untreated samples, there was a small decrease in deviation over time for Al, Si, Fe and Ti but an increase in O. When comparing the treated sample deviation, they show similar behaviour in no consistency and random variations over time.

One aspect to note is the variation observed in the 6-months treated soil compared to 3- and 12- months'-treated soil, with an increase in Al and Si noted, along with a significant drop (~1 %) in potassium observed compared to the pre and proceeding lengths.

Chapter 12
Part II Discussion

12.1 Untreated Soil

Soil analysis of both bulk and clay fraction shows a clear peak in the 10.1 Å region, with a sharp, distinctive peak observed. Such a 10.1 Å peak is typically ascribed to the presence of halloysite within the clay fraction of the soil. This sharp, distinctive 10.1 Å peak is typical of both New Zealand soils and those sampled within the Pahoia Tephra/Tuff unit (Churchman & Theng, 1984; Lowe & Percival, 1993; Lowe & Nelson, 1994; Joussein et al., 2005, 2006; Wyatt, 2009; Arthurs, 2010; Cunningham, 2012; Cunningham et al., 2016; Churchman et al., 2016)

This presence of halloysite is further confirmed with the soil, when exposed to formamide, showing an increase in disorder with the 02,11 and 003 peaks, with the sharp distinctive peaks observed in the initial analysis becoming more disordered as the reflections in the 003 peak undergo a slight increase in basal spacing. The general expectation following formamide treatment is a slight increase in the 001 basal spacing peak, with the clay expanding from 10 Å to around 10.2 Å (Joussein, 2007), this is reflected with a 0.15 Å increase noted in the formamide treated soil. This presence is further supported in the SEM imaging with nanotubes and spheroids typical of halloysite dominating throughout. The purity of this halloysite is also noticeable with little in the way of material, which is not halloysite present in the SEM imagery, or, if it is indeed present, is likely hidden by the sheer quantity of halloysite particles covering all surfaces.

DSC/TGA

Thermal analyses of clays showed a series of changes have occurred over the course of the clay's treatment. The untreated clay on its own, sampled from Kowhai Grove, shows good accord with other New Zealand halloysite rich clays (Lowe & Percival, 1993; Lowe & Nelson, 1994; Churchman & Lowe, 2012)As observed with most halloysite clays, two distinct peaks were observed in the untreated clays. The first peak, an endothermic peak occurring at 506^{o} C, marks the breaking of the OH bonds on the alumina sheet and subsequent de-hydroxylation of the clay surface. This peak also accounts for the only major mass loss event for untreated soil with ~9 % of the 14.4 % mass lost occurring in this one event. The second, a smaller exothermic peak at 952^{o} C is indicative of the

destruction of the Si-O bonds on the silica sheet. These values are slightly higher than those for a number of other New Zealand halloysites, with the bulk of samples producing sub 500^{o} C values for de-hydroxylation, though this fits well within the expected range of values for halloysites both within New Zealand and overseas (Joussein et al., 2005, 2006; Li et al., 2017; Santagata & Johnston, 2022). With this said, these values are not too dissimilar from similar halloysites from within the Bay of Plenty, with halloysites sourced from Te Puke and Opotiki, the latter from a Pahoia Tuff outcrop, showing an initial endothermic peak of 520^{o} C and exothermic peak of 925-950^{o}C (Churchman & Theng, 1984). Crystallinity indices indicate that this is a poorly crystalline halloysite regardless of metric measured, an aspect anticipated due to the domination within the halloysite of spheroidal to semi-spheroidal particles as opposed to the more crystalline tubular morphologies (Takahashi, 1958).

FTIR

The FTIR peaks showed peaks typical of halloysite, with peaks in the upper area at 3697 and 3623 cm^{-1}, indicative of the V_1(surface) and V_2(inner) OH bonds on the alumina sheet. Indications from the FTIR curve suggest that the halloysite still retained a degree of interlayer water, even with the heating to 110^{o}C for 24 hours prior to testing. This is not necessarily unexpected, with there being a degree of water left retained within the structure, potentially left as 'islets' or isolated pockets entrapped in layer space as the halloysite layers making up the spheroid collapsed (Brindley, 1961). This initial FTIR peak further supports the poorly crystalline nature of the soil noted within the XRD crystallinity indices with the 3620cm^{-1} band being notably more intense and having a higher transmittance than the 3690cm^{-1} band, a trait observed in various poorly crystalline halloysites (Theng, 1982; Joussein et al., 2005).

XRF

Analysis of the clay through XRF showed it to be dominated by SiO_2 and Al_2O_3 (44.73 % and 33.09 %, respectively). Fe_2O_3 (6.22 %) is slightly higher than the content of other New Zealand halloysites, but plots within the range expected (0.25-8.23 %) from Churchman and Theng, 1984). The slightly higher proportion of Fe_2O_3 is not necessarily unexpected, as a the morphology is dominated by spheroids, which is typically associated with an elevated percentage of Fe_2O_3 within the deposit, either as ferri-hydrate or as isomorphous substituted Fe^{3+} into the octahedral sheet causing a charge imbalance

subsequently in the silica sheet (West et al., 2004; Joussein et al., 2005; Churchman et al., 2016).

The ratio of SiO_2:Al_2O_3 seemingly indicates and supports the potential case for isomorphous substitution having occurred to some extent with a ratio of 2.29:1 returned in this case, in excess of the idyllic 2:1 presented in literature (Cheng et al., 2017). Though for full confirmation of this, sodium dithionite/citrate extractions would need to be undertaken.

PZC Analysis

The untreated soil showed high streaming potential (-618 mV), with a high level of dispersion as a result at its natural pH (6.43). The negative streaming potential indicative of a net negative charge on the sheet, this negative charging remained until a pH of 3.82 was achieved, when clay surface charge neutrality was achieved. This dispersive behaviour observed from the streaming potential is further noted with a zeta potential of -25.1 mV at natural pH, noticeably lower than values for other New Zealand halloysites (Pasbakhsh et al., 2013). This lower zeta potential also indicates an unstable colloidal system, which on an electrokinetic level, will act in a dispersive manner causing colloids to disperse as a result of instability between particles and their constituent double diffuse layers (Pochapski et al., 2021).

CEC, Base Saturation and Major Cations

CEC was quite low (6 cmol/kg), placing it on the lower end of reported values (2–60 cmol/kg (Joussein et al., 2005)), which is not unexpected due to the dominance in morphology by spheroids (88–92 % spheroids). The influence in this instance of morphology to low CEC is likely related to the fact that the outer surface of the spheroids are made up of the weakly negatively charged siloxane sheet, home to the generally stable Si-O bonds as opposed to the aluminol Al-OH sheet, with the negative charge likely resulting from a small degree of isomorphous substitution of Si^{4+} into the tetrahedral sheet instead of Al^{3+} (Bailey, 1990; Churchman et al., 2016).

Further, base saturation is already high, with 70 % of potentially bondable sites taken up by various cations already. Of these cations, 64 % of sites are taken up by di-valent cations ($Ca^{2+}$and Mg^{2+}), though this is generally expectant of halloysitic rich soils and follows trends observed in other halloysites from within New Zealand (Shoji & Kato, 1978; Pasbakhsh et al., 2013).

Surface Area, Pore Volume and Size Analysis

BET surface area analysis showed the soil was dominated by pores within the micropore range, with the bulk of the adsorption within the micropore range occurring at 7.57 Å, reflective of a surface area of 46.1 m^2g^- of clay. Within the mesopore range, two distinct peaks of adsorption are noted. The first is at 34.2 Å and the second around 100 Å, the former likely representative of finer mesopores on the internal surface, the latter representing the potential lumen of the clay spheroids themselves. Specific surface areas in the micropore range (BET) fit with values observed for other New Zealand halloysites (22-169 m^2g^{-1}), in particular consistent with values observed for other spheroidal dominated samples (42.4 m^2g^{-1}), with drops in S_{ads} and S_{des} of reasonable margins also observed in these samples (Churchman et al., 1995; Levis & Deasy, 2002; Keeling et al., 2012; Pasbakhsh et al., 2013). Adsorption isotherms followed type IIb isotherms, with a hysteresis developing during desorption in the multilayer range indicative of slit shaped pores within the halloysite clays (Rouquerol et al., 2013). It is worth noting though that while isotherms are indicative of slit shaped pores, there is a the potential that these are not representative of the natural soil, with some pores potentially forming as a result of dehydration of the halloysite from 10 Å to 7 Å (Kohyama et al., 1978). With this said, Churchman *et al.* (1995) suggested that for tubular morphologies slit shaped pores are likely due to this collapse, isotherms for spheroidal halloysites within their study suggested similar slit shaped pore sources.

12.2 Treated Soil Comparisons

While it is clear in Part I within the geomechanical and triaxial testing sections that an increase in strength of the extra sensitive Pahoia Tephra was exhibited following treatment of the soil with potassium acetate, the cause and potential source of this strength increase was not determined. This following section of the discussion will look to compare various clay mineralogy and chemical testing methods for untreated and treated soils to establish where this strength increase may be sourced.

12.2.1 DSC-DTA/TGA

Soils treated with the potassium acetate when subjected to gradual heating of 5°C/min showed some noticeable changes when compared to the natural soil. At the lower end of the temperature scale, all soils had an initial mass loss event centred around 60−65°C corresponding to the loss of retained water from within the clay. While the soil was pre-

conditioned prior to analysis through heating to 110ºC and subsequent cooling in a silica bead desiccator, rehydration likely occurred during the preparation and setup phase of testing as the soil was exposed to ambient air during that time. While not a long period of time, this is likely enough due to the potassium acetate intercalated halloysites tendency to rapidly rehydrate under the correct conditions and accept water back into the basal space (Frost et al., 2000b; Joussein et al., 2006).

The second change within the DSC signal, when compared to the untreated soil, is the formation of a new, reasonably significant, exothermic response centred around 325ºC. What this particular peak corresponds to, at this stage, is uncertain. One possibility, according to Lowe and Nelson (1994), is that this response reflects break-down of organic-mineral complexes (possibly together with some iron oxides). The LOI data presented in chapter 11 (Table 3.6A), ranging from 15 to 39 wt %, would support the suggestion relating to organo-mineral complexing. Comparison to other DTA curves shows some degree of similarity in the centre and shape of the thermal peak at 320–380ºC corresponding to the decomposition of the intercalated K-acetate complex, as well as the potential loss of water and dehydroxylation of the remnant halloysite (Cheng et al., 2010, 2014; Adamczyk et al., 2020). It is worth noting though that the dehydroxylation of the halloysite may remain in some cases, though this is usually occurring at a significantly lower temperature than the natural halloysite (Cheng et al., 2019), which is indeed the case for this clay with a reduction in the dehydroxylation temperature to around 400ºC, a 50º C reduction, accompanied by a large drop in size of the mass loss (between 4–5 % less). At this point it is essential to point out that this peak corresponding to the K-acetate complex and dehydroxylation are all endothermic**,** completely at odds with the value measured.

While the temperature corresponds strongly to the melting and decomposition point of potassium acetate, these reactions are both endothermic and should have presented as such, not as an exothermic release of energy (Hazlewood et al., 1966). While not reflected in all samples, after 12 months there was the loss of the Si-O exothermic response at 950ºC, this not being unexpected as a result of the increased disorder in the crystallinity through the influence of the K-acetate intercalate complex.

One interesting aspect over the 12 months of treatment is the decrease in the J/g required (deltaH) to achieve the peak exothermic and endothermic responses. This decrease is likely related to the influence of the K-acetate complex on the internal –OH bonds, with

the potential new, weaker, hydrogen bonds formed between the acetate ion and the halloysite requiring less energy to break, and subsequently less energy to dehydroxylate the remaining Al-OH bonds.

12.2.2 XRD

For the samples soaked in the 2 mol potassium acetate solution for 1 to 12 months, the responses determined and measured for the XRD peaks were unexpected. Halloysite, which produces a natural basal spacing of 10.1 Å in its hydrated form (Joussein et al., 2005), is known for its ability to interact with certain organic and inorganic substances through intercalation, adsorption and cation exchange. In particular, one such of these is the interaction with the inorganic salt of potassium acetate, used within this study as a stabilising and strengthening agent on the soil. Potassium acetate has, in small amounts (2–10 mmol/gram soil (Wada, 1959a)), the ability to intercalate and enter into the halloysite crystal unit structure. The potassium acetate molecule is generally thought to displace the water molecule in the interlayer space present within halloysite and cause an expansion in the *d*001 reflection from 10.1 Å to between 11.5 & 14 Å depending on the initial level of hydration of the halloysite (Frost, et al., 2000a; Li et al., 2017; Adamczyk et al., 2020).

Table 12.1 shows the *d*001 spacing of the halloysites in the refined clay fraction for both the treated and untreated samples analysed in this study. From the data, it is clear that regardless of the length of time that the halloysite was in contact with k-acetate solution, basal space in the *d*001 space did not exhibit any expansion whatsoever, with near identical peaks observed. Initial thoughts with regards to this lack of upshift in basal peak were that it may potentially have been related to the methodology used in preparation and separation of the clay fraction. One option in this instance may have been that the potassium acetate, which theoretically readily intercalates, but does not form any strong bonds, may have been washed from the clay in the preparation process, a trait that is known to occur (Andrew et al., 1960; Wada, 1961).

Table 12.1. d001 spacing for the untreated and treated soils.

Soil Sample	*d*001 peak (Å)
Untreated	10.1
1 Month	10.1
3 Month	10.1
6 Month	10.1
12 Month	10.1

Rehydration Phases & Intercalation

In determining the presence of an intercalate, one option is to examine the rehydration behaviour of the halloysite following thermal dehydration where the sample is heated high enough to remove the interlayer water within the clay, but not high enough that it destroys the intercalate structure. General expectation for the rehydration behaviour of an intercalated halloysite is a collapse of the basal spacing under drying from ~13 Å to either 11 Å or 8.4 Å, which upon rehydration expands out to ~13 Å again along with secondary peaks at 11, 8 (Frost et al., 2000b). This expansion behaviour is noted quite clearly in our 10 molL^{-1} samples with an expansion from 10.1 Å for the initial peak expanding to 13.6 Å following rehydration. It can be confidently stated that the 1- and 3-month- treated samples have not been influenced in any particular fashion by the K-acetate as no expansion of the 7 Å halloysite can be seen, but something is clearly occurring at the 6, and 12 month point with the presence of re-expanded reflections present.

12.2.3 FTIR

Although the natural clays exhibited typical characteristics of a poorly crystalline halloysite, treated clays showed within their FTIR curves the formation of new bonds as a result of the soakage by potassium acetate. As with the XRD traces, there is a wealth of literature that exists on the interaction between potassium acetate, halloysite, and its intercalation complex that is detected through the medium of FTIR spectroscopy or Raman spectroscopy (the latter used for its advantage in the 100-400 cm^{-1} region). From the interaction of halloysite and potassium acetate there should be a number of new peaks and deviations in peaks noted as result of the formation of the K-acetate complex. The first of these occurs in the 4000–3000 cm^{-1} range, being a slight downshift of the 3690 cm^{-1} peaks (usually from around 3696–3693 cm^{-1}). This minor shift often accompanies either a complete loss of the 3620 cm^{-1} peak or a clear decrease in the intensity of the

3690 cm^{-1} peak relative to the 3620 cm^{-1} peak., alongside the formation of a new peak at 3600 cm^{-1}. These peaks form as a result of the formation of a new, weak, hydrogen bond forming on the inner surface hydroxyl of the alumina sheet (Ledoux & White, 1966; Frost, 1997; Frost et al., 2001; Cheng et al., 2019). This bond formation is often accompanied by a general increase in vibration intensity of interstratified water located between 3600 and 3100 cm^{-1}.

The next major differences are noted between 1600 and 1300 cm^{-1} with the formation of three new peaks. The first two occur at approximately 1555 and 1415 cm^{-1}, and represent the symmetric and asymmetric vibration of the COO^{-1} ion. This vibration is usually indicative of the COO ions and H bonding with the inner surface OH groups and is evidence of formation of the K-acetate complex, as opposed to adhesion to the external surface of the halloysite by K-acetate (Cheng et al., 2011b). The third new peak that forms is at around 1330 cm^{-1}, representing the interaction of the deformation caused by the CH_3 ion as a result of its interaction with the outer silica tetrahedral sheet. This interaction with the silica sheet can be further confirmed with the level of difference between the 1555 and 1415 cm^{-1} peaks, as disorder in these peaks represent such an interaction (Mako et al., 2014). There may be the presence of a new peak found at approximately 1600 cm^{-1} providing indication of either the upshifted double bonded COO ion or the downshifting of the bending -OH of the adsorbed water, usually found around the 1630 cm^{-1} peak.

For the treated clays, a number of peaks are formed that are consistent with expectations for a halloysite intercalated with K-acetate. In the upper 4000 to 3000 cm^{-1} range there is an increase in the disorder and relative difference in transmittance between the 3690 and 3620 peaks when compared to values for untreated soil, as shown in Table 12.2. Over the course of the 12 months of analyses, an increase in disorder of almost 6 % transmittance forms. It is worth noting that an odd response for 6 months was noted with the difference between the two wavelengths being less than that for the untreated soil, even after multiple repeats of differing samples.

Table 12.2.Percentage transmittance for treated and untreated soils for the 3690 and 3620 cm^{-1} peaks.

	%Transmittance				
	Untreated	**1 Month**	**3 Months**	**6 Months**	**12 Months**
3690 cm-1	3.80	15.55	10.48	1.47	18.36
3620 cm-1	2.32	8.62	6.13	0.66	11.00
Difference	1.5	6.9	4.4	0.8	7.4

In contrast to this support of the formation of a K-acetate complex, there is no downshift of the 3690 cm^{-1} wavelength observed in the treated samples. There was also no loss of the 3620 cm^{-1} peak, with this upshifting and downshifting by a maximum of 3 cm^{-1} (untreated = 3623 cm^{-1}). With that being said, there is, for all treated samples, the indication of a small deviation and decrease in transmittance at 3600 cm^{-1}. Although this is an incredibly minor peak deviation, nevertheless it is present, thus providing an indication of the K-acetate intercalate complex being present.

Further support for the formation of a K-acetate complex is found within the 1750 to 1000 cm^{-1} range with the four peaks noted as markers for intercalation in the literature(Frost et al., 2000b; Cheng et al., 2011; Mako et al., 2014). The first of these is the downshifted adsorbed water peak at roughly 1600 cm^{-1} noted for all samples. On top of this there is also the presence of all three of the 1,550, 1,415 and 1,350 peaks present providing a relatively strong intensity across all the treated samples. In particular the presence of the 1,550 and 1,415 cm^{-1} peaks are, as previously mentioned, supposedly good markers to indicate the intercalation of the K-acetate complex into the halloysite crystal.

These findings thus pose an issue when paired with the XRD data previously discussed. If observed on their own, the data presented in these FTIR peaks seemingly suggest that, upon immersion into the potassium acetate, the K-acetate intercalate complex forms, but the XRD data on the other hand clearly show that this is not the case.

12.2.4 Crystallinity Index

While there is no clear indication of the presence of the K-acetate intercalate provided by the XRD and FTIR data, one aspect that is clear from the derivative crystallinity indices is that as time goes on during the immersion of the halloysite in K-acetate, there is a

distinct and clear increase in the level of crystal disorder and loss of crystallinity over time. Figure 12.1 shows this drop in crystallinity, being particularly clear for the Hughes and Brown XRD method, with a distinct loss in crystallinity occurring within the first month of immersion (4.86–3.13), before gradually becoming less crystalline over the course of the treatment.

This rapid change and loss of crystallinity fits with the rate at which the K-acetate interacts and reacts with halloysite, with changes occurring rapidly within minutes to hours (Carr, 1978; Frost et al., 2000b). In contrast to this, however, the Parker (FTIR) and Smykatz Kloss (1982) methods show a much smaller decrease in the degree of crystallinity over time, but both still do show a slight drop. This drop in crystallinity fits within expectations for a change occurring to the clay as a result of 'impurities' in the clays crystal structure, which can impact a wide range of factors such as bond strength as observed in the drop in dehydroxylation temperature, as well as bond orientations (Smykatz-Kloss, 1982).

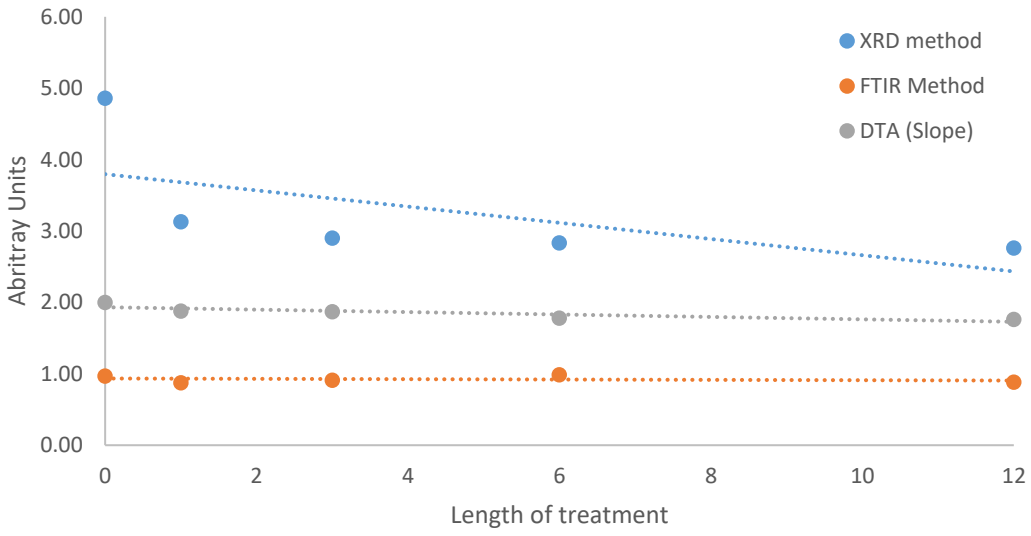

Figure 12.1.Crystallinity indices for the various methods of determining crystallinity index. Methods presented include XRD (blue), FTIR (orange) and DTA (grey).

12.2.5CEC, Zeta and Streaming Potential

Cation exchange capacities for treated soils showed large increases over the natural soil, from 6 cmol/kg up to 92 and114 cmol/kg. This increase is accompanied by an increase in base saturation (70-100 %) as well as noticeable variation in cation contents of the soil.

The cation composition shows a marked increase in monovalent cations, with divalent cations (Mg^{2+}, Ca^{2+}) dropping. While cation exchange capacities are not a perfect measurement of volume of exchangeable cations on the clay surface, as there may be the potential for excess salt present that is neither adsorbed nor intercalated, it is still worthwhile looking at the potential composition of mmol of salt per 100 grams of clay. This measure provides a value comparable to those found in some literature.

For this comparison it is assumed that the potassium cmol/kg is representative of potential intercalated/adsorbed units of potassium acetate onto the clay. This assumption is based on the fact that the extraction and measurement method employed in the determination of the CEC (ammonium acetate buffer) is similar to that employed in several published papers (Carr, 1978; Jaynes, 1986). Upon combining the 91.3 cmol/kg of potassium after 12 months (92.2 cmol/kg after 12 months – 0.92 cmol/kg baseline) with the clay fraction (25.4 %), there is approximately 359 mmol/100g of potassium acetate to clay. When compared to previous values derived by Carr et al. (1978), who, for an optimally intercalated, tube-morphology dominated halloysite, achieved a maximum of 260 mmol/100g, while Wada (1959a) suggests that approximately 200–300 mmol of salt is retained per 100g of air dried clay. These values suggest the clay is able to retain and interact with a far higher number of K-acetate molecules than those measured previously. Although there is a change in morphology when compared to those of previous studies, there are clearly further mechanisms occurring within the soil to cause this when combined with a distinct lack of intercalate XRD reflection.

One aspect to consider in this instance is the morphology, which, due to the narrow pore sizes often found within spheroidal halloysite (Askenasy et al., 1973), may prevent interaction and distribution of the K-acetate throughout the halloysite. In addition to this it is evident that there is a very low number of active and available sites for cations (and thus anions) with which to interact based on the initial CEC (6 cmol/kg). While the introduction of the K-acetate increases pH, allowing for an increased CEC due to the inherent amphoteric effect caused by the increased pH, this increase is not high enough to produce the CEC values observed. One option to explain this increased CEC may be the presence of precipitated salt within the soil, either on external surfaces or within the available clay pore spaces, which, upon extraction leads to a skewed result with the CEC value derived much higher than the actual value of the number of cations present on the clay surface.

Zeta potential measurements of the clay showed an increase in negative charge (-25.1 to -39 mv). This increase in zeta potential suggests an increasingly 'stable' system, which conversely suggests colloids have a larger double diffuse layer (DDL) and are thus more dispersive (Bhattacharjee, 2016). This feature is at odds with the streaming potential values measured, with streaming potentials measured showing a significant decrease following the treatment of the soil (-618 mv to -120 mv), which suggests that following treatment the soil has a much lower charge on the colloid surface and is more likely to agglomerate (Ghernaout, 2015). It should be noted, however, that results for the zeta potential are likely not fully representative of the actual charges at the edge of the DDL due to the presence of potassium acetate within the system. It would be anticipated that due to the higher concentrations of a highly dissociative metal salt, the zeta potential should be much smaller, as in clay colloidal systems the DDL is heavily suppressed as a result of the large concentration gradient created by the metal salt ions (John & Arnepalli, 2019; Yukselen & Kaya, 2003.). A higher pH from the K-acetate may well skew the zeta potential higher as there are higher number of OH^- ions within the system causing this increased charge imbalance and thus increase in zeta potential (Yukselen & Kaya, 2003).

In addition to this the streaming potential suggesting that the treated soil is less 'stable' than the untreated is consistent with what was observed in the preparation of the soil water mixtures, with all treated samples' soil fractions settling out and flocculating within 5 minutes, while the untreated soil remained in suspension for an extended period of time. One point of note though was the pH distance between the initial pH of the soil and the point of zero charge (PZC) was almost identical regardless of whether the soil was treated or not, with a change of ~2.6 required to reach the PZC. With this said, unsurprisingly approximately double the amount of acid was required to reach PZC for the treated soil, accounted for by the excess acetate and OH^- ions found within the system requiring reacting to balance the system out. Overall, this decrease in colloidal stability indicates a positive trait for the treated soil, especially within the soil's remoulded phase at higher water contents, with clay colloids far more likely to try to clump together and have a higher remoulded strength as a result of the increased strength between colloids due to the increased interparticle van der Waal forces.

12.2.6 Specific Surface Area and SEM

Specific surface area testing of the treated soil suggests a change in the size of pores present within the halloysite following treatment. Specific surface area seemed to show

no clear trend with values increasing and decreasing seemingly randomly, this for both solely the micropore range (BET) and for the mesopore range (BJH). Figure 12.2 illustrates this variation well. When plotted against a linear trend, both exhibit low R^2 values (BET = 0.26, BJH = 0.23), with opposite trends seemingly occurring, with the micropore surface area becoming smaller while mesopore surface area increases over time.

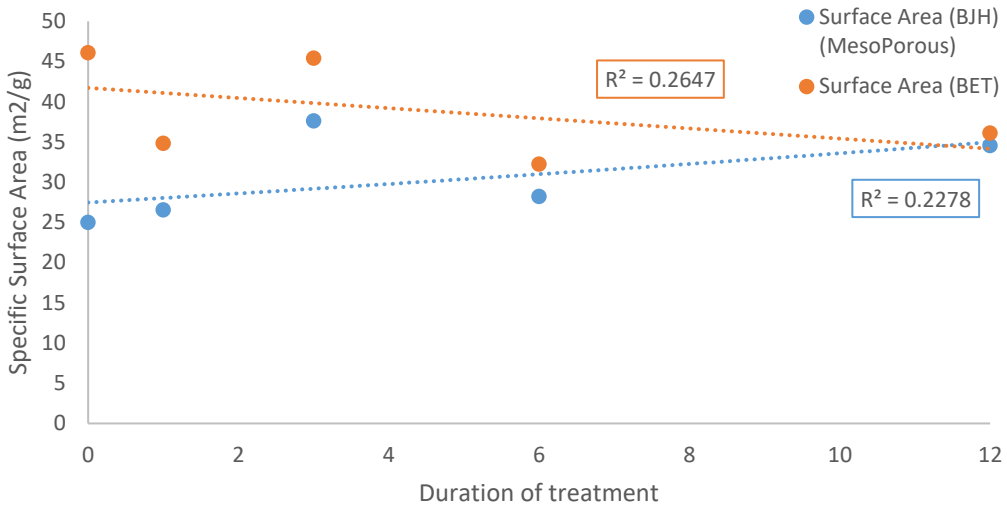

Figure 12.2. Specific surface area for untreated and treated soil across time, with mesopore surface area shown in blue, while orange is micropore surface area.

Pore volume on the other hand did exhibit some trends. Mesopore (blue dots) and micropore (orange dots) volumes are shown in Figure 12.3. These show a trend of gradual change, occurring over the 12 months of treatment. Mesopore volume shows some correlation ($R^2 = 0.64$) over the course of the treatment, with mesopore volume increasing (0.09 cm^3g^{-1}) over time, though this is somewhat inconsistent with both the 1- and -6 months'-treated soil exhibiting mesopore volumes lower than those of untreated soil

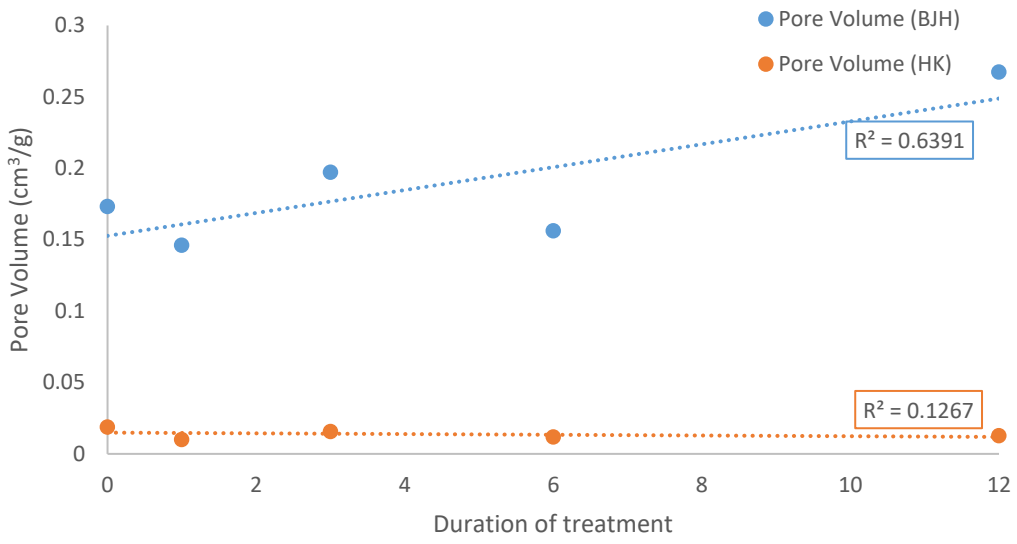

Figure 12.3. Pore volume results for the micropore (orange) and mesopore (blue) range for treated and untreated soils across the 12 months of treatment.

This volume increase was not accompanied by an increase in mesopore diameter Figure 12.4), with mesopores seldom expanding over time with an increase of 1.4 Å noted and no trend noted ($R^2 = 0.03$). Conversely, micropore volume remained relatively consistent, and if anything, showed a small decrease (0.0006 cm^3g^{-1}) over the course of the 12 months. In a complete opposite to the mesopores, micropore size did increase, with micropores increasing from 7.5 Å to 10.97 Å after 12 months with micropore diameter being strongly correlated to length of treatment ($R^2 = 0.88$).

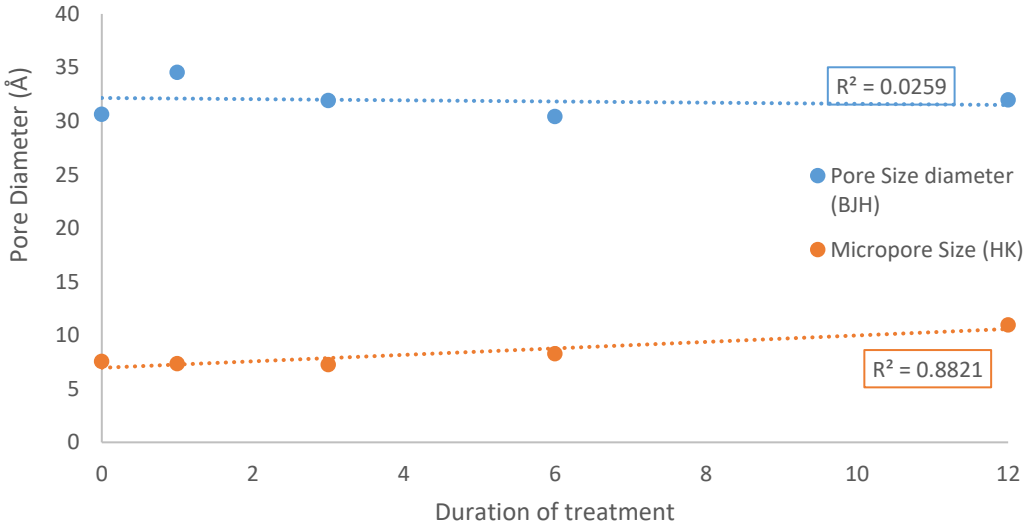

Figure 12.4 Average pore diameter for the micropore (orange) and mesopore (blue) size range for untreated and treated soils across the 2 months of treatment.

Pore volume increases accompanying a decrease in specific surface area following modification and treatment of a clay, especially in kaolins, is not unexpected, with potassium acetate often used as an intercalation, exfoliation agent in the process of modifying kaolin group clays (Zhang et al., 2017). One aspect to examine is the pore size distribution of the sample in the mesopore range. Within the pore volume to pore width data, the peaks align with an increase in adsorbed gas indicating an increase in the number of pores at that diameter. For untreated soil, within the mesopore range, two main peaks occur. The first is at 34 Å, the second 41 Å. After 50 Å there is a smoothing after that peak, indicating consistency in the pore space and a lack of distinct change suggesting few pores of this size. Treated samples after 3- and 6-months treatment displayed a much smoother response, with 6 months, after repeated tests, showing an unexpected response with pore size increasing after 100 Å at a peak, while 3 months' treatment showed a small peak around 35 Å (similar to that of the untreated soil samples). Samples tested for 1 month showed reasonable consistency with the untreated sample with an initial peak at 34 Å, and 52 Å, though the 41 Å peak disappeared. The 12-month sample on the other hand showed a small expansion to 36 Å, as well as either a shrinking from the 50 Å peak, or expanding of the 41 Å peak to 44 Å. This pore size distribution in the mesopore range fits well with the general BJH values, with an expansion of mesopores occurring, although small.

While micropore size and pore volume increased over the course of the 12 months, the approximate width of the halloysite spheroids conversely decreased. SEM-derived width estimations showed a 166 nm decrease in average width over the 12 months of treatment. This decrease was similarly accompanied by a notably reduced standard deviation (57 nm to 46.19 nm). Figure 11.39 plots the average size against the time of soakage (where 0 is equivalent to untreated soil). Within Figure 11.39, when applying an exponential trend to the data, there is a reasonable level of correlation between the width of the clay spheroid and the length of treatment ($R^2 = 0.70$). As previously stated, major changes appear to occur within the first 3 months (~140 nm shrinkage), while the latter 9 months only account for 27 nm of change. Desorption for treated halloysites are not reported here due to the errors caused by the salt present within the soil resulting in no consistency or clearly definable desorption paths.

12.2.7 SEM, EDS and XRF

Treated samples tested through the XRF show, as would be expected, a noticeable increase in the amount of K_2O present within the sample (4.7%), and this is accompanied by a reasonable drop in both SiO_2 and Al_2O_3 (average 6.9% and 5.7% drop, respectively). The only other major change was in CO_2 production, with this increasing on average around 7% across the 12 months of treatment. These changes are not unexpected, as the increased presence of potassium acetate, either adsorbed onto the clays surface or intercalated, is likely to be presented in the XRF as K_2O and CO_2 increases. Interestingly, the decline in Mg^{2+} and Ca^{2+} noted in the CEC analyses is supported and shown in XRF findings, suggesting that these divalent cations have indeed been displaced during the treatment, as would be expected due to the preference for monovalent cations, especially potassium over divalent cations (Jaynes, 1986).

While the presence of an intercalate has been explored in the XRD data, it can be seen from the CEC and XRF analyses that there is indeed the clear presence of potassium (and likely acetate ions) on the clay. One method employable is to examine whether these are surface adsorbed or not is through the employment of EDS (Zhong et al., 2018). As such, EDS indicates that at over the 12 months potassium is now detected on the clay surface, where previously it was not. This percentage ranged between 2.5 and 3.9 % of elements detected. On average, around 68 % of the total potassium detected through XRF is also detected through the EDS. This suggests that around 32 % of the potassium detected through XRF is not adsorbed onto the clays surface, with EDS generally representative of surficial element makeup (Al-Ani & Sarapää, 2008).

Chapter 13
Part II — Summary and Conclusions

The aim of this part of the thesis was to examine various aspects of the clay chemistry and surrounding aspects for this halloysite to determine what exactly is the source of the beneficial and positive geomechanical changes that were observed in the previous part. At this juncture, it could be argued that, after conducting such a wide range of tests that there are more questions than answers. These questions and concerns will be addressed in the following chapter, along with recommendations for future work. From here on it is worthwhile to take in all the data collected and look to put forth a theory as to the source of our positive mechanical outputs.

While the XRD and FTIR data did present somewhat at odds with one another, with the XRD suggesting no intercalate had formed as evidenced by the lack of a distinctive 12-14 Å peak associated with the intercalate (Adamczyk et al., 2020), FTIR curves conversely presented a number of 'indicative peaks' usually associated with the halloysite-K-acetate intercalate (Cheng et al., 2010, 2011; Frost, 1997; Frost et al., 2001; Frost et al., 2000). Literature in which the intercalate complex did not form following treatment was limited, with a single article (Zich et al., 2013) in which the researchers observed a halloysite with no intercalation and simply a 'rehydrated halloysite' mixture with hydrated K-acetate on its external surface. It should be noted though that Zich et al.'s work was undertaken on pre-dried 7 Å halloysite and was subsequently rehydrated to 9 Å which differs to the current case of working with hydrated 10.1 Å halloysite from the outset. The cause of this lack of intercalation in the soils of this study is potentially related to its morphology, with the tight layers and outer siloxane layers of the spheroids preventing penetration into the inner aluminol sheets (Frost & Kovacs, personal communication, 2023). One thing that is evident is that following the introduction of K-acetate to the halloysite, a series of physiochemical changes occurred with the halloysite.

Chapter 14

Overall Discussion and Theories

14.1 Introduction

This chapter recaps the major features determined through analyses in the previous two sections of this thesis (geomechanical testing and clay chemistry) and goes on to provide possible explanations as to the potential causes of impacts that have occurred within the samples. Potential explanations for what has occurred will be discussed

14.2 Review of Findings

Data collected in Part I show several interesting aspects that were somewhat unexpected. Field data showed that the soil examined and analysed from Kowhai Drive fitted the profile desired for this research, being an extra sensitive clayey SILT with relatively high undisturbed and low remoulded strength. These traits were further confirmed by laboratory analyses, with Atterberg limit testing providing further evidence of this being a sensitive material with a liquid limit lower than that of the field moisture of the soil (as expected for extra sensitive material). The soil's characterisation was similar to that of other Tauranga-region extra-sensitive materials (Wyatt, 2009; Cunningham, 2012; Mills, 2016), though one large discrepancy did occur. This was particle density, with the soil having a much higher density than that of similar soils. Triaxial soil testing showed soil with low cohesion and a high friction angle.

Treatment of the soil with potassium acetate (K-acetate) led to the observation of several changes (Figure 14.1), which ultimately achieved the overarching aim of the thesis, whereby a halloysite-rich, sensitive soil deposit was successfully treated and strengthened via K-acetate treatment. Over the 12 months of treatment, some of the major changes noted were a lowering of the soil's moisture content before testing, although an increase in saturation ratio accompanied this. Wet and dry bulk densities were higher than those for the untreated soil (across all time points tested), though a drop in particle density, void ratio and porosity accompanied these higher densities.

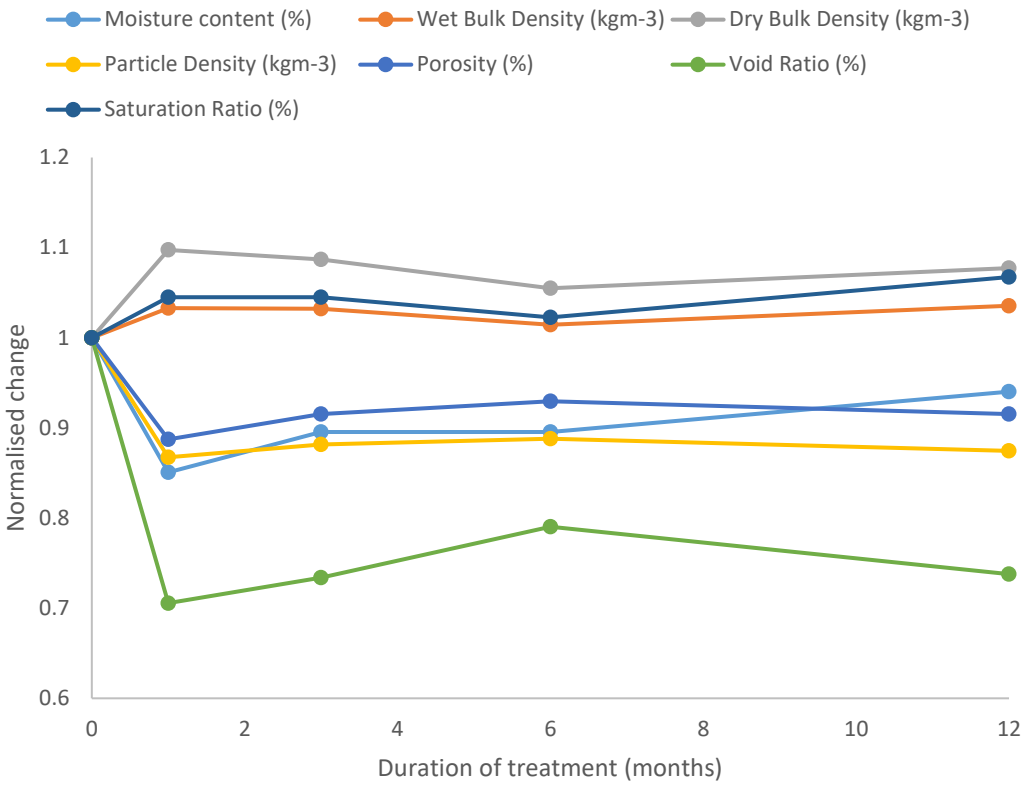

Figure 14.1. A scatter plot of various geomechanical parameters over the course of the treatment. All values have been normalised against the untreated sample so that any trends in the data are more easily visible. Wet bulk density, saturation ratio and dry bulk density all increased compared to the untreated, while particle density, moisture content, porosity and void ratio all decreased.

Atterberg limit testing of the soil (Figure 14.2) showed an increase in the liquid limit following the introduction of K-acetate to the soil, with almost all of the increase occurring within the initial testing time frame, with the 18-month soaked sample showing no subsequent increase on the initial testing. Plastic limits were unchanged by treatment, though the plasticity index and activity increased following treatment, indicating an increase in the soil's 'working' range. The key factor to note from Atterberg testing was the reduction in liquidity index to below one, following 18 months of soaking the sample, indicating a shift for the soil from the range where LI>1, therefore indicating a loss of sensitivity in the soil. In addition, when applying predictive equations for remoulded shear strength, after 18 months, soils appear to have remoulded shear strengths ranging from 4.4 to 7.7 kPa, a reasonable increase from the values of 0.62–0.44 kPa originally predicted for the natural soil.

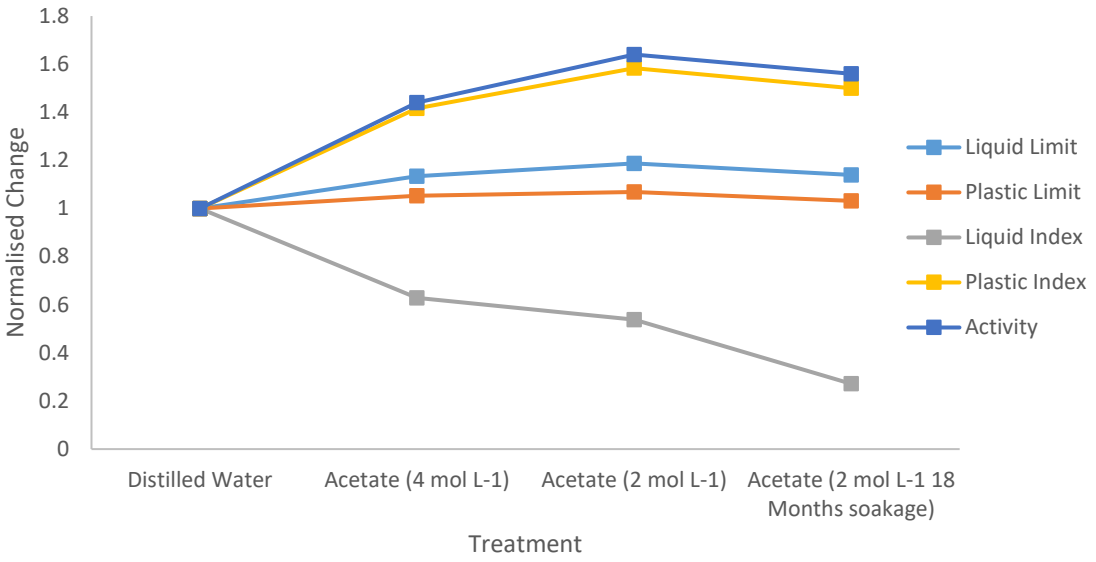

Figure 14.2. K-acetate and distilled concentrations on the x-axis are plotted to the nchange for the various Atterberg limits normalised against the distilled water sample to show changes in the soil for the various concentrations applied.

One point of note from Atterberg limit testing was the discrepancy between the remoulded shear strength derived from lab testing and the one measured in the field through shear vane testing. This difference was then further expanded when applying liquidity index remoulded shear strength calculations (as determined by Lerouil et al., 1983, and Locat & Demers, 1988) that showed the soils of this study should exhibit remoulded shear strengths of 0.3 and 0.35 kPa (leading to sensitivities of >150).

These variations were then explored with a wider view of the extra sensitive soils in the Tauranga region when plotting the liquidity index against the sensitivity (with the range for most Northern Hemisphere clays determined as per Kenney, 1977). These showed that nearly all (bar three measurements) for Tauranga extra-sensitive soils fell outside the range specified by Kenney (1977). This finding suggested that either the extra sensitive soils of Tauranga exhibited a unique strength characteristic that allowed soils with high liquidity indexes to have low sensitivities, or there was an inherent issue with how remoulded shear strength is determined by shear vane standard methodology in New Zealand. Of the two options, it was suggested that the latter is more likely, with remoulded shear strengths of the soil (determined via fall cone) coming out to be 0.62 kPa, a drastic decrease in comparison to the remoulded shear strength determined in the field (5 kPa).

While void ratio and porosity were observed to have dropped following treatment, this did not adversely affect the consolidation characteristics and potential hydrogeological dynamics of the soil, with the time taken to fully consolidate reducing (average decrease of 76 min or 59 %), permeability-increasing ($3.9x10^{-9}$ ms^{-1}/214 % increase) and volume of water expelled increasing (Dvol = 1.089 ml/19 % increase) during the consolidation cycle after the full 12 months of treatment (Figure 14.3). These measurements all point to changes occurring within the soil cores, potentially on the physical clay level.

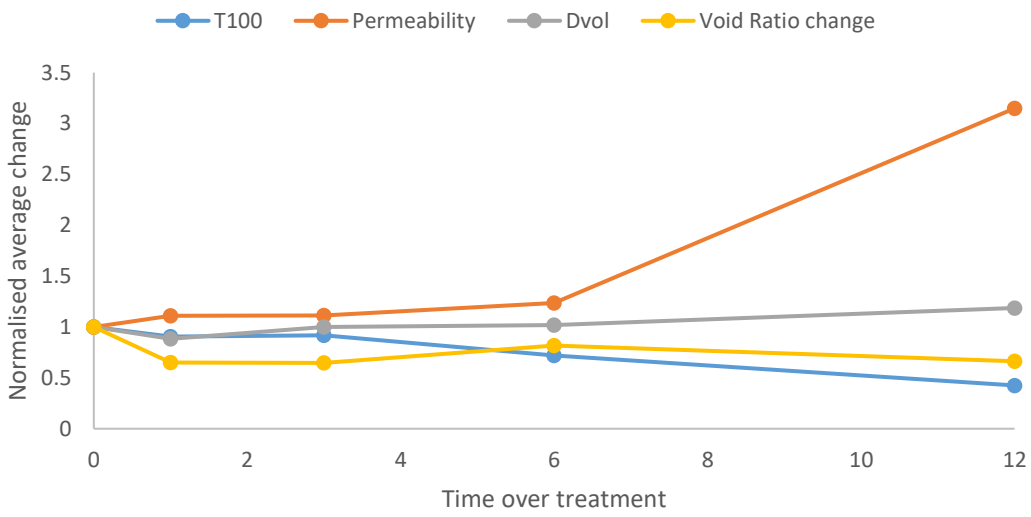

Figure 14.3. A scatter plot showing the changes in various consolidation characteristics over the course of the treatment, with data collected from treated samples normalised against the untreated sample to show any increases or decreases over time.

These consolidation characteristic shifts are accompanied by strength increases with effective cohesion increasing from 4.2 up to 40.6 kPa after 12 months soaking (874 % increase). However, the effective friction angle appears minimally affected with a slight reduction from 29.8° to 25.3°. As noted in Part I, *Geomechanical Characteristics and Triaxial testing*, the relative rate of change over time shows the majority of the changes in peak deviator stress occur within the first month of testing with, on average, a rough 40% increase in peak deviator stress noted after the first month, and subsequent increases over total time typically being less than 10%. In addition to this, it was also observed that strain softening generally reduced after 12 months. However, this change was far less rapid than the deviator strength increase (average changes: deviator stress = 21.7 % increase; strain softening = 4.97 % decrease), with the major changes occurring after the

12-month point of soakage Figure 14.4. Stress paths displayed behavioural changes in the soil under load, especially in the pre-failure range. Untreated soils generally showed initially contractive behaviour followed by dilatant behaviour as they were placed under load before contracting heavily as they sheared and entered the post-shear zone. In contrast to this, in the initial loading phase, treated soil showed strain hardening behaviour, with the soil appearing to dilate under load (according to the stress path) before reaching the CSL and contracting upon failure, exhibiting almost the inverse behaviour of the untreated soil. On top of this, the treated soil behaviour was remarkably consistent with all treated soils following similar stress path orientations.

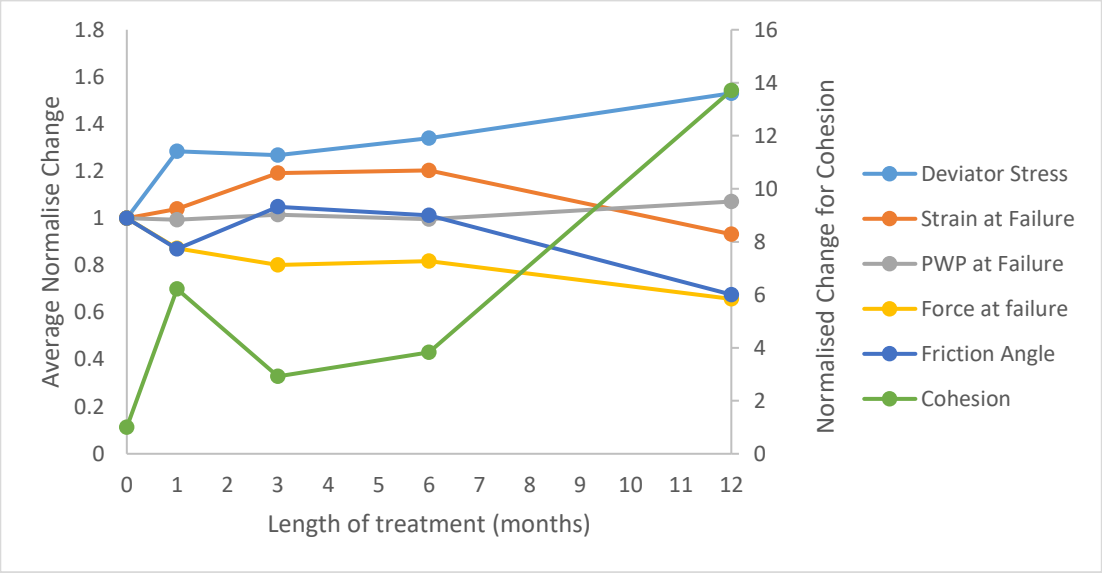

Figure 14.4 A scatter plot showing the changes in various triaxial test parameters over the course of the K-acetate treatment. Values are normalised against the untreated sample to show any changes over time. Due to the size of the change elucidated for effective cohesion, these values are plotted against the right hand Y-axis as opposed to left, this done so that changes to the five other parameters are not hidden by the large changes in effective cohesion.

Part II *Clay chemistry and metal salt-colloid interaction* produced several very interesting results. XRD analyses showed a typical (hydrated) halloysite soil with strong peaks in the 10.1 Å region. There was little in the way of accompanying peaks, indicating that the clay sample was dominated by the 10 Å halloysite. FTIR curves showed some similarity to other potassium acetate-treated halloysites, with peaks within the 1750–650 cm^{-1} range; in particular, the bonds between the silica sheet and the acetate ions appeared to be present. It should be noted that typical shifts expected in the 3850–2850 cm^{-1} range did not occur

(Frost et al., 2000a; Frost et al., 2000b; Cheng et al., 2011; Makó et al., 2014; Adamczyk et al., 2020).

DTA/TGA curves for untreated soils were slightly higher than those observed elsewhere in the literature (506ºC) but fitted the usual expectation for halloysite soils with a dehydroxylation peak centred at 450-500ºC and a degradation of the silica-oxygen bonds at around 950ºC. Treated soils, on the other hand, showed a unique, sharp, exothermic peak centred around 390ºC, which does not seem to fit with any data observed in the literature, as it is lower than the expected combustion temperature of K-acetate (~5-600ºC). One suggestion is that the exothermic peak represents the breakdown of organo-mineral complexes (Lowe and Nelson, 1994), an idea supported by the LOI data. XRF data showed my halloysite had a high proportion of silica to alumina (44.7 %-33 %), outside of which only iron oxides were the main other component (6.22 %), indicating a relatively iron-rich halloysite may be present, or that iron oxides are additionally present, or both. The soil treatment showed a decrease in silica and alumina, as well as most other oxides. However, these were generally at the expense of a significantly increased amount of potassium (which accounts for the drop in the other components).

These changes agreed well with other New Zealand halloysites (Churchman & Theng, 1984). Crystallinity indexes showed a decrease in the order of crystallinity for the halloysites as the length of treatment went on, regardless of the method employed. Unsurprisingly, CEC increased substantially following treatment, with all possible base sites utilised; an interesting addition accompanying this increase, however, was an increase in sodium following treatment at the expense of magnesium and calcium.

Zeta potential tests showed an increase in zeta potential following treatment while streaming potential and PZC analysis showed the clays to have a much-reduced streaming potential following treatment but requiring a larger amount of titrate to reach the PZC (which was subsequently roughly two pH units higher than untreated). BET analysis of the pores showed a small increase in mesopore size and a decrease in micropore size. However, these data come with the caveat that, under hydrated conditions, pores within spheroidal halloysites generally should not exist (Berthonneau et al., 2015). SEM analysis showed our halloysites to be dominated (average 89 %) by spheroid-shaped halloysites, consistent with the report of Kluger et al. (2017).

14.3 Potential Theories

From parts I and II, the data collected provided some indications for achievement of the aims set out at the start of the study, but also provided a number of new questions, these being:

- What is causing the clays to improve their strength over time?
- What is causing the halloysite spheroids to shrink over time?
- Is the rate at which the clay uptakes and improves unique to this halloysite?

The most important question is the cause of the increase in strength. On the surface, it appears the answer to this is simply the introduction of potassium acetate to the soil, but the mechanism for this is not immediately evident. It is clear from the various analyses undertaken in part II that the Pahoia Tephra-derived extra sensitive clay I am dealing with did not act as expected. Based on literature, it was anticipated that the strength increases were related to changes in basal spacings of the clay, with K-acetate intercalating into the halloysite basal space, expanding it from 10.1 Å to around 14 Å (Adamczyk et al., 2020).

This increase in basal space is usually accompanied by an increase in the disorder of the clay unit (leading to a decrease in crystallinity following intercalation) due to the formation of new hydrogen bonds between the acetate unit and the clay surface (Cheng et al., 2011). These new hydrogen bonds, and the disordering of the clay through expansion, increase the number of positively charged sites on the clay surface and increase the opportunity for new bonds to form (due to a shift in the charge balance). This imbalance in charge would then, in theory, lead to increased attraction between the external clay colloid surfaces, with bonds forming between clay colloids due to bridging by free K-acetate molecules (Israelachvili, 2011). Theoretically, this expansion in the clays would account for the decrease in particle density, as the particles being larger (while only a few angstroms) would result in fewer occupying the same space, leading to a decrease in porosity and void ratio as a result of the decrease in available space.

In contrast to expectations, there was no change in the basal space across the full 12 months of treatment, with every treatment point showing the standard 10.1 Å recorded. As an additional check, a sample mixed with 10 $molL^{-1}$ of solute was also tested, showing the same 10.1 Å basal spacing. This finding (lack of expansion) suggests that the theory presented above cannot, in its current form, be put forward as a potential explanation for the numerous positive outcomes derived in part I.

However, while the clay remained at a basal space of 10.1 Å at each testing point across the 12 months, the clay itself did not remain the same size. Across the testing period, the average size of the halloysite spheroids shrank from 343 nm to 176 nm, accompanied by an increase in the uniformity of sizes within the halloysite spheroidal population. Pore size within the clays, within the micropore range at least, showed a slight increase in diameter, though this did not come with an increase in volume or surface area. It should be stated here that the pore size distribution presented in part II was derived from BET analysis of a dried halloysite powder. This finding comes with some caveats, one such being that the results themselves for BET may not be completely reliable in relation to the hydrated pore sizes of clays. This possible unreliability is due to hydrated halloysite's tendency to undergo basal collapse following dehydration, which may result in both over or under estimation of pore surface area, volume and diameter (Berthonneau et al., 2015).

With this said, the presence of salt should provide some resistance to collapse. While dehydration and loss of water from the interlayer space do indeed affect the size of the clay on an angstrom level (halloysites tested in the SEM are theoretically of the 7.3 Å size), morphological size of the clay should be relatively unaffected (Asgar et al., 2021). This is useful to note because there is the potential that the halloysites imaged in the SEM may not have all been fully 'dehydrated'. XRD peaks of dehydrated samples showed a broad shoulder from 10.1 Å to 7 Å for samples treated for 12 months while showing small peaks at 10.1 Å not present in the untreated sample. These peaks are present even after heating the clay at 110^{o}C for 48 hours. Thus, theoretically, if the hydration status of the clay did play a role in the sizes derived from SEM, it would logically suggest that untreated clays would have a smaller diameter due to basal space collapse.

The relationship between pore size and permeability/porosity characteristics cannot be established as BET analysis only looks at the pore sizes of the clays themselves, which should, in theory, be inaccessible unless dehydrated (Berthonneau et al., 2015). Testing via mercury intrusion porosimetry (MIP) would be necessary to determine this.

The forgoing discussion ultimately suggests that the mushroom-cap shaped (partial spheroidal) morphology of the halloysite clay collected from the western Bay of Plenty region 'shrinks' with the increasing length of time for treatment. Where this shrinkage stems from is unclear. On a sheet level, for treated hydrated halloysites, as stated previously, the clay neither increases, nor decreases in size over the 12 months. Thus, the question becomes what is occurring with the clay to cause the diameter to reduce over the course of the treatment. Two possible explanations will be presented here. In addition to

this, based on the clay's resistance to expansion, it suggests that the K-acetate was 'unable' to penetrate the interlayer basal space of the halloysite. For this to occur, it suggests that there were no open edges on the halloysite sheet. Based on this, it is suggested that the entire external outer surface of the halloysite mushroom-cap-shaped spheroids is made up of the siloxane sheet, with the edges of this sheet terminating onto the face of a bottom aluminol sheet, meaning no opportunity for penetration into the basal space for K-acetate.

14.4 Halloysite Spheroid Size Change

14.4.1 Theory 1 - Potassium Acetate Intercalation Mechanism

The first of the two theories is a mechanism similar to that observed in other 1:1 clay upon intercalation and interaction with K-acetate. While differing methods may be used when mixing with K-acetate, kaolinite exhibits similar tendencies to halloysite in that the XRD d001 reflection generally expands out from 7.2 Å to around 14 Å as a result of the expansion in the crystal lattice between corresponding tetrahedral and octahedral sheets, this space usually being occupied by water in the case of halloysite (Bobos et al., 2001; Li et al., 2015; Liu et al., 2016; Zhong et al., 2018).

This model is based on the mechanisms used in the formation of halloysite where the tubular structure is formed as a result of the mismatch between the larger tetrahedral silica plate compared to the smaller octahedral alumina plate (Bates et al., 1950; Bailey, 1990; Yuan et al., 2015). As the two plates are connected via a shared internal vertical oxygen, the Al-O bond from the octahedral plate can constrain this vertical oxygen covalently and thus induce structural stress on the plane of the inner hydroxyl (Yuan et al., 2015). As such, this stress is transmitted to the tetrahedral silica sheet (due to the Si-O covalent bonds) and is observed at the basal (internal) and apical (external surface) oxygen planes. Two mechanisms come into play to compensate for this stress and imbalance: (a) rotation, after which the tetrahedron rotates to compensate for this imbalance, and (b) rolling, where the internal basal oxygens 'drop' closer to the octahedral sheet. In addition to this, the apical oxygens reduce their distance, and a small degree of distance reduction occurs between the internal silicas (Singh, 1996; Al-adwane et al., 2023) (Figure 14.5)

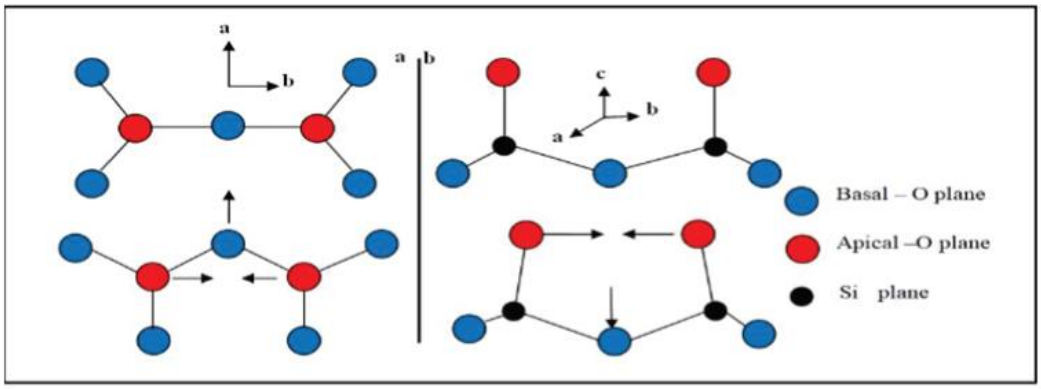

Figure 14.5 A instructional schematic showing the (a) rotation mechanism that occurs in kaolinite/halloysite and (b) the rolling mechanism that also occurs in kaolinite/halloysite clays. From Al-Adwane et al. 2023.

While rotation is an occurrence in nature, rolling is the mechanism of interest in this instance. The induction of rolling within kaolinites is achieved through the repeated intercalation and subsequent washing of the kaolinite with organic salts. Hydration of the 7.2 Å kaolinite via organic salt causes a considerable degree of disorder as a result of expansion in the interlayer space of the clay (Wada, 1961a; Costanzo, 1984; Costanzo & Giese, 1985), with the expansion in this instance (with K-acetate) increasing the basal space from 7.2 Å to around 14 Å. Upon washing of the kaolinite, the clay sheet layers are no longer 'stacked' on top of one another in the same fashion as previously, resulting in an imbalance in sheet stacking. This eventually leads to exfoliation and rolling of the sheets through the dropping of the basal oxygen and shortening the distance between apical oxygens (Singh & Mackinnon, 1996).

With the shrinking of the clays in this study, it is suggested that the potassium acetate is influencing the outer silanol sheet of the halloysite and, as such, results in a smaller 'tighter' halloysite spheroid. It is important to note here that the mechanism occurring to the halloysite spheroids is not going to be the same as that observed in kaolinite-potassium acetate interactions as we have established that there is no intercalation into the halloysite itself (evidenced by the lack of 14 Å peaks in treated halloysites). Instead, what I am proposing in this instance is a variation in the rolling mechanism proposed by Singh (1996). As rolling is induced by a shortening of the apical oxygen bonds and dropping of the internal basal oxygen, three controls on the degree of 'rolling' are put forth by Singh, these being the cation-cation repulsion of the silica, anion-anion repulsion in the basal oxygen plane and the cation-anion bonds.

While the outer surface of the halloysite spheroid is negatively charged (Kluger et al., 2017; Santagata & Johnston, 2022) due to a charge imbalance brought about by the apical oxygens on the outer surface (potentially due to isomorphous substitution within the siloxane sheet), the degree of repulsion and size of double diffuse layer on the clay surface is significantly reduced due to the suppression induced as a result of the high concentration of K-acetate used. As such, this allows for two complementary mechanisms to occur. The first is the displacement of the hole H_2O from the siloxane ditrigonal cavity. Within halloysites, at least two forms of H_2O are found. The first 'associated' H_2O is located within the inter-sheet basal space; this gives rise to the typical 10.1 Å size that differentiates halloysite from kaolinite. This H_2O is relatively strongly hydrogen bonded to the -OH groups of the octahedral aluminol sheet. The second form of H_2O , 'hole' H_2O , is located in the ditrigonal cavities of the siloxane sheet; this H_2O is similarly hydrogen bonded but to the basal oxygens of the silica sheet (Santagata & Johnston, 2022). Of the two forms of H_2O , the 'hole' H_2O is noticeably weaker bonded (Ferrante et al., 2017).

What is proposed here is that the 'hole' H_2O is displaced on the siloxane sheet in its entirety by the potassium ions of the K-acetate within the ditrigonal cavity. As a result, an increased rolling effect occurs with the apical oxygens drawn closer together, giving the smaller diameter of the halloysite after the 12 months of treatment (Figure 14.6). Evidence for this mechanism is established in part II and within literature. From part II, for natural untreated soil, it can be seen from the FTIR peaks of those ascribed to that of hole H_2O at 1650 cm^{-1} (Yi & Gribina, 1972; Costanzo, 1984; Santagata & Johnston, 2022). Following treatment with K-acetate, this peak almost entirely disappears, along with the 1635 cm^{-1} peak for free water and, instead, a new downshifted peak at 1601 cm^{-1} forms. In addition to this, SEM-EDS and XRF show the presence of an increasing percentage of potassium within the soil as the length of treatment goes on. It is fitting that an increasing percentage of potassium displacing the 'hole' H_2O leads to increased scrolling and, thus, smaller diameters of clay.

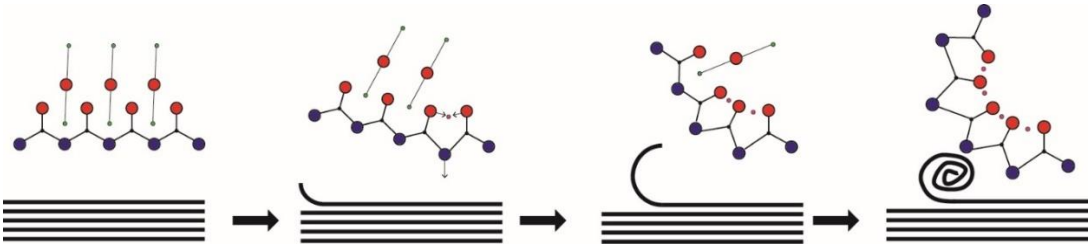

Figure 14.6. A diagram detailing the rolling mechanism both at the sheet level, and the tetrahedron level. Within the mechanism K-Acetate molecules interact with the silanol sheet, and displace the water within the ditrigonal cavity, this causes the apical oxygens of the silica sheet to be drawn together, and a dropping of the basal oxygen, resulting in a slight rolling of the silica sheet. This occurs at numerous points along the clay sheet resulting in an increased rolling, and thus decreased size of scrolled halloysite.

14.4.2 Theory 2 – Halloysite Dehydration

The second theory explaining the shrinkage of clay relates to the degree of dehydration the clays are subject to and the amount of 'collapse' induced in the clays upon dehydration as time goes on. Halloysites exhibiting a spheroidal morphology generally have an 'onion' like internal morphology, with cross-sectional images of the clay showing numerous halloysite sheets making up the clay internals (Figure 14.7a). As a result, the halloysite spheroids have very little in the way of internal pore spaces; in fact, these form as a result of dehydration behaviour (Figure 14.7b) (Berthonneau et al., 2015).

(a) (b)

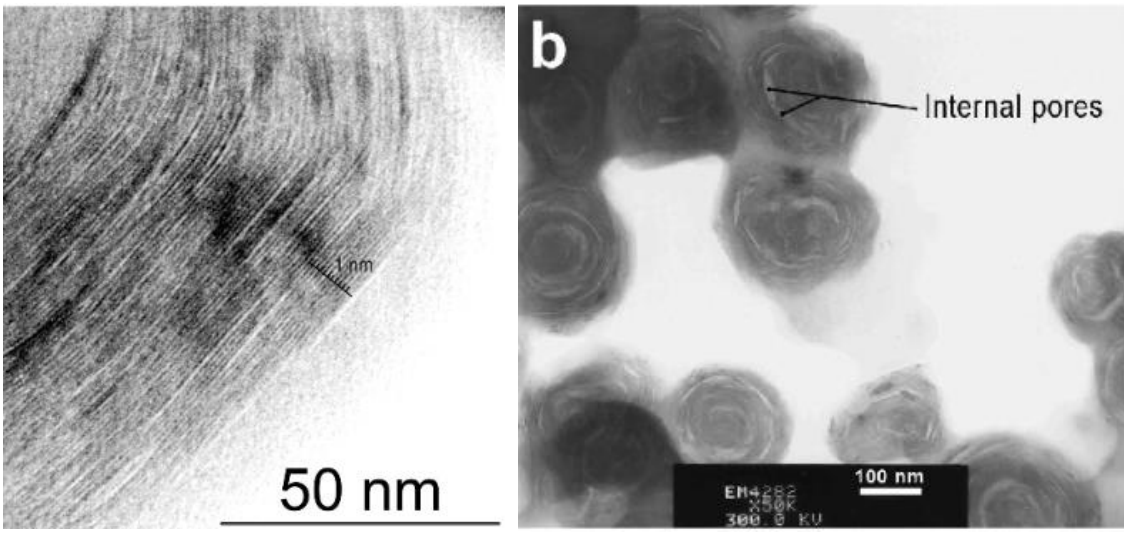

Figure 14.7a,b, Transmission electron micrographs of halloysite spheroids sourced from Pahoia Tephras. (a) shows the individual clay sheets found within the spheroid while (b) highlights the formation of internal pores within the spheroids following dehydration. From Berthonneau et al. 2015.

As stated previously, it is postulated that almost the entire external surface of the halloysite mushroom-cap-shaped spheroids are made up of the siloxane sheet with little to no exposed edge surface, as observed in prior studies, with surface charge imbalances likely related to aspects such as isomorphous substitution (Theng et al., 1982; Theng & Wells, 1995). This means that upon dehydration, there is the potential that not all H_2O will be removed from the halloysite itself. During dehydration, while some of the associated H_2O is removed from the interlayer space, where the larger internal pores form, some H_2O enters into the halloysite itself to form new hole H_2O (on the inner siloxane sheet), as well as the potential for some to be trapped within the halloysite sheets as a result of internal pore formation (Santagata & Johnston, 2022).

In this instance, the increase in 'shrinkage' over the course of treatment may come about due to the presence of acetate on the clay. As the pores begin to form (rapidly within minutes, as per Berthonneau 2015), free K-acetate ions may begin to draw extra H_2O out of the clay during the dehydration process due to the highly deliquescent nature of K-acetate (Arenas et al., 2012). The degree of dehydration may also be related to the degree of disorder within the crystal before dehydration, with the longer treatments having a higher degree of disorder (as shown in part II for crystallinity), which subsequently allows for the drawing of more H_2O out of the clay resulting in a higher degree of collapse for the clay sheets.

Of the two options presented, in my opinion, theory one is much more likely. The justification for this is the wider relation to the strength increases observed in part I. While the shrinkage of the clays in this instance may be accounted for, it does not account for the increase in strength observed in part I. Further to this, one aspect that is not considered with regards to the scrolling mechanism proposed is if the halloysite spheroids are indeed shrinking, with only the outer layers of the clay affected (as evidenced by the lack of any intercalate features found during clay chemistry analyses), the internal sheets of the halloysite spheroid (as can be observed in Figure 14.8) need to be able to accommodate this reduction of space.

To achieve this, the only feasible method would be to reduce the internal pore sizes within the clay as the internal sheets are forced closer and closer together. As the distances between sheets are, on a micropore scale at least, at the smallest possible distance achievable due to the presence of the interlayer water, the accommodation of the internal deformation of the halloysite sheet should, therefore, be observable within the mesopore spaces. Specifically, the difference between the micropore and mesopore space area should theoretically decrease so that they become practically nil, meaning that all pore space available lies almost entirely within the micropore range and is minimally achievable.

When plotting the difference between the micropore (BET) and mesopore (BJH) surface areas against the size of the halloysite spheroids across the 12 months, I see a relatively strong correlation begin to present itself. Indeed, what is observed is a strong correlation ($R^2 = 0.9$) between the difference in surface area and the size of the spheroids, whereas the spheroids shrink as a result of treatment, the difference in surface area decreases.

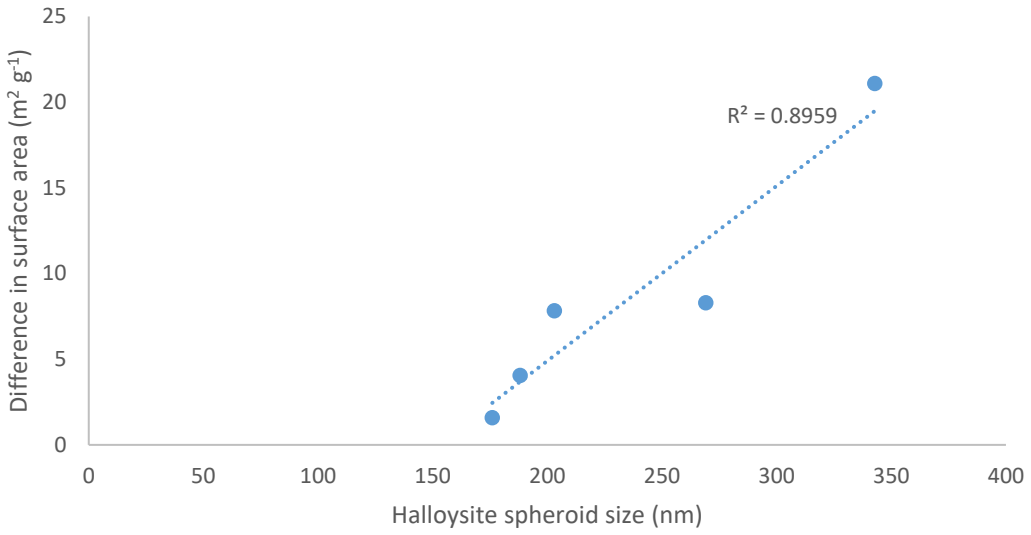

Figure 14.8. A scatter plot showing the average halloysite spheroid plotted against the measured difference in mesopore and micropore surface areas for the respective size. A strong correlation appears to exist between the two parameters (R^2=0.9).

14.5 Strength Increase in Clays

Strength increase within the clay following the treatment with K-acetate is evident. Strength increases in clays generally come about from two main alterations to the soil; mechanical or chemical changes. In this case, I have utilised chemical changes to the soil through the introduction of K-acetate. Chemical changes to the soil usually influence strength through three methods: alteration of the clay mineralogy, cementation, or van der Waals forces changes. In the case of this study, strength increases are theorised to have occurred due to van der Waals forces acting on the clay surfaces.

It is theorised that the mechanical strength increases from surface modifications to the external siloxane surface of the halloysite spheroids, as put forward in theory one above. Due to the pH-induced negative charges on the clay surface (Veerabadran et al., 2007), dissociated potassium ions interact with the siloxane surface, creating short-chain van der Waals forces and adsorb onto the siloxane surface (as observed in the EDS testing) into the ditrigonal cavities. Due to the presence of metal salt, the double diffuse layer, while appearing to be expanded as a result of the higher zeta potential, is, in fact, heavily suppressed (Nowicki & Nowicka, 1994). As a result of the high concentrations of K-acetate used (2 $molL^{-1}$) in this study, the double diffuse layer will likely be heavily suppressed, potentially even a single layer of ions. It should be noted that while the DDL

reduces significantly following the introduction of treatment, interparticle shearing forces will increase. While most major research into these controls have been conducted on soils regarded as the 'extremes' (i.e. kaolinite vs bentonite/montmorillonite), general observations suggest that for kaolin subgroup minerals, due to the larger sizes of the clay particles themselves, interparticle shear forces are the largest controls on liquid limit (Sridharan & Rao, 1975; Sridharan et al., 1988; Widjaja & Setianto, 2019)

These interparticle shear forces subsequently allow for halloysite colloids to more readily coagulate and interact. Combined with the increase of free cations in the pore water, K-Acetate subsequently increases the inter-colloid van der Waals forces, leading to an increase in shear strength. Such an increase can be observed through the increase in peak deviator stresses. Furthermore, this increase in van der Waals forces, accompanied by a reduction in the double diffuse layer, also reduces the potential strain softening (as observed) due to the remoulded clay material in the shear zone having a much lower degree of 'repulsive' forces acting on as a result of lower surface charges, as evidenced by the streaming potential testing.

14.6 Rate of Change in Clays

The largest increases in strength change occurring within the first month is not unexpected, with multiple studies showing the rapid interaction between metal salts and clay surfaces within the kaolin subgroup (Singh & Mackinnon, 1996;Cruz & Duro, 1999; Mitchell et al., 2005; Al-adwane et al., 2023). Data from my study support this, with the bulk of changes and improvements to the soil occurring within the first month of treatment (liquid limit improvements within the first 24 hours).

14.7 Summary

This chapter presents a summary and review of findings from the previous parts of this thesis. Three major questions were posed based on the findings: What is causing the halloysite spheroids to shrink over time? What is causing the clays to improve their strength over time? Is the rate at which the clay uptakes and improves unique to this halloysite? To answer the first question, two hypotheses were put forward, with the most likely of the two, theory 1, a replacement of the hole H_2O on the siloxane sheet with potassium, allowing the halloysite spheroid to 'roll' more using the mechanism often observed in kaolinites treated by K-acetate. The answer to the second question was explained as a follow-up to the first, with the potassium interacting in the siloxane sheet,

allowing short-chain van der Waal bonds to form between spheroids, increasing the clays' shear strength. The third question was conclusively answered with most treatments using K-acetate on kaolin clays noting interaction and intercalations within the first 24 hours.

Chapter 15
Conclusions and Recommendations for Future Work

15.1 Introduction

This chapter summarises the findings documented in this thesis to provide answers to the aims and research questions. These were to determine whether a halloysite-rich, sensitive clay soil prone to large retrogressive landslides can be successfully treated with a potassium metal salt to produce a reduced sensitivity and to increase the strength of the soil, thereby reducing the likelihood of future failure within the soil. The research questions were as follows:

1. To determine how potassium acetate can be introduced to samples of sensitive soil in the laboratory
2. To quantify how geomechanical characteristics (including Atterberg limits, triaxial strength and failure characteristics) of the sensitive soil are influenced by the introduction of potassium acetate
3. To determine the influence of potassium acetate on the clay on a chemical and physical scale.
4. To synthesise objectives (2) and (3) above by developing a theory as to how potassium acetate influences the strength of the halloysite-rich sensitive soil (i.e. a mechanism), considering the chemical and physiological changes that produce the geomechanical changes observed in the clay.

Following the summary of the data found and theories presented, recommendations for future research will be given.

15.2 Summary of Research Findings

15.2.1 Site Selection and Characterisation

While it is known that sensitive soils are commonly found in central and northern North Island, finding an appropriate location to access and sample a sensitive soil was essential for this research. To identify this site, five key criteria were employed. Following a desktop study, the western Bay of Plenty, near Tauranga, was noted to meet several of

these criteria. Within this area, several historical slides in Ōtumoetai, Maungatapu, and Ōmokoroa were found in the literature. While several of these areas did meet some of the criteria, a number did not, with issues around plant growth, remediation or overtopping by colluvium, and other limiting factors found. As such, 26 sites around the Ōmokoroa Peninsula were shortlisted.

The 26 selected sites were further refined through a review of aerial drone imagery to establish whether slip surfaces showed evidence of containing extra-sensitive soil. Subsequently, five sites were selected from the initial 26-site shortlist. Of the chosen landslides, two were discounted due to site remedial works, and one was removed due to lack of access. The two remaining locations were then subjected to field investigations, with site geomorphology, soil profile and *in-situ* soil strength testing undertaken. From this, the slip site at Kowhai Grove was selected due to an extra sensitive material layer (St = 11.4) found within the scarp. Further, it was relatively easily and safely accessed and exhibited all the expected traits for a sensitive soil-sourced landslide: the peak shear vane strength at the site measured 57 kPa, while the remoulded shear strength measured 5 kPa.

15.2.2 Part I — Geomechanical Characterisation and Strength Testing

Due to the high natural moisture content of the soil, it was necessary to first dry the soil to a point close to the plastic limit to allow for the addition of the salt solute to the soil. Atterberg limit testing of the soil showed liquid limits of 55–58 % for the untreated soil collected from Kowhai Grove (for field moisture and distilled water samples). This finding led to some variation in the liquidity index (1.71–2.1); the plastic limit exhibited a similar difference (43–46 %), whereas plasticity index was practically the same (12–13%), and activity similarly low (0.25–0.28).

Remoulded Pahoia Tephra samples were then mixed with a 4 $molL^{-1}$ or a 2 $molL^{-1}$ mixture of K- acetate. In addition, a core that had been soaked for 18 months in 2 $molL^{-1}$ K-acetate was remoulded and also tested, as well as a subsequent remoulded sample soaked for 18 months in a 2 $molL^{-1}$ mixture. The liquid limit increased for all samples treated with K-acetate (62–65 %), with the largest change occurring for the 2 $molL^{-1}$ sample. The plastic limits were relatively unchanged (44–46 %), with the largest changes to the liquidity index occurring for the 18-month-soaked sample (0.57 for 18 months sample, 1.1, and

1.3 for the other samples). Activity slightly increased as well, between 0.36–0.41. Based on this testing, 2 molL^{-1} was selected as the appropriate solute concentration in which to immerse the soil cores. As such, groups of four 150 mm-long, 50 mm-diameter soil cores were immersed within the K-acetate solution for periods of one, three, six and twelve months.

Atterberg limit testing suggested a drop in the liquidity index, a parameter used as an indicator of sensitivity in soil. In particular, after 18 months of soaking, treated soil exhibited a drastically reduced liquidity index. The LI reduced by such an amount that, indicatively, it placed the soil outside the sensitive range (where LI >1). This drop is linked to the changes in the moisture content of the soil. The untreated soil exhibited a high moisture content (67 %), with a wet bulk density of 1576 kg m^{-3} and a corresponding dry bulk density of 944 kg m^{-3}. Particle density, on the other hand, was elevated, registering at 3282 kg m^{-3}. This was accompanied by high porosity (71 %), high void ratio (2.48) and high saturation ratio (89 %). Treatment of the soil cores led to drops in moisture content (57–63 %), particle density (2847–2914 kg m^{-3}), porosity (63–66 %), and void ratio (1.75–1.96), but increases in bulk densities (1599–1632 kg m^{-3} wet, 996–1036 kg m^{-3} dry) and the saturation ratio (91–95 %) were recorded. Particle size was fundamentally similar with little variation regardless of treatment, with the soil comprising 25 % clay, 70 % silt and 5 % sand. These changes were not unexpected, with other research in the literature showing similar behaviours following the increase in salt content present within the clay. However, no clear explanation existed for the high initial particle densities.

To establish a time for likely full diffusion of the metal salt through the clay, conductivity testing within the soil was undertaken with conductivity probes immersed in a remoulded soil paste at three points (30 mm, 90 mm, 120 mm) from a salt reservoir. Changes were observed at 30 mm after 6 hours, with conductive equilibrium with the salt well achieved after 48 hours. The 90 and 150 mm points showed first changes after 12 and 24 hours, respectively, while it took 144 hours to reach equilibrium at 90 mm and another 100 hours (244 hours total) to reach 150 mm. These results provided a rough guide to the time required for the ion plume to travel through the immersed soil cores if only penetrating one exposed face.

Triaxial strength testing was undertaken utilising consolidated undrained tests; this was selected due to it being a closer simulation of the conditions encountered during sensitive soil landslides. Under consolidation, the soil showed an overall decline in time to T100 throughout the treatment, with a loose correlation at all of the confining stresses tested.

Volume expelled and permeability increased as the soaking duration increased all confining stresses. This behaviour is potentially linked to the changing pore structure. Although no clear relationship exists between void ratio before consolidation and permeability for treated samples, there is a clear increase in permeability at lower void ratios compared with untreated soils.

Under shear, there were large increases in peak deviator stress and pore water pressure at all confining stresses with the increasing duration of treatment. While deviator stresses increased over time, most of the change occurred within the first month. The strain at failure remained relatively unaffected by the treatment time, although the strain softening reduced over time. It was also noted that slight pore pressure imbalances began to form across all samples during shear, although these were inconsistent. Triaxial stress paths displayed a shift in behaviour following treatment, with stress paths tending to be left (contractant) initially for untreated samples, while treated samples tended right (dilatant) before failure. All samples contracted heavily upon failure. Mohr circles showed a large increase in effective cohesion following treatment (4.2 kPa untreated, 40.9 kPa 12 months' treatment), while effective friction angle remained relatively unchanged (29.8^{o} untreated, 25.3^{o} after 12 months' treatment).

Sample failure style showed a shift from shear wedge style failure for untreated samples at all confining stresses, with distinctive shear failure planes forming. Treated samples at 1- and 3-months soaking showed shear wedge style to intermediate wedge style of failure following shear. Samples at the 6- and 12-months times showed an increase in barrel style failure, though the 12-month sample showed both intermediate and shear wedge style failures.

For Atterberg limits testing, liquidity index and its role in sensitivity of soil was explored. In particular, when examining the liquidity index/sensitivity correlation often observed in Nordic and Canadian quick to extra sensitive clays some variance appears. When plotted against the ranges specified by Kenney (1977), soils from this study, as well as other Tauranga extra sensitive soils, appear to plot outside the range, showing lower sensitivities than expected for the liquidity index recorded. These issues were previously seen by Wyatt (2009), who utilised a method variation to determine the remoulded shear strength, which showed a good correlation with the liquidity index. Upon re-plotting to these new suggested sensitivities, almost all (except for three data points) plotted within the expected range, suggesting issues with the standard remoulded shear strength determination method in New Zealand. This conformity was further highlighted when

calculating remoulded shear strength utilising the Wood (1990) equation directly derived from drop cone Atterberg limits, and the Leroueil et al. (1983) extrapolated determination of remoulded shear strength. Both the Wood (1990) and Leroueil et al. (1983) methods suggested values for remoulded shear strength were drastically lower than that derived from field shear vane tests (5 kPa shear vane, 0.62 kPa, 0.44 kPa for Wood and Leroueil, respectively). These discrepancies suggest a large difference in remoulded shear strength and the potential for the soil to be classified as a quick clay instead of extra-sensitive soil.

In addition to this, further concerns were noted around the continued use of Casagrande's A-line chart, which, upon plotting onto the modernised Moreno-Marotot and Alonso-Azcarate chart, showed a shift for most Tauranga extra sensitive soils from a clear MH (Silt of high plasticity) to what is described as an intermediate soil (CH-MH) exhibiting both characteristics of highly plastic clay and silt.

The rapid increase in the liquidity index following the introduction of K- acetate, along with the largest increases in shear strength occurring within the first month of treatment, are supported by expected changes through suppression of the double diffuse layer by the large volume of potassium and acetate ions now present within the clay matrix. The clay from this study exhibits similar characteristics to those found in kaolinite-rich clays with similar high concentration solute tests.

While the cause of increases in shear strength are not discussed here, as these are addressed in the clay chemistry section, pore pressure generation is examined in greater detail; Skemptons Ā values are a key focus. Soils of a sensitive nature usually exhibit Ā values over 0.75 at failure. Oddly, while peak Ā values exceed 0.75 for untreated soil, this exceedance was not reflected at failure. However, a noticeable reduction in Ā was observed as the duration of treatment goes on, with Ā at failure remarkably stable across the 12 months of treatment. This behaviour of not achieving Ā of 0.75 at failure is similarly observed in other Tauranga extra sensitive soils, suggesting a difference in the behaviour of the soil under strain when compared with expectations for Northern Hemisphere studies where Ā for extra sensitive soils is typically >0.75. Similarly, Skemptons A value was also examined, providing strong evidence of rapidly forming progressive shear bands within the soil under load, as suggested by Thakur et al. (2018).

15.2.3 Part II — Clay Chemistry

X-ray diffraction (XRD) analyses of the untreated soil clay fraction showed typical reflections for a relatively pure halloysite, with the strongest (characteristic) reflection at 10.1 Å and more minor reflections noted at 4.4 Å and 3.4 Å. Upon heating to 110ºC, a clear 7.2 Å peak began to form, indicating the formation of the dehydrated form of halloysite, with a loss of all peaks upon heating to 550º C. Formamide testing was undertaken to differentiate between halloysite and kaolinite, which showed a strong response at 10.1 Å, reaffirming the presence of halloysite, and no kaolinite, within the clay sample, which is consistent with findings from previous mineralogical studies on similar materials in the region (e.g., Cunningham et al., 2016).

Reflectance peaks of the treated soils showed similar strong 10.1 Å peaks, with the main change between untreated to treated being the increased rate of expansion to 11 Å within the presence of ethylene glycol. Samples tested from the bulk soil, as opposed to the clay fraction, showed near identical results to the clay fraction with a strong, clear peak at 10.1 Å, a very small peak at around 7.2 Å, and secondary reflections for the halloysite at 4.3 Å and 3.4 Å. Further testing was undertaken on samples of treated and untreated soil dehydrated. These samples were heated for 48 hours at 110º C, before being mixed with water following heating to make a 'rehydrated' soil paste, and left for 24 hours. While the characteristic 7.2 Å peak of the dehydrated halloysite was present, upshifts in the reflectance for the 6- and 12-month samples showed peaks at 10.2–9.7 Å, with the peaks having much larger shoulders. On the other hand, the sample treated with 10 molL-1 exhibited a clear expansion to 14.3 Å.

Differential thermal analysis (DTA) and thermo gravimetric analysis (TGA) showed two main features in untreated soil attributed to the de-hydroxylation of the halloysite at around 506º C and decomposition of the siloxane at 952ºC, with only the former resulting in a clear mass loss event. With this said, the treated samples showed the formation of two new peaks, the first around 65ºC relating to the loss of recently adsorbed water onto the clay, and the second an exothermic mass loss at approximately 320ºC that is provisionally attributed as being the result of breakdown of organo-mineral complexes. These two events were also attributed to mass loss events, with the latter often making up to half of the mass loss.

Fourier transform infra-red (FTIR) spectroscopy transmittance curves showed the standard reflections expected for halloysite with peaks within the two major reflectance

ranges of 3850–2850 cm^{-1} (corresponding to Al-OH vibrational modes) and between 1800–650 cm^{-1} (corresponding to Si-OH vibrational modes). Treated samples show the formation of one new peak in the 3850–2850 cm^{-1} range at around 3600 cm^{-1} (although this is slight), as well as four new peaks within the 1800–650 cm^{-1} range corresponding to the interaction between the acetate ion and the silica sheet and the various behaviour of the acetate ion internal bonds. These results indicated an interaction between the halloysite and the potassium acetate ion but did not strongly support the presence of the halloysite-K- acetate intercalate complex.

X-ray fluorescence (XRF) testing for untreated soil showed good agreement with other halloysitic-rich soils of a rhyolitic origin within northern New Zealand. Whilst Fe_2O_3 readings were somewhat on the high side, these were still within the range of values observed in the upper North Island materials. Treated soils showed decreases in SiO_2 and Al_2O_3. K_2O_5 concentrations, as would be expected, increased by the largest margin, with an approximately 7 % increase in loss on ignition. Interestingly, iron was the other major component that increased after treatment with K- acetate.

Crystallinity indices showed an increase in crystal disorder upon treatment, and a decrease in crystallinity was observed as the length and duration of treatment increased. Hydration ratios were relatively stable, with little to no variation for treated samples compared to the untreated sample. Cation exchange capacity (CEC) analyses and testing for major cations showed the untreated soil to be low in CEC (7 cmol/kg), with a 70 % base saturation. Treatment with potassium acetate showed a drastic increase in CEC (92–114 cmol/kg) with significant increases in potassium and sodium, but decreases in divalent cations (calcium and magnesium).

Zeta potential testing showed a decrease in zeta potential following treatment, although corresponding conductivity values, while higher than untreated, showed no trend across the 12 months. Conversely, point zero charge (PZC) analysis showed a large increase in streaming potential (becoming increasingly positive) following treatment. The buffering capacity of the clay also increased following treatment, with a higher PZC pH.

Specific surface area analysis undertaken showed a gradual decrease in the specific surface area within the micropore range (BET) but an overall increase in the mesopore range (BJH). Volume and diameter results show similar trends with decreased micropore sizes but increased mesopore sizes.

Scanning electron microscopy (SEM) analysis showed that treatment did not affect clay morphology, with the clay being dominated by spheroidal halloysites (86 % on average) with a small amount of tubular halloysite (11 % on average), and trace amounts of books were observed. Even though the treatment did not affect the morphologies, there was an impact on the size (diameter) of the halloysite spheroids, with spheroids becoming smaller over the twelve months. In a similar observation to that arising from the triaxial strength analysis, the bulk of the change in the size of the halloysite occurred within the first month of treatment. Similarly, the size variation of samples decreased over 12 months.

Due to the large amount of halloysite present, distinguishing other minerals was challenging as halloysites appear to cover all surfaces. Treated samples showed charging on the clay surfaces, making gathering clear still images challenging. Samples at three months showed fibrous material of quite small diameter (6–15 nm) with lengths ranging from a few to 300 nm, potentially imoglite. As expected, SEM energy dispersive spectroscopy (EDS) showed increased potassium (likely on the clay surface) for treated samples.

The untreated soil overall showed a typical New Zealand halloysite with similar peaks as evident in analyses of Pahoia Tuff/Tephras elsewhere in northern North Island with a typical 10.1 Å peak, dominated by spheroidal halloysite. In contrast, DTA analyses showed the clay slightly higher for de-hydroxylation and de-siloxination. Still, the analyses were well within range and similar to halloysites examined elsewhere in the Bay of Plenty. Analysis of the treated soils presented several results that went against expectations. DTA and TGA showed a consistent, exothermal response around 320–380^{o}C, the cause of which was unclear but which may reflect the presence of organo-mineral complexes (as reported by Lowe and Nelson, 1994).

The temperature at which the spike appears corresponds to potassium acetate's melting and decomposition point, though these usually present as endothermic responses, so it was unlikely to be potassium acetate. Though of note was the decrease in the delta H (energy required) as the length of treatment went on. Regarding basal spacing, while the expectation was an increase in basal space from 10.1 Å to 11.5–14 Å following intercalation of the potassium acetate into the clay, expansion was not observed for treated clays. The only samples that did record any degree of expansion were the rehydrated 12 months' treated samples and rehydrated 10 molL^{-1} treated samples. To ensure that

concentration was not an influencing factor, the 10 $molL^{-1}$ sample was used to validate this and supported the original treated data, showing concentration was not an influencing factor.

FTIR suggested that there may have been some degree of intercalation with the peaks typical of the interaction between acetate ions and the silicon sheet and some degree of shifting in the upper 3620 cm^{-1} peak. However, this shift was noticeably minor and much less than those reported elsewhere in the literature, as well as an upshift as opposed to a downshift as expected from literature. In the lower 1750–1000 cm^{-1} range, the four peaks related to the acetate complex, especially those at 1550 and 1415 $cm^{-1,}$ indicated the strong possibility that an intercalation complex had formed.

This factor is directly contradicted by the XRD peaks not showing any expansion, however. The decrease in crystallinity index as the length of treatment went on also suggested that the K- acetate had an impact on the halloysite clay, causing disorder in the clay's structure. This trait is confirmed to a degree by a large decrease in the average diameter of the halloysite spheroids noted during SEM inspection of the clay. The CEC testing showing such large increases was not unexpected, with a large number of potassium ions present in the solution; these would likely not only bond to free broken edge sites but also likely coat the outer siloxane surface regardless, resulting in potentially anomalously high CEC values. Alternatively, the increase in pH of the soil may have led to an increased number of free bonding sites, increasing the observed CEC. Interestingly, the amount of K- acetate within the clay (per 100 g) was within the expected values, as observed in the literature. On a positive note, the reduction in streaming potential provided a good indication that the soil is less 'stable', with the clay readily flocculating when suspended in solution, suggesting a potential increase in interparticle van der Waal forces, which is a potential positive outcome in a system where the clay undergoes any degree of remoulding.

Specific surface area testing showed a lack of consistency, with a decrease in the micropore and an average increase in mesopore size as the length of the treatment went on. It appears that, in general, as the length of treatment went on, on average, pore sizes reached similar values meaning an increase in pore uniformity. XRF samples, as expected, showed an increase in K_2O and a decrease in MgO and CaO, a similar trait observed with the base saturation testing, indicating the displacement of divalent cations within the clay by the potassium.

15.2.4 Discussion and Theories

Three key questions emerged based on the data collected from the geomechanical characterisation, strength testing, and clay chemistry testing. These were: (1) what is causing the halloysite spheroids to shrink, (2) what is causing the increase in strength of the clay, and (3) is the rate at which the clay uptakes and improves its characterisation, a trait unique to halloysite. The key question is (2), the origin of the strength increase.

Expectations from the literature were that strength increases could come from basal space increases following K-acetate intercalation, with the increased disorder resulting in an increase in charge imbalance on the clay surface. This, in turn, would lead to an increase in colloid attraction with the K- acetate ions free in pore water, acting as bridging short ionic/covalent bonds. This bonding between clay and K-acetate, would, in turn, explain the decrease in particle density due to the larger size of clay colloids and subsequently reduce the porosity and void ratio. No clay expansion was observed, suggesting this initial explanation is incorrect. Looking further into the tests undertaken, however, it was noted that the pore space data derived from specific surface area testing may not be entirely accurate due to the expansion of pores in the halloysite following dehydration. This expansion would provide anomalously high pore space sizes, and hence it was suggested to undertake further testing using mercury intrusion porosimetry to garner an accurate result.

As the potassium acetate could not penetrate the halloysite clay itself, signalled by the lack of expansion in basal space and the measured decrease in average diameter of the halloysite spheroids, two theories were presented as possible explanations. The first of these based the change in spheroid diameter on a mechanism observed in other 1:1 clays under the influence of K- acetate. Based on the interaction of kaolinite and K-acetate, the K-acetate causes an imbalance in the stresses transmitted to the aluminol and siloxane sheets. Within this mechanism, the stress inducers are sourced from the two types of H_2O (‘water’) found to interact with the clay sheets. The stress reduction mechanism is caused by the locations of the water within the clay, resulting in a rolling mechanism. In this instance, the two types of water are associated water and hole water. Associated water is water within the clay hydrogen bonded to the -OH groups of the octahedral aluminol sheet. The hole water comprises water molecules located within the ditrigonal cavities of the siloxane sheen; these are hydrogen bonded with the oxygens of the siloxane sheet, though noticeably weaker than associated water. Upon interaction with K- acetate by the

halloysite, it is proposed that K-acetate ions entirely displace the hole water on the outer siloxane sheet of the halloysite. In this process, the positively charged potassium ion displaces the water within the ditrigonal cavity, causing an increased rolling due to the apical oxygens of the siloxane sheet being drawn together. This contraction would account for the decrease in diameter and the loss of the FTIR peak associated with hole water following treatment.

The second theory regarding clay shrinkage relates to the degree of dehydration experienced by the individual halloysite spheroids. Because the clays have an onion-like internal structure, not all water is necessarily lost upon heating and dehydration. As pore spaces form within the clay following dehydration, this internal pore formation may cause certain water pockets to become trapped, as well as the migration of associated water into hole water upon heating. Increased shrinkage may come about due to the highly deliquescent nature of K-acetate. As there is an increased time that dehydrated K-acetate is in contact with the halloysites, this may allow for an increased amount of water to be lost to the K-acetate over time. While both options may be possible, the second presented does not in any way provide support for a source of strength increase, meaning an entirely separate additional mechanism would need to be at play. In comparison, the first theory does support a putative strength increase.

One theory put forward for strength increase in the soil. Due to the introduction of K-acetate to the clay, it was most likely that strength increases would be due to a chemical change such as a clay mineralogical change, cementation, or van der Waals forces. In this case, it is theorised that dissociated potassium ions interact with the siloxane surface due to pH-induced negative charges on the clay surface (although it is noted that some of the charge on spheroids is likely permanent in origin, being the result of isomorphous substitution). These potassium ions enter into the ditrigonal cavities and create short-chain van der Waals forces with the outer siloxane surface. Combined with the high concentrations of K-acetate in general and suppression of the clay double diffuse layer, individual colloids are attracted to each other as the potassium ions act as a bridge on a colloid-colloid interaction basis or, alternatively, a colloid-acetate-colloid basis. This increase in interparticle shearing force will manifest as an increased peak deviator stress, and not only this but within a failed system, the resultant remoulded material will have a much higher residual shear strength due to the high interparticle van der Waals attraction. Regarding the final question, compared to numerous studies throughout the literature, the

rapid uptake and changes occurring within the clay are consistent with the findings of multiple other studies.

15.3 Aims and Objectives Review

When looking back at the aims and objectives set out in the introduction, it can be stated with a reasonable degree of confidence that the overarching aim of this thesis, to determine whether a halloysite rich sensitive clay soil can be successfully treated to produce a reduced sensitivity and increase in strength, has indeed been achieved. The reduction in sensitivity is supported by the reduction in liquidity index of the soil to below one following 18 months of treatment, while the increase in strength is very much observed following triaxial testing, with increases in both peak deviator stress and overall effective cohesion of the soil.

15.4 Recommendations for Future Work

While several avenues have been explored throughout this thesis, several important aspects remain unanswered and, as such, warrant further research. Some proposals for further research are as follows:

- Assess whether or not the usage of conventional shear vanes accurately determines the strength of sensitive soils in New Zealand. In addition, consider whether the usage of shear vanes potentially disguises the presence of quick clays (remoulded shear strength < 0.5 kPa) within New Zealand. What is the best method to use in determining quick clay strength?
- Consider whether New Zealand sensitive clays are genuinely unique in their correlations between the liquidity index and remoulded shear strength. If so, what is the unique correlation for New Zealand sensitive clays?
- Determine whether or not K-acetate treated sensitive soil retains its strength in a situation where the potassium acetate is flushed from the soil.
- Assess the success of applying K-acetate in a field-scale trial. What are the environmental impacts and are the measured changes observed in the laboratory mirrored in field conditions?
- Examine the relationship between spheroidal halloysite and K- acetate, focusing on the lack of intercalation. Does this lack of intercalation extend to other spheroidal halloysites, or is this a unique trait for weathered deposits of Pahoia Tephra?

- Examine in further detail the shrinkage behaviour of halloysite spheroids under a K- acetate treatment, with a look to examine the degree of shrinkage that can be achieved over a longer period, as well as any additional behaviours such as exfoliation of the clay.
- Examine anion bonding between the acetate ion and the halloysite to see if any interaction exists between the clay sheets and the acetate ion.

References

Adamczyk, M., Małycha, K., Kułacz, K., Pocheć, M., & Orzechowski, K. (2020). Halloysite intercalated by potassium acetate. *Physicochemical Problems of Mineral Processing*, *56*(6), 235–243. https://doi.org/10.37190/ppmp/128740

Adamo, P., Violante, P., & Wilson, M. J. (2001). Tubular and spheroidal halloysite in pyroclastic deposits in the area of the Roccamonfina volcano (Southern Italy). *Geoderma*, *99*(3–4), 295–316.

Al-adwane, O. E., Al-Mallah, A. Y., & Hussein, A. K. (2023). Transform of Kaolinite in Iraqi Kaolin Clay to Halloysite by Intercalation Reaction. *The Iraqi Geological Journal*, 260–271.

Al-Ani, T., & Sarapää, O. (2008). Clay and clay mineralogy. *Physical-Chemical Properties and Industrial Uses*, 11–65.

Alexander, L. T., Faust, G. T., Hendricks, S. B., Insley, H., & McMurdie, H. F. (1943). Relationship of the clay minerals halloysite and endellite. *American Mineralogist: Journal of Earth and Planetary Materials*, *28*(1), 1–18.

Alyamani, M. S., & Şen, Z. (1993). Determination of hydraulic conductivity from complete grain-size distribution curves. *Groundwater*, *31*(4), 551–555.

Andersson-Sköld, Y., Torrance, J. K., Lind, B., Odén, K., Stevens, R. L., & Rankka, K. (2005). Quick clay—A case study of chemical perspective in Southwest Sweden. *Engineering Geology*, *82*(2), 107–118. https://doi.org/10.1016/j.enggeo.2005.09.014

Andresen, L., & Jostad, H. P. (2017). The Role of Instability and Shear Band Localisation in Triggering Landslides in Sensitive Clays. In V. Thakur, J.-S. L'Heureux, & A. Locat (Eds.), *Landslides in Sensitive Clays: From Research to Implementation* (pp. 179–190). Springer International Publishing. https://doi.org/10.1007/978-3-319-56487-6_16

Andrew, R. W., Jackson, M. L., & Wada, K. (1960). Intersalation as a technique for differentiation of kaolinite from chloritic minerals by X-ray diffraction. *Soil Science Society of America Journal*, *24*(5), 422–424.

Aomine, S., & Wada, K. (1962). Differential weathering of volcanic ash and pumice, resulting in formation of hydrated halloysite. *American Mineralogist: Journal of Earth and Planetary Materials*, *47*(9–10), 1024–1048.

Appelo, C. A. J., & Postma, D. (Eds.). (2005). *Geochemistry, Groundwater and Pollution* (2nd ed.). CRC Press.

Arenas, K. J. L., Schill, S. R., Malla, A., & Hudson, P. K. (2012). Deliquescence phase transition measurements by quartz crystal microbalance frequency shifts. *The Journal of Physical Chemistry A*, *116*(29), 7658–7667.

Arthurs, J. (2010). *The nature of sensitivity in rhyolitic pyroclastic soils from New Zealand* [PhD Thesis].

Asgar, H., Jin, J., Miller, J., Kuzmenko, I., & Gadikota, G. (2021). Contrasting thermally-induced structural and microstructural evolution of alumino-silicates with tubular and planar arrangements: Case study of halloysite and kaolinite. *Colloids and Surfaces A: Physicochemical and Engineering Aspects*, *613*, 126106. https://doi.org/10.1016/j.colsurfa.2020.126106

Askenasy, P. E., Dixon, J. B., & McKee, T. R. (1973). Spheroidal Halloysite in a Guatemalan Soil. *Soil Science Society of America Journal*, *37*(5), 799–803. https://doi.org/10.2136/sssaj1973.03615995003700050045x

Bailey, S. W. (1990). Halloysite -A critical assessment. *Sciences Géologiques, Bulletins et Mémoires*, *86*(1), 89–98.

Barr, D. W. (2001). Coefficient of permeability determined by measurable parameters. *Groundwater*, *39*(3), 356–361.

Bates, T. F., Hildebrand, F. A., & Swineford, A. (1950). Morphology and structure of endellite and halloysite. *American Mineralogist: Journal of Earth and Planetary Materials*, *35*(7–8), 463–484.

Beetham, J. (2023). *Maungatapu Landslide Advice*. Tonkin and Taylor.

Bell, H., Richards, L., & Thomson, R. (2003). Relic Slip Verification Study-Tauranga District. In *New Zealand Geotechnical Society (14th: 2003: Tauranga, NZ)* (pp. 281–289). Institution of Professional Engineers New Zealand Wellington, NZ.

Bernander, S. (2011). *Progressive landslides in long natural slopes: Formation, potential extension and configuration of finished slides in strain-softening soils*. Luleå tekniska universitet.

Berry, R. W., & Torrance, J. K. (1998). Mineralogy, grain-size distribution and geotechnical behavior of Champlain clay core-samples, Quebec. *The Canadian Mineralogist*, *36*(6), 1625–1636.

Berthier, P. (1826). Analyse de l'halloysite. *Annales de Chimie et de Physique*, *32*, 332–335.

Berthonneau, J., Grauby, O., Jeannin, C., Chaudanson, D., Joussein, E., & Baronnet, A. (2015). Native Morphology of Hydrated Spheroidal Halloysite Observed by Environmental Transmission Electron Microscopy. *Clays and Clay Minerals*, *63*(5), 368–377. https://doi.org/10.1346/CCMN.2015.0630503

Beyer, W. (1964). Zur bestimmung der wasserdurchlässigkeit von kiesen und sanden aus der kornverteilungskurve. *Wasserwirtschaft Wassertechnik*, *14*(6), 165–168.

Bhattacharjee, S. (2016). DLS and zeta potential – What they are and what they are not? *Journal of Controlled Release*, *235*, 337–351. https://doi.org/10.1016/j.jconrel.2016.06.017

Bird, G. A. (1981). *The nature and causes of coastal landsliding on the Maungatapu Peninsula, Tauranga, New Zealand*. The University of Waikato.

Bjerrum, L. (1954). Geotechnical properties of Norwegian marine clays. *Geotechnique*, *4*(2), 49–69.

Bjerrum, L. (1955). Stability of natural slopes in quick clay. *Géotechnique*, *5*(1), 101–119.

Blake, G. R. (2008). Particle density. In W. Chesworth (Ed.), *Encyclopedia of Soil Science* (pp. 504–505). Springer Netherlands. https://doi.org/10.1007/978-1-4020-3995-9_406

Bobos, I., Duplay, J., Rocha, J., & Gomes, C. (2001). Kaolinite to halloysite-7 Å transformation in the kaolin deposit of São Vicente de Pereira, Portugal. *Clays and Clay Minerals*, *49*, 596–607.

Boettinger, J. L., Graham, R. C., Ming, D. W., & Mumpton, F. A. (1995). Zeolite occurrence in soil environments: An updated review. *Natural Zeolites*, *93*, 23–37.

Brand, E. W., & Brenner, R. P. (1981). *Soft clay engineering*. Elsevier.

Briggs, R., Houghton, B., McWilliams, M., & Wilson, C. (2005). 40Ar/39Ar ages of silicic volcanic rocks in the Tauranga-Kaimai area, New Zealand: Dating the transition between volcanism in the Coromandel Arc and the Taupo Volcanic Zone. *New Zealand Journal of Geology and Geophysics*, *48*(3), 459–469.

Briggs, R. M., Hall, G. J., Hollis, G. R., Houghton, B. F., Hughes, G. R., Morgan, M. D., & Whibread-Edwards, A. R. (1996). *Geology of the Tauranga Area—Sheet U14 1:50 000* (22; Occasional Report 22). Department of Earth Sciences, University of Waikato.

Briggs, R. M., Lowe, D. J., Esler, W. R., Smith, R. T., Henry, M., Wehrmann, H., & Manning, D. (2006). *Geology of the Maketu Area, Bay of Plenty, North Island, New Zealand. Sheet V14 1: 50 000*.

Brindley, G. W. (1961). *The X-ray Identification and Crystal Structures of Clay Minerals*. Mineralogical Society (Clay Minerals Group).

Broms, B. B., & Boman, P. (1979). Lime columns—A new foundation method. *Journal of the Geotechnical Engineering Division*, *105*(4), 539–556.

Brook, M. S., & Nicoll, C. (2024). Brief report of fatal rainfall-triggered landslides from record-breaking 2023 storms in Auckland, New Zealand. *Landslides*, 1–9.

Buck, R. P., Rondinini, S., Covington, A. K., Baucke, F. G. K., Brett, C. M., Camoes, M. F., Milton, M. J. T., Mussini, T., Naumann, R., & Pratt, K. W. (2002). Measurement of pH. Definition, standards, and procedures (IUPAC Recommendations 2002). *Pure and Applied Chemistry*, *74*(11), 2169–2200.

Burns, D., & Cowbourne, A. (2003). Engineering geological aspects of the Ruahihi Power Scheme, Tauranga. *Geotechnics on the Volcanic Edge*, 71–80.

Burns, D., Crawford, S., Farqhar, G., Johnson, D., Wesley, D. L., & Williams, A. (2005). *Field description of Soil and Rock*. New Zealand Geotechnical Society. https://fl-nzgs-media.s3.amazonaws.com/uploads/2022/06/NZGS-2005-Field-description-of-soil-and-rock-3.pdf

Carman, P. C. (1937). Fluid flow through a granular bed. *Trans. Inst. Chem. Eng. London*, *15*, 150–156.

Carr, R. M., Chaikum, N., & Patterson, N. (1978). Intercalation of Salts in Halloysite. *Clays and Clay Minerals*, *26*(2), 144–152. https://doi.org/10.1346/CCMN.1978.0260210

CGSFC, C. G. S. F. C. (2013). *Canadian foundation engineering manual*. Canadian Geotechnical Society.

Chadwick, O. A., Gavenda, R. T., Kelly, E. F., Ziegler, K., Olson, C. G., Elliott, W. C., & Hendricks, D. M. (2003). The impact of climate on the biogeochemical functioning of volcanic soils. *Chemical Geology*, *202*(3–4), 195–223.

Chapuis, R. P. (2004). Predicting the saturated hydraulic conductivity of sand and gravel using effective diameter and void ratio. *Canadian Geotechnical Journal*, *41*(5), 787–795.

Cheng, H., Li, K., Liu, Q., Zhang, S., Li, X., & Frost, R. L. (2014). Insight into the thermal decomposition of kaolinite intercalated with potassium acetate: An evolved gas analysis. *Journal of Thermal Analysis and Calorimetry*, *117*(3), 1231–1239. https://doi.org/10.1007/s10973-014-3934-9

Cheng, H., Liu, Q., Yang, J., Zhang, J., & Frost, R. L. (2010). Thermal analysis and infrared emission spectroscopic study of halloysite–potassium acetate intercalation compound. *Thermochimica Acta*, *511*(1), 124–128. https://doi.org/10.1016/j.tca.2010.08.003

Cheng, H., Liu, Q., Yang, J., Zhang, J., Frost, R. L., & Du, X. (2011). Infrared spectroscopic study of halloysite-potassium acetate intercalation complex. *Journal of Molecular Structure*, *990*(1–3), 21–25. https://doi.org/10.1016/j.molstruc.2011.01.008

Cheng, Z.-L., Cao, B.-C., & Liu, Z. (2019). Study on intercalation in layered structure of halloysite nanotubes (HNTs). *Micro & Nano Letters*, *14*(5), 585–589. https://doi.org/10.1049/mnl.2018.5625

Cheng, Z.-L., Cao, B.-C., Wu, P.-R., Ma, L., & Liu, Z. (2017). Templated synthesis of graphene nanosheets within curling layered nanostructure of halloysite nanotubes. *Materials Letters*, *202*, 62–65. https://doi.org/10.1016/j.matlet.2017.05.071

Childs, C. W. (1992). Ferrihydrite: A review of structure, properties and occurrence in relation to soils. *Zeitschrift Für Pflanzenernährung Und Bodenkunde*, *155*(5), 441–448.

Chorover, J., DiChiaro, M. J., & Chadwick, O. A. (1999). Structural charge and cesium retention in a chronosequence of tephritic soils. *Soil Science Society of America Journal*, *63*(1), 169–177.

Churchman, G., Aldridge, L., & Carr, R. (1972). The relationship between the hydrated and dehydrated states of an halloysite. *Clays and Clay Minerals*, *20*, 241–246.

Churchman, G. J. (1970). *Interlayer water in halloysite*.

Churchman, G. J., & Carr, R. M. (1973). Dehydration of the washed potassium acetate complex of halloysite. *Clays and Clay Minerals*, *21*, 423–424.

Churchman, G. J., & Carr, R. M. (1975). The definition and nomenclature of halloysites. *Clays and Clay Minerals*, *23*, 382–388.

Churchman, G. J., Davy, T. J., Aylmore, L. A. G., Gilkes, R. J., & Self, P. G. (1995). Characteristics of fine pores in some halloysites. *Clay Minerals*, *30*(2), 89–98. https://doi.org/10.1180/claymin.1995.030.2.01

Churchman, G. J., Pasbakhsh, P., Lowe, D. J., & Theng, B. K. G. (2016). Unique but diverse: Some observations on the formation, structure and morphology of halloysite. *Clay Minerals*, *51*(3), 395–416.

Churchman, G. J., & Sumner, M. E. (2000). The alteration and formation of soil minerals by weathering. *Handbook of Soil Science*, 3–76.

Churchman, G. J., & Theng, B. K. G. (1984). Interactions of halloysites with amides: Mineralogical factors affecting complex formation. *Clay Minerals*, *19*(2), 161–175. https://doi.org/10.1180/claymin.1984.019.2.04

Churchman, G. J., Whitton, J. S., Claridge, G. G. C., & Theng, B. K. G. (1984). Intercalation method using formamide for differentiating halloysite from kaolinite. *Clays and Clay Minerals*, *32*(4), 241–248.

Churchman, G., & Lowe, D. (2012). *Alteration, formation and occurrence of minerals in soils In: Huang PM, Li Y & Sumner ME (Eds.) Handbook of Soil Sciences: Properties and Processes*. CRC press.

Costanzo, P., & Giese, R. (1985). Dehydration of synthetic hydrated kaolinites: A model for the dehydration of halloysite (10Å). *Clays and Clay Minerals*, *33*, 415–423.

Costanzo, P. M. (1984). Static and Dynamic Structure of Water in Hydrated Kaolinites. I. The Static Structure. *Clays and Clay Minerals*, *32*(5), 419–428. https://doi.org/10.1346/CCMN.1984.0320511

Cravero, F., & Churchman, G. J. (2016). The origin of spheroidal halloysites: A review of the literature. *Clay Minerals*, *51*(3), 417–427.

Crovelli, R. A. (2000). *Probability models for estimation of number and costs of landslides* (2331–1258). US Geological Survey,.

Cunningham, M. J. (2012). *Sensitive rhyolitic pyroclastic deposits in the Tauranga region: Mineralogy, geomechanics and microstructure of peak and remoulded states* [PhD Thesis]. University of Waikato.

Cunningham, M. J., Lowe, D. J., Wyatt, J. B., Moon, V. G., & Churchman, G. J. (2016). Discovery of halloysite books in altered silicic Quaternary tephras, northern New Zealand. *Clay Minerals*, *51*(3), 351–372.

De Rosa, J., Pontolillo, D. M., Di Maio, C., & Vassallo, R. (2016). Chemical clay soil improvement: From laboratory to field test. *Procedia Engineering*, *158*, 284–289.

Domenico, P. A., & Schwartz, F. W. (1997). *Physical and chemical hydrogeology*. John wiley & sons.

Eide, O., & Bjerrum, L. (1955). The slide at Bekkelaget. *Géotechnique*, *5*(1), 88–100.

Ferrante, F., Armata, N., Cavallaro, G., & Lazzara, G. (2017). Adsorption Studies of Molecules on the Halloysite Surfaces: A Computational and Experimental Investigation. *The Journal of Physical Chemistry C*, *121*(5), 2951–2958. https://doi.org/10.1021/acs.jpcc.6b12876

Flint, A. L., & Flint, L. E. (2002). 2.2 Particle Density. In *Methods of Soil Analysis* (pp. 229–240). John Wiley & Sons, Ltd. https://onlinelibrary.wiley.com/doi/abs/10.2136/sssabookser5.4.c10

Frost, R. L. (1997). Intercalation of Halloysite: A Raman Spectroscopic Study. *Clays and Clay Minerals*, *45*(4), 551–563. https://doi.org/10.1346/CCMN.1997.0450407

Frost, R. L., Kristof, J., Horvath, E., & Kloprogge, J. T. (2000). Rehydration and Phase Changes of Potassium Acetate-Intercalated Halloysite at 298 K. *Journal of Colloid and Interface Science*, *226*(2), 318–327. https://doi.org/10.1006/jcis.2000.6807

Frost, R. L., Kristof, J., Mako, E., & Kloprogge, J. T. (2000). Modification of the hydroxyl surface of potassium acetate intercalated halloysite between 25 and 300 C. *American Mineralogist*, *85*(11–12), 1735–1743. https://doi.org/10.2138/am-2000-11-1217

Frost, R. L., Locos, O. B., Kristof, J., & Kloprogge, J. T. (2001). Infrared spectroscopic study of potassium and cesium acetate-intercalated kaolinites. *Vibrational Spectroscopy*, *26*(1), 33–42.

Garrett, W. G., & Walker, G. F. (1959). The cation-exchange capacity of hydrated halloysite and the formation of halloysite-salt complexes. *Clay Minerals Bulletin*, *4*(22), 75–80.

Gella, K. P. (2017). *Geotechnical and Geological Characterization of a Quick Clay Site at Flotten, Trondheim*.

Ghernaout, D. (2015). Controlling Coagulation Process: From Zeta Potential to Streaming Potential. *American Journal of Environmental Protection*, *4*(5), 16. https://doi.org/10.11648/j.ajeps.s.2015040501.12

Giese, R. F. (1988). Kaolin minerals; structures and stabilities. *Reviews in Mineralogy and Geochemistry*, *19*(1), 29–66.

Giles, D. P. (2020). Chapter 7 Quick clay behaviour in sensitive Quaternary marine clays – a UK perspective. *Geological Society, London, Engineering Geology Special Publications*, *29*(1), 205–221. https://doi.org/10.1144/EGSP29.7

Gulliver, C. P., & Houghton, B. F. (1980). *Omokoroa Point land stability investigation*. Tonkin & Taylor.

Gylland, A., Jostad, H., & Nordal, S. (2014). Experimental study of strain localization in sensitive clays. *Acta Geotechnica*, *9*, 227–240. https://doi.org/10.1007/s11440-013-0217-8

Gylland, A. S. (2012). *Material and slope failure in sensitive clays*.

Gylland, A. S., Rueslåtten, H., Jostad, H. P., & Nordal, S. (2013). Microstructural observations of shear zones in sensitive clay. *Engineering Geology*, *163*, 75–88. https://doi.org/10.1016/j.enggeo.2013.06.001

Haynes, W. M. (2016). *CRC handbook of chemistry and physics*. CRC press.

Hazlewood, F. J., Rhodes, E., & Ubbelohde, A. R. (1966). Melting mechanisms and melt properties of alkali acetates. *Transactions of the Faraday Society*, *62*, 3101. https://doi.org/10.1039/tf9666203101

He, P., Ohtsubo, M., Higashi, T., & Kanayama, M. (2015). Sensitivity of Salt-leached Clay Sediments in the Ariake Bay Area, Japan. *Marine Georesources & Geotechnology*, *33*(5), 429–436. https://doi.org/10.1080/1064119X.2014.952854

Head, K. H. (1998). *Manual of soil laboratory testing. Volume 3: Effective stress tests.* John Wiley & Sons.

Head, K. H., & Epps, R. J. W. (2011). *Manual of Soil Laboratory Testing—Volume 2: Permeability, Shear Strength and Compressibility Tests* (3rd ed., Vol. 2). Caithness.

Hegan, B., Wesley, L., & Richards, L. (2005). *Tauranga Storm Event of 18 May 2005: Landslip Issues*. TCC.

Helle, T. E., Aagaard, P., & Nordal, S. (2017). In Situ Improvement of Highly Sensitive Clays by Potassium Chloride Migration. *Journal of Geotechnical and Geoenvironmental Engineering*, *143*(10), 04017074. https://doi.org/10.1061/(ASCE)GT.1943-5606.0001774

Helle, T. E., Bryntesen, R. N., Amundsen, H. A., Emdal, A., Nordal, S., & Aagaard, P. (2015). Laboratory setup to evaluate the improvement of geotechnical properties from potassium chloride saturation of a quick clay from Dragvoll, Norway. *GEOQuébec 2015–Challenges from North to South, Québec*.

Hewitt, A. E., Balks, M. R., & Lowe, D. J. (2021). *The Soils of Aotearoa New Zealand*. Springer.

Hillier, S., & Ryan, P. C. (2002). Identification of halloysite (7 Å) by ethylene glycol solvation: The 'MacEwan effect'. *Clay Minerals*, *37*(3), 487–496. https://doi.org/10.1180/0009855023730047

Holt, R. M., Bakk, A., Stenebråten, J. F., Bauer, A., & Fjær, E. (2018, June 17). *Skempton's A — A Key to Man-Induced Subsurface Pore Pressure Changes*. https://onepetro.org/ARMAUSRMS/proceedings-abstract/ARMA18/All-ARMA18/139129

Hopkins, J. L., Lowe, D. J., & Horrocks, J. L. (2021). Tephrochronology in Aotearoa New Zealand. *New Zealand Journal of Geology and Geophysics*, *64*(2–3), 153–200.

Hughes, I. R. (1966). *Mineral changes of halloysite on drying*.

Hungr, O., Leroueil, S., & Picarelli, L. (2014). The Varnes classification of landslide types, an update. *Landslides*, *11*(2), 167–194. https://doi.org/10.1007/s10346-013-0436-y

Israelachvili, J. N. (2011). *Intermolecular and surface forces*. Academic press.

Jacob, S., Chavali, R. V. P., Saeidi, A., & Sadrekarimi, A. (2023). Remoulding energy as a criterion in assessing retrogressive landslides in sensitive clays: A review and its applicability to Eastern Canada. *Natural Hazards*, *118*(3), 1833–1853. https://doi.org/10.1007/s11069-023-06088-6

Jacquet, D. (1990). Sensitivity to remoulding of some volcanic ash soils in New Zealand. *Engineering Geology*, *28*(1–2), 1–25.

Janik, L. J., & Keeling, J. L. (1993). FT-IR partial least-squares analysis of tubular halloysite in kaolin samples from the Mount Hope kaolin deposit. *Clay Minerals*, *28*(3), 365–378.

Jaynes, W. (1986). Multiple Cation-Exchange Capacity Measurements on Standard Clays Using a Commercial Mechanical Extractor1. *Clays and Clay Minerals - CLAYS CLAY MINER*, *34*, 93–98. https://doi.org/10.1346/CCMN.1986.0340112

Joussein, E. (2007). Behavior of halloysite clay under formamide treatment. *Applied Clay Science*, *35*(1–2), 17–24. https://doi.org/10.1016/j.clay.2006.07.002

Joussein, E., Petit, S., Churchman, J., Theng, B., Righi, D., & Delvaux, B. (2005). Halloysite clay minerals—A review. *Clay Minerals - CLAY MINER*, *40*, 383–426. https://doi.org/10.1180/0009855054040180

Joussein, E., Petit, S., Claire, F., Philippe, V., & Righi, D. (2006). Differences in the dehydration-rehydration behavior of halloysites: New evidence and interpretations. *Clays and Clay Minerals - CLAYS CLAY MINER*, *54*, 473–484. https://doi.org/10.1346/CCMN.2006.0540408

Kameda, J. (2022). Rheological properties of halloysite soil slurry: A case study of weathered tephra involved in a shallow landslide triggered by the 2018 Eastern Iburi earthquake in Hokkaido, Japan. *Earth, Planets and Space*, *74*(1), 70. https://doi.org/10.1186/s40623-022-01623-4

Kameda, J., Kamiya, H., Masumoto, H., Morisaki, T., Hiratsuka, T., & Inaoi, C. (2019). Fluidized landslides triggered by the liquefaction of subsurface volcanic deposits during the 2018 Iburi–Tobu earthquake, Hokkaido. *Scientific Reports*, *9*(1), 13119.

Kameda, J., & Morisaki, T. (2022). Rheological properties of concentrated allophane, halloysite, and kaolinite suspensions. *Applied Clay Science*, *226*, 106557.

Karlsrud, K., Aas, G., & Gregerson, O. (1986). *Can we predict landslide hazards in soft sensitive clays? Summary of Norwegian practice and experiences.*

Keeling, J. L., Pasbakhsh, P., & Jock Churchman, G. (2012). Halloysite from the Eucla basin, South Australia–comparison of physical properties for potential new uses. *Proceedings of the 10th International Congress for Applied Mineralogy (ICAM)*, 351–359.

Keller, W. D., Reynolds, R. C., & Inoue, A. (1986). Morphology of Clay Minerals in the Smectite-to-Illite Conversion Series by Scanning Electron Microscopy. *Clays and Clay Minerals*, *34*(2), 187–197. https://doi.org/10.1346/CCMN.1986.0340209

Kirkman, J. H. (1977). Possible structure of halloysite disks and cylinders observed in some New Zealand rhyolitic tephras. *Clay Minerals*, *12*(3), 199–216.

Kirschbaum, D., Stanley, T., & Zhou, Y. (2015). Spatial and temporal analysis of a global landslide catalog. *Geomorphology*, *249*, 4–15.

Kitchen, E. (2021). *Sensitive soils of the Puketoka Formation, Hamilton, New Zealand*. The University of Waikato.

Kluger, M. O. (2017). *Failure mechanisms and mobilization processes of coastal landslides in sensitive soils*. Universität Bremen.

Kluger, M. O., Jorat, M. E., Moon, V. G., Kreiter, S., de Lange, W. P., Mörz, T., Robertson, T., & Lowe, D. J. (2020). Rainfall threshold for initiating effective stress decrease and failure in weathered tephra slopes. *Landslides*, *17*(2), 267–281.

Kluger, M. O., Kreiter, S., Moon, V. G., Roskoden, R. R., & Mörz, T. (2022). Compressibility and permeability of weathered, sensitive volcanic ash (tephra) deposits at the Omokoroa flow slide, New Zealand. *Engineering Geology*, *310*, 106885. https://doi.org/10.1016/j.enggeo.2022.106885

Kluger, M. O., Moon, V. G., Kreiter, S., Lowe, D. J., Churchman, G. J., Hepp, D. A., Seibel, D., Jorat, M. E., & Mörz, T. (2017). A new attraction-detachment model for explaining flow sliding in clay-rich tephras. *Geology*, *45*(2), 131–134. https://doi.org/10.1130/G38560.1

Knauf, L. (2022). Site Behaviour And Management Of Sensitive Volcanic Soils. *NZ Geomechanics News*, *103*.

Kodaka, T., Higo, Y., Kimoto, S., & Oka, F. (2007). Effects of sample shape on the strain localization of water-saturated clay. *International Journal for Numerical and Analytical Methods in Geomechanics*, *31*(3), 483–521. https://doi.org/10.1002/nag.585

Kohyama, N., Fukushima, K., & Fukami, A. (1978). Observation of the hydrated form of tubular halloysite by an electron microscope equipped with an environmental cell. *Clays and Clay Minerals*, *26*, 25–40.

Kollannur, N. J., & Arnepalli, D. N. (2019). Methodology for determining point of zero salt effect of clays in terms of surface charge properties. *Journal of Materials in Civil Engineering*, *31*(12), 04019286.

Lambe, T. W., & Whitman, R. V. (1991). *Soil mechanics* (Vol. 10). John Wiley & Sons.

Larsson, R., & Åhnberg, H. (2003). *Long-term effects of excavations at crests of slopes. Pore pressure distribution-Shear strength properties-Stability-Environment*. Statens geotekniska institut.

Ledoux, R. L., & White, J. L. (1966). Infrared studies of hydrogen bonding interaction between kaolinite surfaces and intercalated potassium acetate, hydrazine, formamide, and urea. *Journal of Colloid and Interface Science*, *21*(2), 127–152.

Levis, S. R., & Deasy, P. B. (2002). Characterisation of halloysite for use as a microtubular drug delivery system. *International Journal of Pharmaceutics*, *243*(1), 125–134. https://doi.org/10.1016/S0378-5173(02)00274-0

Li, X., Liu, Q., Cheng, H., Zhang, S., & Frost, R. L. (2015). Mechanism of kaolinite sheets curling via the intercalation and delamination process. *Journal of Colloid and Interface Science*, *444*, 74–80. https://doi.org/10.1016/j.jcis.2014.12.039

Li, Y., Zhang, Y., Zhang, Y., Liu, M., Zhang, F., & Wang, L. (2017). Thermal behavior analysis of halloysite selected from Inner Mongolia Autonomous Region in China. *Journal of Thermal Analysis and Calorimetry*, *129*(3), 1333–1339. https://doi.org/10.1007/s10973-017-6324-2

Li, Z.-S., Zhang, Y., Janiszewski, M., & Korkiala-Tanttu, L. (2022). Radial deformation and failure of stabilised soft clay under uniaxial compression. *Soils and Foundations*, *62*(5), 101213. https://doi.org/10.1016/j.sandf.2022.101213

Liu, Q., Li, X., & Cheng, H. (2016). Insight into the self-adaptive deformation of kaolinite layers into nanoscrolls. *Applied Clay Science*, *124–125*, 175–182. https://doi.org/10.1016/j.clay.2016.02.015

Liu, Z., L'Heureux, J.-S., Glimsdal, S., & Lacasse, S. (2021). Modelling of mobility of Rissa landslide and following tsunami. *Computers and Geotechnics*, *140*, 104388. https://doi.org/10.1016/j.compgeo.2021.104388

Locat, A., Demers, D., Locat, P., & Geertsema, M. (2017). Sensitive clay landslides in Canada. *Proceedings of the 70th Canadian Geotechnical Conference, Ottawa, Paper*, *875*(8).

Locat, A., Leroueil, S., Bernander, S., Demers, D., Jostad, H. P., & Ouehb, L. (2011). Progressive failures in eastern Canadian and Scandinavian sensitive clays. *Canadian Geotechnical Journal*, *48*(11), 1696–1712.

Locat, J. (1995). On the development of microstructure in collapsible soils: Lessons from the study of recent sediments and artificial cementation. In *Genesis and properties of collapsible soils* (pp. 93–128). Springer.

Lowe, D. (1995). *Teaching clays: From ashes to allophane*. 19–23.

Lowe, D. (2023). Soils and landscapes of the Hamilton Basin and part South Waikato area-a summary. *Earth*.

Lowe, D. J. (1986). Controls on the rates of weathering and clay mineral genesis in airfall tephras: A review and New Zealand case study. *Rates of Chemical Weathering of Rocks and Minerals.*, 265–330.

Lowe, D. J. (2019). Using soil stratigraphy and tephrochronology to understand the origin, age, and classification of a unique Late Quaternary tephra-derived Ultisol in Aotearoa New Zealand. *Quaternary*, *2*(1), 9.

Lowe, D. J., & Churchman, G. J. (2016). *Tales of the unexpected: Halloysite delivers surprises and a paradox*.

Lowe, D. J., & Nelson, C. S. (1983). *Guide to the nature and methods of analysis of the clay fraction of tephras from the South Auckland region, New Zealand.*

Lowe, D. J., & Nelson, C. S. (1994). *Guide to the nature and methods of analysis of the clay fraction of tephras from the South Auckland region, New Zealand.*

Lowe, D. J., & Percival, H. (1993). *Clay mineralogy of tephras and associated paleosols and soils, and hydrothermal deposits, North Island [New Zealand]*.

Lowe, D. J., Tippett, J. M., Kamp, P. J., Liddell, I. J., Briggs, R. M., & Horrocks, J. L. (2001). *Ages on weathered Plio-Pleistocene tephra sequences, western north Island, New Zealand*.

Makó, É., Kovács, A., Horváth, E., & Kristóf, J. (2014). Kaolinite-potassium acetate and halloysite-potasium acetate complexes prepared by mechanochemical, solution and homogenization techniques: A comparative study. *Clay Minerals*, *49*(3), 457–471. https://doi.org/10.1180/claymin.2014.049.3.08

Manning, D. (1996). Middle-late Pleistocene tephrostratigraphy of the eastern Bay of Plenty, New Zealand. *Quaternary International*, *34*, 3–12.

Marsters, S. (1978). Report upon the extraction and industrial uses of halloysite. *Proc. Ann. Conf. Australasian Institute of Mining and Metallurgy, Whangarei, New Zealand 1978*, 91–100.

Matocha, C. J. (2005). Clay: Charge Properties. In *Encyclopedia of Soil Science—Two-Volume Set* (2nd ed.). CRC Press.

Mesri, G., & Olson, R. E. (1971). Mechanisms controlling the permeability of clays. *Clays and Clay Minerals*, *19*, 151–158.

Mesri, G., & Rokhsar, A. (1974). Theory of consolidation for clays. *Journal of the Geotechnical Engineering Division*, *100*(8), 889–904.

Mills, P. (2016). *Failure mechanisms in sensitive volcanic soils in the Tauranga Region, New Zealand* [PhD Thesis]. University of Waikato.

Mitchell, J. K., Soga, K., & others. (2005). *Fundamentals of soil behavior* (Vol. 3). John Wiley & Sons New York.

Moon. (2016). Halloysite behaving badly: Geomechanics and slope behaviour of halloysite-rich soils. *Clay Minerals*, *51*(3), 517–528. https://doi.org/10.1180/claymin.2016.051.3.09

Moon, Cunningham, M. J., Wyatt, J. B., Lowe, D. J., Morz, T., & Jorat, M. E. (2013). *Landslides in sensitive soils, Tauranga, New Zealand.*

Moon, Mills, P. R., Geotechnics, C., Kluger, M. O., Lowe, D. J., Churchman, G. J., de Lange, W. P., Hepp, D. A., Kreiter, S., & Mörz, T. (2017). Sensitive pyroclastic soils in the Bay of Plenty, New Zealand: Microstructure to failure mechanisms. *20th New Zealand Geotechnical Society Symposium NZGS2017*, 1–8.

Moreno-Maroto, J. M., & Alonso-Azcárate, J. (2018). What is clay? A new definition of "clay" based on plasticity and its impact on the most widespread soil classification systems. *Applied Clay Science*, *161*, 57–63. https://doi.org/10.1016/j.clay.2018.04.011

Moreno-Maroto, J. M., Alonso-Azcárate, J., & O'Kelly, B. C. (2021). Review and critical examination of fine-grained soil classification systems based on plasticity. *Applied Clay Science*, *200*, 105955. https://doi.org/10.1016/j.clay.2020.105955

Moum, J., Løken, T., & Torrance, J. K. (1971). A geochemical investigation of the sensitivity of a normally consolidated clay from Drammen, Norway. *Geotechnique*, *21*(4), 329–340.

Moum, J., Sopp, O. I., & Loken, T. (1968). Stabilization of undisturbed quick clay by salt wells. *Norwegian Geotechnical Institute Publ*.

Ndayiragije, S., & Delvaux, B. (2004). Selective sorption of potassium in a weathering sequence of volcanic ash soils from Guadeloupe, French West Indies. *Catena*, *56*(1–3), 185–198.

NGI. (2011). *EILEDNING FOR SYMBOLER OG DEFINISJONER I GEOTEKNIKK IDENTIFISERING OG KLASSIFISERING AV JORD*. NORSK GEOTEKNISK FORENING.

Nikhil John, K., & Arnepalli, D. N. (2019). Factors Influencing Zeta Potential of Clayey Soils. In V. K. Stalin, M. Muttharam, V. K. Stalin, & M. Muttharam (Eds.), *Geotechnical Characterisation and Geoenvironmental Engineering* (Vol. 16, pp. 171–178). http://link.springer.com/10.1007/978-981-13-0899-4_21

Odenstad, S. (1952). *Landslide at Sköttorp on the Lidan River*. Statens geotekniska institut.

O'Kelly, B. C., Vardanega, P. J., & Haigh, S. K. (2018). Use of fall cones to determine Atterberg limits: A review. *Géotechnique*, *68*(10), 843–856. https://doi.org/10.1680/jgeot.17.R.039

Oliver, R. C. (1997). *A geotechnical characterisation of volcanic soils in relation to coastal landsliding on the Maungatapu Peninsula, Tauranga, New Zealand.*

Ouehb, L. (2007). *Analyse du glissement de Saint-Liguori (1989): Dans l'optique d'une rupture progressive*. Université Laval.

Pane, V., Croce, P., Znidarcic, D., Ko, H.-Y., Olsen, H. W., & Schiffman, R. L. (1983). Effects of consolidation on permeability measurements for soft clay. *Geotechnique*, *33*(1), 67–72.

Papoulis, D., Tsolis-Katagas, P., & Katagas, C. (2004). Progressive stages in the formation of kaolin minerals of different morphologies in the weathering of plagioclase. *Clays and Clay Minerals*, *52*(3), 275–286.

Parfitt, R., & Kimble, J. (1989). Conditions for formation of allophane in soils. *Soil Science Society of America Journal*, *53*(3), 971–977.

Parfitt, R. L., & Wilson, A. D. (1985). *Estimation of allophane and halloysite in three sequences of volcanic soils, New Zealand. No. 7*, 1–8.

Parfitt, R., Russell, M., & Orbell, G. (1983). Weathering sequence of soils from volcanic ash involving allophane and halloysite, New Zealand. *Geoderma*, *29*(1), 41–57.

Parfitt, R., Saigusa, M., & Cowie, J. (1984). Allophane and halloysite formation in a volcanic ash bed under different moisture conditions. *Soil Science*, *138*(5), 360–364.

Pasbakhsh, P., Churchman, G. J., & Keeling, J. L. (2013). Characterisation of properties of various halloysites relevant to their use as nanotubes and microfibre fillers. *Applied Clay Science*, *74*, 47–57. https://doi.org/10.1016/j.clay.2012.06.014

Penner, E. (1965). A study of sensitivity in Leda clay. *Canadian Journal of Earth Sciences*, *2*(5), 425–441.

Petley, D. (2012). Global patterns of loss of life from landslides. *Geology*, *40*(10), 927–930.

Pittari, A., Prentice, M. L., McLeod, O. E., Yousef Zadeh, E., Kamp, P. J., Danišík, M., & Vincent, K. A. (2021). Inception of the modern North Island (New Zealand) volcanic setting: Spatio-temporal patterns of volcanism between 3.0 and 0.9 Ma. *New Zealand Journal of Geology and Geophysics*, *64*(2–3), 250–272.

Pochapski, D. J., Carvalho Dos Santos, C., Leite, G. W., Pulcinelli, S. H., & Santilli, C. V. (2021). Zeta Potential and Colloidal Stability Predictions for Inorganic Nanoparticle Dispersions: Effects of Experimental Conditions and Electrokinetic Models on the Interpretation of Results. *Langmuir*, *37*(45), 13379–13389. https://doi.org/10.1021/acs.langmuir.1c02056

Prentice, M., Pittari, A., Lowe, D. J., Kilgour, G., Kamp, P. J., & Namaliu, M. (2022). Linking proximal ignimbrites and coeval distal tephra deposits to establish a record of

voluminous Early Quaternary (2.4–1.9 Ma) volcanism of the Tauranga Volcanic Centre, New Zealand. *Journal of Volcanology and Geothermal Research*, *429*, 107595.

Pullar, W., Birrell, K. S., & Heine, J. C. (1973). Named tephras and tephra formations occurring in the central North Island, with notes on derived soils and buried paleosols. *New Zealand Journal of Geology and Geophysics*, *16*(3), 497–518.

Pusch, R. (1970). *Clay microstructure. A study of the microstructure of soft clays with special reference to their physical properties*. Statens geotekniska institut.

Pusch, R., & Söderblom, R. (1967). *Recent Quick-clay Studies*. Swedish Geotechnical Institute.

Quantin, P., Herbillon, A. J., Janot, C., & Siefferman, G. (1984). L''halloysite'blanche riche en fer de vate (vanuatu)—Hypothese d'un edifice interstratifie halloysite-hisingerit. *Clay Minerals*, *19*(4), 629–643.

Quigley, R. M. (1980). Geology, mineralogy, and geochemistry of Canadian soft soils: A geotechnical perspective. *Canadian Geotechnical Journal*, *17*(2), 261–285.

Quinn, P., Hutchinson, D., Diederichs, M., & Rowe, R. (2011). Characteristics of large landslides in sensitive clay in relation to susceptibility, hazard, and risk. *Canadian Geotechnical Journal*, *48*(8), 1212–1232.

Rankka, K., Andersson-Sköld, Y., Hultén, C., Larsson, R., Leroux, V., & Dahlin, T. (2004). *Quick clay in Sweden*. Statens geotekniska institut.

Robertson, T. P. (2017). *Is there a salty solution to sensitive soil sliding in the Bay of Plenty, New Zealand?* The University of Waikato.

Rosenqvist, I. T. (1953). Considerations on the sensitivity of Norwegian quick-clays. *Geotechnique*, *3*(5), 195–200.

Rosenqvist, I. T. (1977). *A general theory for Quick Clay Properties*. 215–228.

Rosser, B., Dellow, S., Haubrock, S., & Glassey, P. (2017). New Zealand's national landslide database. *Landslides*, *14*, 1949–1959.

Rouquerol, J., Rouquerol, F., Llewellyn, P., Maurin, G., & Sing, K. (2013). *Adsorption by powders and porous solids: Principles, methodology and applications*.

Ruiz Cruz, M. D., & Franco Duro, F. I. (1999). New data on the kaolinite-potassium acetate complex. *Clay Minerals*, *34*(4), 565–577. https://doi.org/10.1180/000985599546451

Saigusa auSadao Shoji, M., & Kato, T. (1978). Origin and nature of halloysite in Ando soils from Towada tephra, Japan. *Geoderma*, *20*(2), 115–129. https://doi.org/10.1016/0016-7061(78)90039-3

Santagata, M., & Johnston, C. T. (2022). A study of nanoconfined water in halloysite. *Applied Clay Science*, *221*, 106467. https://doi.org/10.1016/j.clay.2022.106467

Schmitz, R. M., & Van Paassen, L. A. (2003). The decay of the liquid limit of clays with increasing salt concentration. *Ingeokring Newsletter*, *9*(1), 10–14.

Sherwood, P. T. (1970). The reproducibility of the results of soil classification and compaction tests. *Rrl Reports, Road Research Lab/UK/*.

Sherwood, P. T., & Ryley, M. D. (1970). An investigation of a cone-penetrometer method for the determination of the liquid limit. *Géotechnique*, *20*(2), 203–208.

Sim, K. B., Lee, M. L., & Wong, S. Y. (2024, April 24). *An Overview of Socioeconomic Impacts of Landslides*. 43rd Annual Conference of the International Association for Impact Assessment, Dublin, Ireland.

Singh, B. (1996). Why does halloysite roll?—A new model. *Clays and Clay Minerals*, *44*, 191–196.

Singh, B., & Mackinnon, I. D. (1996). Experimental Transformation of Kaolinite to Halloysite. *Clays and Clay Minerals*, *44*(6), 825–834. https://doi.org/10.1346/CCMN.1996.0440614

Singleton, P., McLeod, M., & Percival, H. (1989). Allophane and halloysite content and soil solution silicon in soils from rhyolitic volcanic material, New Zealand. *Soil Research*, *27*(1), 67–77.

Sivakumar, V., Glynn, D., Cairns, P., & Black, J. A. (2009). A new method of measuring plastic limit of fine materials. *Géotechnique*, *59*(10), 813–823.

Skempton, A. W. (1954). The Pore-Pressure Coefficients A and B. *Geotechnique*, *4*, 143–147.

Skempton, A. W., & Northey, R. D. (1952). The sensitivity of clays. *Geotechnique*, *3*(1), 30–53.

Slichter, C. S. (1899). Theoretical investigation of the motion of ground waters. *The 19th Ann. Rep. US Geophys Survey.*, 304–319.

Smalley, I. J., Fordham, C. J., & Callander, P. F. (1984). Towards a general model of quick clay development. *Sedimentology*, *31*(4), 595–598.

Smalley, I. J., Ross, C. W., & Whitton, J. S. (1980). Clays from New Zealand support the inactive particle theory of soil sensitivity. *Nature*, *288*(5791), 576–577.

Smith, N. D. (1978). Sedimentation processes and patterns in a glacier-fed lake with low sediment input. *Canadian Journal of Earth Sciences*, *15*(5), 741–756.

Smykatz-Kloss, W. (1982). Application of differential thermal analysis in mineralogy. *Journal of Thermal Analysis and Calorimetry*, *23*(1–2), 15–44.

Söderblom, R. (1969). *Salt in Swedish clays and its importance for quick clay formation. Results from some field and laboratory studies*. Statens geotekniska institut.

Spagnoli, G., & Feinendegen, M. (2017). Relationship between measured plastic limit and plastic limit estimated from undrained shear strength, water content ratio and liquidity index. *Clay Minerals*, *52*(4), 509–519.

Sridharan, A., & Rao, G. (1975). Mechanisms Controlling The Liquid Limit Of Clays. *Proc. of the Istanbul Conference on Soil Mechanics and Foundation Engineering*, *1*.

Sridharan, A., Rao, S. M., & Murthy, N. S. (1988). Liquid limit of kaolinitic soils. *Geotechnique*, *38*(2), 191–198.

Stewart, D. L. (2021). Responses to three 2017 landslide events affecting road networks in the lower North Island of New Zealand. *21st NZGS Symposium*. NZGS Symposium 2021, Dunedin.

Takahashi, H. (1958). Structural variations of kaolin minerals. *Bulletin of the Chemical Society of Japan*, *31*(3), 275–283.

Takahashi, T., Dahlgren, R. A., Theng, B. K. G., Whitton, J. S., & Soma, M. (2001). Potassium-selective, halloysite-rich soils formed in volcanic materials from northern California. *Soil Science Society of America Journal*, *65*(2), 516–526.

Takahashi, Y., Dahlgren, R. A., Kanno, H., Nanzyo, M., & Takahashi, T. (2018). Mechanisms for high potassium selectivity of soils dominated by halloysite from northern California, USA. *Soil Science and Plant Nutrition*, *64*(1), 90–99. https://doi.org/10.1080/00380768.2017.1411167

Tanaka, H., Hirabayashi, H., Matsuoka, T., & Kaneko, H. (2012). Use of fall cone test as measurement of shear strength for soft clay materials. *Soils and Foundations*, *52*(4), 590–599. https://doi.org/10.1016/j.sandf.2012.07.002

Tavenas, F. (1986). *Landslides in Canadian sensitive clays-a state-of-the-art.*

Tavenas, F., Chagnon, J.-Y., & Rochelle, P. L. (1971). The Saint-Jean-Vianney landslide: Observations and eyewitnesses accounts. *Canadian Geotechnical Journal*, *8*(3), 463–478.

Tazaki, K. (2005). Microbial formation of a halloysite-like mineral. *Clays and Clay Minerals*, *53*, 224–233.

Terzaghi, K. (1944). *Ends and means in soil mechanics*. Harvard University.

Thakur, V. (2007). *PhD Thesis: Strain Localization in sensitive SOFT CLAYS.*

Thakur, V., L'Heureux, J.-S., & Locat, A. (2017a). Landslide in Sensitive Clays – From Research to Implementation. In V. Thakur, J.-S. L'Heureux, & A. Locat (Eds.), *Landslides in Sensitive Clays: From Research to Implementation* (pp. 1–11). Springer International Publishing. https://doi.org/10.1007/978-3-319-56487-6_1

Thakur, V., L'Heureux, J.-S., & Locat, A. (Eds.). (2017b). *Landslides in Sensitive Clays* (Vol. 46). Springer International Publishing. https://doi.org/10.1007/978-3-319-56487-6

Thakur, V., Nordal, S., Viggiani, G., & Charrier, P. (2018). Shear bands in undrained plane strain compression of Norwegian quick clays. *Canadian Geotechnical Journal*, *55*(1), 45–56. https://doi.org/10.1139/cgj-2016-0443

Theng, B. K. G., Churchman, G. J., Whitton, J. S., & Claridge, G. G. C. (1984). Comparison of intercalation methods for differentiating halloysite from kaolinite. *Clays and Clay Minerals*, *32*, 249–258.

Theng, B. K. G., Russell, M., Churchman, G. J., & Parfitt, R. L. (1982). Surface Properties of Allophane, Halloysite, and Imogolite. *Clays and Clay Minerals*, *30*(2), 143–149. https://doi.org/10.1346/CCMN.1982.0300209

Theng, B. K. G., & Wells, N. (1995). The flow characteristics of halloysite suspensions. *Clay Minerals*, *30*(2), 99–106.

Tonkin, P. J. (1970). *Contorted stratification with clay lobes in volcanic ash beds, Raglan-Hamilton region, New Zealand*.

Torrance, J. K. (1983). Towards a general model of quick clay development. *Sedimentology*, *30*(4), 547–555.

Torrance, J. K. (1992). Discussion on sensitivity to remoulding ofsome volcanic ash soils in New Zealand, by D. Jacquet. *Engineering Geology*, *32*(1–2), 101–105.

Torrance, J. K. (2014). Chemistry, sensitivity and quick-clay landslide amelioration. *Landslides in Sensitive Clays: From Geosciences to Risk Management*, 15–24.

Torrance, J. K., & Ohtsubo, M. (1995). Ariake Bay quick clays: A comparison with the general model. *Soils and Foundations*, *35*(1), 11–19.

Varnes, D. J. (1958). Landslide types and processes. *Landslides and Engineering Practice*, *24*, 20–47.

Varnes, D. J. (1984). *Landslide hazard zonation: A review of principles and practice* (Issue 3).

Veerabadran, N. G., Price, R. R., & Lvov, Y. M. (2007). Clay nanotubes for encapsulation and sustained release of drugs. *Nano*, *2*(02), 115–120.

Vilder, S. de, Dellow, S., Archibald, G., & Morgenstern, R. (2019). *The 23rd January 2019 Cape Kidnappers Coastal Cliff Collapse, Hawke's Bay, New Zealand* [GNS Science Report 2019/26]. GNS Science. https://static.geonet.org.nz/info/reports/landslide/SR_2019-026.pdf

Wada, K. (1959a). Oriented penetration of ionic compounds between the silicate layers of halloysite. *American Mineralogist: Journal of Earth and Planetary Materials*, *44*(1–2), 153–165.

Wada, K. (1959b). Reaction of phosphate with allophane and halloysite. *Soil Science*, *87*(6), 325–330.

Wada, K. (1961). Lattice expansion of kaolin minerals by treatment with potassium acetate. *American Mineralogist: Journal of Earth and Planetary Materials*, *46*(1–2), 78–91.

Waltham, T. (2009). *Foundations of engineering geology*. CRC press.

Wei, R., Jia, C., Liu, L., & Wu, N. (2022). Analysis of the characteristics of pore pressure coefficient for two different hydrate-bearing sediments under triaxial shear. *Journal of Marine Science and Engineering*, *10*(4), 509.

Wesley, L. D. (1973). Some basic engineering properties of halloysite and allophane clays in Java, Indonesia. *Geotechnique*, *23*(4), 471–494.

West, S. L., White, G. N., Deng, Y., McInnes, K. J., Juo, A. S. R., & Dixon, J. B. (2004). Kaolinite, Halloysite, and Iron Oxide Influence on Physical Behavior of Formulated Soils. *Soil Science Society of America Journal*, *68*(4), 1452–1460. https://doi.org/10.2136/sssaj2004.1452

White, R. E. (2013). *Principles and Practice of Soil Science: The Soil as a Natural Resource*. John Wiley & Sons.

Widjaja, B., & Setianto, K. M. (2019). Effect of NaCl and CaCl2 solutions on the liquid limit, plastic limit, and plasticity index of clay. *IOP Conference Series: Materials Science and Engineering*, *508*, 012045. https://doi.org/10.1088/1757-899X/508/1/012045

Wood, D. M. (1990). *Soil behaviour and critical state soil mechanics*. Cambridge university press.

Wyatt, J. B. (2009). *Sensitivity and clay mineralogy of weathered tephra-derived soil materials in the Tauranga region* [PhD Thesis]. The University of Waikato.

Yi, T., & Gribina, I. A. (1972). IR - Spectroscopic Study of State of Water in Halloysite. *Kolloidnyi Zhurnal*, *34*(3), 405-+.

Yuan, J., Zhang, Q., Li, B., & Zhao, X. (2013). Experimental analysis of shear band formation in plane strain tests on Shanghai silty clay. *Bulletin of Engineering Geology and the Environment*, *72*(1), 107–114. https://doi.org/10.1007/s10064-012-0453-4

Yuan, P., Tan, D., & Annabi-Bergaya, F. (2015). Properties and applications of halloysite nanotubes: Recent research advances and future prospects. *Applied Clay Science*, *112–113*, 75–93. https://doi.org/10.1016/j.clay.2015.05.001

Yukselen, Y., & Kaya, A. (2003). Zeta potential of kaolinite in the presence of alkali, alkaline earth and hydrolyzable metal ions. *Water, Air, and Soil Pollution*, *145*, 155–168.

Zhang, X., Liu, H., Xing, H., Li, H., Hu, H., Li, A., & Yao, H. (2017). Improved sodium adsorption by modified kaolinite at high temperature using intercalation-exfoliation method. *Fuel*, *191*, 198–203. https://doi.org/10.1016/j.fuel.2016.11.067

Zhong, X.-H., Liu, Y., Xu, T., & Liu, W.-Y. (2018). Influencing factors of intercalation of potassium acetate into dickite using immersion method. *Journal of Alloys and Compounds*, *742*, 996–1001. https://doi.org/10.1016/j.jallcom.2017.12.267

Zich, D., Zacher, T., Darmo, J., Szöcs, V., Lorenc, D., & Janek, M. (2013). Far-infrared investigation of kaolinite and halloysite intercalates using terahertz time-domain spectroscopy. *Vibrational Spectroscopy*, *69*, 1–7. https://doi.org/10.1016/j.vibspec.2013.09.003